Optical Fiber Interferometric Sensors

New Production Methodologies and Novel Applications

Edited by

Maria de Fatima Domingues, Nélia J. Alberto and Paulo André

MDPI

Optical Fiber Interferometric Sensors: New Production Methodologies and Novel Applications

Optical Fiber Interferometric Sensors: New Production Methodologies and Novel Applications

Editors

Maria de Fatima Domingues
Nélia J. Alberto
Paulo André

Editors

Maria de Fatima Domingues
Instituto de Telecomunicações
and University of Aveiro
Portugal

Nélia J. Alberto
Instituto de Telecomunicações
and University of Aveiro
Portugal

Paulo André
Instituto de Telecomunicações
and Department of Electrical and
Computer Engineering,
Instituto Superior Técnico,
University of Lisbon
Portugal

For citation purposes, cite each article independently as indicated on the article page online and as indicated below:

LastName, A.A.; LastName, B.B.; LastName, C.C. Article Title. *Journal Name* **Year**, *Volume Number*, Page Range.

Contents

About the Editors

Maria de Fatima Domingues (Dr.), received her MSc in Applied Physics in 2008, and in 2014 she finished her PhD in Physics Engineering, both at the University of Aveiro, Portugal. In 2015, Dr. Domingues started a Research Fellow position at the Instituto de Telecomunicações—Aveiro and the Consejo Superior de Investigaciones Científicas (CSIC)-Madrid, Spain. At present, Dr. Domingues is a Researcher at Instituto de Telecomunicações—Aveiro, and her current research interests embrace new solutions of optical fibre based sensors and its application in e-Health scenarios, with a focus on physical rehabilitation architectures. Dr. Domingues has authored and co-authored more than 100 journal and conference papers, 5 book chapters and 3 books.

Nélia J. Alberto (Dr.), received her PhD degree in Physics in 2011 at University of Aveiro, Portugal. During the 2012–2017 period, she worked under a FCT post-doctoral research fellowship, and in 2018, she was hired as Researcher by the Instituto de Telecomunicações—Aveiro (Portugal). She has acquired expertise in the design and development of optical fibre sensors, fibre coatings and application in different contexts, with a special focus on medical environments. Dr. Alberto is author/co-author of 6 book chapters, 50 papers in international peer-review journals, and more than 60 papers in conference proceedings. Since 2020, she has been dedicated to teaching activities at Physics Department of the Aveiro University (Portugal).

Paulo André (Prof.) was born in 1971. He received his bachelor's degree in physics engineering (1996), the Ph.D. degree in physics (2002), and the Agregação title (habilitation) from the Universidade de Aveiro, Portugal. Since 2019 he is full professor of the department of electrical and computer engineering at Instituto Superior Técnico (IST), University of Lisbon and is senior researcher at Instituto de Telecomunicações. His current research interests include the study and simulation of photonic and optoelectronic components, for sensing, communications and energy applications. Paulo André is a senior member of the Institute of Electrical and Electronics Engineers (IEEE).

Editorial

Special Issue "Optical Fiber Interferometric Sensors: New Production Methodologies and Novel Applications"

M. Fátima Domingues [1,*], Nélia Alberto [1] and Paulo André [2]

[1] Instituto de Telecomunicações and University of Aveiro, Campus Universitário de Santiago, 3810-193 Aveiro, Portugal; nelia@ua.pt

[2] Department of Electrical and Computer Engineering and Instituto de Telecomunicações, Instituto Superior Técnico, University of Lisbon, 1049-001 Lisbon, Portugal; paulo.andre@lx.it.pt

[*] Correspondence: fatima.domingues@ua.pt

Abstract: The collection of papers presented in this Special Issue (SI) portraits the state-of-the-art of photonic-based interferometric sensors, where new application areas were explored (such as spirometry) and novel sensitivity limits were achieved, using innovative sensing techniques for the monitoring of parameters, such as displacement, temperature or salinity.

Keywords: interferometric sensors; optical fiber; photonics

1. Introduction

Optical fiber interferometric sensors have been an expanding research topic in recent years, mainly due to its ability to perform measures with extreme accuracy on a variety of physical parameters, which range from temperature, strain, pressure, and chemical quantities to physiological parameters. For this Special Issue (SI), both original research papers and review articles describing the current state-of-the-art in this research field were requested and welcome, with the aim to provide a collection of high-quality papers, reporting on the present status and future outlook of the following topics:

— New and/or low-cost interferometers production methods;
— Novel optical fiber Fabry–Perot, Mach-Zehnder, Michelson, and Sagnac-based sensors;
— Optical fiber interferometric-based sensing for physical and chemical parameters;
— Optical fiber interferometric systems with microfluid integration;
— Low-cost, miniaturized, selective and multiparameter optical fiber interferometric devices;
— New bio/chemical probes for biomedical applications;
— Wearable/biomedical interferometric sensors;
— Advanced signal processing techniques;
— New interrogation techniques for interferometric sensors;
— New applications of optical fiber interferometric sensors.

The contributions to this SI resulted in a collection of 12 papers reporting on the advances in the research of interferometric optical fiber-based sensors and its novel applications. The scope of this SI intends to provide a synopsis of the current research trends and state-of-the-art in this field, covering recent technological improvements, new production methodologies and emerging applications, for researchers coming from different fields of science and industry.

The manuscripts published under this SI report on topics that range from interferometric sensors for thickness and dynamic displacement measurement, up to pulse wave (PW) and spirometry applications. A brief overview of the collection of papers present in this SI will be described in the following section.

We appreciate the authors' contributions to this SI, which gathers original papers with a comprehensive and up-to-date overview on a variety of topics, with the common denominator based on new optical fiber and photonic-based interferometric sensors.

Additionally, we would like to thank the academic editors and reviewers for their efforts and contributions to guarantee the scientific rigor and quality of the manuscripts published and, consequently, of this SI.

2. Contributed Papers

The papers collected in this SI reflect the importance of the topic for the research community, and the wide field of applications in which such novel technological advances can have improved performance.

Among the diverse fields of applications gathered in this SI, Gao et al. reported on a speckle interferometry system for micro-electromechanical systems (MEMs) dynamic displacement measurement. They proposed a large-field microscopic speckle interferometer, based on two embedded doublet lens groups for the realization of an improved optical Mach-Zehnder system. With the proposed solution, the authors can expand the field of view, while reducing the coherent noise of the reflected signal, achieving a high precision and real time dynamic measurement of MEMS [1].

On a different application, the authors from [2] reported on the use of digital grating Moiré effect, to be applied in the measurement of the curvature radius and focal lengths of biconvex and biconcave spherical lenses and mirrors. With the proposed methodology, they proved to be able to provide measurements of focal length and a radius of curvature with errors below 0.5% [2].

The authors of [3] report on the development and implementation of an optical contactless technique to monitor the production of plastic films which thicken in real time. The developed apparatus is a low-coherence fiber interferometer, based on a cross between an auto-correlator and a white light interferometer, which is able to measure blown film thickness during production [3].

Stolarik et al. contributed to this SI with a report on promising alternatives for vibration measurements, with an optical fiber Michelson interferometer, designed with passive demodulation technique using three mutually phase-shifted optical outputs [4]. The performance of this device was compared with existing seismic devices, and the results demonstrate its great potential, with correlation coefficients above 0.9, and average deviations of the amplitude of the oscillation velocity around 0.02. [4].

Another paper that contributed to the success of this SI, from the authors of [5], reports on different optical fiber-based interferometric techniques to monitor the PW signal. The authors provide an exhaustive comparison of performance (signal to noise ratio, repeatability, and suitability of demodulated signals), of the optical fiber sensors based on fiber Bragg grating (FBG), Fabry–Perot interferometer (FPI), single mode–multimode–single mode intermodal interferometer and optical coherence tomography (OCT), to monitor the PW signal [5]. From the presented study, it was concluded that OCT-based sensors outperform the other solutions in terms of signal demodulation quality and robustness and presented a clear discussion of the advantages and drawbacks of all compared PW measurement approaches [5].

Marques et al., contributed to this SI, with a manuscript in which the suitability of the Master–Slave (MS) procedures for processing/calibration of the signal from interferometers, driven by akinetic sources, that exhibit non-linear tuning, was evaluated [6]. The authors explore the use of two different MS-processing techniques for the akinetic source calibration, being able to recover, in both cases, the spectral depth information, enabling an improved analysis of phase errors, which may occur around invalid-to-valid transactions or due to the source performance [6].

Additionally, an enhanced temperature sensor, based on a dual-core fiber with an eccentric core and a central core in-fiber Mach-Zehnder sensor, was reported by Qiu et al. [7]. The central core effective refractive index is modulated by the glycerol–water solution in the fluidic channel, adjacent to the central core. The sensor-transmitted spectra are shifted, according to the temperature variations, with a sensitivity of 2.77 nm/°C (for a channel with 15 cm). The authors also found a relation between the sensitivity of the sensor and the

length of the fluidic channel, showing that the longer the channel, the higher the sensor's sensitivity (a length of 29.5 cm will provide an increased sensitivity of 5.69 nm/°C) [7].

The report on a high sensitivity displacement interferometer-based sensor, combining the Vernier effect and the push and pull method, was reported in [8]. The combination of these two methodologies, and the optimization of the two interferometers, resulted in a sensitivity of 254 ± 6 nm/µm, a magnification factor (M) of 1071 and an $M_{Vernier}$ of 1.9 [8].

Additionally, the development of solutions to monitor seawater salinity was presented by Zhou et al. The solution proposed is based on a novel microfiber coupler interferometer, produced by connecting the two out ports of a microfiber coupler, to Faraday rotating mirrors. The proposed solution exhibited a spectral red shift with a water salinity increase, with the highest sensitivity reaching 303.7 pm/‰ and a resolution of 0.03‰ [9].

Another temperature sensor, based on a photonic crystal fiber (PCF) Sagnac interferometer, was presented in [10], where the authors, theoretically and experimentally, reported on a liquid-filled highly asymmetric PCF structure for temperature monitoring. The proposed structure presented a sensitivity of 17.53 nm/°C with a resolution of 5.7×10^{-4} °C [10].

As part of this SI collection, is also the review manuscript provided by Hillmer et al., focusing on a detailed comparison (spectral range required, resolution, tunability, efficiency, multiplexing capabilities, miniaturization limits, and potential of nanoimprint), of different miniaturized sensor concepts for nanoimprint. The study ranges from classical optical transmission and reflection gratings, up to fiber tip sensors, also exploring static FPI filter arrays, plasmonic filters and MEMS tunable FPI interferometers. The work presented by these authors provides a thorough analysis of the above-mentioned technologies, and its potential to be fabricated by nanoimprint techniques [11].

Finally, a novel application of FPI-based sensors was reported by Nepomuceno et al., where the authors presented an optical fiber FPI-based, 3D printed device to evaluate the individual pulmonary capacity by spirometry [12]. The spirometer is based on the conversion of the air flow into strain variations applied to the optical fiber, which modulates the FPI spectral response. In this contribution, an exhaustive theoretical analysis of the device, as well as its preliminary results, is presented, from which it was possible to acquire spirometry critical parameters: forced expiratory volume in 1 s (FEV1), forced vital capacity (FVC), FEV1/FVC index and the peak expiratory flow (PEF) [12].

3. Outlook and Prospects

The papers collected in this SI represent only a small window of the current interest and developments in photonic-based sensors, with a particular focus on interferometric devices. The development of new production methodologies, targeting more cost effective and less complex production lines, still has room to grow. Innovative and promising developments of the production methods, devices and techniques for spectral analysis, and new areas of application are to be expected for this type of sensing device.

Author Contributions: M.F.D. wrote the manuscript draft. N.A. and P.A. contribute to the manuscript revision. All authors have read and agreed to the published version of the manuscript.

Conflicts of Interest: The authors declare no conflict of interest.

References

1. Gao, C.; Gao, Z.; Niu, Y.; Wang, X.; Zhao, J.; Deng, L. An Improved Large-Field Microscopic Speckle Interferometry System for Dynamic Displacement Measurement of MEMS. *Photonics* **2021**, *8*, 271. [CrossRef]
2. Han, C.-Y.; Lo, W.-T.; Chen, K.-H.; Lee, J.-Y.; Yeh, C.-H.; Chen, J.-H. Measurement of Focal Length and Radius of Curvature for Spherical Lenses and Mirrors by Using Digital-Grating Moiré Effect. *Photonics* **2021**, *8*, 252. [CrossRef]
3. Norgia, M.; Pesatori, A. Interferometric Instrument for Thickness Measurement on Blown Films. *Photonics* **2021**, *8*, 245. [CrossRef]
4. Stolarik, M.; Nedoma, J.; Martinek, R.; Kepak, S.; Hrubesova, E.; Pinka, M.; Kolarik, J. New Methods to Seismic Monitoring: Laboratory Comparative Study of Michelson Fiber-Optic Interferometer and Pneumatic Measurement Systems. *Photonics* **2021**, *8*, 147. [CrossRef]
5. Ushakov, N.; Markvart, A.; Kulik, D.; Liokumovich, L. Comparison of Pulse Wave Signal Monitoring Techniques with Different Fiber-Optic Interferometric Sensing Elements. *Photonics* **2021**, *8*, 142. [CrossRef]
6. Marques, M.J.; Cernat, R.; Ensher, J.; Bradu, A.; Podoleanu, A. Akinetic Swept-Source Master–Slave-Enhanced Optical Coherence Tomography. *Photonics* **2021**, *8*, 141. [CrossRef]
7. Qiu, H.; Zhao, C.; Hu, X.; Chen, H.; Yu, Q.; Lian, Z.; Qu, H. Glycerol–Water Solution-Assisted Mach–Zehnder Temperature Sensor in Specialty Fiber with Two Cores and One Channel. *Photonics* **2021**, *8*, 103. [CrossRef]
8. Robalinho, P.; Frazão, O. Giant Displacement Sensitivity Using Push-Pull Method in Interferometry. *Photonics* **2021**, *8*, 23. [CrossRef]
9. Zhou, L.; Yu, Y.; Huang, H.; Tao, Y.; Wen, K.; Li, G.; Yang, J.; Zhang, Z. Salinity Sensing Characteristics Based on Optical Microfiber Coupler Interferometer. *Photonics* **2020**, *7*, 77. [CrossRef]
10. Monfared, Y.E.; Ahmadian, A.; Dhasarathan, V.; Liang, C. Liquid-Filled Highly Asymmetric Photonic Crystal Fiber Sagnac Interferometer Temperature Sensor. *Photonics* **2020**, *7*, 33. [CrossRef]
11. Hillmer, H.; Woidt, C.; Kobylinskiy, A.; Kraus, M.; Istock, A.; Iskhandar, M.S.Q.; Brunner, R.; Kusserow, T. Miniaturized Interferometric Sensors with Spectral Tunability for Optical Fiber Technology—A Comparison of Size Requirements, Performance, and New Concepts. *Photonics* **2021**, *8*, 332. [CrossRef]
12. Nepomuceno, A.C.; Paixão, T.; Alberto, N.; André, P.S.d.B.; Antunes, P.; Domingues, M.F. Optical Fiber Fabry–Perot Interferometer Based Spirometer: Design and Performance Evaluation. *Photonics* **2021**, *8*, 336. [CrossRef]

Miniaturized Interferometric Sensors with Spectral Tunability for Optical Fiber Technology—A Comparison of Size Requirements, Performance, and New Concepts

Hartmut Hillmer [1,*]**, Carsten Woidt** [1]**, Aliaksei Kobylinskiy** [1,2]**, Matthias Kraus** [1,2]**, André Istock** [1]**, Mustaqim S. Q. Iskhandar** [1]**, Robert Brunner** [2] **and Thomas Kusserow** [1,†]

[1] Institute of Nanostructure Technologies and Analytics (INA) and Center for Interdisciplinary Nanostructure Science and Technology (CINSaT), University of Kassel, 34132 Kassel, Germany; woidt@ina.uni-kassel.de (C.W.); Aliaksei.Kobylinskiy@eah-jena.de (A.K.); Matthias.Kraus@eah-jena.de (M.K.); istock@ina.uni-kassel.de (A.I.); iskhandar@uni-kassel.de (M.S.Q.I.); kusserow@ina.uni-kassel.de (T.K.)

[2] Applied Optics, Department SciTec, University of Applied Sciences Jena, Carl-Zeiss-Promenade 2, 07745 Jena, Germany; Robert.Brunner@eah-jena.de

* Correspondence: hillmer@ina.uni-kassel.de

† Present address: Institute of Microsystems Technology, Hamburg University of Technology, Eißendorferstr. 42, 21073 Hamburg, Germany.

Abstract: Optical interferometric sensors have acquired significant importance in metrology and information technology, especially in terms of their potential application in launching size, selectivity, sensitivity, resolution, spectral tuning ranges, efficiency, and cost. However, these demands are often contradictory and counteract one another, and are thus difficult to simultaneously fulfill during their interaction. This review focuses on a detailed comparison of seven different strongly miniaturized sensor concepts investigating the limits of these demands. For the visible and near-infrared spectral range, seven optical sensors were reviewed based on the following methodologies: classical optical transmission and reflection gratings, arrayed waveguide gratings, static Fabry–Pérot (FP) filter arrays, MEMS tunable FP interferometers, MEMS tunable photonic crystals, plasmonic filters, and fiber tip sensors. The comparison between the selected concepts concentrates on (i) the minimum space required for a particular spectral range, (ii) resolution, (iii) the integration in optical fiber technology, (iv) tunability to save space, (v) efficiency in using available light, (vi) multiplexing, (vii) miniaturization limits, and (viii) the potential of nanoimprint for cost reduction. Technologies for enhancing efficiency to obtain more available light and their applicability to the different methodologies were studied.

1. Introduction

Wearable interferometric sensors require a small size, high selectivity, and sensitivity if biomedical applications are envisaged. These three requirements often involve counterrunning demands and have previously been found to be difficult to satisfy in a single system. Such a limitation is also relevant in many other application fields of photonic methodologies: highly accurate metrology; health and environmental monitoring; food sensing; quality control in industrial fabrication; smart personal environments; and high data rate communication technologies. Wearable interferometric sensors are characteristically lightweight with a small footprint as a result of miniaturization, which at the same time enables low-cost, precision, and high efficiency. Photonic sensorics [1–10] enable extraordinary sensitivity, outstanding selectivity, and broad application fields [1] such as industrial production control, environmental trace gas detection, agriculture growth monitoring, medical prevention and medical diagnosis, and fiber optic communication technologies. Many of the optical sensors use fiber or optical waveguide technology and are already integrated in communication systems, with high

potential for future integration in wearable interferometric sensors or in devices used for smart personal environments. However, a key challenge remains that of combining their outstanding performance in terms of resolution and efficiency while being miniaturized as much as possible at the same time.

In this review, methodologies of optical sensing in the near-infrared (NIR), visible (VIS), and ultraviolet (UV) spectral wavelengths ranges are introduced. This review also refines one of our recent papers [11], extending it toward integration into optical fiber technology and the improvement of the estimation of minimum size requirements, as well as formulates new insight into tunability efficiency.

A systematic overview of the different spectroscopic sensing principles is shown as a block diagram in Figure 1. In principle, the wide variety of sensor types can be categorized into different schemes. From a physical point of view, classification in accordance with the optical working principles is appropriate. For potential economic exploitation, classification with respect to robustness, complexity, recording and analyzing speed, potential applicability for high volume manufacturing, and the consideration of price aspects would be rather helpful. The block diagram shown here distinguishes in the first level between different optical working principles and focuses in the second level on sensor concepts that are particularly suitable for miniaturization and compatible with waveguide technology. The sensor concepts listed in the bottom row are considered in detail in this contribution.
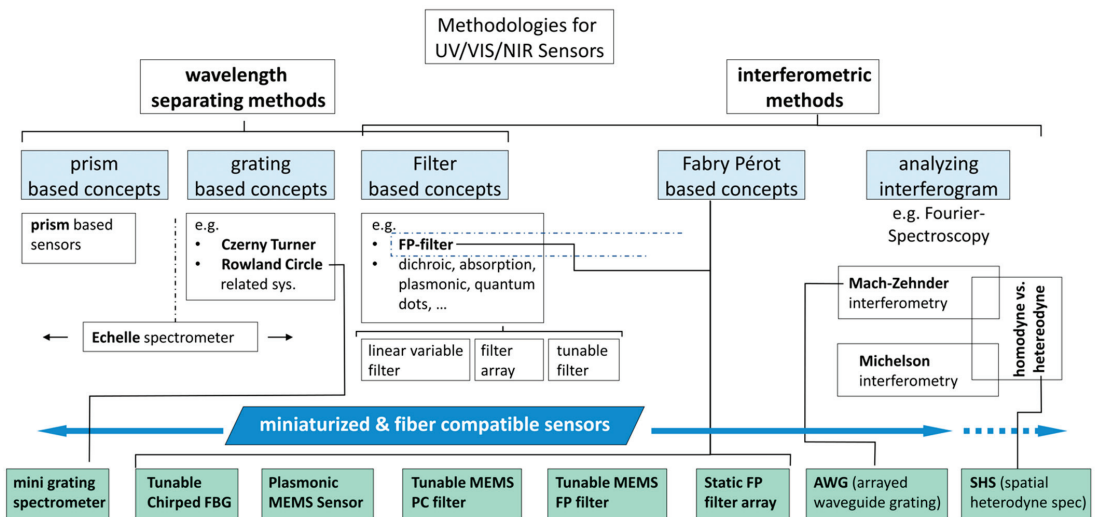
Figure 1. Block diagram of the sensor and spectrometer types considered in this review. This diagram should provide a general overview and an orientation throughout this extensive paper.

Traditional optical spectrometers [4,8–10] use prisms or gratings as dispersive or diffractive elements to dissolve the studied optical information into a spectrum (intensity versus wavelength plot). A transmission grating is depicted in Figure 2. As a general rule, a higher grating order means higher resolution; however, unfortunately, this also means a smaller intensity. To overcome this major disadvantage, the gratings are often blazed (exhibiting e.g., a saw-tooth structure) to transform the desired highest intensity from the zero order into higher diffraction orders [4]. This enables a rather high resolution and a relatively high intensity to be achieved at the same time.
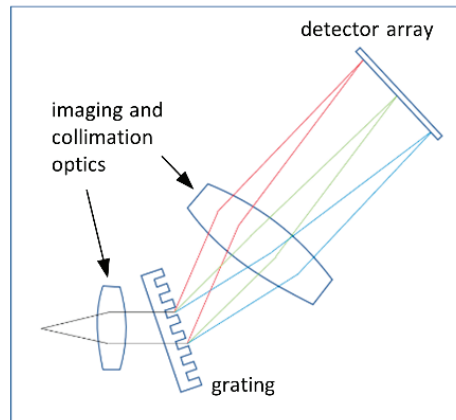
Figure 2. Schematic design of a transmission grating spectrometer with a symbolic grating shape.

There are different options to miniaturize the sensors, and Micro-Electro-Mechanical Systems (MEMS) represent one miniaturization option that enables wavelength tuning. In particular, FP and photonic crystal sensor systems or grating spectrometers can be miniaturized using MEMS. Actuation in MEMS-based devices was demonstrated for different material systems and wavelength ranges using different methodologies such as thermal, electromagnetic, piezoelectric or electrostatic actuation methodologies. Even in traditional grating spectrometers, MEMS can be applied to rotate the grating [12–15] and enable good performance.

More advanced methodologies use interferometry [3,4,16–20] for optical sensing based on the Mach–Zehnder, Fabry–Pérot, Michelson, and Sagnac principle. Additionally, there are many others which are closely related to these concepts. In the Michelson interferometer [3,4] the incident light beam (input) is split into two parts that are reunified again at a later stage before reaching the photodiode sensor as the output beam. Precisely delaying one of the two beams generates a distinct phase shift, though a proper calibration has to be completed before using the interferometric sensor. Next, the interferogram (intensity as a function of the varying phase delay) is converted into the wavelength range, thus, delivering the spectrum of the input. The smaller the considered light wavelength, the higher mechanical precision required to obtain the phase shifts. Therefore, the involved mechanics is less complex in the NIR compared to the VIS range. Fourier spectroscopy [3] uses the Michelson interferometer in the NIR, in which the interferogram is the Fourier transform of the input signal [3].

The input beam is also separated into two branches in the Mach-Zehnder interferometer [19,20]. Likewise, the two waves propagating through the branches experience different optical path lengths (defined as the product of refractive index and physical length). The two beams are then reunified, and the varying phase shifts between the two beams result in different corresponding intensities of the output beam. Integrated Mach-Zehnder interferometers can be implemented using ridge or embedded waveguides. Today, integrated Mach-Zehnder interferometers are often applied as modulators or sensors and were demonstrated in many various materials such as Si, InP, $LiNbO_3$, dielectric materials, inorganic glass, organic glass and polymers. By integrating a plate capacitor to one of the waveguide branches, the effective refractive index of that waveguide branch can be tuned via the capacitor voltage (i.e., the variable electrical field), making use of the electrooptic effect. Tuning the voltage produces an interferogram, and Fourier transforming the interferogram gives the spectra. A very important variant of the Mach-Zehnder interferometer is the derived arrayed waveguide grating (AWG) [21–27]. The AWG and Mach-Zehnder interferometers are perfectly adapted for use in fiber optical systems. There-

fore, the AWG represents a significant waveguide-based sensor type and a basic device in dense wavelength division multiplex (DWDM) systems for present high-speed and high bitrate optical data and telecommunication systems. More than 100 waveguide branches of tailored lengths can be combined in an AWG. These interferometric devices are also named phased arrays. Yoshikuni et al. have contributed pioneering work in the field of AWGs for fiberoptic telecommunication in the 1.5 μm communication bands, in which channel spacings of 50 GHz were achieved [22–24]. AWG consist of M waveguides (related to M fiberoptic DWDM channels) of different optical path lengths which are introduced not by the effective refractive index, but by the varying physical lengths. The individually tailored lengths lead to distinct phase shifts at the output of the different waveguides. The waveguide couples the waves out into a free beam section in which (mode) confinement is only given by a vertical waveguide structure. At the opposite end of the free beam section, light constructively interferes only at specific positions. Another M waveguides are beginning exactly at these positions, representing the output ports. The waveguides are spectrally ordered. Therefore, each individual output waveguide only guides light in an interval of $\Delta\lambda i$ with a central wavelength λi (vacuum wavelength), where $i = 1 \ldots M$. These Mach-Zehnder and AWG sensors constitute a second interferometric sensor design.

The third sensor design, based on the Fabry-Pérot (FP) principle [4,28–58], uses also interferometric methodologies and is well suitable for fiberoptic sensors. Although no beam splitters are involved and only two transparent dielectric parallel mirrors are present, the FP interferometer involves multipath interference and is highly complex. The important optical element embedded between the two mirrors is the FP cavity. Inside the FP interferometer cavity, some wavelengths are dimensioned in a way that they can constitute standing light waves, and thus fulfilling the FP condition. For a vacuum (air) cavity and two perfectly flat metal mirrors embedding the cavity, the condition can be described by a simple formula: a multiple of half of the vacuum wavelength equals the cavity length. These explicit standing wavelengths are the cavity modes. However, in real conditions which have to be considered in interferometric sensorics, the modes (standing waves) penetrate into the dielectric mirrors. Even by replacing the vacuum wavelength in the FP condition with the wavelength in the medium (vacuum wavelength divided by the cavity refractive index), it is still a very rough approximation. This phenomenon is detailed later in Section 10. The wavelength of each specific mode (standing wavelength) passes the interferometer nearly unattenuated (almost 100% of the input intensity). It is quite common to refer to FP interferometers as FP filters, where the modes are also defined as FP filter lines. The reason for a specific wavelength passes the filter unattenuated and unreflected is due to constructive interference of all multipath waves at the FP output. All the remaining wavelengths which do not constitute modes experience destructive interference at the output. They are reflected by the FP filter and show constructive interference in the reflected beam. By shifting one of the mirrors precisely parallel along the optical axis, the corresponding spectrum, i.e., a spectral tuning of the wavelength, is obtained. Therefore, this interferometer also constitutes a spectrometer. By applying MEMS technology, wavelength tuning can be obtained by displacing one or both mirrors using MEMS actuation [37–57].

Adding optical substructures in the nanometer range onto membranes or cantilevers of MEMS offers further options to optimize the optical sensor assets. As the substructure size is roughly a factor of 100 below the typical dimensions of MEMS membranes or cantilevers, an integration of substructures is not affecting the general contour or functionality of these MEMS sensors. Often, 1D or 2D photonic crystal (PC) structures are integrated into membranes to enable specific guided mode resonances (GMR) [59,60]. In this case, the released MEMS layer is a slab waveguide with light waves incident in normal direction to the interfaces of the slab. Without integrating a PC structure, the free space mode is not able to couple to a guided mode in the slab. In contrast, it will be reflected and transmitted at each interface, constituting a typical thin-film spectrum. If a grating pattern with a period in the range of the desired wavelength range is added, this will lead to resonant coupling

of a part of the incident wave into a leaky mode inside the slab. Because of its leaky nature, the mode will couple back—out of the slab—into both vertical directions and superimpose with the residual incident and transmitted free space mode (known as continuous mode). This results in a filter resonance line with Fano characteristics, both in transmission and reflection [61]. If the resonant coupling conditions are tailored appropriately, line shape and spectral width are influenced. Narrow linewidths are accomplished by applying low coupling strengths, while broadband reflections can be obtained using strong coupling and applying an overlap of several individual resonances. Sensors using the GMR can be strongly miniaturized [62] since they replace vertical periodic patterns of distributed Bragg reflectors (DBR) by horizontal pattern inside a single membrane. This means that they translate full FP filters into a narrowband Fano resonance of a PC slab. However, their fabrication and application are a real challenge due to their strong angle dependency. Therefore, use of very flat membranes or cantilevers is crucial, but this effect also restricts the acceptable angular spectrum of the incident light beam. As a consequence, the spot diameter and related divergence which can be used are restricted.

If the axial symmetry of 90° is disturbed in the PC-based sensors or in the sensor lattice itself, altered conditions are obtained for in- and out-coupling along the x- and y-direction, thus enabling further polarization selectivity of the sensor element. In the simplest case, this is obtained by a line grating (1D PC). A higher degree of control on coupling properties is achieved by 2D PC patterns with elements owning elliptical [63–65] or keyhole [66] shapes. Please note that the x- and y-coordinates are spanning the in-plane directions. An alternative to enable polarization selectivity is using sub-wavelength structures. In this case, the interaction with the incident waves is defined by the effective refractive index method. Appropriate designs of the pattern disrupt the 90° symmetry, leading to different effective indices for transverse magnetic (TM) and transverse electric (TE) polarization, and subsequently resulting in structural birefringence [67].

Nano-optic effects may be also used to substitute the dispersive elements of sensors. Surface-plasmon-polaritons (SPP) reveal resonances and interact efficiently in the optical nearfield. However, they experience the same critical trade-off between resolution of grating spectrometers and their ability for downscaling because they are based on the angular dispersion of the spectrum as well. In addition, the standard Kretschmann method of excitation makes downscaling quite difficult due to the required bulky prisms. The problem was addressed using a metallic grating coupler for surface plasmons positioned on a scanning MEMS cantilever, and then to read out the influence on the photodiode current of an integrated photosensor [68]. An alternative to improve the resolution of miniaturized spectrometers is achieved via the super prism effect in PC structures. The dispersion properties of a periodic 2D pattern can be designed to be much more pronounced than those of a 1D grating if the shape of the photonic bands is appropriately tailored close to the bandgap [69]. Nonetheless, it was shown that with 1D structures in form of chirped, resonant, or general layer stacks, a strong super prism effect is possible as well [70].

Continuing with this general overview of optical sensing, methodologies and instrumentation, the focus is now placed on the miniaturization potential of grating spectrometers. Concerning size, optical grating spectrometers used in the NIR, VIS, and UV span a length between several mm and a few meters. The optical resolution $\Delta\lambda/\lambda$ of the grating spectrometer is obtained by multiplying the diffraction order n with the number of illuminated grating periods N, approximately. If we have to miniaturize the grating spectrometer, we are forced to reduce N since it is impossible to reduce the grating period (the application defines the wavelength range we have to consider). In addition to the resolving power of the grating, the pixel sizes and the path lengths determine the resolution of the spectrometers, as can be seen in Figure 2. Thus, we can only reduce the size of the grating, and this means to reduce the total number of grating lines N and to shorten the optical path length inside the spectrometer. Decreasing N reveals a strong and negative impact on the spectral resolution. The first two photos (from left) in Figure 3 display the mini transmission grating spectrometer PEBBLE from the company Ibsen Photonics, Denmark [71] and the mini

reflection grating spectrometer C10988MA-01 from the japanese company Hamamatsu Photonics, in which that of Hamamatsu reveals stronger miniaturization. In the second column (from left) in Figure 3, data from the two smallest grating spectrometers, C12880MA and C14384MA [72], are included. Currently, the C14384MA-01 and the PEBBLE are most probably the smallest grating-based optical mini spectrometers available in the market. The corresponding package dimensions of the C14384MA-01 are located in the sub-centimeter range. Scaling down this spectrometer could only be accomplished at the expense of the grating size, i.e., to work with a rather limited number of grating lines N. For the spectral range of 540–1050 nm, the datasheets of the spectrometer reveal full width at half maximum (FWHM) of 17–25 nm (equivalent to linewidths) and corresponding resolutions $\Delta\lambda/\lambda$ of 42–56. This sensor type makes the most efficient use of available light compared to all other sensor methodologies, and it is compatible with fiberoptic systems since it is also available with fiber pigtails. However, if strong miniaturization is required, the achievable resolution is often not sufficient: As already mentioned, grating spectrometer resolution and is strongly decreasing with shrinking size. Luckily, there are many alternative methodologies providing high resolution independent of size, and some of them will be discussed and compared in this review.

Concerning wavelength dispersing options for fiberoptic, sensor principles which (i) are compatible to fiber technology, (ii) have high resolution, and (iii) reveal strong miniaturization potential are considered. The following alternatives are included (and summarized in Figure 3): Static FP filter arrays on complementary metal oxide semiconductor (CMOS) sensor arrays or charge coupled devices (CCD) [28–37], MEMS tunable FP filter arrays [38–57] on photodetector (PD) arrays, AWG structures [21–27], MEMS tunable photonic crystal (PC) filters [62,73–77], plasmonic MEMS cantilevers [68] and thermally tuned chirped fiber Bragg gratings (FBG). Compared to the mini grating spectrometers mentioned above, all these alternatives reveal higher resolution, lower FWHM, and are much smaller in size. The content of Figures 1 and 3 will be considered throughout the whole review. Please note that there are other alternatives than those mentioned in Figure 3, such as MEMS grating spectrometers or Fourier spectrometers which were also strongly miniaturized in the past. However, these are beyond the scope of our paper. The focal points of our review are (i) to describe their method of integration into optical fiber systems, (ii) to show alternative fabrication technologies such as nanoimprint, (iii) to enlarge wavelength tuning behavior, (iv) to identify limits for optical sensor miniaturization, and (v) to envisage performance improvement and cost reduction.

This review emphasizes FWHM, resolution, and potential miniaturization limits with the focus on FP-type interferometers, and delivers various quantitative comparisons. The efficiency in using available light is discussed in detail and the different sensor methodologies are compared with respect to efficiency in this review. There is another recent and well elaborated review paper about miniaturized spectrometers [78] emphasizing the classification of spectrometer methodology and focusing on computational (reconstructive) and Fourier transform methodologies. It is more qualitative rather than quantitative with regard to miniaturization limits, since it only gives the extension in 1D. In contrast, our review gives the required area in 2D. Efficiency is not included in the scope of [78], but it is crucial for signal-to-noise ratio. Thus, our review and the review [78] ideally complement each other.
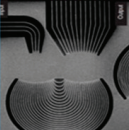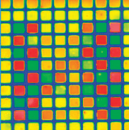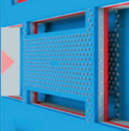
Miniaturized spectrometers for larger spectral ranges	Mini Spectrometer	Mini Spectrometer	AWG	Static FP filter array	Tunable MEMS FP filter	MEMS tunable PC filter	Plasmonic MEMS Sensor	Tunable Chirped FBG
Operation principles	Transmission Grating	Reflection Grating	Mach Zehnder interf.	FP interferometer	FP interferometer	Photonic crystal PC	Plasmonic coupling	Grating phase shift
Spectral range	340–830 nm [71] / 950–1700 nm [71]	340–850 nm [72] / 640–1050 nm [72]	643–863 nm [26] / 1530–1565 nm	400–1700 nm	200–2000 nm	1290–1340 nm	550–1700 nm	200–2000 nm
Active tuning range					221 nm @ 1.5 µm [56]	30 nm	300 nm @ 1.4 µm [68]	16.5 nm @ 1.5 µm [79]
FWHM Δλ typical values VIS	6 nm [71]	13 nm [72]	0.1 nm	2.5 nm @ 500 nm	2 nm @ 600 nm	-	-	-
FWHM Δλ typical values NIR	12 nm [71]	20 nm [72]	0.4–0.8 nm [24]	5–6 nm @ 1.5 µm	3 nm @ 1.5 µm	-	-	-
FWHM Δλ record values VIS	4.3 nm @ 480 nm [71] / 4.2 nm @ 725 nm [71]	12 nm @ 420 nm [72]	0.05 nm [26]	1 nm @ 500 nm	1 nm single air-gap			
FWHM Δλ record values NIR		17 nm @ 950 nm [72]	0.22 nm @ 1.5 µm [22]	5 nm @ 1.5 µm [36]	0.1 nm InP/multi air-gaps @ 1.5 µm [48]	0.08 nm @ 1.3 µm [77]	10 nm @ 1.3 µm [68]	0.007 nm @ 1.5 µm [79]
Resolution VIS λ/Δλ	100–170 [71]	35–50 [72]	-	500	-	-	-	-
Resolution NIR λ/Δλ	~100 [71]	42–56 [72]	7000 @ 1.5 µm	300 [36]	300–15000	3000–10000	100–150	220000
Recording speed	very fast	very fast	very fast	very fast	medium	fast	medium	slow
Production challenge	Automation. The rest are proprietary information	proprietary information; most probably alignment of PD array and blazed grating	to achieve effective refractive index homogeneities in the individual ridge waveguides	perfect resist filling of templates, residual layer homogeneity or effort in individual etching and deposition	flat membranes, vertical stress gradient compensation	QD spatial positioning and adjusting its spectral line, e-beam lithography serial writing	flat cantilever, stress in metal layer, large angle stroke	fabrication of precise chirp in fiber, positioning and actuation of heater element
Nanoimprint applicable	probably	no	yes	yes	yes	yes	yes	no
Potential space requirements to cover 400nm in vis	43 mm²	200 mm²	90 mm²	small 0.07 mm²	small 0.06 mm²	-	-	-
Potential space requirements to cover 500nm in NIR	43 mm²	46 mm²	50 mm²	small 0.09–1 mm²	small 0.05 mm²	small 0.33 mm²	medium 9.5 mm²	large 300 mm²
package size in vis range	medium	large	large	small	small	small	medium	very large
package size in NIR range	medium	medium	large	small	small	high	medium	very large
Current and tendative price	600€ PEBBLE vis 500€	500€ C12880MA						
Yield	100% [80]	high	high	low	high	high	medium	high
Efficiency in available light	very high 70–80% [80]	very high	medium	weak, can be boosted	weak, can be boosted	weak, can be boosted	weak, can be boosted	medium

Figure 3. This review benchmarks different miniaturized optical sensors. The comparison concerns mainly optical properties, economic questions and manufacturing challenges. λ always denotes the vacuum wavelength. The abbreviations have the following meaning: arrayed waveguide grating (AWG), Fabry-Pérot (FP), micro-electro-mechanical system (MEMS), full width of half maximum (FWHM) and quantum dot (QD). References inside the table: transmission grating spectrometer [71,80], reflection grating spectrometer [72], AWG [22–24,26], static FP filter [36], tunable MEMS FP filters [48,56], MEMS tunable PC filter [76], plasmonic MEMS sensor [68], tunable chirped FBG [79].

The review is organized as follows: Section 2 deals with FP filter methodologies, microspectrometers based on FP filter arrays, and our nanospectrometer based on static FP filter arrays which is fabricated by nanoimprint. The digital fabrication methodology for cavity arrays of different heights is demonstrated for the technological fabrication of 3D nanoimprint templates by digital etching in Section 3. This methodology is applied for the fabrication of static FP filter arrays in the VIS spectral range and is also demonstrated in Section 3. Here, a single nanoimprint is demonstrated over three DBR stacks of different design wavelengths and thus different total heights. Section 4 includes experimental results of static FP filter arrays in the VIS range. In Section 5, the design an FP filter array on a detector array with mounted fiber is shown. Section 6 deals with the question to make the most of available light. A methodology is demonstrated which partially compensates for the low efficiency in using available light. This weakness is characteristic for many high resolution optical sensors which have the ability of being strongly miniaturized without loss in resolution. Efficiency boosting is demonstrated by spectral preselection and shown in a laboratory demonstrator. Section 7 briefly describes differences in fabrication of static FP filter arrays if we switch from the VIS to the NIR spectral range. Section 8 describes single air-gap MEMS tunable FP filters for the VIS and NIR spectral range. Section 9 presents methodology, fabrication and characterization of InP multiple airgap MEMS tunable sensors for the NIR. Section 10 provides a broader view on the limits of MEMS tunable FP filters regarding materials and geometric design. Section 11 contains an overview of further concepts for miniaturized optical sensors based on plasmonics, ring resonators, quantum dots, spatial heterodyning, and photonic crystals on fiber tips and in MEMS membranes. Section 12 estimates and illustrates potential space requirements for different sensor methodologies with maximum miniaturization. For the optical sensors shown in Figure 3, the potential space in the area is calculated according to the requirement to cover 400 nm in the VIS spectral range and 500 nm in the NIR for the case of maximum miniaturization. Section 13 deals with the limits of 2D and 3D nanoimprint lithography and discusses the strength of nanoimprint to reduce fabrication time and cost with regard to the six sensor types compared in Figure 3. Subsequently, the limits of wide wavelength tuning are summarized.

2. Methodology of Static FP Sensor Arrays

The static FP sensor array consists of an FP filter array on a photodiode CMOS array or a CCD array. In the literature, these static FP sensor arrays are also called microspectrometers or nanospectrometers, depending on whether or not nanoimprint technology is applied in the fabrication.

2.1. Microspectrometers

An FP filter interferometer is defined as a transparent resonance cavity layer embedded in between two highly reflective mirrors. Within the high reflective spectral range (stopband) defined by the DBRs, only one or several filter lines are allowed to transmit with almost 100% transmission. Each filter transmission line is characterized by its FWHM and its spectral transmission peak (maximum of the filter line). The position within the spectral stopband can be adjusted by a distinct choice of the cavity layer thickness. Please note that the term cavity height or cavity length are used as well in the literature. The longer the cavity, the longer the wavelength of the filter line. For the highly reflective DBRs, dielectric materials of low absorption loss are chosen. For each DBR, thin films are stacked with low and high optical refractive indices alternating in sequence. The higher the width of the stopband, the larger the contrast of refractive indices of the two chosen materials.

By combining an FP filter array and a detector array matching in size, a microspectrometer sensor is obtained. Miniaturizing these sensors does not reduce the spectral resolution as opposed to conventional grating-based spectrometers. These microspectrometers based on FP filter array [28–31] may require complicated fabrication steps for defining all the different heights of the filter cavities. Various methodologies were reported to generate the

unequal cavity heights. Digital etching was used by Correia et al. [28,29] to fabricate 16 different FP cavity heights using four lithography and four corresponding etching steps (4 steps for 16 pixels). Digital deposition was applied by Wang et al. in 2007 [31] to define 128 different FP cavity heights with nine lithography and nine corresponding deposition steps (9 steps for 128 pixels). Digital masking [11] allows (i) digital etching if it is combined with a sequence of etching steps [28,29] and (ii) digital deposition if it is combined with a sequence of deposition steps [31]. The higher the number of different cavity heights (being fabricated) is, the more filter transmission lines (pixels) can be included in an FP filter array. However, these high number of steps might not be cost-efficient in industrial fabrication.

2.2. Nanospectrometers

To significantly reduce the number of required fabrication steps by consolidating them into a single step, nanoimprint is used to define all required different cavity heights for a complete FP filter array [11,32–34]. Thus, nanoimprinted cavities are used with precisely defined heights between the two identical highly reflecting DBRs. From the usage of nanoimprint technology in their fabrication, we were introducing the term nanospectrometers—a combination of an FP filter array and its corresponding detector array—as shown in Figure 4a with a selection of four FP filters out of the whole array. The filter array comprises of two DBRs (shown in gray) and the cavities (shown in orange). The cavities were fabricated in a single nanoimprint step. Each individual filter cavity height defines the wavelength of a characteristic different narrow filter line. One option is to directly deposit the filter array on a detector array (black and magenta). In Figure 4a, each FP filter has one detector, constituting one pixel. However, each filter can also correspond to many detector pixels (e.g., 4, 9, 16, etc.). In Figure 4a, the right part displays the spectral transmission spectra of these four FP filters. Since they have the same DBR, they reveal the same spectral stopband widths (i.e., same spectral width of minimum transmission). However, the spectral positions of the filter lines vary due to the tailored different cavity heights. Within a single step, 3D nanoimprint allows fabrication of all different cavities (even 100,000 or more, theoretically). In the following, the static FP filter arrays are discussed in Sections 2–7 (fixed, i.e., static cavity heights), and the variable MEMS tunable FP filter arrays are considered in Sections 8 and 9.
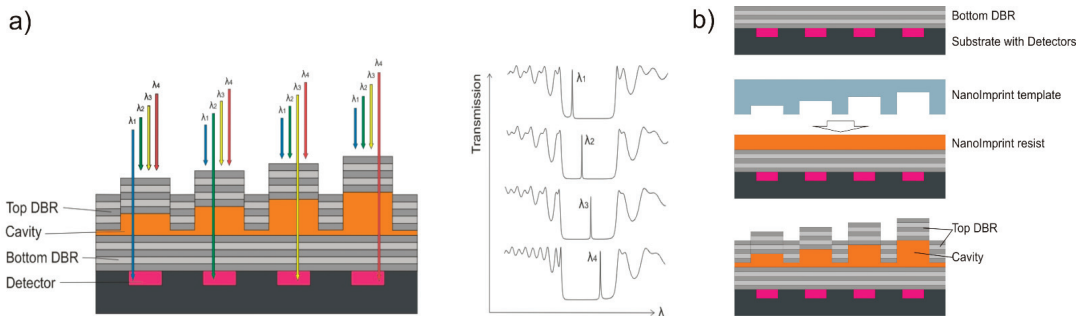
Figure 4. (**a**) Cross section Fabry–Pérot (FP) filter array with a detector array below constituting a nanospectrometer (**left**) and the related calculated transmission spectra (**right**); (**b**) The fabrication process uses Substrate Conformal Imprint Lithography (SCIL). Reprinted with permission from ref. [11]. Copyright 2021 MDPI.

Applying a single 3D nanoimprint step, 192 unequal cavity heights are defined with a single nanoimprint step, generating 192 pixels. This 3D nanoimprint does not require time-consuming digital etching [28,29] or digital deposition [31]. Since the nanoimprint template can be reused many times, this technology is cost-efficient. The digital etching is only used once to fabricate the 3D nanoimprint template, and not permanently during cavity fabrication.

Figure 4b illustrates the sequence of main fabrication steps from top to bottom. It starts with the deposition of the bottom DBR on the detector array. Next, the liquid cavity material (orange) is deposited by spin-coating. Subsequently, the 3D cavity structure is defined using a transparent 3D stamp (light blue) which is pressed into the cavity material and hardened via UV light. After lifting the stamp, the top DBR is deposited.

Nanoimprint is a process of shaping deformable materials by means of molding technology. Presently, many variants of nanoimprint technologies [81–84] are used to generate high resolution 2D structures. On the contrary, 3D nanoimprint is less common but essential for our nanospectrometer. It is challenging to accurately control the vertical dimension (3D) in addition to the lateral dimension. For mass production, a master template (as a positive), including in our case the checkerboard-type arranged mesa structures (various cavity structure heights), is replicated into many identical stamps (as a negative). The 3D nanoimprint is performed using one of these replicated stamps, generating the orange 3D cavity structures (again positive) simultaneously in a single step (Figure 4). Please note that the process described in Figure 4 is involving only a single DBR, thus, revealing a single stopband.

In the following section, three bottom DBR stacks which reveal different heights are imprinted in a single step to produce 192 different FP filters as a proof-of-principle. This imprints over the vertical steps located at the lateral borders of the DBR stacks, each of which has a different vertical extension.

3. Static FP Filter Array Fabrication in the VIS Spectral Range Demonstrating a Single Nanoimprint over 3 DBR Stacks of Different Height

3.1. DBR Mirrors: Materials and Geometrical Issues

Before fabrication, the filter array design has to be performed. The individual cavity heights were identified via simulations using "OpenFilters" [85] in the range of 26–215 nm. However, nanoimprint process is often associated with residual layers that has to be considered in the design. To keep the residual layer constant in lateral directions despite the different mesa volumes, four adjoining mesa heights are laterally grouped in a 2×2 submatrix consistently, where all sub-matrices of four mesas have the same combined volume. Thus, the lateral positioning of these cavities is done applying the volume-equalized design methodology [86] to ensure that the residual layer thickness is as constant as possible.

Since DBRs are used as highly reflecting mirrors, the cavity heights have to be designed in such a way that the transmission lines are within the spectral stopbands of the DBRs. If a DBR with a 100 nm stopband width is used, the different filter transmission lines must be spectrally located inside the stopband width of 100 nm. In that case, the detectable range is a bit smaller than 100 nm. As already mentioned, the DBR stopband width depends on the refractive index contrast of the used materials, which can be deposited for example via Plasma Enhanced Chemical Vapor Deposition (PECVD) or ion beam sputter deposition (IBSD) [34]. In the VIS spectral range, SiO_2/Si_3N_4 DBRs allows about 100 nm stopband width, and a TiO_2/SiO_2 DBR enlarges the spectral stopband to about 200 nm. It is important to mention that the interface quality of cavity and DBR mirror as well as the steadiness of the periods within a DBR are important for high optical quality of the sensor, by ensuring high filter line transmissions and low linewidths.

3.2. Definition of 3D Nanoimprint Templates Using Digital Etching and Digital Deposition

The fabrication of the 3D templates (corresponding to the design) is the most important part of 3D nanoimprint lithography. Since many different mesa height levels are required with height differences located in nm range and accuracies in sub-nm range, the fabrication of 3D templates is a challenge of enabling multiple mesa heights and accurate height differences in the nm range combined with accuracies in the sub-nm range. In comparison, it is by far less challenging to define 2D templates. A single step in e-beam lithography and subsequent etching are enough to fabricate 2D structures with a complex lateral pattern since a constant height can be obtained throughout the imprint area. However, fabricating

3D templates is by far more challenging since the key requirements for the sensors are determined by the third dimension (height). The number of lithography and etching steps can be dramatically reduced if the heights are arranged in a digital way, allowing application of digital masking [34] during lithography, followed by a tailored etching step, respectively. More details can be found in [11], in which the fabrication of the master template (made of Si or GaAs in our case) is described.

The accuracy demand for the FP filter arrays is very low in lateral resolution and contrarily very high in vertical direction. A highly accurate etch depth control is required in the use of digital etching and lithography methodology for the 3D nanoimprint templates.

The digital lithography and etching methodology is used to define all the different checkerboard-like arranged mesa of different heights in the master template. As already mentioned, the master template is replicated to create stamps, thus transforming the different mesa into the required different cavity dimensions. Nanoimprinting with the stamps translates the stamp with its checkerboard-like cavities of different depths again into the different checkerboard-like arranged mesa morphology of different mesa heights.

As a comparison, Correia et al. [28,29] applied digital etching to directly fabricate the checkerboard mesa structure and Wang et al. [31] applied digital directly to deposit the checkerboard mesa structure. Such approach works as an initial demonstration of the principle; however, this would be not desirable for industrial production. A more efficient approach is using digital lithography and etching only to define the nanoimprint master template, which can be reused (replicated) multiple times; therefore it is well applicable for future mass production.

3.3. Combining Three DBR Stopbands in the Fabrication Process of an FP Filter Array

Often, the width of a single DBR stopband is not broad enough. In this case, combining several stopbands to extend to the usable total spectral range of the nanospectrometer is required. A proof-of-principle is demonstrated for this purpose, in which three spectrally neighboring stopbands are combined. 3D nanoimprint was performed across these three DBR stacks of different heights, and filter arrays were fabricated. In Figure 5, only three different FP filters out of many are depicted for each of three DBRs (with different stopbands). This results in nine individual cavities, displayed here as a part of a whole sensor device. Since the lower DBRs can be directly defined on a detector chip, expensive micro-mounting at later fabrication stage can be avoided.

For a DBR, the central wavelengths of the DBR stopbands are defined by the thicknesses of the thin quarter-wave films. A proof-of-concept with SiO_2/Si_3N_4 DBRs fabricated by PECVD is shown, in which less than 120 min is required to deposit a single 9.5-period DBR in this material system. Structuring of the DBRs is performed by means of lithography, lift-off, and an etching process as described in detail in [11]. If the application requires more stopbands to enhance the total spectral range, this is also possible with additional lithography steps. The important point in fabricating sensors with multiple DBRs is simply to maintain a high fabrication quality of the devices even after repeating the process cycle several times.

According to Figure 5, the three bottom-DBRs with spectrally neighbored stopbands provide different vertical total heights of 224 nm and 188 nm for the step height (height difference) between bottom DBR 1 and bottom DBR 2 and the step height between bottom DBR 2 and bottom DBR 3, respectively. Using Substrate Conformal Imprint Lithography (SCIL) with flexible stamps, we performed 3D nanoimprint across these vertical steps. The flexible stamp combines hard-PDMS (polydimethylsiloxane) to ensure structure conformity and soft-PDMS connecting it to a flexible transparent carrier (i.e., thin glass or polymer), thus providing the large scale conformal property. In general, nanoimprint lithography enables large area imprinting up to 12 inch, and SCIL reaches 8 inch with resolutions below 10 nm [84]. The SCIL stamp can be reused for 500 prints using hard-PDMS and 600 prints using X-PDMS [84]. The tricky masking before depositing the next DBR is described in [11,37] in detail.
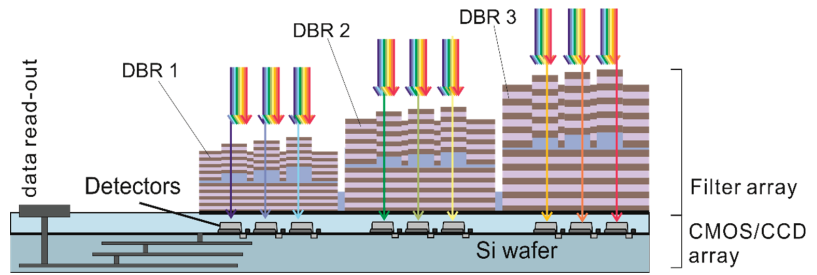
Figure 5. Cross section a nanospectrometer combining three different, spectrally neighbored DBRs in an FP filter array with a sensor array in CMOS or CCD technology. The definition of the blue cavity layer is achieved in just one nanoimprint step. The inclusion of nanoimprint for this sensor provides the term nanospectrometer, which we introduced for this sensor device. Shown here is the first option, namely by placing the FP filter array directly on the photodetector array including the processing integrated electronics. Reprinted with permission from ref. [11]. Copyright 2021 MDPI.

3.4. The Complete Array: Lateral Arrangement of the FP Filters

All FP filters of each of the three arrays are organized in a formation of 12×12 (144) checkerboard. The central 64 (8×8) filters comprise 64 different cavity heights, while the residual 80 filters surrounding the central part are used as control elements for the nanoimprint quality and the residual layer thickness, only for research purposes. More details on this subject is provided in [11]. To estimate the minimum required space in Section 11, the lateral size of each mesa is considerably minimized. Each filter array containing 64 different cavity heights reveals 64 distinct transmission lines per array. A total of 192 different transmission lines were obtained by combining three stopbands. Please note that each of the 192 cavities has different heights and they were imprinted altogether via a single 3D nanoimprint process step. This enormously simplifies the fabrication process.

4. Experimental Results of Static FP Filter Arrays in the VIS Range

4.1. Transmission Spectra of Static FP Filter Arrays

Optical spectra of all FP filter lines were recorded using a microscope spectrometer setup which includes a confocal microscope (Imager D1m Zeiss), a lateral active aperture manipulation, a halogen lamp, a photodetector, a lateral active aperture manipulation and a commercial grating spectrometer (HR 2000 Ocean Optics) with a resolution of 0.5 nm [35]. Figure 6 displays spectra of 192 filter lines of the FP filter array consisting of three DBRs (spectrally neighbored). The 192 filter lines cover a total spectral range of 163 nm (i.e., 507–670 nm) with spectral increments of about 1 nm or below and without any gaps. The transmission intensities of the different filter lines vary due to an interplay between material absorption, linewidth variation, reflectivity changes, and further effects. The material absorption is higher for shorter wavelengths than that for longer wavelength since the strong material absorption of glass in the UV region is approached. This explains the strongly reduced transmission intensities with decreasing wavelength for each stopband. In addition, stopbands with larger central wavelength have thicker DBR stacks and thus suffer more from absorption. In contrast, stopbands with smaller central wavelength suffer less from absorption. This explains the trends measured in Figure 6. For details see [11,37].
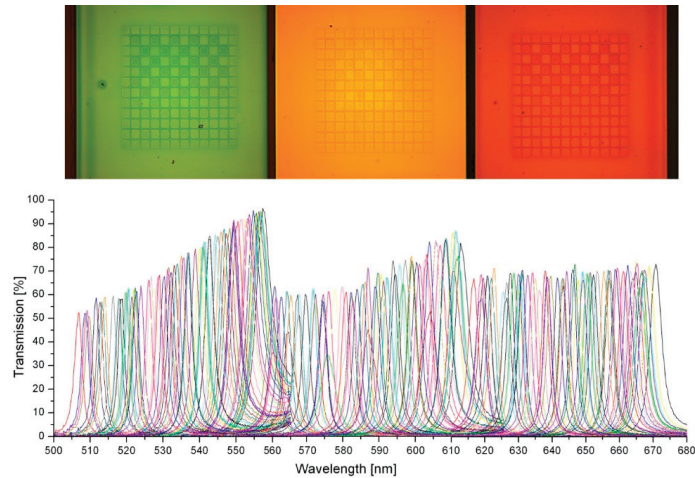
Figure 6. (**Top**) optical micrograph displaying three FP filter arrays and (**bottom**) related optical transmission spectra. Reprinted with permission from ref. [37]. Copyright 2018 Springer Applied Nanoscience.

4.2. Interpretation of Experimental Results Concerning Linewidths

The experimental linewidths (FWHM) presented in Figure 5 of [11] were measured in the FP filter array, as shown in Figure 6 in this review. The measured FWHM are found to be between 1.7 and 5 nm. The closer we come to the borders of the stopbands, the higher the measured values. This observed strong variation of the FWHM as a function of wavelength is due to an interplay of many effects: reflectivity changes, spectral variation of material absorption interface roughness, and further effects.

The spectral reflectivity of each DBR is dependent on the precise spectral position inside its stopband, which is strongly influencing the dependence of FWHM on wavelength. The highest reflectivity exists at the center of the spectral stopband, leading to smallest FWHM at these spectral positions. As the filter lines come closer to the stopband borders, the lower the reflectivity, and thus the higher the FWHMs of the filter transmission lines. This is by far the most dominating effect and explains the main FWHM features that were observed experimentally.

Next, the role of interface roughness is discussed, first by considering one stopband in the VIS range. Assuming that the same interface roughness is occurring at the two interfaces between cavity and DBR for all the FP filters, the influence of interface roughness Δl has a stronger influence on smaller cavity lengths L. For $L_1 < L_2$, a larger relative cavity length fluctuation is obtained for smaller cavities $\Delta L_1 = L_1 \pm \Delta l$ than for longer cavities $\Delta L_2 = L_2 \pm \Delta l$. Increasing FWHM of a transmission line automatically leads to a reduction of the peak intensity. Since this effect is not clearly visible in the experiments, we conclude that the interface roughness is not very pronounced in our case. In addition, another effect is involved: the scattering probability increases with decreasing wavelength, since the averaging over interface roughness is more pronounced for larger wavelengths.

In our experiments, the lowest FWHM value of 1 nm [33,34] are observed; however, not in FP arrays as depicted in Figure 6, but in an FP filter processed individually. We estimate that smaller values down to 0.5 nm should be possible with 15.5 periods of SiO_2/TiO_2, using ultrapure Si and Ti targets and extended vacuum pumping.

5. Static FP Sensor Array in a Fiber Technology System

In our previous paper [11], a laboratory demonstrator is presented as a proof-of-principle. In the demonstrator, an FP filter array with optical bandpass filters was integrated into a commercial grayscale CCD camera and equipped with a telecentric lens. To

implement the signal processing, a procedure similar to that described by Emadi et al. [87] is used. In [11], free beam optics was involved in remote sensing of fruit on a tree or bread inside an oven, whereas the focus in this review is on sensing integrated in fiber technology. Figure 7 presents the schematic design of a sensing system consisting of a nanospectrometer (FP filter array plus detector array), bandpass filters, and fiber input. The divergent light leaving the fiber is parallelized by an achromatic lens system. The bandpass filters block the spectral light outside the FP stopbands, which otherwise would also transmit, reach the Si detector array and increase the noise level. The electrical output and signal processing is not shown here. This was presented in our previous paper [11].
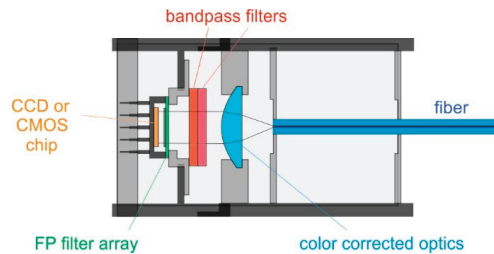

Figure 7. Schematic cross section of an FP filter array mounted parallel and in close vicinity of the Si detector array (CCD or CMOS). The divergent light of the fiber is made almost parallel by the lens system. In this option, the FP filter array is defined on a glass substrate which is aligned here in a bottom-up way on the CCD or CMOS photodiode array. As a comparison, in the first option shown previously in Figure 4 the FP filter array is defined directly on the detector array.

6. Laboratory Demonstration of Efficiency Boosting by Spectral Preselection

The benefits of the FP filter-based sensor concepts are their compactness with further miniaturization potential and their ability to detect a broad spectral range with high resolution. However, one considerable drawback of filter-based systems is their very low detection efficiency. Notwithstanding, this disadvantage is also typical for other interferometric or plasmonic sensor principles (Figures 1 and 3). This chapter presents a methodology for boosting the efficiency (making full use of available light), demonstrated for FP filter sensors. Moreover, it can also be applied to all methodologies suffering from the abovementioned disadvantage. In our previous paper [11], it was demonstrated in free beam optics methodology for remote optical sensing. In this paper, it is presented for fiber-based sensing systems.

The reason for this disadvantage is visualized in Figure 8a. The available "white" light to be analyzed is delivered by an optical fiber, where a parallel light bundle is subsequently produced by collimation optics. To record a complete spectrum, the light must be distributed over the entire area covered by the filters or filter arrays. Finally, the light arrives at the filter arrays or filter array groups (depicted as 1 to N). In this case, each narrowband filter receives the entire broadband spectrum, but only a small fraction of the incident light is transmitted through it and can be used for detection. This means that most of the analyzed light is reflected and lost for application. The narrower the transmission line of the filter, the greater the loss. As one solution to drastically improve the efficiency of filter-based systems, the spectral preselection concept was proposed [88]. Figure 8b demonstrates the basic principle of the preselection concept that comprises the spectral and spatial separation of the highly concentrated incoming light. In particular, the resulting partial spectra (subbands) are spatially separated and delivered to the corresponding filter arrays which only cover a limited spectral range. Each single filter acquires the increased intensity because the spectral preselection method concentrates the necessary wavelength region there, where it is most needed. As an example, Figure 8c shows the photo of the FP filter array [37] as one of the suitable filters for the described concept.
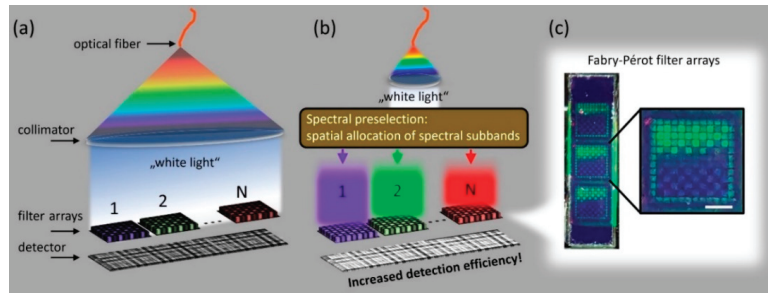
Figure 8. Basic principle of efficiency enhancement of filter-based spectrometers. (**a**) Typical case without spectral preselection: filter arrays are illuminated with broadband light. (**b**) Special optics "spectrally preselects" the incoming light to illuminate correspondent filter arrays. Thus, efficiency increase is achieved, and the filters transmit more light. (**c**) Photo of illuminated FP filter arrays (with scale bar of 200 µm, in gray).

In principle, there are various methods to achieve a spectral preselection, e.g., employing micro prisms, Köster prisms or dichroic beam splitters [88], which significantly differ in their complexity and spatial expansion. A suitable method ensures an optimized compromise between efficiency enhancement and minimum increase in complexity.

A very simple approach of the preselection concept can be realized using multiple dichroic longpass beam splitters arranged successively in a row and aligned to the filter arrays for the respective spectral subbands [89]. Figure 9a shows a photo of the manufactured preselection module superimposed with the schematic beam path. At first, the incoming light, provided by an optical fiber and collimated by appropriate optics, hits a deflecting prism which aligns the ray bundle with respect to the subsequent optical components. In more detail, the prism is equipped with a shortpass dichroic layer acting as a beam splitter that reflects longer wavelengths and transmits shorter wavelengths. The dichroic filter serves to separate the light that falls within the sensitivity range of the subsequent filter arrays from the wavelengths outside the stopband. In our case, wavelengths longer than 491 nm are reflected, which comprises all spectral ranges of the following FP filter arrays with dissimilar DBRs (521–571 nm, 576–630 nm, and 628–685 nm). Each of these applied dichroic splitter elements have a longpass characteristic. These beam splitters reflect the desired wavelength range toward the suitable filter array and transmit the residual wavelengths used for the subsequent splitters and filter arrays. The last element is also a dichroic mirror that transmits all wavelengths longer than the upper limit of the corresponding stopband.

The preselection module with the integrated FP filter arrays is combined to a mechanical adapter that allows for a connection to a CCD camera. Figure 9b shows a photo of the front side of the preselection module and the mechanical adapter with all optical elements clearly visible. The comparison with the 1 Euro coin substantiates the compactness of the module ($17.5 \times 17.5 \times 7.8$ mm^3). Figure 9c demonstrates the back side of the module with FP filter arrays. Figure 9d shows a photograph of the final measurement setup with the closed module connected to a CCD camera and fed by the input light delivered by an optical fiber. With this approach, an efficiency enhancement by a factor larger than four compared to the used reference system [11,89] was experimentally demonstrated.

As already mentioned, the example presented serves exclusively as a proof-of-concept. A sensor that is simultaneously optimized in terms of compactness, efficiency and spectral properties can be achieved through a joint, tailored development of detector, filter arrays and preselection setup. Although the introduction of preselection module moderately increases the overall effort for the spectral sensor, a good compromise between efficiency enhancement and increase in complexity is achieved.
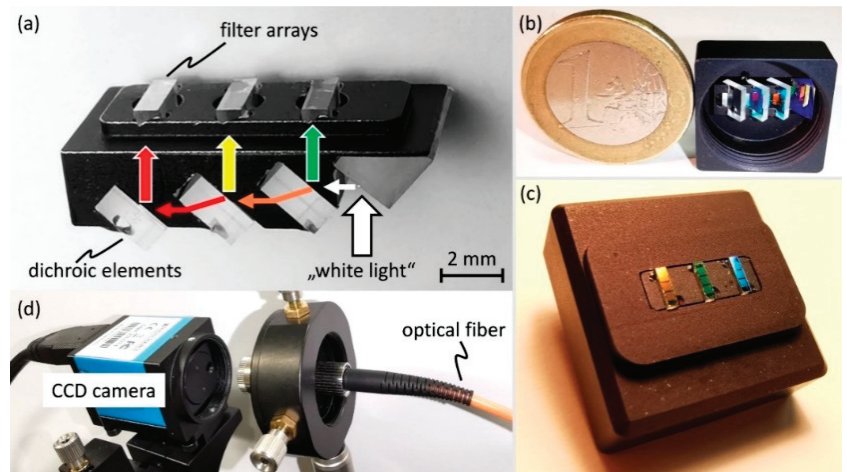
Figure 9. Efficiency increased module comprising dichroic beam splitters and FP filter arrays. (**a**) Photo of the preselection module with schematic beam path. (**b**,**c**) Photos of the module integrated in a housing. (**b**) Front side of the module displayed together with a coin (1EUR) for size comparison. (**c**) Back side of the module, where the three glass substrates carrying FP filter arrays are visible. (**d**) Measurement setup: closed module connected to a CCD camera is illuminated by an optical fiber.

7. Static FP Filter Arrays for the NIR: Fabrication and Characterization

The near-infrared (NIR) spectral range is very interesting for sensing, e.g., for chemical analytics. This range was also considered in our previous paper [11] and is repeated briefly in this review. For the NIR spectral range, the FP filter arrays were designed in the 1.4–1.5 µm wavelength range, and 9.5 periods of Si_3N_4/SiO_2 were deposited by PECVD for the top and bottom DBR at 120 °C temperature. This avoids degradation of the polymeric cavity layer due to higher process temperatures. The mr-NIL210 resist was used to obtain cavity heights much larger than those used in Sections 3 and 4 fabricated for the VIS spectral range. Each filter element here is 40×40 µm^2 in lateral dimensions, and the vertical height of the imprinted cavities ranges between 365 and 530 nm. The experimental characterization [11] reveals high maximum transmission values up to 90% and average transmissions well above 70%. The smallest FWHM (4.7 nm) is achieved at 1450 nm. This provides an FP filter resolution $\lambda/\Delta\lambda$ of 300, defined as filter transmission wavelength divided by the FWHM. Again, a comparison of experimental and simulated FWHMs had been performed. The description of the theoretical model calculations and the discussion of the FWHM variations were already described in Section 4.2. The surface roughness of layered heterostructures on the very thick resist mr-UVCur06 was investigated by an atomic force microscopy (AFM), revealing rms-values of <4 nm for a single layer and <8 nm for a double layer. This agrees with our FWHM observations since in layered heterostructures, this measured surface roughness is embedded in the heterostructure and transformed into interface roughness.

Finally, the influence of temperature changes on the structure and heat distribution is discussed. Having more interfaces in the heterostructure will shrink the overall thermal conductivity vertical to the interfaces. For more details see [36,90]. A good heat transfer to the heat sink is desirable since the ensemble of filter line wavelengths will shift with changing temperature. The dominating effect in the shifts results from the temperature dependence of the refractive indices of all involved materials. A much smaller effect is the influence of thermal expansion of all the layers in vertical direction. Such temperature changes for interferometric sensing application can be substantially suppressed either by implementation of Peltier elements that are commonly used in fiber optical communication

systems, or using temperature sensors and data processing software to execute correction of temperature shifts, since this information will be captured in any case by the arrays of spectrally neighboring filters with a wide spectral span. Figures of spectra and FWHM can be found in [11].

Contrary to the static FP filter arrays in Sections 3–7, the MEMS tunable FP filters in the following sections are considered to have a single air-gap (Section 8) or multiple air-gaps (Section 9).

8. MEMS Tunable FP Filters with a Single Air-Gap for the VIS and NIR Spectral Range

In the range 300–1100 nm, Si enables cheap and reliable detectors which can be integrated to powerful arrays in CCD or CMOS photodetector technology. Due to different designs, e.g., different channel geometries, they have a different spectral sensitivity. For sensorics in VIS spectral range, the combination of Si as detector material and static FP filter arrays (Sections 4 and 5) is a good and cheap solution. Therefore, MEMS tunable FP sensors in the VIS range are not as urgently required as in the NIR spectral range.

However, CMOS photodetector arrays or CCD arrays based on Silicon cannot be applied for the NIR spectral range of >1.2 μm, since Si becomes transparent and is no longer sensitive for light in that range. Therefore, detector arrays such as InGaAs have to be used for the NIR instead. Considering the aspect of cost reduction of IR spectrometers, MEMS tunable spectral sensors are very attractive in the NIR applications. A large spectral range of 1.15–1.8 μm (650 nm span) can be spanned using only three InGaAs photodiodes (an array of three photodiodes) and three related MEMS tunable filters that are neighbored in the spectrum. If each MEMS filter can be tuned over 220 nm, three of them are enough to cover 650 nm, with overlap. In the literature, various MEMS tunable filter designs were demonstrated in different material systems [38–58]. However, this review focuses on two MEMS concepts, namely the actuation of a single or several air-gaps.

Figure 10 depicts a MEMS tunable FP filter including a single air-gap. The lower DBR is directly connected to the substrate (not shown), which means that it remains flat and unactuated. The electrostatic actuation is displacing only the top DBR and varies the air-gap cavity height. All the incident wavelengths are reflected, except those which are able to constitute a standing wave in the cavity, and only this standing wave is allowed to transmit the filter. As already mentioned above, the following FP condition is only an approximation: The cavity height is a multiple of half of the wavelength in the cavity medium. Details on why it is only an approximation are given in Section 10.

However, this design has some disadvantages: (i) limited stopband widths and (ii) the rather bulky and stiff DBR stacks which require relatively long suspensions. The required large membrane displacements to allow large tuning ranges are only possible with such extended suspensions. If semiconductor DBRs (e.g., GaAs/AlAs) are used, the most elegant option is to n- and p-dope each of the two DBRs and to use electrostatic tuning by varying the applied voltage, as shown in Figure 10. Increasing the tuning voltage leads to a decreasing air-gap and decreasing filter wavelength (blue-shift).

If dielectric DBRs (SiO_2/Si_3N_4 or SiO_2/TiO_2) are used, electrostatic actuation can also be applied, but this requires the specific definition of additional electrode layers since the light transmissive part of the filter must stay metal-free. In case dielectric mirrors thermal tuning is preferred, thin-film heaters are defined only on the suspensions. Increasing the tuning current through the thin-film heaters leads to increase of air-gap, thus increasing filter wavelength (red-shift).
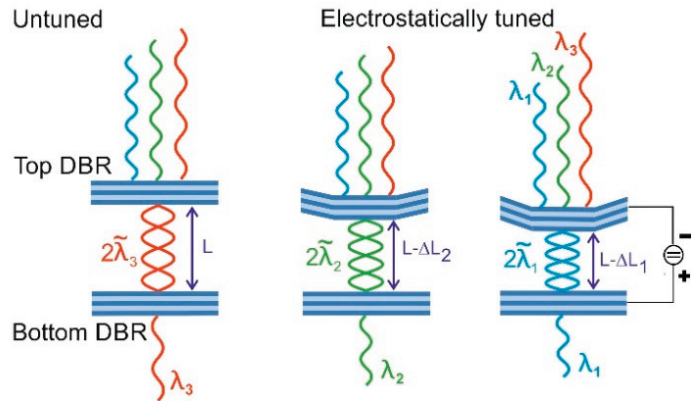
Figure 10. Single air-gap MEMS tunable FP filters with four times half-a-wavelength cavity $(4 \cdot \lambda/2)$ and semiconductor DBRs.

Figure 11a depicts a cross section of a single air-gap FP filter with two SiO_2/Si_3N_4 DBRs, each with 12 periods of quarter-wave layers. The white part in between the two DBRs is the air-gap cavity with a thickness of $L = 800$ nm. The absolute value of the electrical field (black line), shown as an overlay, is depicted on this multilayer structure. This visualizes the standing fundamental mode inside the interferometer for an air-gap cavity of $L = 800$ nm thickness. The electrical field clearly visualizes that all dielectric layers in the DBRs are quarter-wave layers. For the same cavity thickness of $L = 800$ nm, the corresponding reflectance spectrum is displayed in Figure 11b (also in black color). Since the mirrors are dielectric and not conductive, thermal MEMS tuning is applied here. Figure 11b displays corresponding reflectance spectra for different air-gap cavities of width L. In Figure 11b, a red-shift is observed with increasing tuning current, in accordance to electrostatic MEMS tuning methodology.
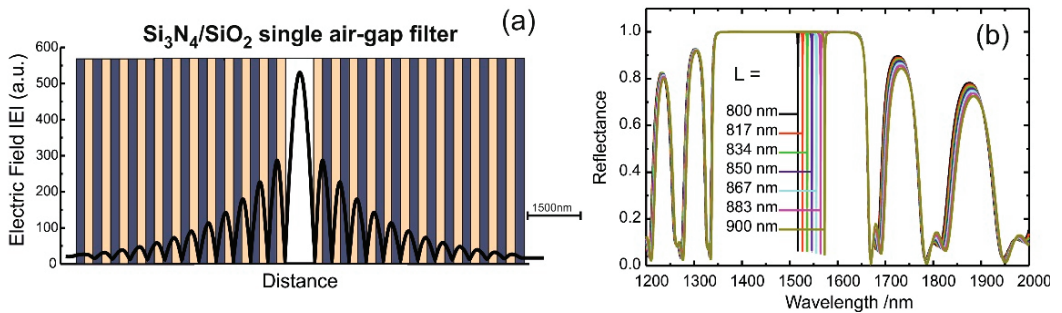
Figure 11. MEMS tunable FP filters with half-a-wavelength cavity and SiO_2/Si_3N_4 DBRs. (**a**) Cross section of the cavity embedded by dielectric DBRs together with the absolute value of the standing electrical field (black profile). (**b**) Corresponding reflectance spectra for different air-gap cavity widths L addressed by MEMS tuning.

9. MEMS Tunable FP Filter Sensors in the NIR Range with Multiple Air-Gaps: Methodology, Simulations, Fabrication and Characterization

The abovementioned disadvantages resulting from thick DBR layer stacks and limited stopband widths can be overcome in the second airgap-based option. The second option uses multiple air-gap FP filters and is visualized in Figure 12. The cross section of the multiple air-gap FP filter is shown in Figure 12a, in which the larger central air-gap has

the width *L*. In the DBRs, the blue InP layers are three-quarter-wave in optical thickness, and the white air-gaps in between are quarter-wave layers. This can be clearly seen from the absolute value of the standing electrical field, displayed in black. Figure 12b depicts corresponding reflectance spectra for different central air-gap widths *L* addressed by MEMS tuning. A blue-shift is observed with increasing tuning voltage, in accordance to electrostatic MEMS tuning methodology.
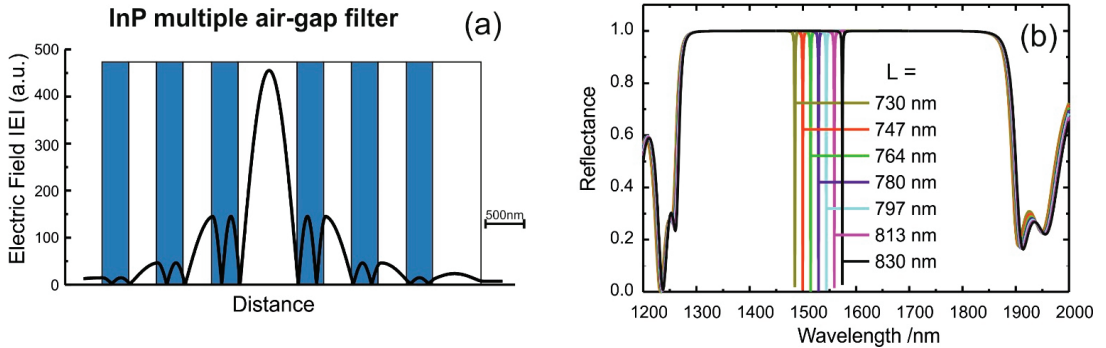
Figure 12. MEMS tunable InP multiple air-gap FP filter with half-a-wavelength central cavity. (**a**) Cross section of an InP multiple air-gap FP filter including the larger central air-gap of width *L*. The absolute value of the standing electrical field is displayed in black. (**b**) Corresponding reflectance spectra for different central air-gap widths *L*, which is obtained by MEMS tuning. In this case only *L* is varied, all the $\lambda/4$ air-gaps remain unchanged.

This multiple air-gap design enables large tuning ranges with a slim design and the resulting wide stopband widths, thus overcoming the disadvantages mentioned for the single air-gap design (Figure 10). Actuation of the mirrors and hence varying the cavity length is accomplished by p-doping the top DBR, n-doping the bottom DBR and applying a reverse bias. Including us, four groups have investigated vertical-cavity tunable filters based on micromachined InP/air-gap DBR using different approaches [42,45–57]. Each DBR consists of $3\lambda_{InP}/4$ InP membranes and two $\lambda/4$ air-gaps. The left part of Figure 13 shows a top view on an InP filter element with four supporting posts, four suspensions and the central top membrane. The right part of Figure 13 displays a cross section which is orientated according to the white broken line (left). Within the membrane and suspension posts, InGaAs served as sacrificial layers and is replaced by air upon removal. However, InGaAs within the supporting posts still remains as substantial layers.
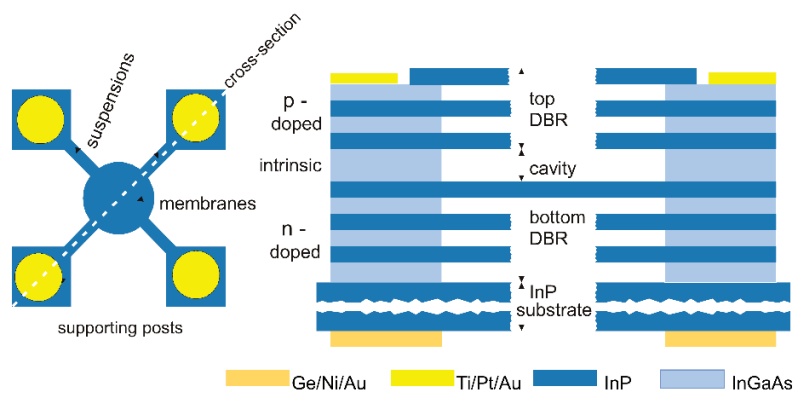
Figure 13. (**Left**) top view on an InP filter element showing four supporting posts with four contact

pads (yellow), four suspensions and the top membrane (the topmost one out of the six membranes). The orientation of cross section on the right is indicated by the white broken line. (**Right**) cross section of the MEMS multilayer structure. InGaAs exists only inside the supporting posts. Between the suspensions and central membranes, InGaAs was serving as a sacrificial layer and had been selectively removed and replaced by air. The bottom contacts are shown in orange.

Doping of the DBRs considerably increases the tuning efficiency. Charging capabilities of metals is larger than that of semiconductors. The higher the doping level of semiconductors, the closer the semiconductor resembling a metal. Therefore, doped semiconductors are more suitable for electrostatic tuning than undoped. Reverse biasing is only shifting charges, and the current through the supporting posts is very small due to both very small areas and reverse biasing.

Metal organic chemical vapor epitaxy (MOCVD) is applied to grow the required lattice-matched multi heterostructure on [100] n-InP substrates: $\lambda_{air}/4$ InGaAs layers alternating in the stack with $3\lambda_{InP}/4$ InP membranes. The $\lambda_{air}/4$ InGaAs layers act as sacrificial layers and are eventually etched, transforming into air-gaps. The top DBR located above the air-gap cavity is p-doped, and the bottom DBR layers located below the air-gap cavity is n-doped. First, the contacts are defined by lithography, evaporation and lift-off directly on the epitaxial structure. Then, Si_3N_4 is deposited by PECVD, and lithography and reactive ion etching (5.1 sccm Ar, 3.5 sccm CHF3, 6.7 Pa, 100 W) is used to generate the Si_3N_4 etch mask. Only the uncovered parts of the semiconductor surface are dry-etched in vertical direction using reactive ion etching (20 sccm CH_4, 70 sccm H_2, 4.7 Pa, 200 W) to achieve an etch depth down to ~5.5 μm. Use of a Si_3N_4 mask instead of a resist mask reveals improved selectivity in the dry-etching process and avoids polymer deposition which is highly unsought on the side walls of the mesa. This process is non-selective and provides vertical side walls, and sharp edges. Then, the etch mask is removed by wet-chemical etching (HF/H_2O), producing pure semiconductor mesa. The supporting posts are masked by a protective layer to avoid underetching. To underetch the InP membranes, $FeCl_3/H_2O$ is used to selectively remove the InGaAs sacrificial layers with an excellent selectivity of about 1000. The precise value depends on doping and temperature. This provides very smooth semiconductor/air interfaces. An etching time of 35 minutes at a temperature of 21 °C is used. It is important that the membranes and suspensions are underetched completely to ensure free vertical motion. The final structure after critical point drying and removal of the protection mask is depicted in Figure 13. A total of 500 filter elements were fabricated simultaneously on a wafer area of 1 cm². The chance was used to fabricate multiple design variants differing in suspension lengths and membrane diameters on the same wafer. The filter variants have membrane diameters of 15–40 μm with three or four suspensions of 10–80 μm length and 10 μm width connecting the membrane to the supporting posts. Straight or bent suspensions and circular or square membranes were implemented.

Figure 14 displays the scanning electron microscope (SEM) images of filters with four suspensions. The optical quality of the two surfaces of each membrane is guaranteed by the high quality of the epitaxial heterointerfaces which is preserved in the selective chemical etching step, providing very low optical roughness. Our surface micromachining fabrication process demands no micro-mounting since the entire structure is fabricated in a sequence of process steps. Furthermore, a monolithic integration is obtained within the GaInAsP/InP material system, allowing the integration of photodiodes and vertical-cavity surface emitting lasers. The central, light gray circular areas in Figure 14a–c show unprotected regions to allow underetching of membranes and suspensions. The dark gray areas outside of the circular areas show protected regions. Figure 14d provides a closer look on the suspension region, especially through the wider central air-gap that allows a view through the structure to the ground behind, marked with "*". The ground level in front is marked with "**". A single suspension has a width of 10 μm (light blue). The top DBR consists of the layers 1, 2, and 3 and the bottom DBR is made of layers 4, 5 and 6. At the central area, a view on top of suspension 4 is possible (marked with number 4 in white).
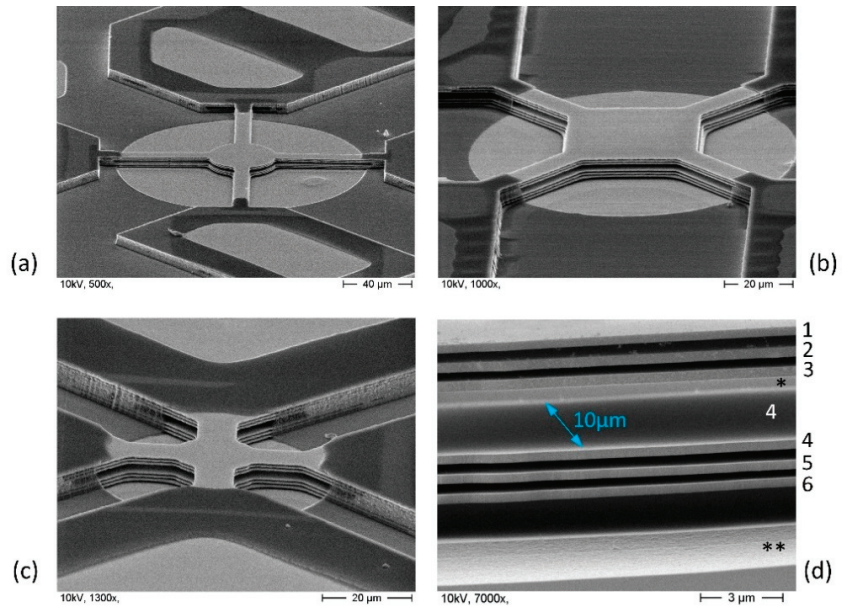
Figure 14. SEM micrographs of InP/InGaAs multiple air-gap MEMS tunable FP filters. Each DBR consists of three InP layers and two air-gaps. (**a**) 60 μm long suspensions and a circular membrane with 40 μm diameter. (**b**) Square membranes. (**c**) Short suspensions and small membranes. (**d**) Details of the suspension region. It allows a view through the structure to the ground behind marked with "*". The ground level in front is marked with "**".

Figure 15a displays an SEM micrograph top view of an InP multiple FP filter prior to the wet-chemical under-etching. The light gray circular region allows the etching solution to remove the sacrificial layers therein. The dark gray region outside prevents the underlying structures from being etched. Figure 15b shows a detailed close-up image of the suspension and membrane region, allowing a view through the central air-gap. Figure 15c displays the filter line wavelength as a function of actuation voltage, and the corresponding reflectance spectra is shown in the inset. A very wide tuning range of 221 nm [56] for a variation of the actuation voltage of 0–28 V is measured for our MEMS filters. To the best of our knowledge, this is the largest tuning range measured for any InP/multiple air-gap DBR-based vertical-cavity filter. The FWHM is very narrow (about 1 nm) at lower actuation voltages; however, it broadens with increasing actuation voltage due to buckling of the membranes.

MEMS tunable filters were also fabricated using nanoimprint technology, successfully reducing the sacrificial layer to zero. A methodology proposed by Cheng et al. [91] was selected and adapted using selective curing in silica template. It was modified and transformed into our hybrid SCIL stamps [92]. Using UV-blocking metal layers in the otherwise transparent stamps, areas with non-cured nanoimprint resist could be generated. Therefore, cured hard resist remains only in the area of supporting posts, while other areas with non-cured resist show non-existent residual layers during resist removal. Being able to avoid residual layers was an important step forward for our SCIL 3D nanoimprint technology [92].

Figure 16 presents a 3D perspective view of the whole sensor attached to a fiber. A MEMS tunable FP filter is integrated with an InGaAs photodiode. The MEMS filter and the photodiode were grown within the same MOCVD epitaxial run on InP substrate.
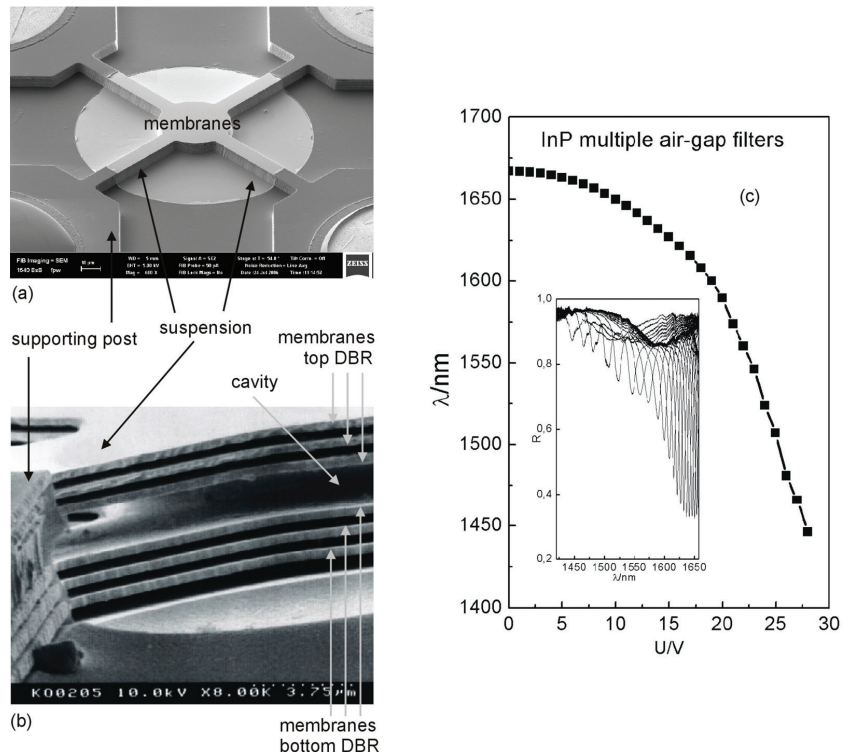
Figure 15. (**a**) SEM image in tilted top view on an InP multiple air-gap MEMS tunable FP filter with InP/InGaAs supporting posts with contacts on top; (**b**) SEM image in tilted side view, enabling a look through the central airgap between the suspensions; (**c**) Tuning characteristic showing the filter peak wavelength as a function of the actuation voltage. A selection of experimental reflection spectra $R(\lambda)$ is displayed in the inset. Various spectra are shown for different actuation voltages U. Reprinted with permission from ref. [11]. Copyright 2021 MDPI.
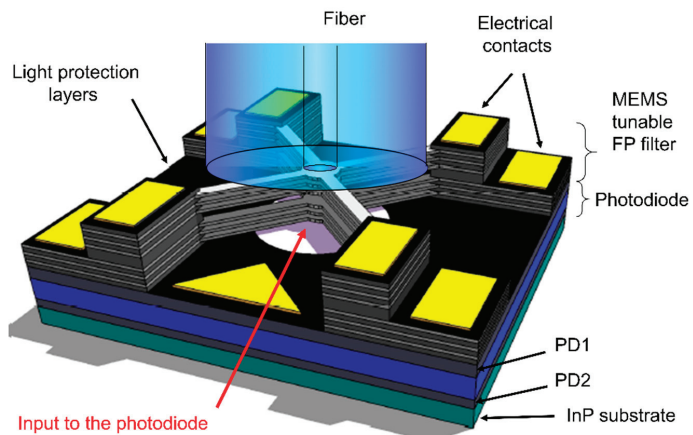
Figure 16. Interferometric sensor for the NIR spectral range, consisting of a MEMS tunable filter and

a photodiode. The actuation voltage will be applied between the rectangular and triangular contact pads. The photodiode is biased via the two highly doped semiconductor layers PD1 and PD4, and the sensor signal is also picked off between PD1 (triangular contact pad) and PD4 (substrate contact). To allow light incidence only on the white area, the rest of the PD top is covered by light protection layers. The rectangular contact pads correspond to the round contact pads in Figures 13 and 15, as well as to the rectangular contact pads in Figure 14.

The InP material system enabling monolithic integration with InGaAs photodiodes is not only beneficial for NIR sensorics, but also very favorable for receiver systems to be used for NIR wavelengths tailored for telecommunication requirements of low fiber dispersion and low fiber absorption. Our lab demonstrator including MEMS tunable FP filters and InGaAs photodiodes in monolithic integration was working well in the laboratory practice. In addition, a packaged MEMS tunable filter with two fiber pigtails was demonstrated using the InP/multiple air-gap material system.

10. Limits of Semiconductor and Dielectric Material Systems for MEMS-Based Sensorics: Geometry, FWHM, Tuning and Stopband Width

In this section, further conceptional facts and details are presented as a continuation to Sections 8 and 9. A separate Section 10 was chosen for this purpose to avoid overloading and interruption of the common thought in the previous two sections.

The first question is, how do the membranes of the top and bottom DBR move under electrostatic actuation? Figure 17a shows the InP multiple air-gap FP filter without applied voltage (unactuated), and Figure 17b displays the real situation when an actuation voltage is applied (actuated state). Because of applied voltage, charges are shifted. The charges accumulate mainly at the inner surfaces of the two central membranes. Therefore, the two central membranes are mainly actuated. Consequently, the outer membranes stay nearly uncharged and remain nearly unactuated. The outer membranes remain nearly unaffected due to shielding effects. Figure 17c displays a hypothetic situation, in which all the membranes of the top DBR are actuated in the same way and the whole bottom DBR moves in unity.

In Figure 18a,b the difference in tunability between the two cases shown in Figure 17b,c are investigated. Performing detailed theoretical model calculations using the Transfer-Matrix method the respective spectra, tuning ranges and FWHM have been calculated. The comparison starts from the same unactuated situation (blue spectrum) and studies different actuation states ΔL = 50 nm, 100 nm and 150 nm (the remaining central air-gap is $L - \Delta L$). The spectra corresponding to these tuning conditions are displayed in different colors. The hypothetic case is shown in Figure 17c actuating all membranes, and the realistic cases is displayed in Figure 17b actuating only the central membranes.

For the two cases, the wavelength tuning $\Delta\lambda$ of the filter line is plotted as a function of the central air-gap height difference ΔL in Figure 19. Moving all the membranes of each DBR leads to a higher MEMS tunability.

The tuning efficiency is $\Delta\lambda/\Delta L$ = 0.92 if all membranes are actuated, and it is otherwise $\Delta\lambda/\Delta L$ = 0.8 if only central membranes are actuated. In comparison, the obtained tuning efficiency in Figure 11b is much smaller, i.e., $\Delta\lambda/\Delta L$ = 0.56 for SiO_2/Si_3N_4 DBRs. The multiple air-gap InP methodology is not only much better in MEMS tuning but also much more compact. The InP multiple air-gap FP filter reveals the smallest extension of the whole multilayer unit in the literature, with exception to photonic crystal membranes. Please note that the length scales of the two FP filters in Figures 11a and 12a are not identical.
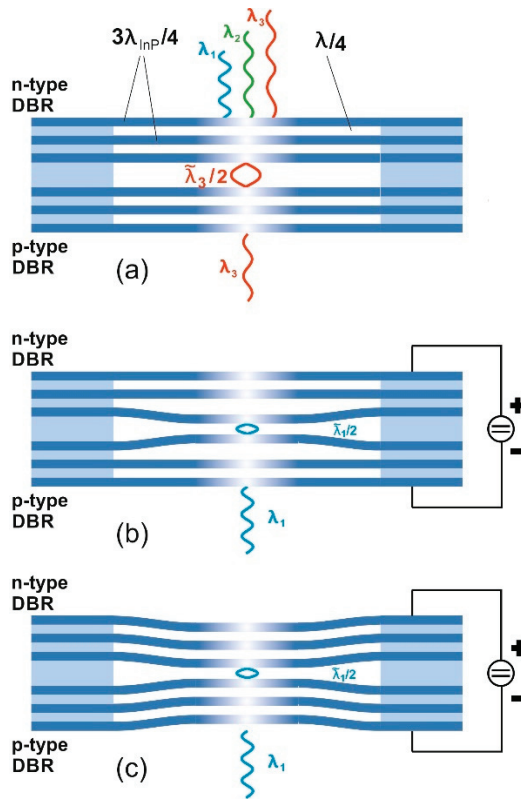
Figure 17. Schematic of MEMS tunable FP filters including multiple air-gaps and membranes and suspensions made of InP. The supporting posts are built of the complete InP/InGaAs multilayer stack, as grown by epitaxy. (**a**) Unactuated state; (**b**) Actuated state where only the two central membranes of the DBRs are actuated; (**c**) Actuation of all membranes (i.e., actuating the whole two DBR stacks). This tuning configuration is shown in Figures 12 and 18a. The meaning of $\widetilde{\lambda}$ used in (**a**–**c**) is explained hereinafter in this section.
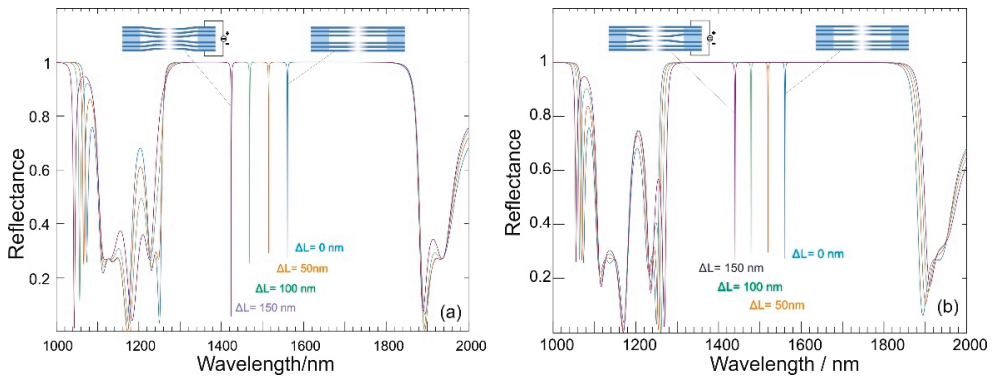
Figure 18. Electrostatic MEMS tuning of InP multiple air-gap filters, (**a**) actuating all membranes of the DBRs and (**b**) actuating only the two central membranes.
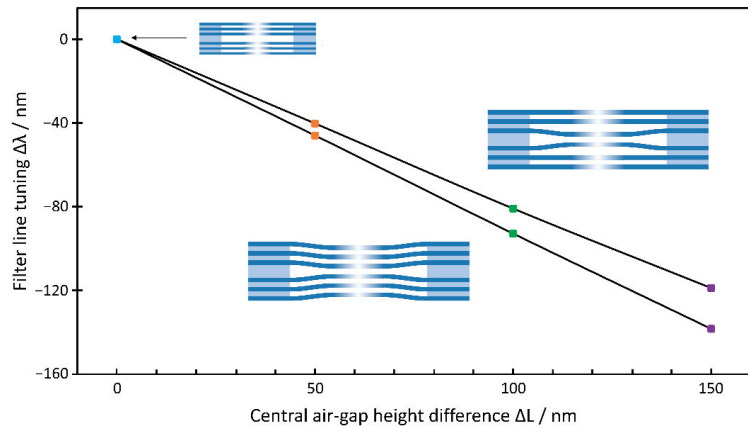
Figure 19. Electrostatic MEMS tuning of InP multiple air-gap filters with two different cases: Actuating all membranes of the DBRs (lower curve) and actuating only the two central membranes (upper curve). The colors of the symbols correspond to those used in Figure 18.

It is also worth noting that many misunderstandings are related to the often and commonly used term "half-a-wavelength cavity". The FP condition for two metallic mirrors states reads: the cavity length L is a multiple of half of the wavelength in the medium. Figures 11a, 12a and 17a show half-a-wavelength cavities. Since the electromagnetic wave penetrates into the DBR mirrors, the figures show a feature which looks like half a wavelength inside the mode (Eigenfunction), but that is an effective wavelength $\tilde{\lambda}$ and not the half vacuum wavelength. It is not the same, and it depends on the DBR mirrors. During the tuning of the length L, the nodes are no longer located at the interfaces between the layers as shown in Figures 11a and 12a. Considering the insufficient idea of half of the vacuum wavelength inside the cavity, the tuning efficiency $\Delta\lambda/\Delta L$ should be 1, independent of the materials of the DBR. A detailed explanation can be found in one of our doctorate dissertations [93].

The FWHM are nearly identical in both cases compared in Figure 18. A possible explanation could be that the FWHM is dominantly related to the number of periods. Since the number of periods is equal in both cases in Figure 18, the FWHM remain nearly identical.

Figure 19 reveals that the difference in tuning of the two cases is 13%. The wavelength tuning is dominantly related to changes in the airgap thicknesses. Therefore, the differences between the two cases are more pronounced in tunability rather than in the FWHM. However, quantifying 13%, the difference is still relatively small. This might be due to the fact that the mode shapes adapt not only to the changes in the central air-gap but also to the changes of the two other air-gaps which are located next to the central air-gap. For the complex localization of nodes and interfaces during the tuning, please refer to [93].

Next, the limits of FWHM are studied for multiple air-gap InP filters and displayed in Figure 20. Theoretical model calculations based on the transfer-matrix method are used to simulate the spectra of InP multiple air-gap FP filter lines. Measured data for the spectral InP absorption coefficient is given as α_{InP} = 3.43 cm^{-1}. The DBRs consist of 357 nm InP ($3\lambda_{InP}/4$) and 3675 nm air ($\lambda_{air}/4$) which are embedding the central air-gap of L = 815 nm ($0.53\,\lambda_{air}$). The red curve is simulated for DBRs with three InP membranes, resulting in FWHM of 1.01 nm and dip reflectance of 0.00043 at a dip wavelength of 1562.995 nm. The black curve is simulated for DBRs with four InP membranes, resulting in FWHM of 0.112 nm and dip reflectance of 0.028 at a dip wavelength of 1562.906 nm.
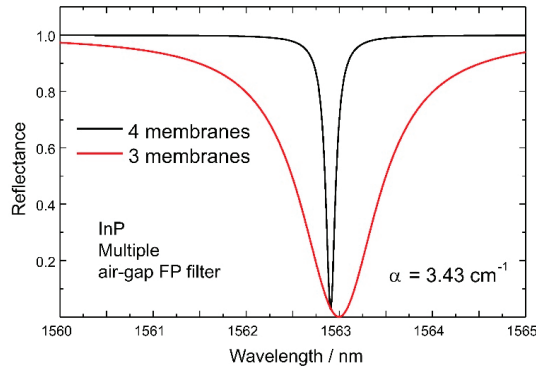
Figure 20. Transfer-matrix model calculations of InP multiple air-gap FP filter line spectra with DBRs including 3 and 4 InP membranes each.

These low values could be confirmed experimentally with four InP membranes, in which a FWHM of 0.1 nm was measured at 1.55 µm. However, such a low value was only measured once from a single sample. Such linewidth broadening can only be avoided if the non-bending (buckling) of the central membrane areas is completely absent. Notwithstanding, the simulations and measurements showed what is possible. The optical resolution of the FP filter methodology is predicted to be around 15,000 in the best case.

Next, the maximum potential DBR characteristics are reviewed and shown in Figure 21. Applying transfer-matrix model calculations, transmission and reflectance spectra are calculated for different numbers of periods p and the appropriate material absorption coefficients α. The spectral variation of absorption $\alpha = \alpha(\lambda)$ is taken from experimental results. In the inset of Figure 21a, the spectral reflectance is shown for a Si_3N_4/SiO_2 DBR ($p = 12$, $\lambda_i/4$ layers, $\alpha = 0$). The maximum spectral reflectivity R_{max} for $\lambda = 1.55$ µm (see arrow) is extracted from all the spectra which were calculated for Si_3N_4/SiO_2 and InP/air-gap DBRs. R_{max} for $\lambda = 1.55$ µm is plotted in Figure 21a as a function of the number of periods p. Numerous spectra ranging the absorption loss $\alpha = 0, 0.1, 0.3, 1, 3, 10, 20$, and 100 cm^{-1} were calculated for Si_3N_4/SiO_2 DBR's. Please note that the values of α are determined by the technological fabrication and the appropriate process parameters. However, for ultra-pure semiconductor material, the optical loss dominantly is related only to the band structure in defect-free crystalline material of high quality. Therefore, low material loss can be guaranteed, and it is understood well in these crystalline materials. Figure 21a reveals that R_{max} of a DBR strongly grows with increasing p, but it saturates for higher values of p. The level of R_{max} saturation is strongly decreased with growing loss. As already mentioned, the extended spectral region of high reflectivity (i.e., the spectral plateau in the center, as shown in the inset of Figure 21c) represents the stop-band.

According to Figure 21a, the dielectric Si_3N_4/SiO_2 system ($\lambda = 1.55$ µm, $\Delta n = 0.47$, $n_{Si3N4} = 1.94$, $\alpha_{Si3N4} = \alpha_{SiO2}$ both varied, $n_{SiO2} = 1.47$) yields $R_{max} > 0.998$ already for $p \geq 12$ if loss is neglected. For $\alpha_{Si3N4} = \alpha_{SiO2} = 15$ cm^{-1}, a reflectivity of 99.8% is exceeded for $p > 14$. In contrast, 99.8% reflectivity cannot be reached for $\alpha_{Si3N4} = \alpha_{SiO2} = 20$ cm^{-1} since R_{max} saturates at $R_{max,sat} = 0.997$. Please note that Δn is much larger for InP/air-gap structures on InP substrates which was the motivation to use and study this system ($\lambda = 1.55$ µm, $\Delta n = 2.167$, $n_{InP} = 3.167$, $n_{Air} = 1$, $\alpha_{InP} = 3.4$ cm^{-1}) which provides a maximum reflectance R_{max} of 0.9998 for $p = 4$ and yields R_{max} exceeding 99.8% if $p \geq 3$. To share further values, three InP/air-gap membranes embedded in air on both sides (in contrast to the previous structure no InP substrate is considered) reveal $R_{max} = 0.99993$ for $p = 4.5$ and 0.9996 for $p = 3.5$. This demonstrates that using an air "substrate" instead of an InP substrate reveals a much larger R_{max} already for smaller p due to a larger refractive index contrast at the

exterior ends of the DBR mirror. In summary, type and presence of a substrate strongly influence the optical data, especially for smaller number of periods p.
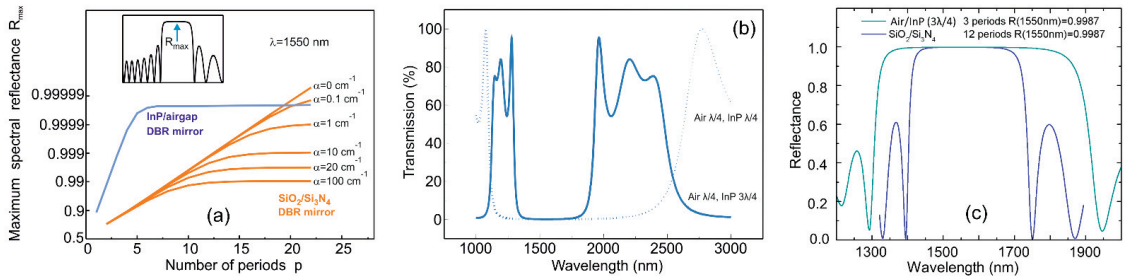

Figure 21. (**a**) Calculated maximum spectral reflectance R_{max} for Si_3N_4/SiO_2 DBRs (orange) as a function of the number of periods p showing the absorption coefficient α as a variation parameter. In the case of the InP multiple air-gap DBRs (blue), $\alpha_{InP} = 3.43$ cm^{-1}. The inset displays the calculated reflectance spectrum indicating the spectral position of the maximum spectral reflectance R_{max}. (**b**) Transmission spectra for InP multiple air-gap DBRs. The dotted line shows a DBR structure including thinner InP layers ($\lambda_{InP}/4$) revealing a huge stopband of 1500 nm. The full line shows a structure including thicker InP layers ($3\lambda_{InP}/4$) revealing a smaller stopband of 500 nm. (**c**) Reflectance spectra for Si_3N_4/SiO_2 DBRs and InP multiple airgap DBRs.

In Figure 21b, the benefit is seen resulting from a very large refractive index contrast between 1 (air) and 3.167 (InP) existing between the two DBR materials for $\lambda = 1.55$ µm. This high contrast enables very large stopbands: 500 nm for the combination of $\lambda_{air}/4$ with $3\lambda_{InP}/4$, and 1500 nm for the combination of $\lambda_{air}/4$ with $\lambda_{InP}/4$. Even the $3\lambda_{InP}/4$ InP membranes is already sufficient to produce the stopband width exceeding the values of Si_3N_4/SiO_2 by far (Figure 21c).

Notwithstanding, none of the four groups fabricating InP multiple air-gap DBRs has achieved to successfully fabricate $\lambda_{InP}/4$ suspended InP membranes up until now. The main issue lies in the breaking of the suspensions and membranes during the drying process after selectively removing the InGaAs sacrificial layers. For this reason, the dotted profile in Figure 21b remains a dream. Hopefully, improved future fabrication technologies with solvents implying less turbulences and improved drying processes can enable further progress on this challenging field. Thus, the full line in Figure 21b dealing with $3\lambda_{InP}/4$ thick membranes is the state-of-the-art in the present times.

Due to the arsenic carry-over in the epitaxial growth of the . . . InP/InGaAs/InP . . . heterostructure layer, the two interfaces are not identical. After finishing the InGaAs growth and switching to InP, traces of arsenic are still in the MOCVD reactor and are incorporated into the InP close to the interface. In contrast: after finishing the InP growth and switching to InGaAs, no arsenic can be carried back into the already finished InP layer. This arsenic carry-over leads to small stress gradients and subsequently buckling (bending) of the membranes and suspensions after removal of the InGaAs sacrificial layers. Completely flat membranes were obtained in our epitaxial growth after additional doping of arsenic in the opposite interface, and thus creating symmetric structures: arsenic-doped InP/undoped InP/arsenic-doped InP.

11. Further Concepts for Miniaturization Based on Plasmonics, Ring Resonators, Quantum Dots, Spatial Heterodyning, and Photonic Crystals on Fiber Tips and in MEMS Membranes

Beside the widely applied concepts of interferometric sensors beeing discussed in the previous sections, further options for miniaturization of sensors exist. In some of them, DBRs or even a complete FP filter are replaced by a single layer with 1D or 2D periodic patterns. Other concepts make use of different interaction effects such as plasmonic

resonances or Raman scattering. In the following section, a short overview to examples of all these approaches is given.

11.1. Sensors Based on Photonic Crystals in MEMS Membranes

As already covered in the introduction, guided mode resonances allow either broad- or narrowband resonances by coupling a wave in and out of a slab waveguide, and then superimpose this resonant mode with the directly reflected and transmitted continuous mode, respectively. The result is a Fano shaped resonance line in the spectrum, where bandwidth and line shape are given by the coupling condition. The basic concept of coupling resonant and continuous modes is shown In Figure 22a, and an example of a single InP MEMS membrane with a square lattice of elliptical holes can be seen in Figure 22b.
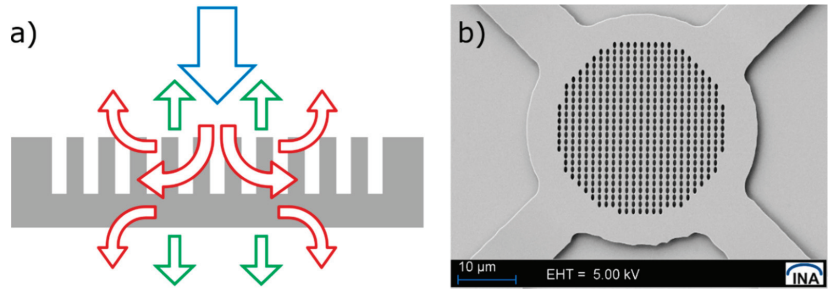
Figure 22. (**a**) Principle of a guided mode resonance. The incident wave (blue) is partly transmitted and reflected in form of continuous modes (green) and partly couples in and out the slab in form of a resonant mode (red). Superposition of both parts leads to the typical Fano line shape. (**b**) A MEMS membrane with elliptical air holes as base elements in a 2D square lattice, breaking the symmetry and leading to polarization dependent reflection and transmission.

Zobenica et al. [77] applied two parallel membranes including photonic crystals (PCs) and quantum dots (QDs), which were coupled evanescently. In this case, a single DBR is replaced by two PC layers. This idea was shown first in [62,73]. The graph in the third column from the right-hand side in Figure 3 depicts the design of the MEMS PC membrane. These devices reveal a very low FWHM of 0.08 nm for central wavelength at 1319 µm. The spectral filter lines could be tuned in the experiments across 30 nm by electrostatic MEMS actuation. However, it is challenging to adjust position and size of the QD for distinct wavelengths.

Using PC structures with MEMS tunable narrowband filters, polarization selectivity can be additionally implemented. This maintains the compactness of MEMS devices by introducing holes with pronounced elliptical symmetry in the PC structure of the top membrane in the top DBR [64]. Here, most commonly guided mode resonance structures [63,66] or structural birefringence [67] are applied. In both cases, the selective behavior of the filter device regarding electric field orientation of the incident wave is based on disturbing the 90°-symmetry by either line gratings or introducing elliptical base elements in a 2D PC.

11.2. Nano-Optical Sensor Concepts

A spectroscopic MEMS sensor using the excitation of surface plasmon-polariton (SPP) resonance on a cantilever was reported by Oshita et al. [68]. The device is fabricated from a SOI wafer, and a metallic grating is applied on top to provide the excitation condition for SPPs. In operation, the cantilever is oscillating at resonance frequency close to 400 Hz and provides the largest angular stroke. As the coupling condition for SPP to the metallic grating is strongly angle dependent, the signal recorded for half an oscillation period can be evaluated to get the spectral information. In the cited work, a spectral scanning range of 300 nm was achieved with a FWHM of approximately 10 nm or more. The spectral range

is mainly limited by the properties of the materials and the grating. Further data are given in Figure 3 in the second column from the right-hand side.

Another approach, presented by Faraji-Dana et al., applies tailored dispersion properties of diffractive elements using a folded beam path in a thin glass plate where light is reflected at three specifically designed metasurfaces [94]. The authors showed a spectrometer covering 100 nm spectral range with 1.2 nm resolution and device volume of 7 mm³.

11.3. Sensors with Links to Telecom Devices

Strong ties exist between spectroscopic sensors and devices used in multiplexing systems of optical telecommunication systems. In both cases, the goal is to analyze spectrally encoded information, but the focus for telecommunication is mostly on spectral linewidth, whereas in spectroscopy a broad spectral range is often required as well. Transfer of concepts from one field to the other is generally beneficial, and the most common device types such as FP or AWG are frequently found in both fields. Two examples of spectroscopic sensors derived from telecom concepts are presented in the following.

Filters with extremely small FWHM were demonstrated by Li et al. [78] and are included in Figure 1 at the right-hand side. This device is based on a fiber Bragg grating (FBG) with linear chirp. Local heating at a defined position of the FBG introduces a change in refractive index and therefore a phase shift in the grating period. Phase shifts in periodic patterns lead to resonant conditions and high transmission for a certain wavelength. Such behavior can also be understood by looking at the cavity of a DBR FP filter in the same way. A $\lambda/2$ layer in a periodic sequence of $\lambda/4$ layers represents a phase shift in the layer structure as well. The device presented by Li et al. is tunable for 16.5 nm in the spectral range around 1.55 μm, with a FWHM of only 0.007 nm.

The application of ring resonators is another path to achieve sub-nm spectral resolution. These devices are commonly used in telecom systems and are known to have very high Q factors of more than 100,000, but also small free spectral ranges as they work in a high order. Nitkowski et al. showed such a spectrometer integrated to a microfluidic chip [95]. From the same group, an improved device combining a ring resonator, a diffraction grating and a waveguide array was presented later, with 0.05 nm FWHM in the near IR spectral range and a footprint of 2 mm² [96]. Smooth sidewalls of the stripe waveguides and accurate dimensions of the ring structures are crucial, but the planar technology is well understood and commercially applied in the telecom field for many years already.

11.4. Sensors with Computational Signal Evaluation

For several recently developed spectrometer devices, such as the plasmonic MEMS sensor shown by Oshiita et al., computational post-processing of the acquired data are an essential part of the sensing principle. A very interesting and compact example in this direction is the nanowire-based spectrometer of Yang et al. [97]. The II-VI semiconductor of the nanowire is grown with gradually varying composition along the length of the wire, leading to a varying band gap. By choosing the appropriate base material, several spectral ranges can be addressed. An array of small electrodes is contacted to the nanowire and allows the measurement of a locally generated photocurrent. Evaluation of the signals is based on a pre-calibrated response function and an algorithm to extract the spectral data. The authors show results over a spectral range of 130 nm with FWHM of approximately 8 nm in the visible range. The device size is determined by the length of the nanowire and the dimension of the electrode array, both being on the order of 100 μm or less.

11.5. Sensors on the Fiber Tip

A highly efficient way to integrate optical measurement methods with fiber systems is to use the optical fiber itself as sensor. Beside the small size given by the fiber diameter, the typical advantages of fiber optics, namely its mechanical flexibility and immunity to electromagnetic interference, make this type of sensors interesting for measurements in difficult locations and harsh environments. However, most of the sensors are not tunable

or require additional electrical components at the opposite end of the fiber, thus increasing the overall size of the system again. Furthermore, the fabrication of fiber-based sensors can be quite challenging and will be addressed at the end of this discussion. Interaction with light waves can occur inside the fiber based on structures such as fiber Bragg gratings or on evaluation of scattering effects. In the following overview, a different approach where the sensor is fabricated on the tip of an optical fiber will be covered. In such a configuration, interaction with light waves occurs locally at the tip, and the fiber is merely used for guiding the wave to a detector.

As previously introduced, guided mode resonances (GMR) in 1D or 2D photonic slab waveguides enable very compact filter elements on MEMS devices. Tailoring the coupling strength between resonant and continuous mode allows for narrowband spectral properties, whereas breaking symmetries will lead to polarization dependent behavior. In a similar way, GMR filter elements can be implemented on the tip of optical fibers, as shown in Figure 23. A high refractive index thin film of ZrO_2 was deposited by ion beam sputter deposition on the fiber tip and acts as a slab waveguide with SiO_2 and air as surrounding materials. The periodic pattern, centered at the core of the single-mode fiber, was fabricated by FIB milling lithography. Nanoimprint lithography on a fiber tip is another possible fabrication method, in which the whole facet is covered and patterned in a single process step as shown by Tabassum et al. [98]. The fabrication is far simpler to implement than using sputter deposition and focused ion beam (FIB) milling, but it lacks the precise control of layer thickness or alignment to the fiber core.
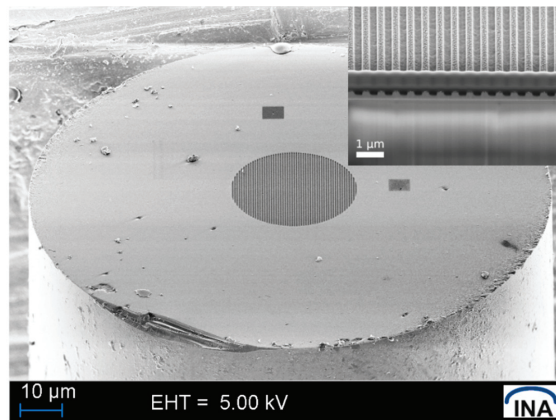
Figure 23. Tip of an optical fiber with GMR structure aligned to the core. The inset shows an FIB cross section of the ZrO_2 slab waveguide layer deposited by ion beam sputter deposition and the 1D periodic pattern fabricated by FIB milling. The dark bar covering a part of the pattern is a locally deposited protection layer to avoid damage of the pattern during preparation of the cross section and to enhance contrast for imaging.

Several research groups showed FP filters on fiber tips, mainly for sensing applications in gases and liquids. Mostly, air cavities are implemented by splicing a short section of multi-mode fiber or capillary to a single-mode fiber. Ma and Wang showed that fabricating a MEMS mirror on the spliced segment by sputter coating and FIB milling and subsequent selective underetching leads to an FP with the single-mode fiber facet being the second mirror. Target application of this sensor was detection of H_2 in gas atmospheres [99]. The combination of a single-mode fiber and a short photonic crystal fiber (PCF) segment with high index core and large surrounding air holes as fiber tip sensor was presented by Zhu et al. [100]. An FP cavity forms by reflections due to the mode mismatch at the splice and at the PCF to air interface and was applied to measure temperatures by tracing the optical path length variation resulting from thermal expansion and effective refractive

index change. A similar pressure sensor fabricated of a short capillary spliced to a single-mode fiber and covered by a few-layer graphene sheet as flexible membrane and FP mirror was shown by Ma et al. [101]. Kilic et al. [102] presented an acoustic sensor working on the FP principle as well, but first they fabricated a PC mirror on a released MEMS membrane using the GMR effect with a broadband resonance. The silicon on insulator chip was then mounted with high-viscosity epoxy to the fiber tip, forming an air cavity between silicon membrane and a metal layer coated on the fiber facet. Monolithic fabrication of an FP cavity by FIB milling was reported by Alberts et al. [103] using an off-centered, partly metal coated reflector for application as refractometer in liquids.

Beside the interferometric principles for sensors, plasmonic fiber tip devices are also a viable option. Still, using surface plasmon polariton resonances is difficult due to the required excitation condition. De Maria et al. [104] showed, however, that polishing the fiber tip under the excitation angle and coating the surface with silver is a possible solution for this problem. More common is the application of localized plasmon polariton (LPP) resonance by exciting free electron oscillations in nano-sized particles or structures [105,106]. Since excitation of LPP resonances can be accomplished by free space modes, no extra preparation is required. A typical application is the enhancement of weak intensity signals in Raman spectroscopy using the local field enhancement around the metallic nano structures, known as surface enhanced Raman spectroscopy (SERS) [107]. Kostovski et al. showed that this method can be integrated into a fiber tip sensor using nanoimprint lithography and subsequent deposition of a metal layer [108]. Probes based on nanoscale fiber tips and with additional metallization [109] are applied widely for scanning near field optical microscopy. Plasmonic effects or optical antennas are used to characterize optical properties which are not accessible to other methods. For example, Burresi et al [110] report on probing the magnetic field of an optical wave by applying a metallic split ring aperture at a tapered fiber tip.

Further implementations of sensor on fiber tips exist. In some, the optical fiber is only used as signal path, whereas the interaction with a sample is based on non-optical effects. The fiber tip atomic force microscope, presented by Iannuzzi et al. is an example from this group of sensors [111]. As mentioned, the technology required for the fabrication of fiber tip devices can be challenging. This is due to the small and not perfectly flat surface of a fiber facet, which makes resist coating or lithography quite difficult. Nevertheless, several routes for possible processes have already been shown [112]. These include FIB milling, nanoimprint lithography, align & shine photo lithography, two photon polymerization lithography, or mounting of chips fabricated by conventional methods.

11.6. Spatial Heterodyne Sensors

As a complement to the different, mainly FP-based sensor concepts discussed so far, the Spatial Heterodyne Spectrometer (SHS) is considered in the following section. The attractiveness of the SHS concept is based on the possibilities for tailoring its optical properties to specific user requirements in combination with its significant potential for miniaturization.

Essentially, the SHS is based on the configuration of a Michelson interferometer, where the mirrors in each arm are substituted by diffraction gratings [113]. The gratings are fixed in a tilted mount and do not require moving parts.

The basic working principle of SHS is schematically shown in Figure 24 (according to [114]). The incoming polychromatic wavefronts are separated by the beam splitter into two partial wavefronts, each striking on a respective grating. The orientation of the grating determines the Littrow wavelength, whose wavefront is diffracted exactly backward to the incident direction. All other wavelengths have different diffraction angles and propagation directions. At the detector, the superimposed light from both gratings is recorded. In detail, the periodicity of the interference pattern Λ for a specific wavelength λ depends on the half angle between intersecting wavevectors θ and the refractive index n of the ambient medium. The entire recorded interferogram is composed by the contribution of all involved wavelengths. Finally, the interferogram must be converted to a conventional

spectrum by Fourier transformation. The working principle allows very high spectral resolution for a small spectral bandwidth.

Applications for SHS range from space born projects e.g., satellite-based atmospheric temperature measurements [115] to Raman Spectroscopy of minerals [114]. Particularly impressive are the small dimensions that can be achieved. A SHS system was presented in [115], operating between 761.9 nm and 765.3 nm with a resolving power of about 8000, and requiring only a volume of $38 \times 38 \times 27$ mm^3 in size. In the meantime, progress has also been made in the production technology of SHS. Yi et al. [116] reported on the fabrication procedure of monolithic interferometers for SHS systems with ultraviolet curing adhesive and commercial optical elements, which may open the door to high volume manufacturing.
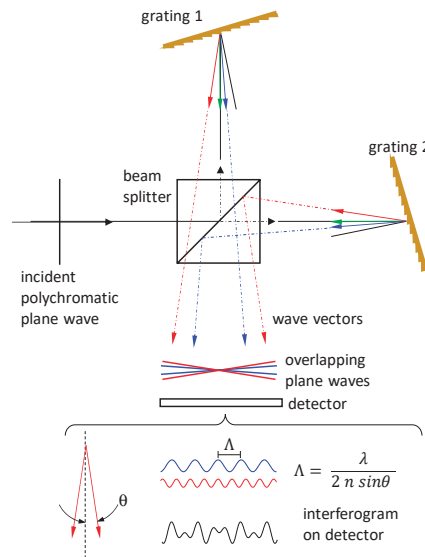
Figure 24. Illustration of the basic principle of spatial heterodyne spectroscopy (SHS).

12. Estimation of Potential Space Requirement after Utmost Miniaturization

Concerning grating spectrometers, the company Hamamatsu and Ibsen Photonics most probably came close to the miniaturization limits defined by such an optical resolution, which is still sufficient for some applications. In the case of our VIS and NIR FP filter arrays, the miniaturization potential in lateral direction was not used in our proof-of-principle. With 40×40 µm^2 in lateral direction, the mesa is considerably very big, and therein lies a high miniaturization potential to make them smaller. In this section, the potential limits for miniaturization of all six sensor principles are estimated: AWG, static FP filter array, MEMS tunable FP filter arrays, plasmonic sensors, MEMS tunable PC filters, and chirped fiber Bragg gratings. To identify the miniaturization limits, best case scenarios (ideal conditions) and optimum vertical light incidence are considered. For the static arrangements (FP filter array, AWG), $\Delta\lambda = 2$ nm in the VIS range was chosen for the spectral step size (channel spacing) between spectrally neighboring transmission lines; and in the NIR range, a channel spacing of $\Delta\lambda = 4$ nm. A spectral span of 400 nm in the VIS range and a spectral span of 500 nm in the NIR range has to be covered. Although a preliminary estimation was already performed in [11], here it is further complemented with inclusion of two additional sensor concepts and supplementary figures visualizing the lateral arrangements.

12.1. Static FP Filter Arrays Covering 400 nm in the VIS Spectral Range

In Figure 25a, the minimum space requirements for a static FP filter array for the VIS spectral range is shown. To eliminate effects from borders within a single pixel, the lateral size of the square optically active mesa (orange) has to be approximatively $8\lambda \times 8\lambda$ or larger, which was derived from experiments and simulations. This means that 6 µm side dimensions of the square mesa are sufficient for the wavelength range $\lambda = 400$–800 nm. Choosing a spatial spacing of 4 µm between the square mesa, results in a period of 10 µm and reveals an area of $10 \times 10 \ \mu m^2$ for each pixel. The material system TiO_2/SiO_2 for the DBRs allows stopband widths of 200 nm, thus, 100 spectrally adjacent filter lines in each stopband are required. Two neighboring stopbands are required to span 400 nm (Figure 25a). To be on the safe side for mounting issues, empty frames of 50 µm width surrounding both arrays are chosen. A space of $204 \times 358 \ \mu m^2$ is required, resulting in a chip size of about 0.07 mm^2. This is well compatible with commercial Si CCD detector arrays or Si CMOS detector arrays. All signal recording and processing electronics are located behind the layer containing the filters as depicted in Figure 25a, leading to a very compact layout.
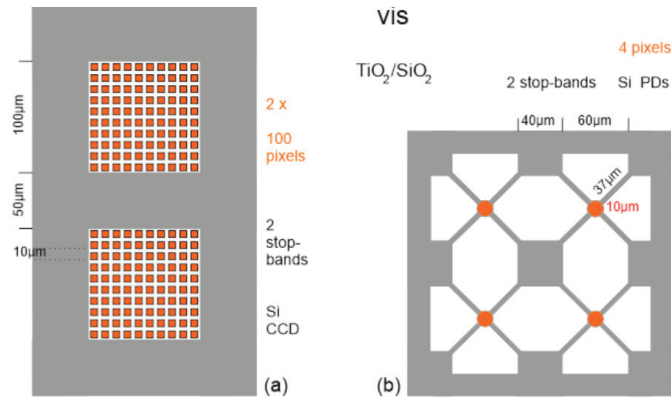
Figure 25. Space requirement to cover 400 nm in the VIS spectral range using two neighboring TiO_2/SiO_2 stopbands for the DBRs and PDs/CCDs in the Si material system. (**a**) Static FP filter array. (**b**) MEMS tunable FP filters.

12.2. Static FP Filter Arrays Covering 500 nm in the NIR Spectral Range

Since Si cannot be used for this purpose, other detector material such as InGaAs is required. However, photodiodes in the InGaAs material system are by far more expensive than Si CCD or CMOS detector arrays. The company Hamamatsu offers linear InGaAs photodiode arrays which have stripe-like active areas (orange in Figure 26) of $15 \times 100 \ \mu m^2$ which are followed by stripes of $10 \times 100 \ \mu m^2$ as spacers (white in Figure 26). Therefore, the period of the spacer/stripe arrangement is 25 µm. For $\lambda = 1500$ nm, this also fulfills the required 8λ minimum pixel size. A minimum of 125 pixels are required for one DBR in the TiO_2/SiO_2 material system with a stopband of 500 nm, which translates to $100 \times 3125 \ \mu m^2$ (Figure 26). Considering an empty frame of 100 µm width around the linear array, $300 \times 3325 \ \mu m^2$ space are required, resulting in 1 mm^2 chip size. Such approximated size excludes any signal processing electronics that still have to be integrated in this commercial solution.

Figure 26. Space requirement to cover 500 nm in the NIR spectral range using commercial InGaAs PDs. Please note that this array is considerably scaled down in size compared to Figures 25 and 27.

This requires a huge amount of space. However, if tailored square photodiodes would be used, the required space would shrink considerably. However, this technology is not yet available on the market. Figure 27a displays an estimate for the required space for that case. To avoid bor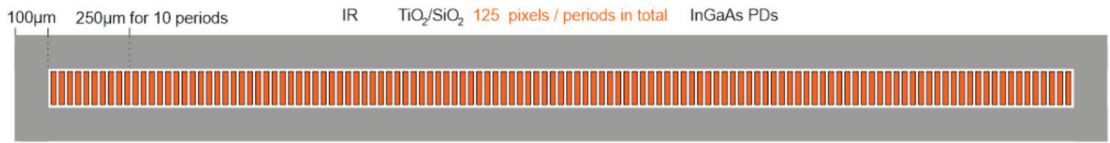der effects within a single pixel, the lateral size of the square optically active mesa (orange in Figure 27a) should also be approximately $8\lambda \times 8\lambda$ or larger, known from experiments and simulations. Thus, 13 μm for both sides of the squares are sufficient for the wavelength range of $\lambda = 1500$ nm. Using 4 μm spatial spacing between the mesa, the period is 17 μm in length. Thus, an area of 17×17 μm^2 are required for each pixel. A single TiO$_2$/SiO$_2$ DBR with a stopband of 500 nm already covers the required spectral range. Since the required 125 pixels are not practical for a rectangular array, 130 pixels are chosen (Figure 27a) and arranged in a 10×13 array. Applying empty frames of 50 μm width surrounding arrays, a total of 274×325 μm^2 space is required. This results in a chip size of about 0.09 mm^2. For a very compact design, the complete signal processing electronics should be placed behind the sensor part as depicted in Figure 27a. However, such technology (corresponding to Si CCD or Si CMOS) has not yet been developed in the InGaAs/InP-based material system. Nevertheless, a hybrid solution with a Si CMOS chip behind the InP chip is also possible, as shown in Figure 5.
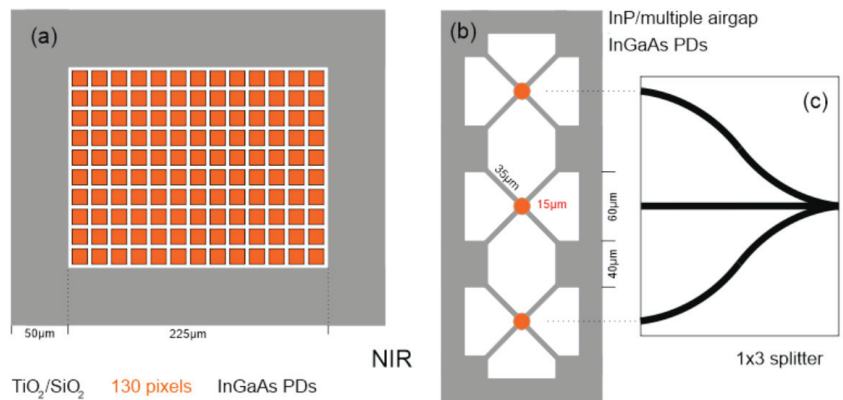
Figure 27. Space requirement to cover 500 nm in the NIR spectral range using tailored InGaAs PDs, not yet available on the market. (**a**) Static FP filter array with a single TiO$_2$/SiO$_2$ DBR. (**b**) MEMS tuneable FP filters in the InP multiple airgap system. (**c**) 1×3 splitter, schematically aligned to the 3 MEMS membranes.

12.3. MEMS Tunable FP Filter Arrays Covering 500 nm in the NIR Spectral Range

The InP/multiple airgap material system allows DBRs with a stopband width between 500 nm and 1500 nm, depending on the InP layer thicknesses ($3\lambda_{InP}/4$ or $\lambda_{InP}/4$), respectively. Therefore, a single stopband is already enough to cover the required 500 nm wavelength span in the NIR spectral range. In the experiment, a tuning range of 221 nm was obtained. To be on the safe side, three MEMS tunable filters are used to cover the

required 500 nm. For our minimum space estimation, the following required elements are arranged according to Figure 27b: supporting posts spanning a lateral area of 40×40 µm^2, suspensions with 35 µm lengths, and circular membranes with 15 µm diameters. The 15 µm diameter is fully sufficient to cover the wavelength range between 1.2–1.7 µm. As shown in Figure 27b, the central filter is sharing its supporting posts with the two neighboring filters. Applying empty frames of 20 µm all around the three filters ensures that the optically active membrane (orange) is at least 50 µm apart from the chip borders. This requires 340×140 µm^2 space and reveals a chip size of 0.05 mm^2. As demonstrated, the advantage in this concept is that the InGaAs Photodiode can be fabricated together with the MEMS filter within the same epitaxial step (monolithic integration), as depicted in Figure 16. Concerning fiber and waveguide optics, a 1×3 integrated waveguide splitter (Figure 27c) could be used to divide the light from the fiber and to guide it to the three active regions (shown in orange). Please note that the plane spanned in Figure 27c is perpendicular to the plane spanned in Figure 27b, and the three ends of the splitter are ending centrally to the three orange membranes. This is indicated by the two dotted lines relating Figure 27b,c. The fiber would be coupled to the right-hand side waveguide end of Figure 27c.

12.4. MEMS Tunable FP Filter Arrays Covering 400 nm in the VIS Spectral Range

The material system TiO$_2$/SiO$_2$ is chosen for the DBRs, allowing stopband widths of about 200 nm. According to Figure 25b, the required elements are supporting posts with an area of 40×40 µm^2, four suspensions with lengths of 35 µm, and circular membranes (orange) of 10 µm diameter. This diameter is sufficient for application at $\lambda = 400 \ldots 800$ nm. Please note that the dielectric material system exhibits much smaller tuning ranges due to the single air-gap MEMS in comparison to the slim InP multiple airgap system. Although they have 200 nm wide stopbands, four tunable FP filters (each with 100 nm tuning range) are required to cover the targeted 400 nm (Figure 25b). Neighboring filters share supporting posts which are located in between. As in Section 12.3, applying empty frames of 20 µm all around the four filters ensures that the optically active membrane (orange) is at least 50 µm apart from the chip borders. This requires 240×240 µm^2 space and results in a chip size of 0.06 mm^2. Similar to previous cases, the complete signal processing electronics is placed behind the sensor part depicted in Figure 25b to make it very compact. Concerning fiber and waveguide optics, a linear arrangement of the four MEMS filters would be a better option (like in Figure 27b), and a 1×4 integrated waveguide splitter should be used to divide the light from the fiber to the four active regions (orange) as in Figure 27c.

It is important to note that in Sections 12.1–12.4, the photodetectors and the electronics are hidden behind the filters elements and not visible in Figures 25–27.

12.5. MEMS Tunable PC Filter to Cover a Spectral Span of 500 nm in the NIR Range

Zobenica et al. [77] measured a tuning range of 30 nm (1308–1338 nm) and pointed out that there is a potential to extend it to 40 nm. A wavelength span of 500 nm can be covered by combining 15 spectrally neighbored filters, supporting posts of 15×50 µm^2, PC membranes with suspensions requiring in total an area of 15×15 µm^2, and additionally the electronics. As discussed in Sections 12.3 and 12.4 the filters are considered with overlapping tuning ranges, just to ensure reliable operation. Similar to previous cases, here the neighboring MEMS filters share their supporting posts in between the filters. Considering the additional space for contacts of sensing and actuation diodes, the estimate yields 0.33 mm^2 for the total chip size. The papers do not provide enough information concerning space for signal processing, electronics and contacts. However, extrapolating from what is visible in Figure 1c in [77], we assume that there might be a miniaturization potential of a factor of 6, which is considered in our estimation.

12.6. AWG Covering 500 nm in the NIR Spectral Range

During his time at the company NTT, Japan, Y. Yoshikuni et al. [24] performed pioneering work on arrayed waveguide gratings (AWGs). His team demonstrated 64 channels with

50 GHz frequency spacing for fiberoptic long-haul telecommunication at 1.55 μm. The corresponding sample was already downscaled and had lateral dimensions of 7×3.6 mm^2 [22–24]. At the time of publication, they also implemented the most complex InP photonic device integration in the world, including semiconductor optical amplifiers, photodiode arrays and several AWGs. On the basis of these early and also recent publications, a space requirement of 50 mm^2 including 125 channels was estimated for the NIR spectral range.

12.7. Plasmonic MEMS Cantilever Covering 500 nm in the NIR Spectral Range

The device presented by Oshita et al. already shows a very broad tuning range of 300 nm in the NIR spectral range [68]. Increasing this parameter could be accomplished by a larger stroke of the deflection angle, but this will be limited by several constraints. Flatness of the cantilever during actuation is crucial as the coupling condition to a SPP is angle dependent and bending of the grating would lead to increased FWHM. Reducing this cantilever size will decrease the efficiency of light coupling to the grating considerably. There may be some room for improvement based on optimization of the geometric shape of the device. In the end, using a second device with different spectral tuning range to reach 500 nm spectral span seems to be the more promising option. In such implementation, two identical MEMS cantilevers would be fabricated, but different grating structures and possible different metals would lead to SPP resonance excitation in different spectral ranges for the same deflection angle. The required space of such a sensor system would be around 20 mm^2 if no reduction in size of the single devices is considered.

12.8. Locally Heated Chirped FBG to Cover a Spectral Span of 500 nm in the NIR Spectral Range

Tunable filters based on a chirped FBG as reported by Li et al. [78] work only for a limited spectral span of 15–20 nm. Therefore, tuning over a range of 500 nm would require at least 30 individual chirped fibers. Since the outer diameter of a conventional single-mode fiber is only 125 μm, even an array of 30 fibers, positioned for example in a template of etched channels on a silicon substrate, would only require 5 mm in width. The length of the chirped FBG is given by the required number of periods and is in this case in the range of 50 mm. The presented sensor is not yet optimized for miniaturization since the thermal actuation is based on a heating wire attached to a very bulky linear positioning stage. A possible approach that will not lead to any further increase of the device size would be to integrate an array of heater elements into the silicon wafer template. This would finally lead to a space requirement of 250 mm^2 for the sensor alone, excluding other elements such as a photodiode, any further optical fibers for wave transport, coupling elements or control of the heater array.

13. Where Are the Minimum Structure Size Limits in 3D Nanoimprint Lithography?

The potential of 2D nanoimprint lithography for replication of extremely small structures was demonstrated by patterns with 5 nm lateral half-pitch [117], and most recently, even a reduction to 2 nm was reported [118]. The 5 nm dimension were imprinted with a III/V semiconductor stamp. It was grown by molecular beam epitaxy, subsequently cleaved and selectively etched on the cleaved side. Finally, the cleaved side represented the nanoimprint stamp [117]. An even more exotic stamp is a substrate with carbon nanotubes on top. 2 nm in lateral direction were demonstrated by imprinting with these carbon nanotubes [118]. In addition to experimental investigations, theoretical studies have also been performed by modeling the stamp-resist interface. The most relevant forces between the stamp surface and the nanoimprint resist surface, considering the individual atoms of both surfaces, were studied in sub-nanoscale using theoretical model calculations [119,120]. The result shown that the stamp could not be released from the cured and hardened imprint resist if lateral structure dimensions are below 0.5 nm. This represents a theoretical limit for minimum lateral size dimensions for nanoimprint lithography. In general, the smaller the molecules used in the nanoimprint resist, the smaller the minimum structure dimensions

which are obtainable via nanoimprint lithography. Typically, a monomer has a size of 1–2 nm, i.e., even for short-chained polymers, only a small space is remaining in the structure.

Many different template materials are possible, such as glass, Si or III/V semiconductors. Imprints can be directly performed using the template, as what was done in our experiments using GaAs templates. Alternatively, the master template (mother-structure) has also been replicated into polydimethylsiloxane (PDMS) serving as a daughter-structure which is used for the subsequent imprinting in mr-UVcur06. This resist is cured with UV light.

In the following discussion, an intuitive visualization is made in Figure 28 to illustrate the vertical mesa height differences in the sub-nm range in relation to the scale of resist molecules. For the purpose of simplicity, the influence of surface roughness is not included.
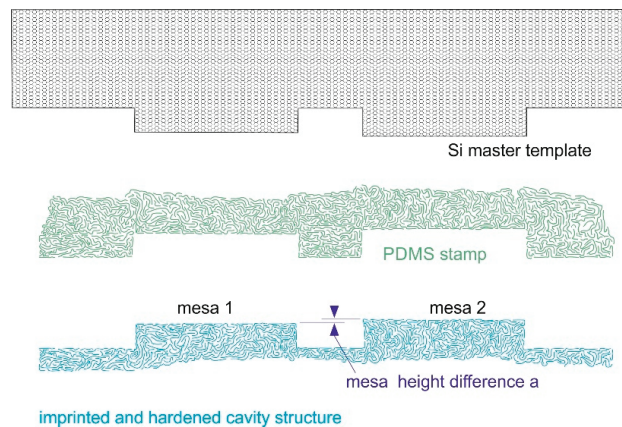

Si master template

PDMS stamp

mesa 1   mesa 2

mesa height difference a

imprinted and hardened cavity structure

Figure 28. Cross sections of schematic surface profiles. The crystalline structure of the Si master template is visualized by the periodic honey-comb structure (**top**). The master template is replicated in PDMS and rotated by 180°, as shown in green (**center**). The schematic includes a possible arrangement of organic molecules in the PDMS. Subsequently, 3D nanoimprints were performed using this PDMS stamp. After imprinting the resist, hardening the resist and releasing the stamp the blue schematic surface is resulting (**bottom**). The figures do not have the same scale in vertical and lateral direction: differences exist in vertical mesa heights between $a = 0.2$ nm and 1 nm, lateral mesa widths between 6 μm and 40 μm, and vertical mesa heights between 10 nm and 300 nm.

Our smallest height difference which was measured with an interference microscopy was $a = 0.2$ nm [33,34]. On a first glance, this result might be in contradiction to the smallest lateral structure sizes of 0.5 nm which were predicted in the abovementioned theoretical model calculations [119,120]. However, there is no contradiction since the lateral dimensions of our mesa are in the range of >6 μm (see Section 12) or even 40 μm in our proof-of-principle (Sections 2–4). The chains of the nanoimprint resist molecules will spread in lateral directions. This means that a very high vertical accuracy can be obtained if comparably large lateral dimensions can be tolerated or are even required as in our case. Furthermore, very high vertical resolution can be obtained if larger residual layers are acceptable or reservoir for excess resist are included in the design. Even if our technology which enables zero-residual layers is used [92], these reservoir technologies and volume equalizing technologies [86] have to be applied.

Measuring $a = 0.2$ nm [33,34] using an interference microscopy is executed by averaging over an area containing many polymer chains (diffraction-limited focal diameter). Please note that the exact same approach is applied in the optical sensor, therefore, this is a relevant value for the height differences.

A schematic FP array structures with two different mesa heights is displayed in Figure 25 to envisage vertical resolution limits in 3D nanoimprint lithography. The polymer

chains of the nanoimprint resist reveal different lengths and shape, and they have a lateral thickness of approximatively 0.2 nm. In lateral directions, the molecules can easily migrate and spread during the filling of the stamp (mold) with imprint resist. Due to these microfluidic aspects, our 3D nanoimprints could reveal vertical mesa height differences down to 0.2 nm since the lateral dimension is large enough to allow material migration and spreading. In summary, 2D nanoimprint technology uses constant vertical step heights and the smallest structure sizes in lateral directions were 2–5 nm in the experiments [117,118] and 0.5 nm in theoretical model calculations [119,120], as already mentioned. In our 3D nanoimprint experiments, 0.2 nm in mesa height difference was obtained in structures with rather large lateral sizes in the range of several μm, due to viable allow material migration and spreading. At the moment, it is hard to estimate the limits for 3D nanoimprint if ultra-small variations are involved in vertical and lateral dimension simultaneously, but it could be in the sub-nm range in all combined three directions.

14. Can Nanoimprint Be Applied to Fabricate the Seven Sensor Types Compared Here?

Today, a variety of molding technologies exist, such hot embossing, nanoimprint, injection molding and LIGA. The acronym LIGA consist of the German words **Li**thographie, **G**alvanik, **A**bformung, which means (X-ray) lithography, electroplating, molding [121] and is used worldwide. In nanoimprint technology, structures are replicated using a stamp with structure sizes between a few nm up to several μm. In contrast, LIGA technology is replicating structures from a stamp generating structures between a few μm to several mm [121]. Even larger objects are replicated by injection molding ranging in size between several μm to the range of a few meters.

Using molding technologies, miniaturized grating spectrometers [72] can be generated to define curved mirrors, grating, cavities to insert detector arrays, guide elements and housing parts in a single step. To lower fabrication cost, molding is always a very good strategy. Micro-grating spectrometers were also replicated applying LIGA processes [122]. Using InGaInAs, waveguide structures were lithographically treated and etched to define transmission grating, curved mirrors and trenches for optical fibers [123].

In this last section, the question is raised whether nanoimprint can be applied in the fabrication of AWG sensors, miniaturized spectrometers, plasmonic MEMS sensors, static FP filter array sensors, MEMS tunable FP array, tunable chirped fiber Bragg gratings, and MEMS tunable PC arrays, all of which are shown in Figure 1. Several advantages of nanoimprint concerning cost, time, and effort were already presented and confirmed by results presented in the previous sections. The lithography included in manufacturing can be replaced by nanoimprint lithography in five out of the seven sensor types. However, in cannot be used in the fabrication of the classical grating spectrometers and the chirped fiber Bragg gratings. Moreover, nanoimprint might not be ideal for the precise positioning of the QDs within the PC structure [77]. We expect that the positioning of the QD would be arduous and might require, e.g., electron or ion beam lithography. Thus, nanoimprint lithography might not reveal clear advantages in manufacturing of MEMS tunable PC structures. However, it is highly desirable to use nanoimprint lithography for the fabrication of AWGs since it has clear advantages in replacing optical lithography in large scale production. Furthermore, nanoimprint is very desirable, but not absolutely necessary, in manufacturing MEMS tunable FP filter arrays. Most essential is it for static FP filter arrays. Using nanoimprint technology, the whole cavity structure including millions of FP filters (pixels) can be imprinted in a single step. Furthermore, the stamp/mold is reusable for many times. Theoretically, there is no limit in the number of FP filters (pixels) which can be defined within a single imprint step that generates all the different 3D cavities altogether [33–37]. Alternative methodologies have to use many more fabrication steps [28–31], which limits the number of pixels which can be manufactured in a realistic way. Among all the considered sensor types, the static FP filters make the most of the advantages of 3D nanoimprint lithography. Many FP filter arrays can be imprinted in a batch process at the same time, potentially resulting in a significant cost reduction. For

repetitive processes in large scale (mass production), nanoimprint lithography reveals its characteristic superiority in saving time, cost and effort.

15. Conclusions

Limits of wide wavelength tuning, FWHM and stopband widths are investigated for the InP multiple air-gap system. Wavelength tuning efficiency for said sensor system is found to be the closest to 1, and additionally with much smaller size compared to other systems and different sensor methodologies.

In our comparison, the tunable chirped fiber Bragg grating reveals by far the smallest FWHM of 0.007 nm at 1.5 µm. However, the space requirement is the largest in this case. The next lowest FWHM of typically 0.1 nm at λ = 1.3 µm are measured in MEMS tunable PC filters. Potentially, the space requirement is also very small. However, in order to obtain larger spectral spans of e.g., 400 nm, the combination of several neighboring spectral tuning ranges is required. For that purpose, the QD have to be adjusted and varied in all the PC crystal in a defined way. This might be quite challenging concerning the spectral adjustment and defined variation from array to array. On the other hand, AWGs also provide small linewidths, and the arrangement of several arrays next to each other is very easy. However, the fabrication of AWGs for the VIS spectral range is still an enormous challenge.

The typical linewidths measured for FP filter arrays are higher than the typical values of PC or AWG sensors. Although 0.1 nm linewidth could be achieved at λ = 1.5 µm in an InP/multiple air-gap FP filter in a single case, it was not reproducible in tunable filters or in static FP filter arrays. Using the InP multiple airgap MEMS technology, very small linewidths are extremely challenging in the tunable technology, but on the other hand, it is very attractive in terms of scalability. Since various static FP filter arrays can be manufactured next to each other within a single 3D nanoimprint step, this technology enables lowest tentative price per spectral range for visible spectral ranges.

A chance to achieve small linewidths in MEMS tunable filters lies in the application of stable cavities. A small linewidth of <0.15 nm was reported over the whole tuning range, although the tuning range is limited and only thermal tuning was applied [124].

The current version of the plasmonic MEMS sensor evaluates charge carriers induced by the SPP resonance into a diode structure and transforming this angle dependent current into the spectral information. At the moment this is limited to a rather high FWHM value of 10 nm or more. On the other hand, this concept is very promising due to its wide tuning range.

Thermally tuned chirped FBG shows narrow band filter lines with FWHM of 0.007 nm and can potentially be implemented in any working spectral range of an optical fiber. The small tuning rang of only 16.5 nm requires, however, an array of many individual chirped FBG to cover broader spectral spans.

The classical grating spectrometer is definitely the best in our comparison in terms of the efficiency in making most out of available light. However, the grating spectrometer suffers considerably from strongly reduced spectral resolution when downscaling the devices, whereas such limitations are not relevant for all the other sensor types compared in our review. In all these cases, the resolution is very high and independent from miniaturization. The AWG uses available light much more efficiently than the static and tunable FP filter arrays and the tunable PC filter array. The latter three own rather low efficiencies, but the efficiencies can be boosted by spectral preselection as shown in this review.

Fourier spectroscopy in the infrared spectral range is using the amount of light much more efficiently than grating spectrometers (Multiplex and Jacquinot advantages) in large set-ups. The disadvantage is that the miniaturization achieved up to now is by far less than that obtained for PC and FP-based sensors.

Nanoimprint can be applied to all the compared sensors, except the chirped fiber Bragg grating and the classical grating spectrometer. Transmission gratings could be fabricated by nanoimprint lithography. Notwithstanding, nanoimprint technology can only reveal its full potential in manufacturing static FP filter arrays. Here, 192 different filter lines were demonstrated using a single 3D nanoimprint step to define accurate and

diverse 3D cavity layers. In a proof-of-concept, 192 spectrally different filter lines were successfully demonstrated, which is far better than the three different broad filter lines used in modern digital cameras. There are no limits on the principle to considerably increase these values in static FP filter arrays. At the same time, nanoimprint substantially reduces fabrication time, cost and effort.

16. Patents

For FP filter arrays, PC sensors and plasmonic sensors, the obvious disadvantage concerning less efficiency in using available light (in comparison to grating spectrometers) can be partly compensated by spectral preselection: R. Brunner, H. Hillmer and A. Gatto: Spektralsensor zur spektralen Analyse einfallenden Lichts, German Patent 2016, DE 10 2014 108 138 B4. Recently, this concept has been proven, experimentally [11,89]. See Section 6.

Abbreviations

1D	one-dimensional
2D	two-dimensional
3D	three-dimensional
α_{InP}	absorption coefficient of InP
α_{Si3N4}	absorption coefficient of silicon nitride
α_{SiO2}	absorption coefficient of silicon dioxide
AWG	arrayed waveguide grating
CCD	charge coupled device
CMOS	complementary metal oxide semiconductor
$\Delta\lambda$	wavelength tuning range, wavelength interval, wavelength difference
$\Delta\lambda_i$	wavelength interval, wavelength spacing
$\Delta\lambda/\lambda$	optical resolution of an optical sensor or spectrometer
Δl	interface fluctuations
ΔL	displacement of DBR mirrors, cavity tuning
$\Delta L_1, \Delta L_2$	cavity lengths fluctuations
$\Delta\lambda/\Delta L$	tuning efficiency
Δn	refractive index difference
DBR	distributed Bragg reflector
DWDM	dense wavelength division multiplex
FBG	fiber Bragg grating

FIB	focused ion beam
FP	Fabry-Pérot
FWHM	full width at half maximum, linewidth
GMR	guided mode resonance
L, L_1, L_2	cavity thickness, cavity height, cavity length
λ	vacuum wavelength
λ_{air}	wavelength of light in air
λ_i	central wavelength of DBR number i
$\lambda_i/4$	quarter-wavelength optical thickness of a single DBR material layer of index i
$\tilde{\lambda}$	effective wavelength
λ_{InP}	wavelength of light in InP
Λ	periodicity of interference pattern
LIGA	Lithographie, Galvanik, Abformung = lithography, electroplating, molding
LPP	localized plasmon polariton
M	number of waveguides in an AWG
MEMS	micro-electro-mechanical-system
MOCVD	metal-organic chemical vapor deposition
n	refractive index
n_{InP}	refractive index of indium phosphide
n_{Si3N4}	refractive index of silicon nitride
n_{SiO2}	refractive index of silicon dioxide
N	number of grating lines, or number of different FP filter arrays
NIR	near-infrared
QD	quantum dot
p	number of periods in the DBR
PC	photonic crystal
PCF	photonic crystal fiber
PD	photodiode
PD1, PD2	highly doped semiconductor layers in a photodiode
PDMS	polydimethylsiloxane
PECVD	plasma enhanced chemical vapor deposition
R_{max}	Maximum reflectance in the center of the stopband
$R_{max,sat}$	Saturation value of the maximum reflectance in the center of the stopband
SCIL	substrate conformal imprint lithography
SEM	scanning electron microscope
SERS	surface enhanced Raman spectroscopy
SHS	spatial heterodyne spectroscopy
SOI	silicon on insulator
SPP	surface plasmon polariton
Θ	half angle between intersecting wavevectors
VIS	visible (spectral range)
UV	ultraviolet

References

1. Lindon, J.C.; Tranter, G.E.; Koppenaal, D. *Encyclopedia of Spectroscopy and Spectrometry*, 3rd ed.; Academic Press: Cambridge, MA, USA, 2016; ISBN 978-0-12-803224-4.
2. Haken, H.; Wolf, H.C. Modern Methods of Optical Spectroscopy. In *The Physics of Atoms and Quanta*; Springer: Berlin, Heidelberg, Germany, 1996. [CrossRef]
3. Baeten, V.; Dardenne, P. Spectroscopy: Developments in Instrumentation and Analysis. *Grasas Aceites* **2002**, *53*, 45–63. [CrossRef]
4. Tkachenko, N.V. *Optical Spectroscopy: Methods and Instrumentations*, 1st ed.; Elsevier: Amsterdam, The Netherlands, 2006; ISBN 978-0-444-52126-2.
5. Dakin, J.P.; Chambers, P. Review of Methods of Optical GAS detection by Direct Optical Spectroscopy, with Emphasis on Correlation Spectroscopy. In *Optical Chemical Sensors*; NATO Science Series; II: Mathematics, Physics and Chemistry; Baldini, F., Chester, A., Homola, J., Martellucci, S., Eds.; Springer: Dordrecht, The Netherlands, 2006; Volume 224, pp. 457–477. ISBN 978-1-4020-4609-4.
6. Hodgkinson, J.; Tatam, R.P. Optical gas sensing: A review. *Meas. Sci. Technol.* **2013**, *24*, 012004. [CrossRef]
7. Rolinger, L.; Rüdt, M.; Hubbuch, J. A critical review of recent trends, and a future perspective of optical spectroscopy as PAT in biopharmaceutical downstream processing. *Anal. Bioanal. Chem.* **2020**, *412*, 2047–2064. [CrossRef]

8. Neumann, W. *Fundamentals of Dispersive Optical Spectroscopy Systems*; Society of Photo-Optical Instrumentation Engineers (SPIE): Bellingham, WA, USA, 2013; PM242; ISBN 978-081-949-824-3.

9. Appenzeller, I. Optical-Range Grating and Prism Spectrometers. In *Introduction to Astronomical Spectroscopy (Cambridge Observing Handbooks for Research Astronomers)*; Cambridge University Press: Cambridge, UK, 2012; pp. 81–126. [CrossRef]

10. Thorne, A.P. Dispersion and resolving power: Prism spectrographs. In *Spectrophysics*; Springer: Dordrecht, The Netherlands, 1988. [CrossRef]

11. Hillmer, H.; Woidt, C.; Istock, A.; Kobylinskiy, A.; Nguyen, D.T.; Ahmed, N.; Brunner, R.; Kusserow, T. Role of Nanoimprint Lithography for Strongly Miniaturized Optical Spectrometers. *Nanomaterials* **2021**, *11*, 164. [CrossRef]

12. Kenda, A.; Frank, A.; Kraft, M.; Tortschanoff, A.; Sandner, T.; Schenk, H.; Scherf, W. Compact High-Speed Spectrometers Based on MEMS Devices with Large Amplitude In-Plane Actuators. *Procedia Chem.* **2009**, *1*, 556–559. [CrossRef]

13. Tormen, M.; Lockhart, R.; Niedermann, P.; Overstolz, T.; Hoogerwerf, A.; Mayor, J.-M.; Pierer, J.; Bosshard, C.; Ischer, R.; Voirin, G.; et al. MEMS tunable grating micro-spectrometer. In Proceedings of the International Conference on Space Optics—ICSO, Toulouse, France, 14–17 October 2008; Society of Photo-Optical Instrumentation Engineers (SPIE): Bellingham, WA, USA, 2008; p. 1056607. [CrossRef]

14. Huang, J.; Wen, Q.; Nie, Q.; Chang, F.; Zhou, Y.; Wen, Z. Miniaturized NIR Spectrometer Based on Novel MOEMS Scanning Tilted Grating. *Micromachines* **2018**, *9*, 478. [CrossRef]

15. Truxal, S.T.; Kurabayashi, K.; Tung, J.-C. Design of a MEMS Tunable Polymer Grating for Single Detector Spectroscopy. *Int. J. Optomechatronics* **2008**, *2*, 75–87. [CrossRef]

16. Harmon, K. *Interferometers: Fundamentals, Methods and Applications (Physics Research and Technology)*; Nova Science Publishers: Hauppauge, NY, USA, 2015; ISBN 978-1-63483-692-0.

17. Hariharan, P. *Basics of Interferometry*; Academic Press: Boston, MA, USA, 1992; ISBN 978-012-325-218-0.

18. Andersson, P.O.; Edwall, G.; Persson, A.; Thylén, L. Fiber Optic Mach-Zehnder Interferometer Based on Lithium Niobate Components. In *Integrated Optics*; Springer Series in Optical, Sciences; Nolting, H.P.J., Ulrich, R., Eds.; Springer: Berlin/Heidelberg, Germany, 1985; Volume 48, pp. 26–28. ISBN 978-3-540-39452-5.

19. Zetie., K.P.; Adams, S.F.; Tocknell, R.M. How does a Mach-Zehnder interferometer work? *Phys. Educ.* **2000**, *35*, 46–48. [CrossRef]

20. Russel, J.; Cohn, R. *Mach-Zehnder Interferometer*; Book on Demand: Norderstedt, Germany, 2013; ISBN 978-551-267-842-8.

21. Smit, M.K.; van Dam, C. PHASAR-Based WDM-Devices: Principles, Design and Applications. *IEEE J. Sel. Top. Quantum Electron.* **1996**, *2*, 236–250. [CrossRef]

22. Kohtoku, M.; Sanjoh, H.; Oku, S.; Kadota, Y.; Yoshikuni, Y.; Shibata, Y. InP-based 64-channel arrayed waveguide grating with 50GHz channel spacing and up to −20dB crosstalk. *Electron. Lett.* **1997**, *33*, 1786–1787. [CrossRef]

23. Kohtoku, M.; Sanjoh, H.; Oku, S.; Kadota, Y.; Yoshikuni, Y. Polarization Independent Semiconductor Arrayed Waveguide Gratings Using a Deep-Ridge Waveguide Structure. *IEICE Trans. Electron.* **1998**, *E81-C*, 1195–1204.

24. Yoshikuni, Y. Semiconductor Arrayed Waveguide Gratings for Photonic Integrated Devices. *IEEE J. Sel. Top. Quantum Electron.* **2002**, *8*, 1102–1114. [CrossRef]

25. Cvetojevic, N.; Jovanovic, N.; Bland-Hawthorn, J.; Haynes, R.; Lawrence, J. Miniature Spectrographs: Characterization of Arrayed Waveguide Gratings for Astronomy. *Proc. SPIE Int. Soc. Opt. Eng.* **2010**, 77394H. [CrossRef]

26. Seyringer, D.; Sagmeister, M.; Maese-Novo, A.; Eggeling, M.; Rank, R.; Muellner, P.; Hainberger, R.; Drexler, W.; Vlaskovic, M.; Zimmermann, H.; et al. Technological verification of size-optimized 160-channel silicon nitride-based AWG-spectrometer for medical applications. *Appl. Phys. B* **2019**, *125*, 88. [CrossRef]

27. Muneeb, M.; Ruocco, A.; Malik, A.; Pathak, S.; Ryckeboer, E.; Sanchez, D.; Cerutti, L.; Rodriguez, J.B.; Tournié, E.; Bogaerts, W.; et al. Silicon-on-insulator shortwave infrared wavelength meter with integrated photodiodes for on-chip laser monitoring. *Opt. Express* **2014**, *22*, 27300–27308. [CrossRef]

28. Correia, J.H.; Bartek, M.; Wolffenbuttel, R.F. High-selectivity single-chip spectrometer in silicon for operation in visible part of the spectrum. *IEEE Trans. Electron. Devices* **2000**, *47*, 191–197. [CrossRef]

29. Correia, J.H.; de Graaf, G.; Kong, S.H.; Bartek, M.; Wolffenbuttel, R.F. Single-chip CMOS optical micro-spectrometer. *Sens. Actuators* **2000**, *82*, 191–197. [CrossRef]

30. Wolffenbuttel, R.F. MEMS-based optical mini- and microspectrometers for the visible and infrared spectral range. *J. Micromech. Microeng.* **2005**, *15*, 145–152. [CrossRef]

31. Wang, S.W.; Li, M.; Xia, C.S.; Wang, H.Q.; Chen, X.S.; Lu, W. 128 channels of integrated filter array rapidly fabricated by using the combinatorial deposition technique. *Appl. Phys. B* **2007**, *88*, 281–284. [CrossRef]

32. Hillmer, H. Optisches Filter und Verfahren zu Seiner Herstellung (Optical Filter and Its Fabrication Technology). Patent DE 10,2006,039,071, 19 April 2012.

33. Albrecht, A.; Wang, X.; Mai, H.H.; Schotzko, T.; Memon, I.; Hornung, M.; Bartels, M.; Hillmer, H. High vertical resolution 3D Nano-Imprint Technology and its application in optical nanosensors. *Nonlinear Opt. Quantum Opt.* **2012**, *43*, 339–353.

34. Wang, X.; Albrecht, A.; Mai, H.H.; Woidt, C.; Meinl, T.; Hornung, M.; Bartels, M.; Hillmer, H. High resolution 3D nanoimprint technology: Template fabrication, application in Fabry–Pérot filter-array-based optical nanospectrometers. *Microelectron. Eng.* **2013**, *110*, 44–51. [CrossRef]

35. Mai, H.H.; Albrecht, A.; Woidt, C.; Wang, X.; Daneker, V.; Setyawati, O.; Woit, T.; Schultz, K.; Bartels, M.; Hillmer, H. 3D nanoimprinted Fabry-Pérot filter arrays and methodologies for optical characterization. *Appl. Phys. B Lasers Opt.* **2012**, *107*, 755–764. [CrossRef]

36. Nguyen, D.T.; Ababtain, M.; Memon, I.; Ullah, A.; Istock, A.; Woidt, C.; Xie, W.; Lehmann, P.; Hillmer, H. 3D nanoimprint for NIR Fabry-Pérot filter arrays: Fabrication, characterization and comparison of different cavity designs. *Appl. Nanosci.* **2016**, *6*, 1127–1135. [CrossRef]

37. Shen, Y.; Istock, A.; Zaman, A.; Woidt, C.; Hillmer, H. Fabrication and characterization of multi-stopband Fabry–Pérot filter array for nanospectrometers in the VIS range using SCIL nanoimprint technology. *Appl. Nanosci.* **2018**, *8*, 1415–1425. [CrossRef]

38. Larson, M.C.; Harris, J.S. Broadly-tunable resonant-cavity light-emitting diode. *IEEE Photonics Technol. Lett.* **1995**, *7*, 1267–1269. [CrossRef]

39. Larson, M.C.; Pezeshki, B.; Harris, J.S. Vertical Coupled-Cavity Microinterferometer on GaAs with Deformable-Membrane Top Mirror. *IEEE Photonics Technol. Lett.* **1995**, *7*, 382–384. [CrossRef]

40. Vail, E.C.; Wu, M.S.; Li, G.S.; Eng, L.; Chang-Hasnain, C.J. GaAs micromachined widely tunable Fabry-Perot filters. *Electron. Lett.* **1995**, *31*, 228–229. [CrossRef]

41. Wu, M.S.; Vail, E.C.; Li, G.S.; Yuen, W.; Chang-Hasnain, C.J. Tunable micromachined vertical cavity surface emitting laser. *Electron. Lett.* **1995**, *31*, 1671–1672. [CrossRef]

42. Spisser, A.; Ledantec, R.; Seassal, C.; Leclercq, J.L.; Benyattou, T.; Rondi, D.; Blondeau, R.; Guillot, G.; Viktorovitch, P. Highly selective and widely tunable 1.55-mInP/Air-Gap micromachined Fabry–Perot filter for optical communications. *IEEE Photonics Technol. Lett.* **1998**, *10*, 1259–1261. [CrossRef]

43. Tayebati, P.; Wang, P.; Azimi, M.; Maflah, L.; Vakhshoori, D. Microelectromechanical tunable filter with stable half symmetric cavity. *Electron. Lett.* **1998**, *34*, 1967–1968. [CrossRef]

44. Peerlings, J.; Dehe, A.; Vogt, A.; Tilsch, M.; Hebeler, C.; Langenhan, F.; Meissner, P.; Hartnagel, H.L. Long resonator micromachined tunable GaAs-AlAs Fabry-Perot filter. *IEEE Photonics Technol. Lett.* **1997**, *9*, 1235–1237. [CrossRef]

45. Streubel, K.; Rapp, S.; Andre, J.; Chitica, N. 1.26 *μm* vertical cavity laser with two InP/air-gap reflectors. *Electron. Lett.* **1996**, *32*, 1369–1370. [CrossRef]

46. Le Dantec, R.; Benyattou, T.; Guillot, G.; Spisser, G.; Seassal, C.; Leclercq, J.L.; Victorovitch, P.; Blondeau, R. Tunable microcavity based on InP-Air Bragg mirrors. *IEEE J. Sel. Top. Quantum Electron.* **1999**, *5*, 111–114. [CrossRef]

47. Hillmer, H.; Daleiden, J.; Prott, C.; Römer, F.; Irmer, S.; Rangelov, V.; Tarraf, A.; Schüler, S.; Strassner, M. Potential for micromachined actuation of ultra-wide continuously tunable optoelectronic devices. *Appl. Phys. B* **2002**, *75*, 3–13. [CrossRef]

48. Daleiden, J.; Chitica, N.; Strassner, M.; Spisser, A.; Leclercq, J.L.; Victorovitch, P.; Rondi, D.; Goutain, E.; Peerlings, J.; Pfeiffer, J.; et al. Tunable InP/air gap Fabry Perot filter for wavelength division multiplex fiber optical transmission. In Proceedings of the 11th International Conference on Indium Phosphide and Related Materials (IPRM'99) (Cat. No.99CH36362), Davos, Switzerland, 16–20 May 1999; pp. 285–287. [CrossRef]

49. Strassner, M.; Daleiden, J.; Chitica, N.; Keiper, D.; Stålnacke, B.; Greek, D.; Hjort, K. III-V semiconductor material for tunable Fabry-Perrot filters for coarse and dense WDM systems. *Sens. Actuators A Phys.* **2000**, *85*, 249–255. [CrossRef]

50. Chitica, N.; Strassner, M. Room-temperature operation of photopumped monolithic InP vertical cavity laser with two air-gap Bragg reflectors. *Appl. Phys. Lett.* **2001**, *78*, 3935–3937. [CrossRef]

51. Irmer, S.; Daleiden, J.; Rangelov, V.; Prott, C.; Römer, F.; Strassner, M.; Tarraf, A.; Hillmer, H. Ultralow biased widely continuously tunable fabry-Perot filter. *IEEE Photonics Technol. Lett.* **2003**, *15*, 434–436. [CrossRef]

52. Daleiden, J.; Hillmer, H. Multiple air-gap filters and constricted mesa lasers—Material processing meets the front of optical device technology. *Appl. Phys. B* **2003**, *76*, 821–832. [CrossRef]

53. Hillmer, H.; Daleiden, J.; Irmer, S.; Römer, F.; Prott, C.; Tarraf, A.; Strassner, M.; Ataro, E.; Scholz, T. Potential of micromachined photonics: Miniaturization, scaling and applications in continuously tunable vertical air-cavity filters. In *Laser Diodes, Optoelectronic Devices, and Heterogenous Integration*; International Society for Optics and Photonics: Bellingham, WA, USA, 2003; Volume 4947, pp. 197–211. [CrossRef]

54. Prott, C.; Römer, F.; Ataro, E.O.; Daleiden, J.; Irmer, S.; Tarraf, A.; Hillmer, H. Modeling of ultrawidely tunable vertical cavity air-gap filters and VCSELs. *IEEE J. Sel. Top. Quantum Electron.* **2003**, *9*, 918–928. [CrossRef]

55. Römer, F.; Prott, C.; Irmer, S.; Daleiden, J.; Tarraf, A.; Hillmer, H.; Strassner, M. Tuning efficiency and linewidth of electrostatically actuated multiple air-gap filters. *Appl. Phys. Lett.* **2003**, *82*, 176–178. [CrossRef]

56. Hasse, A.; Irmer, S.; Daleiden, J.; Dharmarasu, N.; Hansmann, S.; Hillmer, H. Wide continuous tuning range of 221nm by InP /air-gap vertical-cavity filters. *Electron. Lett.* **2006**, *42*, 974–975. [CrossRef]

57. Römer, F. *Charakterisierung und Simulation Optischer Eigenschaften von Mikromechanisch Abstimmbaren Filterbauelementen (Characterization and Simulation of Optical Properties of Micromachined Tunable Filter Devices)*; Kassel University Press: Kassel, Germany, 2006; ISBN 978-3-89958-196-6.

58. Williams, C.; Hong, N.; Julian, M.; Borg, S.; Kim, H.J. Tunable mid-wave infrared Fabry-Perot bandpass filters using phase-change GeSbTe. *Opt. Express* **2020**, *28*, 10583–10594. [CrossRef]

59. Magnusson, R.; Wang, S.S. New principle for optical filters. *Appl. Phys. Lett.* **1992**, *61*, 1022–1024. [CrossRef]

60. Kanskar, M.; Paddon, P.; Pacradouni, V.; Morin, R.; Busch, A.; Young, J.F.; Johnson, S.R.; MacKenzie, J.; Tiedje, T. Observation of leaky slab modes in an air-bridged semiconductor waveguide with a two-dimensional photonic lattice. *Appl. Phys. Lett.* **1997**, *70*, 1438–1440. [CrossRef]
61. Hessel, O.; Oliner, A.A. A new theory of Wood's anomalies on optical gratings. *Appl. Opt.* **1965**, *4*, 1275–1297. [CrossRef]
62. Boutami, S.; Benbakir, B.; Letartre, X.; Leclercq, J.L.; Regreny, P.; Viktorovitch, P. Ultimate vertical Fabry-Perot cavity based on single-layer photonic crystal mirrors. *Opt. Express* **2007**, *15*, 12443–12449. [CrossRef]
63. Boutami, S.; Bakir, B.B.; Hattori, H.; Letartre, X.; Leclercq, J.-L.; Rojo-Rome, P.; Garrigues, M.; Seassal, C.; Viktorovitch, P. Broadband and compact 2-D photonic crystal reflectors with controllable polarization dependence. *IEEE Photonics Technol. Lett.* **2006**, *18*, 835–837. [CrossRef]
64. Zamora, R.; Benes, M.; Kusserow, T.; Hillmer, H.; Akcakoca, U.; Witzigmann, B. Optical characterization of photonic crystals as polarizing structures for tunable optical MEMS devices. In Proceedings of the 16th International Conference on Optical MEMS and Nanophotonics, Istanbul, Turkey, 8–11 August 2011; pp. 83–84. [CrossRef]
65. Kupec, J.; Akcakoca, U.; Witzigmann, B. Frequency domain analysis of guided resonances and polarization selectivity in photonic crystal membranes. *J. Opt. Soc. Am. B* **2011**, *28*, 69–78. [CrossRef]
66. Kilic, O.; Digonnet, M.; Kino, G.; Solgaard, O. Controlling uncoupled resonances in photonic crystals through breaking the mirror symmetry. *Opt. Express* **2008**, *16*, 13090–13103. [CrossRef]
67. Kikuta, H.; Toyota, H.; Yu, W. Optical Elements with Subwavelength Structured Surfaces. *Opt. Rev.* **2003**, *10*, 63–73. [CrossRef]
68. Oshita, M.; Takahashi, H.; Ajiki, Y.; Kan, T. Reconfigurable Surface Plasmon Resonance Photodetector with a MEMS Deformable Cantilever. *ACS Photonics* **2020**, *7*, 673–679. [CrossRef]
69. Momeni, B.; Hosseini, E.S.; Askari, M.; Soltani, M.; Adibi, A. Integrated photonic crystal spectrometers for sensing applications. *Opt. Commun.* **2009**, *282*, 3168–3171. [CrossRef]
70. Gerken, M.; Miller, D.A.B. Multilayer Thin-Film Structures with High Spatial Dispersion. *Appl. Opt.* **2003**, *42*, 1330–1345. [CrossRef]
71. Ibsen Photonics A/S. OEM Spectrometers. Available online: https://ibsen.com/products/oem-spectrometers/ (accessed on 17 July 2021).
72. Hamamatsu Photonics, K.K. Mini-Spectrometers. Available online: https://www.hamamatsu.com/eu/en/product/optical-sensors/spectrometers/mini-spectrometer/index.html (accessed on 29 November 2020).
73. Suh, W.; Yanik, M.F.; Solgaard, O.; Fan, S. Displacement-sensitive photonic crystal structures based on guided resonance in photonic crystal slabs. *Appl. Phys. Lett.* **2003**, *82*, 1999. [CrossRef]
74. Notomi, M.; Taniyama, H.; Mitsugi, S.; Kuramochi, E. Optomechanical Wavelength and Energy Conversion in High-Q Double-Layer Cavities of Photonic Crystal Slabs. *Phys. Rev. Lett.* **2006**, *97*, 023903-4. [CrossRef]
75. Midolo, L.; van Veldhoven, P.J.; Dündar, M.A.; Nötzel, R.; Fiore, A. Electromechanical wavelength tuning of double-membrane photonic crystal cavities. *Appl. Phys. Lett.* **2011**, *98*, 211120. [CrossRef]
76. Liapis, A.C.; Gao, B.; Siddiqui, M.R.; Shi, Z.; Boyd, R.W. On-chip spectroscopy with thermally tuned high-Q photonic crystal cavities. *Appl. Phys. Lett.* **2016**, *108*, 021105. [CrossRef]
77. Zobenica, Ž.; van der Heijden, R.W.; Petruzzela, M.; Pagliano, F.; Leijssen, R.; Xia, T.; Midolo, L.; Cotrufo, M.; Cho, Y.J.; van Otten, F.W.; et al. Integrated nano-opto-electro-mechanical sensor for spectrometry and nanometrology. *Nat. Commun.* **2017**, *8*, 2216. [CrossRef]
78. Yang, Z.; Albow-Owen, T.; Cai, W.; Hasan, T. Miniaturization of optical spectrometers. *Science* **2021**, *371*, 480. [CrossRef] [PubMed]
79. Li, S.; Ngo, N.; Tjin, S.; Shum, P.; Zhang, J. Thermally Tunable Narrow-Bandpass Filter Based on a Linearly Chirped Fiber Bragg Grating. *Optics Letters* **2004**, *29*, 29–31. [CrossRef]
80. Thomas Rasmussen (Technical Representative of the Company IBSEN Photonics Denmark). Personal communication, 1 July 2021.
81. Michel, A.; Ruprecht, R.; Harmening, M.; Bacher, W. Abformung von Mikrostrukturen auf prozessierten Wafern (Molding of microstructures on processed wafers). *Ber. Des. Kernforsch. Karlsr.* **1993**, *KfK 5171*. ISSN 0303-4003. [CrossRef]
82. Chou, S.Y.; Krauss, P.R.; Renstrom, P.J. Nanoimprint lithography. *J. Vac. Sci. Technol. B Microelectron. Nanometer Struct.* **1996**, *14*, 4129–4133. [CrossRef]
83. Ji, R.; Hornung, M.; Verschuuren, M.A.; van de Laar, R.; van Eeckelen, J.; Plachetka, U.; Moeller, M.; Moormann, C. UV enhanced substrate conformal imprint lithography (UV-SCIL) technique for photonic crystals patterning in LED manufacturing. *Microelectron. Eng.* **2010**, *87*, 963–967. [CrossRef]
84. Verschuuren, M.A.; Megens, M.; Ni, Y.; van Sprang, H.; Polman, A. Large area nanoimprint by substrate conformal imprint lithography (SCIL). *Adv. Opt. Technol.* **2017**, *6*, 243–264. [CrossRef]
85. Larouche, S.; Martinu, L. OpenFilters: Open-source software for the design, optimization, and synthesis of optical filters. *Appl. Opt.* **2008**, *47*, C219–C230. [CrossRef] [PubMed]
86. Memon, I.; Shen, Y.; Khan, A.; Woidt, C.; Hillmer, H. Highly uniform residual layers for arrays of 3D nanoimprinted cavities in Fabry–Pérot filter array based nanospectrometers. *Appl. Nanosci.* **2015**, *6*, 599–606. [CrossRef]
87. Emadi, A.; Wu, H.; de Graaf, G.; Wolffenbuttel, R. Design and implementation of a sub-nm resolution microspectrometer based on a Linear-Variable Optical Filter. *Opt. Express* **2012**, *20*, 489. [CrossRef]
88. Brunner, R.; Hillmer, H.; Gatto, A. Spektralsensor zur Spektralen Analyse Einfallenden Lichts. Patent DE 10,2014,108,138 B4, 29 December 2016.

89. Kobylinskiy, A.; Laue, B.; Förster, E.; Höfer, B.; Shen, Y.; Hillmer, H.; Brunner, R. Substantial increase in detection efficiency for filter array-based spectral sensors. *Appl. Opt.* **2020**, *59*, 2443–2451. [CrossRef] [PubMed]
90. Abramson, A.R.; Tien, C.; Majumdar, A. Interface and strain effects on the thermal conductivity of heterostructures: A molecular dynamics study. *J. Heat Transf.* **2002**, *124*, 963–970. [CrossRef]
91. Cheng, X.; Guo, L.J. A combined-nanoimprint-and-photolithography patterning technique. *Microelectron. Eng.* **2004**, *71*, 277–282. [CrossRef]
92. Kolli, V.R.; Woidt, C.; Hillmer, H. Residual-layer-free 3D nanoimprint using hybrid soft templates. *Microelectron. Eng.* **2016**, *149*, 159–165. [CrossRef]
93. Wang, Y. Model Calculations and Implementation of Filters and Hybrid Green VCSELs Based on Optical Thin Film Stacks. Ph.D. Thesis, University of Kassel, Kassel, Germany, 2010.
94. Faraji-Dana, M.; Arbabi, E.; Arbabi, A.; Kamali, S.M.; Kwon, H.; Faraon, A. Compact Folded Metasurface Spectrometer. *Nat. Commun.* **2018**, *9*, 4196. [CrossRef] [PubMed]
95. Nitkowski, A.; Chen, L.; Lipson, M. Cavity-Enhanced on-Chip Absorption Spectroscopy Using Microring Resonators. *Opt. Express* **2008**, *16*, 11930–11936. [CrossRef]
96. Kyotoku, B.B.C.; Chen, L.; Lipson, M. Sub-Nm Resolution Cavity Enhanced Micro-Spectrometer. *Opt. Express* **2010**, *18*, 102–107. [CrossRef]
97. Yang, Z.; Albrow-Owen, T.; Cui, H.; Alexander-Webber, J.; Gu, F.; Wang, X.; Wu, T.-C.; Zhuge, M.; Williams, C.; Wang, P.; et al. Single-Nanowire Spectrometers. *Science* **2019**, *365*, 1017–1020. [CrossRef] [PubMed]
98. Tabassum, S.; Kumar, R.; Dong, L. Nanopatterned Optical Fiber Tip for Guided Mode Resonance and Application to Gas Sensing. *IEEE Sens. J.* **2017**, *17*, 7262–7272. [CrossRef]
99. Ma, C.; Wang, A. Optical Fiber Tip Acoustic Resonator for Hydrogen Sensing. *Opt. Lett.* **2010**, *35*, 2043. [CrossRef]
100. Zhu, T.; Ke, T.; Rao, Y.; Chiang, K.S. Fabry–Perot Optical Fiber Tip Sensor for High Temperature Measurement. *Opt. Commun.* **2010**, *283*, 3683–3685. [CrossRef]
101. Ma, J.; Jin, W.; Ho, H.L.; Dai, J.Y. High-Sensitivity Fiber-Tip Pressure Sensor with Graphene Diaphragm. *Opt. Lett.* **2012**, *37*, 2493. [CrossRef]
102. Kilic, O.; Solgaard, O.; Digonnet, M.; Kino, G. External Fibre Fabry–Perot Acoustic Sensor Based on a Photonic-Crystal Mirror. *Meas. Sci. Technol.* **2007**, *18*, 3049–3054. [CrossRef]
103. Alberts, C.J.; Man, S.D.; Berenschot, J.W.; Gadgil, V.J.; Elwenspoek, M.C.; Iannuzzi, D. Fiber-Top Refractometer. *Meas. Sci. Technol.* **2009**, *20*, 034005. [CrossRef]
104. De Maria, L.; Martinelli, M.; Vegetti, G. Fiber-Optic Sensor Based on Surface Plasmon Interrogation. *Sens. Actuators B Chem.* **1993**, *12*, 221–223. [CrossRef]
105. Kazuma, E.; Tatsuma, T. Localized Surface Plasmon Resonance Sensors Based on Wavelength-Tunable Spectral Dips. *Nanoscale* **2014**, *6*, 2397–2405. [CrossRef]
106. Strobbia, P.; Languirand, E.R.; Cullum, B.M. Recent Advances in Plasmonic Nanostructures for Sensing: A Review. *Opt. Eng.* **2015**, *54*, 100902. [CrossRef]
107. Alvarez-Puebla, R.; Cui, B.; Bravo-Vasquez, J.-P.; Veres, T.; Fenniri, H. Nanoimprinted SERS-Active Substrates with Tunable Surface Plasmon Resonances. *J. Phys. Chem. C* **2007**, *111*, 6720–6723. [CrossRef]
108. Kostovski, G.; Chinnasamy, U.; Jayawardhana, S.; Stoddart, P.R.; Mitchell, A. Sub-15nm Optical Fiber Nanoimprint Lithography: A Parallel, Self-Aligned and Portable Approach. *Adv. Mater.* **2010**, *23*, 531–535. [CrossRef]
109. Bierlich, J.; Kobelke, J.; Brand, D.; Kirsch, K.; Dellith, J.; Bartelt, H. Nanoscopic Tip Sensors Fabricated by Gas Phase Etching of Optical Glass Fibers. *Photonic Sens.* **2012**, *2*, 331–339. [CrossRef]
110. Burresi, M.; van Oosten, D.; Kampfrath, T.; Schoenmaker, H.; Heideman, R.; Leinse, A.; Kuipers, L. Probing the Magnetic Field of Light at Optical Frequencies. *Science* **2009**, *326*, 550–553. [CrossRef] [PubMed]
111. Iannuzzi, D.; Deladi, S.; de Man, S.; Heeck, K.; Elwenspoek, M.C. Fiber-Top Atomic Force Microscope. *Rev. Sci. Instrum.* **2006**, *77*, 106105. [CrossRef]
112. Kostovski, G.; Stoddart, P.R.; Mitchell, A. The Optical Fiber Tip: An Inherently Light-Coupled Microscopic Platform for Micro- and Nanotechnologies. *Adv. Mater.* **2014**, *26*, 3798–3820. [CrossRef]
113. Harlander, J.M. Spatial Heterodyne Spectroscopy: Interferometric Performance at Any Wavelength without Scanning. Ph.D. Thesis, University of Wisconsin, Madison, WI, USA, 1991.
114. Zettner, A.; Gojani, A.B.; Schmid, T.; Gornushkin, I.B. Evaluation of a Spatial Heterodyne Spectrometer for Raman Spectroscopy of Minerals. *Minerals* **2020**, *10*, 202. [CrossRef]
115. Kaufmann, M.; Olschewski, F.; Mantel, K.; Solheim, B.; Shepherd, G.; Deiml, M.; Liu, J.; Song, R.; Chen, Q.; Wroblowski, O.; et al. A highly miniaturized satellite payload based on a spatial heterodyne spectrometer for atmospheric temperature measurements in the mesosphere and lower thermosphere. *Atmos. Meas. Tech.* **2018**, *11*, 3861–3870. [CrossRef]
116. Yi, Y.; Zhang, S.; Liu, F.; Zhang, Y.; Yi, F. Laboratory fabrication of monolithic interferometers for one and two-dimensional spatial heterodyne spectrometers. *Opt. Express* **2017**, *25*, 29121–29134. [CrossRef]
117. Austin, M.D.; Ge, H.; Wei, W.; Li, M.; Yu, Z.; Wassermann, D.; Lyon, S.A.; Chou, S.Y. Fabrication of 5 *nm* linewidth and 14n m pitch features by nanoimprint lithography. *Appl. Phys. Lett.* **2004**, *84*, 5299–5301. [CrossRef]

118. Hua, F.; Sun, Y.; Gaur, A.; Meitl, M.A.; Bilhaut, L.; Rotkina, L.; Wang, J.; Geil, P.; Shim, M.; Rogers, J.A.; et al. Polymer imprint lithography with molecular-scale resolution. *Nano Lett.* **2004**, *4*, 2467–2471. [CrossRef]
119. Yasuda, M.; Hirai, Y. Molecular Dynamics Simulations of Local Polymer Flow. In *Program and Abstracts, Proceedings of the 9th International Nanoimprint & Nanoprint Technology Conference, Copenhagen, Denmark, 13–15 October 2010*; NIL Technology: Lyngby, Denmark; Obducat: Lund, Sweden, 2010; p. 32.
120. Taga, A.; Yasuda, M.; Kawata, H.; Hirai, Y. Impact of molecular size on resist filling process in nanoimprint lithography: Molecular dynamics study. *J. Vac. Sci. Technol. B* **2010**, *28*, C6M68. [CrossRef]
121. Wallrabe, U.; Salle, V. LIGA Technology for R&D and Industrial Applications. In *MEMS: A Practical Guide to Design, Analysis, and Applications*; Korvink, J.G., Paul, O., Eds.; Springer: Berlin/Heidelberg, Germany, 2006; pp. 853–899. ISBN 978-3-540-21117-4.
122. Müller, C.; Mohr, L. Microspectrometer Fabricated by the Liga Process. *Microsyst. Technol.* **1993**, *18*, 273–279. [CrossRef]
123. Gibbon, M. Technologies for Photonic Integration. Ph.D. Thesis, University of Bath, Bath, UK, 1995. Available online: https://ethos.bl.uk/OrderDetails.do?uin=uk.bl.ethos.760668 (accessed on 13 August 2021).
124. Julijan, C. SiO$_x$-SiC$_z$ MEMS-DBR-Based Tunable Optical Devices. Ph.D. Thesis, University of Darmstadt, Darmstadt, Germany, 2020. [CrossRef]

Liquid-Filled Highly Asymmetric Photonic Crystal Fiber Sagnac Interferometer Temperature Sensor

Yashar E. Monfared [1],*, Amir Ahmadian [2], Vigneswaran Dhasarathan [3,4] and Chunhao Liang [5],*

[1] Department of Chemistry, Dalhousie University, Halifax, NS B3H 4R2, Canada
[2] Department of Electrical and Computer Engineering, Science and Research Branch, Azad University, Tehran 147789385, Iran; amir.ahmadian@ieee.org
[3] Division of Computational Physics, Institute for Computational Science, Ton Duc Thang University, Ho Chi Minh City 700000, Vietnam; vigneswaran.d@tdtu.edu.vn
[4] Faculty of Electrical and Electronics Engineering, Ton Duc Thang University, Ho Chi Minh City 700000, Vietnam
[5] Shandong Provincial Engineering and Technical Center of Light Manipulations & Shandong Provincial Key Laboratory of Optics and Photonic Device, School of Physics and Electronics, Shandong Normal University, Jinan 250014, China
* Correspondence: y.monfared@dal.ca (Y.E.M.); cliang@dal.ca (C.L.)

Abstract: In this paper, we theoretically designed and numerically studied a high-resolution and ultrasensitive photonic crystal fiber temperature sensor by selective filling of a liquid with high thermo-optic coefficient in one of the airholes of the fiber. The finite element method was utilized to study the propagation characteristics and the modal birefringence of the fiber under different ambient temperatures. A large base birefringence value of 7.7×10^{-4} as well as a large birefringence sensitivity of almost 29% to a 10 °C temperature variation was achieved for the optimized fiber design with liquid chloroform between 15 °C and 35 °C. We also studied the performance of the proposed optical fiber in a temperature sensing Sagnac interferometer. An average linear temperature sensitivity of 17.53 nm/°C with an average resolution of 5.7×10^{-4} °C was achieved over a temperature range of 20 °C (15 °C to 35 °C).

Keywords: fiber-optic temperature sensor; chloroform fiber; Sagnac interferometer

1. Introduction

Optical properties and applications of photonic crystal fibers (PCFs), either as a nonlinear medium for nonlinear optics or as an optical functional device such as a sensor, have been the focus of intense research in recent years [1–4]. Comparing to conventional optical fibers, PCFs demonstrate important characteristics including design flexibility, controllable effective area, adjustable dispersion, and the potential to achieve a highly birefringent structure to confine light [1–3]. The regular PCFs made from silica are not sensitive to temperature as silica does not exhibit a large thermo-optic coefficient [4]. However, the design flexibility of PCFs can assist scientists to increase the temperature sensitivity of the fiber via liquid infiltration into the fiber holes [4].

Most of the liquids exhibit a large thermo-optic coefficient (TOC). A large TOC can be used to realize various effective mode indices of the fundamental guided mode in the fiber infiltrated with liquids at different temperatures [4]. By introducing an asymmetry in the fiber structure, the mode indices will also be sensitive to the polarization of the light, which can enable us to design highly birefringent PCFs [5]. By simultaneously infiltrating the PCF and introducing asymmetry in the design of the fiber, one can design an optical fiber that is sensitive to both the temperature and the polarization of the light. An interferometric technique, like Sagnac interferometry, can be used to detect changes in the light transmission spectrum in a fiber loop depending on the fiber birefringence [4,6]. Therefore,

one can use a highly birefringent PCF in a fiber-loop Sagnac interferometer as a tool for accurate temperature sensing in hard-to-reach environments.

There have been multiple studies on the properties of selectively liquid-filled PCF temperature sensors based on interferometric techniques. Qian et al. [7] proposed an alcohol-filled PCF temperature sensor with a sensitivity of 6.6 nm/°C. Lu et al. [8] proposed a temperature sensor based on a PCF filled with silver nanowires and liquid, and they achieved a sensitivity of 2.7 nm/°C. Cui et al. [6] proposed a selectively water-filled PCF based on Sagnac interferometry with a sensitivity of 2.58 nm/°C. Han et al. [9] reported a selective-filling PCF by infiltrating a liquid into two adjacent air holes of the innermost ring of holes, and a temperature sensitivity of around −10.0 nm/°C was achieved. Recently, Vera et al. [10] proposed a metal-filled PCF for a Sagnac interferometry temperature sensor with a sensitivity of −9 nm/°C. Monfared et al. [4] also studied a toluene-filled PCF temperature sensor via a Sagnac interferometer with a sensitivity of −11 nm/°C and a temperature range of 20–30°C.

In this paper, we study a simple PCF structure with only two rings of air holes and two smaller modified holes, filled with fluid as a temperature-sensitive material and close to the core of the fiber. We also study the design parameters and performance of the proposed temperature sensor in different temperatures and demonstrate the possibility of temperature sensing with measuring the variations in the transmission spectrum of the fiber.

2. Sensor Design

2.1. Materials and Methods

In the PCF structure, we used silica as the background material (core and cladding), two rings of air holes with diameter d and center-to-center spacing Λ_2, and two modified-location holes ($\Lambda_1 = 1.5\,\Lambda_2$) with diameters D_1 and D_2. The larger hole is filled with liquid chloroform. We simulated the PCF structure using the finite element method (FEM) applied with the COMSOL Multiphysics software. Perfectly matched layer (PML) boundary conditions as well as ultrafine mesh size with a minimum element size of 5 nm and a maximum element size of 500 nm were applied to the model. Furthermore, strict convergence analyses were conducted to ensure the accuracy of the results (error threshold of 10^{-5}). The cross section of the proposed PCF is shown on Figure 1a. It should be noted that only two rings of airholes will be an advantage during the fabrication process of the PCF, as having fewer rings with low filling ratios (d/Λ and D/Λ) is technologically easier and can significantly reduce fabrication-induced imperfections [5].
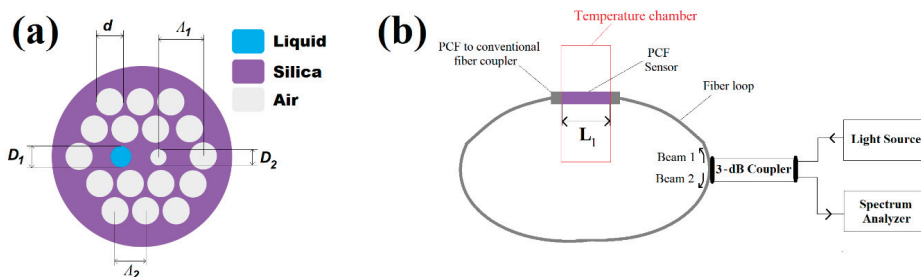

Figure 1. (**a**) Cross section of the selectively liquid-filled photonic crystal fibers (PCF) with hole diameter d, two modified-position holes with diameters D_1 and D_2, modified-location hole pitch Λ_1, and nonmodified-location hole pitch Λ_2. (**b**) The schematic of the potential experimental setup of the PCF sensor in a Sagnac interferometer.

In Figure 1b, we also demonstrate a possible experimental setup for our sensor. The mechanism of a Sagnac-interferometer-based optical fiber sensor is based on the phase difference of light beams that propagate through the fiber loop which was described in [4,6]. In summary, a laser source emits

an optical beam, which is split into two beams using a beam splitter or a 3-dB optical coupler [9,10]. These beams (beam 1 and beam 2) counter-propagate through a fiber loop that usually consists of a conventional optical fiber with a negligible loss at operation wavelengths close to 1200 nm [4,6]. The beams recombine at the output while undergoing a phase difference (as a result of a different optical path lengths) which is caused by a temperature-sensitive birefringence value of the sensing element (the proposed birefringent chloroform-filled optical fiber) during propagation in the fiber loop.

There are numerous methods to fill the holes of the PCF with liquids, including the photo-lithographic masking technique [11] and utilizing different flow speeds of the liquids [12], which already are taken into practice. As our fiber cross section is relatively large (larger than 10 μm), its coupling efficiency with conventional optical fibers can be as large as 90% using an appropriate coupler—for example, the fused biconical tapering technique [13], which makes the propagation of light possible in the prospective setup. Furthermore, the previous tests on liquid-filled Sagnac interferometer fiber sensors show consistent, accurate, and stable results [6,14], which makes the proposed sensor a potential candidate in many industrial applications.

2.2. Optical Materials

We started by comparing the thermo-optic coefficient (TOC) of different liquids. A liquid with a high TOC shows a large variation in refractive index as a function of temperature, which can be utilized to design a highly sensitive temperature sensor. The TOC values are obtained from [15,16], and they are close to our operation wavelengths in visible and near infrared regions. As seen in Figure 2, liquid chloroform ($CHCl_3$) and carbon disulfide (CS_2) show the most promising TOC values. While chloroform and CS_2 have the highest TOCs, chloroform has lower linear and nonlinear refractive indices than CS_2 (nearly 1.435 and 85×10^{-20} m^2/W, compared to 1.585 and 320×10^{-20} m^2/W of CS_2), which help with suppressing unwanted nonlinear processes and nonlinearity in the sensing performance of the fiber [17]. Therefore, chloroform has a greater overall merit compared to other liquids for the temperature sensing application proposed here, and for this reason we used chloroform in our proposed sensor and all simulations.
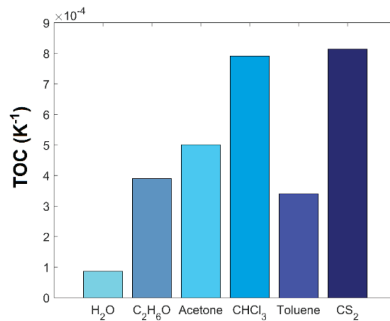

Figure 2. The magnitude of the thermo-optic coefficient of different liquids close to the operation wavelengths. H_2O is water, C_2H_6O is ethanol, $CHCl_3$ is chloroform, and CS_2 is carbon disulfide.

In our simulations, we considered the material dispersion of silica and chloroform to accurately simulate the resulting structure. The relationship between the refractive index of silica and the wavelength is given by the following Sellmeier's equation [18,19]:

$$n_{silica}^2 = 1 + \frac{0.6961663\lambda^2}{\lambda^2 - 0.0684043^2} + \frac{0.4079426\lambda^2}{\lambda^2 - 0.1162414^2} + \frac{0.8974794\lambda^2}{\lambda^2 - 9.896161^2} \tag{1}$$

where λ is the wavelength of incident light. The relationship between the refractive index of liquid chloroform, wavelength, and temperature is given by the following equation [20]:

$$n_{chlroform}\ (\lambda,\ T) = n_{chlroform@20}(\lambda) + (\Delta T\ dn_T) \tag{2}$$

Here, T is the temperature in Celsius; ΔT is the difference between 20 °C and the chosen temperature; dn_T is the rate of variation in refractive index as a function temperature, which is equal to $-7.91 \times 10^{-4}\ K^{-1}$; and $n_{chlroform@20}(\lambda)$ is the refractive index of chloroform as a function of wavelength at 20 °C, which is given by the following Sellmeier's equation [20]:

$$n_{chlroform@20}(\lambda)\ =\ 1.431364 + \frac{5632.41}{\lambda^2} - \frac{2.0805 \times 10^8}{\lambda^4} + \frac{1.2613 \times 10^{13}}{\lambda^6} \tag{3}$$

In Figure 3, we can see the relationship between the ambient temperature and the refractive index of chloroform for different temperatures ranging from 20 °C to 30 °C with different excitation wavelengths.
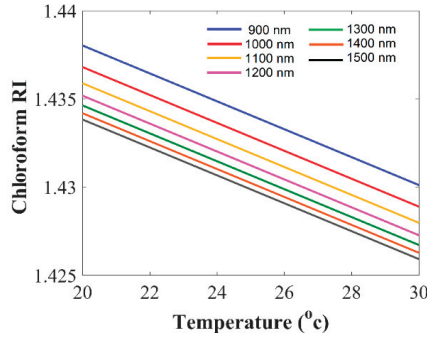

Figure 3. Chloroform refractive index as a function of temperature for different excitation wavelengths.

Finally, we considered the refractive index of air to be 1. This completes our numerical model for simulations in the proposed chloroform-filled PCF.

2.3. Birefringence and Sagnac Interferometry

The key parameter for an optical fiber in a Sagnac interferometer is birefringence (B), which is defined in [4] as

$$B = n_{fast} - n_{slow,} \tag{4}$$

where n_{fast} and n_{slow} are the effective mode indices of the two orthogonal states of the fundamental guided mode in the fiber core. In a birefringence fiber, the effective modal indices of these orthogonally polarized modes differ significantly. Here, a FEM analysis applied with Comsol MultiPhysics is used to calculate the fundamental guided modes and their effective modal indices to calculate the birefringence parameter of the fiber. It should be noted that as seen in Figure 1a, the nonsymmetric arrangement of the air holes and infiltration of chloroform into one of the holes results in a highly asymmetric fiber structure and a large birefringence parameter for the guided modes in the fiber core. The phase of the unheated part of fiber (Φ_1), the heated part of fiber (Φ_2), and the phase difference can be calculated as follows [4]:

$$\Phi_1\ =\ \frac{2\pi B(\lambda, T0)(L - L_1)}{\lambda} \tag{5}$$

$$\Phi_2\ =\ \frac{2\pi B(\lambda, T)(L_1)}{\lambda} \tag{6}$$

$$\Delta\Phi\ =\ \frac{2\pi\Delta B\ L}{\lambda} \tag{7}$$

where ΔB is the birefringence variation between two temperatures, L_1 is the liquid infiltrated length of the fiber sensing element, and λ is the excitation wavelength. Under a phase matching condition ($\phi1 + \phi2 = 2m\pi$), the transmission spectrum of the fiber reaches a minimum, and the interference dip wavelength appears. The transmission spectrum (SP_{trans}) of the fiber loop (and proposed PCF sensor) in the Sagnac interferometer is a cosine function of wavelength, fiber birefringence, temperature, and length of the fiber, given by [4]:

$$SP_{trans} = (1 - cos\,(\phi1 + \phi2)) \times 0.5 \tag{8}$$

It should be noted that the most important parameter in a Sagnac interferometer temperature sensor is the spacing between dip wavelengths due to different temperatures. One can find a dip wavelength shift caused by temperature variations for a certain excitation wavelength [4]:

$$\Delta\lambda_{dip} = \lambda\frac{\Delta B}{B}\frac{L_1}{L} \tag{9}$$

where L is the total length of the fiber. In the experiments, the whole sensing element or a part of the fiber loop can be placed in a temperature chamber to study the sensitivity, resolution, and detection range of the sensor. Here, we assume that the whole length of the sensing element is inside the temperature chamber for simplicity. As seen in Equation (9), the ultimate parameter that determines the dip wavelength shift and consequently the sensitivity for a certain temperature change is the birefringence sensitivity, which can be defined as the ratio of birefringence variations and the base birefringence ($\Delta B/B$). This parameter is studied in detail in the next section, where we show how we can optimize our design to maximize this parameter.

3. Design of the Sensor and Birefringence Sensitivity

Fiber birefringence and the sensitivity of the birefringence to the variations in the temperature are the most important parameters in a Sagnac interferometer that is based on optical fibers. Therefore, we studied multiple different structures, designs, and dimensions to find an optimized design with a large birefringence at a specific temperature ($B_{@T0}$), a large birefringence variation between two temperatures ($\Delta B = B_{@T1} - B_{@T0}$), and as a result, a large birefringence sensitivity for a large range of temperatures ($\Delta B/B$). In Figure 4, we demonstrate a number of these designs, their birefringence sensitivity, and the corresponding electrical field distributions for the fundamental guided mode with an x-polarized excitation at 1200 nm. It should be noted that the proposed final structure has six different design parameters: the location of liquid holes (and type of liquid), hole diameter d, two modified-position holes with diameters D_1 and D_2, modified-location hole pitch Λ_1, and nonmodified-location hole pitch Λ_2. As mentioned before, chloroform has the highest TOC and a low refractive index, and therefore it is the preferable choice for our temperature sensing application. As expected, the fiber does not show any significant birefringence sensitivity (close to 0%) without chloroform infiltration in Figure 4a. Interestingly, filling all the holes with chloroform does not increase the birefringence sensitivity of the PCF (sensitivity still close to 0%). The birefringence sensitivity increases as we infiltrate only the two airholes close to the core of the fiber (Figure 4b), but the sensitivity (12.5%) is not large enough to guarantee a significant difference in the transmission spectra in a Sagnac interferometer.

We tried to introduce asymmetries in the fiber cross section by changing the size of two adjacent airholes to the fiber core to improve the birefringence sensitivity (Figure 4c). The birefringence sensitivity improved from 12.5% to 16.6%. As seen in Figure 4d, by infiltrating only one of the holes the birefringence sensitivity increases from 16.6% to 28.6% which is considerably a large sensitivity for a given temperature variation. By choosing the optimized design (Figure 4d), we then studied the relationship between fiber birefringence and the ambient temperature with a 1200 nm laser excitation. As seen in Figure 5, there is an almost linear relationship ($R^2 = 0.989$) between the birefringence

parameter and temperature in our proposed fiber. The birefringence decreases from 7.7×10^{-4} to 2.6×10^{-4} with an increase in the temperature from 15 to 45 °C.
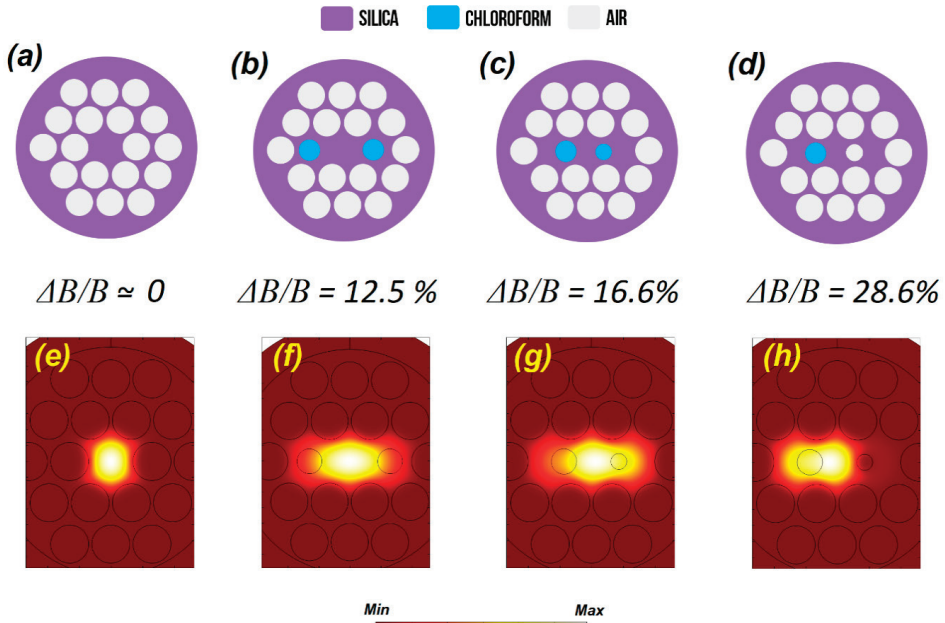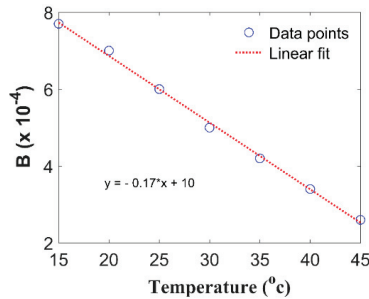

Figure 4. (**a**–**d**) Birefringence sensitivity and cross section of chloroform-filled PCFs with different design and infiltration patterns. (**e**–**h**) The corresponding electrical field distribution of the fundamental guided mode in the PCF core for an x-polarized light excitation at 1200 nm.

Figure 5. Fiber birefringence as a function of temperature for the optimized design with $d = 1.2$ µm, $\Lambda_1 = 2.6$ µm, $\Lambda_2 = 3.9$ µm, $D_1 = 0.8$ µm, and $D_2 = 0.5$ µm.

Next, we studied the role of the design parameters on birefringence sensitivity in detail. It should be noted that the birefringence sensitivity has a direct impact on the dip wavelength shift and the overall temperature sensitivity of the fiber in the Sagnac interferometer, as demonstrated in Equation (9). We started with the role of spacing between two adjacent holes to the fiber core in Figure 6a. As expected, the location and spacing of the holes is crucial to ensure we have an optical fiber with high birefringence sensitivity. The optimized value for spacing between the adjacent holes to the fiber core is 1.5 according to the simulations; we therefore utilized this ratio in the proposed optimized design by choosing $\Lambda_1 = 2.6$ µm and $\Lambda_2 = 3.9$ µm. It is important to mention that by choosing a different ratio between holes spacing—for example, 1 instead of 1.5—the sensitivity decays very fast to values smaller than

10%. The role of airhole dimension (Figure 6b), the size of the larger adjacent hole to the core (Figure 6c), and the size of the smaller adjacent hole to the core (Figure 6d) are also studied. To maximize birefringence sensitivity, we chose design parameters that correspond to the maximum sensitivity in each case. The optimized design parameters in the proposed fiber (which are determined after a significant amount of trial and error) are $d = 1.2$ μm, $\Lambda_1 = 2.6$ μm, $\Lambda_2 = 3.9$ μm, $D_1 = 0.8$ μm, and $D_2 = 0.5$ μm. Interestingly, the small variations (on the orders of a 0.01 μm) in the airhole dimensions do not have a major effect on the birefringence sensitivity of the fiber as demonstrated in Figure 6b–d. In summary, Figure 6 shows the importance of the location and size of two adjacent holes to the fiber core in the birefringence sensitivity of the proposed PCF. It should be noted that the proposed design has an overall good tolerance to fabrication-induced imperfections, especially imperfections related to the minor variations in the hole size, as demonstrated in Figure 6.
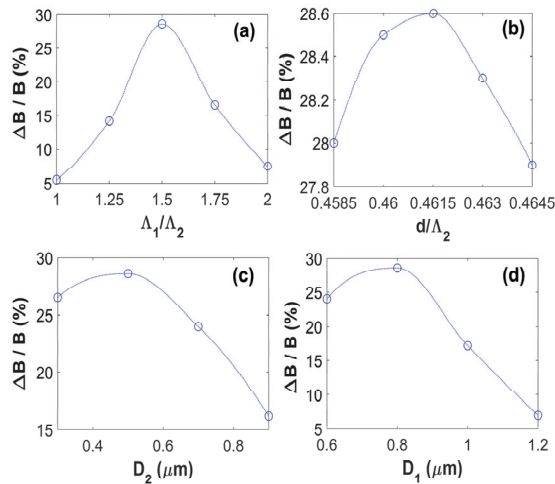

Figure 6. Birefringence sensitivity as a function of different design parameters: (**a**) hole pitch ratio where $d = 1.2$ μm, $\Lambda_2 = 3.9$ μm, $D_1 = 0.8$ μm, and $D_2 = 0.5$ μm; (**b**) hole ratio where $\Lambda_1 = 2.6$ μm, $\Lambda_2 = 3.9$ μm, $D_1 = 0.8$ μm, and $D_2 = 0.5$ μm; (**c**) unfilled central hole diameter where $d = 1.2$ μm, $\Lambda_1 = 2.6$ μm, $\Lambda_2 = 3.9$ μm, $D_1 = 0.8$ μm; (**d**) filled-hole diameter where $d = 1.2$ μm, $\Lambda_1 = 2.6$ μm, $\Lambda_2 = 3.9$ μm, and $D_2 = 0.5$ μm.

4. Performance Analysis

By using the optimized design parameters, we analyzed the temperature sensing performance of the proposed fiber in a Sagnac interferometer. As seen in Figure 7, by increasing the temperature from 15 to 35 °C, the transmission dip wavelength blueshifts from 1155 to 629 nm. While the variations of the transmission spectra are significant within the 15–35 °C window, the variations are significantly reduced outside this temperature range. We also studied the role of fiber length on the transmission spectra in Figure 8 at a constant temperature of 30 °C. It is clear that by increasing the fiber length from 1.5 to 15 mm, the number of transmission dips increases significantly (from 1 to 6 between 600 and 1200 nm). The increase in the number of transmission dips can make the detection of the dip wavelength more difficult and challenging, and therefore we chose 1.5 mm as the optimized fiber length in all of the calculations.
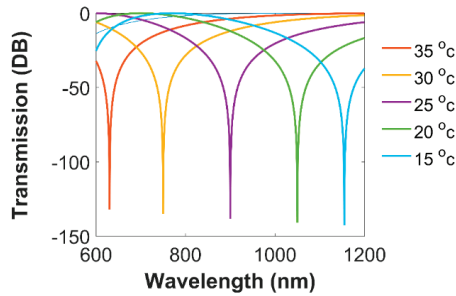
Figure 7. Transmission spectra of the Sagnac interferometer optical fiber sensor as a function of wavelength for different temperatures.
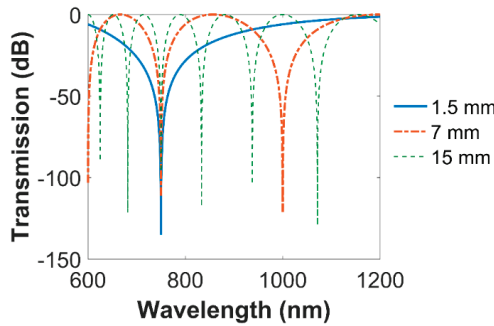

Figure 8. Transmission spectra of the Sagnac interferometer optical fiber sensor as a function of wavelength for different fiber lengths.

Finally, we examined the variations in the dip wavelength of the proposed sensor as a function of the ambient temperature. According to Figure 9a, the proposed sensor consists of two main regions. The first region is a linear region (15–35 °C), in which the sensor is highly sensitive to any changes in the ambient temperature, and the relationship between dip wavelength and temperature is almost linear ($R^2 = 0.986$), as seen in Figure 9b. In optical fiber-based sensors, in addition to the working range, usually sensitivity and resolution are the most important parameters that determine the merit of the sensing component [21,22]. The temperature sensitivity and temperature resolution of the proposed sensor can be calculated from [21,22]:

$$S\,(\text{nm/C}) \;=\; \frac{\Delta\lambda_{dip}}{\Delta T} \tag{10}$$

$$R\,(\text{C}) \;=\; \frac{\Delta T \times \Delta\lambda_{min}}{\Delta\lambda_{dip}} \tag{11}$$

where ΔT is the difference between the minimum and maximum ambient temperatures, and $\Delta\lambda_{min}$ is the minimum spectral resolution of the detector. The average linear temperature sensitivity of the proposed sensor in the linear region is 17.53 nm/°C, which is higher than that of the most recent fiber-optic-based Sagnac interferometer temperature sensors with liquid infiltration. Considering a minimum spectral resolution of 0.01 nm in the detector [6], an average resolution of 5.7×10^{-4} °C is also achieved. In particular, the proposed sensor has a large linear sensitivity of 25.6 nm/°C between 20 and 30 °C. In the second region (larger than 35 °C or smaller than 15 °C) there is no linear relationship between dip wavelength and temperature. The temperature sensitivity in the nonlinear region also decreases significantly comparing to the linear region.
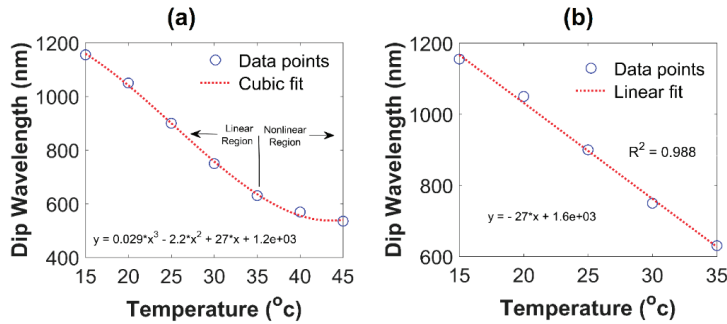
Figure 9. Dip wavelength of transmission spectra of the Sagnac interferometer optical fiber sensor as a function of ambient temperature for (**a**) linear and nonlinear regions with a temperature range of 15–45 °C and (**b**) a linear region with a temperature range of 15–35 °C.

In Table 1, we compared the performance of our proposed temperature sensor with other similarly reported temperature sensors based on liquid-filled optical fibers. It is clear that our proposed chloroform-filled sensor has a higher spectral sensitivity and resolution comparing to other previously reported structures in the literature. Furthermore, the operation range (linear regime) of our sensor is slightly higher than the previously reported Sagnac-interferometer-based optical fiber sensors (30 nm in our case compared to 17 nm in [6], 26 nm in [7], and 10 nm in [4]). It should be mentioned that due to the limitation in detection range of small-size optical detectors, it is not possible to improve the sensitivity and detection range (at the same time) over a certain limit without compromising the cost and size of the sensor. The current small-size cost-effective optical detectors are based on ultraviolet–visible spectroscopy (UV–Vis), which usually cannot detect optical signals below 200 nm and over 1200 nm.

Table 1. The temperature sensing performance of a water-filled PCF in [6], alcohol-filled PCF in [7], toluene-filled PCF in [4], and the proposed chloroform-filled PCF in a Sagnac interferometer.

	Ref [6]	Ref [7]	Ref [4]	This Work
Infiltration Liquid	Water	Alcohol	Toluene	Chloroform
Maximum Birefringence	1.999×10^{-4}	3.5×10^{-4}	8.68×10^{-5}	7.7×10^{-4}
Average Sensitivity (nm/°C)	2.58	6.6	11	17.53
Temperature Range (°C)	25–42	8–34	20–30	15–35
Resolution (°C)	4×10^{-3}	-	-	5.7×10^{-4}

Comparing to other temperature sensing technologies like thermocouples, thermistors, and resistance temperature detectors, our proposed design offers important advantages, including possible remote sensing, possible distributed sensing, immunity to electromagnetic waves interference, and higher detection limits (resolutions). Furthermore, we should emphasize that optical fiber-based temperature sensors can enable temperature sensing in harsh environments, as the sensing element is a fiber that can easily reach hard-to-reach points for temperature sensing. Examples of harsh environments that an optical fiber-based temperature sensor can be a preferable option are inflammable atmospheres, all-electrical aircraft batteries, ocean floors, and oil pipelines [23,24].

5. Conclusions

A new design of an ultrasensitive Sagnac-interferometer-based optical fiber temperature sensor was theoretically and numerically proposed here. Using the finite element method, the modal birefringence of the fiber under different ambient temperatures and the birefringence sensitivity of the

fiber were numerically investigated while one of the airholes was infiltrated with liquid chloroform. A large birefringence sensitivity of almost 29% to a 10 °C temperature variation was reported for the optimized fiber design. The performance of the proposed optical fiber in a temperature sensor Sagnac interferometer is studied in detail, and an average linear temperature sensitivity of 17.53 nm/°C with an average resolution of 5.7×10^{-4} °C was achieved over a temperature range of 20 °C (15 °C to 45 °C).

Author Contributions: Conceptualization, Y.E.M.; Methodology, Y.E.M. and C.L.; Software, A.A.; Validation, V.D.; Formal Analysis, Y.E.M. and A.A.; Data Curation, Y.E.M. and V.D.; Writing-Original Draft Preparation, Y.E.M.; Writing-Review & Editing, Y.E.M and A.A. and C.L.; Visualization, Y.E.M. All authors have read and agreed to the published version of the manuscript.

Conflicts of Interest: The authors declare no conflict of interest.

References

1. Bowden, C.M.; Zheltikov, A.M. Nonlinear optics of photonic crystals introduction. *J. Opt. Soc. Am. B* **2002**, *19*, 2046–2048. [CrossRef]
2. Pathak, A.K.; Singh, V.K. A wide range and highly sensitive optical fiber pH sensor using polyacrylamide hydrogel. *Opt. Fiber Technol.* **2017**, *39*, 43–48. [CrossRef]
3. Wadsworth, W.; Knight, J.; Birks, T. State-of-the-art photonic crystal fiber. *Opt. Photonics News* **2012**, *23*, 24–31. [CrossRef]
4. Monfared, Y.E.; Liang, C.; Khosravi, R.; Kacerovska, B.; Yang, S. Selectively toluene-filled photonic crystal fiber Sagnac interferometer for temperature sensing applications. *Results Phys.* **2019**, *13*, 102297. [CrossRef]
5. Ahmadian, A.; Monfared, Y.E. Chalcogenide-tellurite composite photonic crystal fiber: Extreme non-linearity meets large birefringence. *Appl. Sci.* **2019**, *9*, 4445. [CrossRef]
6. Cui, Y.; Shum, P.; Hu, D.; Wang, G.; Humbert, G.; Dinh, X. Temperature sensor by using selectively filled photonic crystal fiber Sagnac interferometer. *IEEE Photonics J.* **2012**, *4*, 1801–1808. [CrossRef]
7. Qian, W.; Zhao, C.; He, S.; Dong, X.; Zhang, S.; Zhang, Z.; Jin, S.; Guo, J.; Wei, H. High-sensitivity temperature sensor based on an alcohol-filled photonic crystal fiber loop mirror. *Opt. Lett.* **2011**, *36*, 1548–1550. [CrossRef]
8. Lu, Y.; Wang, M.; Hao, C.; Zhao, Z.; Yao, J. Temperature sensing using photonic crystal fiber filled with silver nanowires and liquid. *IEEE Photonics J.* **2014**, *6*, 1–7. [CrossRef]
9. Han, T.; Liu, Y.; Wang, Z.; Guo, J.; Wu, Z.; Wang, S.; Li, Z.; Zhou, W. Unique characteristics of a selective-filling photonic crystal fiber Sagnac interferometer and its application as high sensitivity sensor. *Opt. Express* **2013**, *21*, 122–128. [CrossRef]
10. Vera, E.; Cordeiro, C.; Torres, P. Highly sensitive temperature sensor using a Sagnac loop interferometer based on a side-hole photonic crystal fiber filled with metal. *Appl. Opt.* **2017**, *56*, 156–162. [CrossRef]
11. Sasaki, M.; Ando, T.; Nogawa, S.; Hane, K. Direct photolithography on optical fiber end. *Jpn. J. Appl. Phys.* **2002**, *41*, 4350–4355. [CrossRef]
12. Huang, Y.; Xu, Y.; Yariv, A. Fabrication of function microstructured optical fibers through a selective-filling technique. *Appl. Phys. Lett.* **2005**, *85*, 5182–5184. [CrossRef]
13. Liu, J.; Cheng, T.; Yeo, Y.; Wang, Y.; Xue, L.; Xu, Z.; Wang, D. Light beam coupling between standard single mode fibers and highly nonlinear photonic crystal fibers based on the fused biconical tapering technique. *Opt. Express* **2009**, *17*, 3115–3123. [CrossRef] [PubMed]
14. Martínez-Manuel, R.; May-Arrioja, D.A.; Acevedo-Mijangos, J.; Domínguez-Cruz, R.F.; López-Cortés, D.; Torres-Cisneros, M. Ultra-high sensitivity temperature sensor using a fiber loop mirror based on a water-filled asymmetric two-hole fiber. *IEEE Sens.* **2020**. [CrossRef]
15. Pilla, V.; Munin, E.; Gesualdi, M.R.R. Measurement of the thermo-optic coefficient in liquids by laser-induced conical diffraction and thermal lens technique. *J. Opt. A Pure Appl. Opt.* **2009**, *11*, 105201. [CrossRef]

16. Kim, Y.H.; Park, S.J.; Jeon, S.; Ju, S.; Park, C.; Han, W.; Lee, B. Thermo-optic coefficient measurement of liquids based on simultaneous temperature and refractive index sensing capability of a two-mode fiber interferometric probe. *Opt. Express* **2012**, *20*, 23744–23754. [CrossRef]

17. Monfared, Y.E.; Ponomarenko, S.A. Extremely nonlinear carbon-disulfide-filled photonic crystal fiber with controllable dispersion. *Opt. Mater.* **2019**, *88*, 406–411. [CrossRef]

18. Monfared, Y.E.; Hajati, M.; Liang, C.; Yang, S.; Qasymeh, M. Quasi-D-shaped fiber optic plasmonic biosensor for high-index analyte detection. *IEEE Sens.* **2019**. [CrossRef]

19. Malitson, I.H. Interspecimen comparison of the refractive index of fused silica. *J. Opt. Soc. Am.* **1965**, *55*, 1205–1208. [CrossRef]

20. Ayyanar, N.; Vasanth, R.; Rajab, J.; Vigneswaran, D.; Lakshmi, B.; Sumathia, M.; Porseziand, K. Highly efficient compact temperature sensor using liquid infiltrated asymmetric dual elliptical core photonic crystal fiber. *Opt. Mater.* **2017**, *64*, 482–574. [CrossRef]

21. Monfared, Y.E. Refractive index sensor based on surface plasmon resonance excitation in a d-shaped photonic crystal fiber coated by titanium nitride. *Plasmonics* **2020**, *15*, 535–542. [CrossRef]

22. Rifat, A.A.; Mahdiraji, G.A.; Sua, Y.M.; Ahmed, R.; Shee, Y.G.; Adikan, F.R.M. Highly sensitive multi-core flat fiber surface plasmon resonance refractive index sensor. *Opt. Express* **2016**, *24*, 2485–2495. [CrossRef] [PubMed]

23. Vázquez, C.; Tapetado, A.; Pinzón, P.J.; Montero, D.S.; López-Cardona1, J.D.; Contreras, P.; Zubia, J. Temperature sensing using optical fibers in harsh environments. In Proceedings of the 19th International Conference on Transparent Optical Networks (ICTON), Girona, Spain, 2–6 July 2017; pp. 1–4.

24. Zhang, M.; Ma, X.; Wang, L.; Lai, S.; Zhou, H.; Zhao, H.; Liao, Y. photonic sensors review progress of optical fiber sensors and its application in harsh environment. *Photonic Sens.* **2011**, *1*, 84–89. [CrossRef]

Salinity Sensing Characteristics Based on Optical Microfiber Coupler Interferometer

Lingjun Zhou [1,2], Yang Yu [2,3,*], Huimin Huang [1], Yuyu Tao [1], Kui Wen [2], Guofeng Li [1], Junbo Yang [2] and Zhenrong Zhang [1]

[1] Guangxi Key Laboratory of Multimedia Communications and Network Technology, School of Computer, Electronic and Information, Guangxi University, Nanning 530004, China; lingjunzhou@st.gxu.edu.cn (L.Z.); 1813301006@st.gxu.edu.cn (H.H.); taoyuyu@st.gxu.edu.cn (Y.T.); 1813391006@st.gxu.edu.cn (G.L.); zzr76@gxu.edu.cn (Z.Z.)

[2] Center of Material Science, College of Liberal Arts and Sciences, National University of Defense Technology, Changsha 410073, China; kuiwen93@hotmail.com (K.W.); yangjunbo@nudt.edu.cn (J.Y.)

[3] Deep Sea Technology Laboratory, College of Meteorology and Oceanology, National University of Defense Technology, Changsha 410073, China

* Correspondence: yuyang08a@nudt.edu.cn

Abstract: In this paper, we report a novel and compact sensor based on an optic microfiber coupler interferometer (OMCI) for seawater salinity application. The OMCI device is fabricated by connecting Faraday rotating mirrors to the two out-ports of the microfiber coupler, respectively. The sensor signal processing is based on a wavelength demodulation technique. We theoretically analyze the sensing characteristics with different device structure parameters. Besides, the results show that the date reading error decreases with the thinner waist region and longer arm difference. Through the experiment, the reflection spectra red-shifted as the sea water salinity increased; the highest response sensitivity of the OMCI salinity sensor reached 303.7 pm/‰ for a range of 16.6–23.8‰, and the resolution was less than 0.03‰. This study provides a new technical solution for the development of practical optical fiber seawater salinity sensors.

Keywords: optical microfiber coupler; interferometer; salinity sensing; optic fiber sensor

1. Introduction

Salinity is one of the basic parameters of the ocean state equation. At the same time, it plays an important role in global water cycle change, and provides a means of studying the linkages of the oceans with the terrestrial water cycle, which affects marine phenomena such as precipitation and circulation [1–4]. In addition, the salinity directly determines the halocline of the seawater [5], which poses a threat to the safe operation of underwater equipment. Therefore, real-time and large-scale online monitoring of seawater salinity distribution is of great significance to ecosystem protection, the global climate, sea creatures, ocean economic development, and marine equipment operation.

Traditionally, the equipment used to measure the salinity of seawater is mainly the electrical conductivity-temperature-depth (CTD) system. Among them, its salinity sensor works by using the correspondence between the chloride ion content and the conductivity in the water solution. Although this technology can achieve higher precision, it is vulnerable to electromagnetic interference, and other conductive ions in seawater can also cause measurement errors [5,6]. Because of its large size and complicated structure, it is not applicable for salinity measurement at the micro scale and the water vapor interface [7]. Moreover, in order to obtain salinity data with high spatial resolution, many CTDs must be used in series, which greatly increases the cost. Therefore, there is an urgent need to develop low-cost and compact sensors to meet the demand of subtle measurement in the ocean.

In the last decades, optical fiber sensors have attracted significant research attention due to the advantages of small size, low cost, immunity to electromagnetic interference, and easy integration and reuse [8–12]. There are some fiber optic sensor structures that have been developed and applied to ocean salinity measurement, such as optical reflection [13,14], fiber Bragg grating [15–17], fiber surface plasmon resonance [2,18], and interferometer [19,20]. However, the above types of optical fiber seawater salinity sensors have various problems such as low sensitivity and susceptibility to temperature crosstalk. In recent years, researchers have discovered that optical microfiber (OM) is very sensitive to surrounding environmental changes due to the characteristics of large evanescent field transmission (a light field transmitted outside the boundary surface of the waveguide) [21]. It demonstrates important research value in highly sensitive sensing applications that can gradually be used in ocean salinity sensing research, including the microfiber knot resonator [6], optical microfiber coupler (OMC) [22–24], and OMC-Sagnac [25]. However, to truly succeed in the monitoring of seawater salinity, the optical fiber salinity sensor based on evanescent field transmission must adopt a particular package design to eliminate the influence of seawater impurities, algae and other stray parameters on the detection accuracy and stability of the sensor [24]. Thus, the optical fiber sensor must have a simple and compact optical path to facilitate probe package integration.

In this paper, a sensing device based on an optical microfiber coupler combined with an interferometer (OMCI) is proposed for the first time. The seawater salinity sensing mechanism and signal demodulation error are theoretically analyzed. Meanwhile, the salinity sensing experiment shows that the maximum salinity sensitivity is 303.7 pm/‰. The sensor demonstrated here is high sensitivity, simple and compact, easy to fabricate, convenient to be encapsulated due to the simple and compact optical path, and provides new technical solutions for the development of practical optical fiber seawater salinity sensors.

2. Sensing Principle

The OMC proposed in this article is fabricated by fusing and tapering two twisted conventional single mode fibers (SMFs) [26,27]. As shown in Figure 1a, the OMC is mainly composed of three parts, including a uniform waist region, two tapered transition regions and four input/output ports. As shown in Figure 1a, the OMCI is constructed by connecting two faraday rotating mirrors (FRMs) to Port3 and Port4 of the OMC, respectively. Figure 1b shows the microscope images of OMC uniform waist region. The waist region with the characteristics of large evanescent field transmission is the main sensing unit of OMCI. While the two FRMs are only used as mirrors to simplify the optical path and make the structure more compact, the interferometer does not participate in salinity sensing.
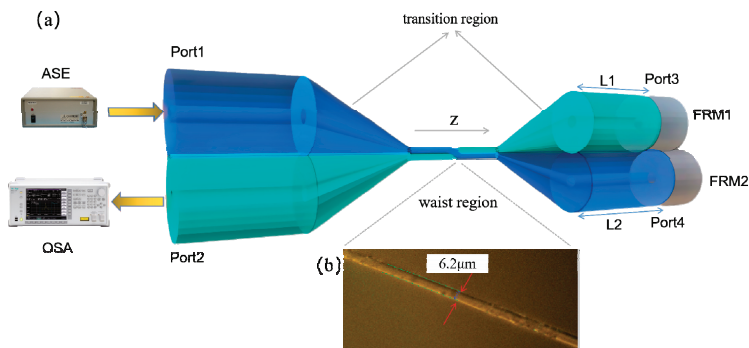

Figure 1. (**a**) Schematic of OMCI composition; it is constructed by connecting two faraday rotating mirrors to port3 and port4 of the OMC, respectively, the amplified spontaneous emission (ASE) broadband light source injecting to port1 and monitoring the signal from port2 by using the optical spectrum analyze (OSA). (**b**) Microscopic image of the OMC waist region.

For the dual-fiber fusing and tapering OMC, optical coupling at the waist region can be regarded as the coupling between two optical microfibers. If the input light P_0 is injected into Port1, the output light intensity of Port3 and Port4 can be expressed as [23,24]:

$$P_3 = P_0 \cos^2(\int_0^l c(\lambda, n_2, n_3, z)dz) = P_0 \cos^2 \varphi$$
$$P_4 = P_0 \sin^2(\int_0^l c(\lambda, n_2, n_3, z)dz) = P_0 \sin^2 \varphi \tag{1}$$

where l is the coupling length and $c(\lambda, n_2, z)$ is the coupling coefficient at wavelength λ and location z. The fusing and tapering OMC is manufactured according to the volume conservation model. The uniform waist length L and the coupling length l satisfy a specific relationship [28], and the thin uniform waist region plays a leading role in the coupling characteristics of the whole OMC [26]. Assuming that the OMC uniform waist region matches the condition of strong coupling, the coupling coefficient C can be expressed as [26]:

$$C(\lambda, n_2, n_3, z) = \frac{3\pi\lambda}{32n_2r^2} \times \frac{1}{(1+1/V)^2} \tag{2}$$

where $V = [(2\pi r)/\lambda](n_2^2 - n_3^2)^{1/2}$ is the normalized frequency, λ is the incident light wavelength, r is the radius of the OMs at the uniform waist region. n_2 and n_3 are the refractive indexes (RIs) of the fiber cladding (silica) and the external environment (sea water), respectively.

When the probe light output from Port3 and Port4 of OMC are reflected by the FRMs and re-enter the coupling area, secondary coupling and interference occur. Assuming that the reflection efficiency of the FRMs is 100%, the output light intensity at Port2 can be expressed as:

$$P_2 = 2P_0 \cos^2 \phi \sin^2 \phi(1 + \cos \theta) \tag{3}$$

where $\theta = 2\pi n_2 l_a / \lambda$ is the interference phase difference, and l_a is the interferometer arm difference. Due to the large evanescent field transmission characteristics of OMC's thin waist region, seawater can be regarded as the OMs' cladding in the waist area of the OMC when OMCI is immersed in seawater [6]. As can be seen from Equations (2) and (3), the seawater RI n_3 changes with the variation of seawater salinity, which results in the shift of specific wavelength. It means that the OMCI's waist region with the characteristics of large evanescent field transmission is the main sensing unit in seawater salinity sensing applications. When tracking a specific wavelength (dip or peak) of the OMCI output spectra, the seawater salinity response sensitivity of OMCI can be expressed [25]:

$$S = \frac{d\lambda}{dS} = -\frac{\partial\lambda}{\partial\varphi} \cdot \frac{\partial\varphi}{\partial n_3} \cdot \frac{dn_3}{dS} \tag{4}$$

In the condition of atmospheric pressure, the relationship between seawater salinity and refractive index is [29]:

$$n_3(S, T, \lambda) = 1.3247 - 2.5 \times 10^{-6}T^2 + S(2 \times 10^4 - 8 \times 10^7 T) + \frac{3300}{\lambda^2} - \frac{3.2 \times 10^7}{\lambda^4} \tag{5}$$

where S and T represent salinity and temperature, respectively; the units are ‰ and °C. As can be known in Equation (5), the RI of seawater is controlled by the seawater temperature, salinity and detection light wavelength at atmospheric pressure. Under the condition that the seawater temperature T is 25 °C, the OMC uniform waist length L is 2 mm, and the radius of the OM is 1.55 μm, the salinity response characteristics of the OMCI transmission spectra under different arm differences are simulated and analyzed. The calculation results are shown in Figure 2, when the arm difference l_a is 0; that is, in the case of equal arms, the output spectra only have intensity fluctuations related to the filter beam splitting characteristics of OMC. When the arm of the OMCI is not equal, the difference is that the interference peaks (phase interference signals) related to the interferometer arm differences appear in

the output spectra, and there is an intensity envelope on the interference peaks when the arm of the OMCI is not equal. In addition, the larger the OMCI arm difference, the denser the interference peaks in its output spectrum.
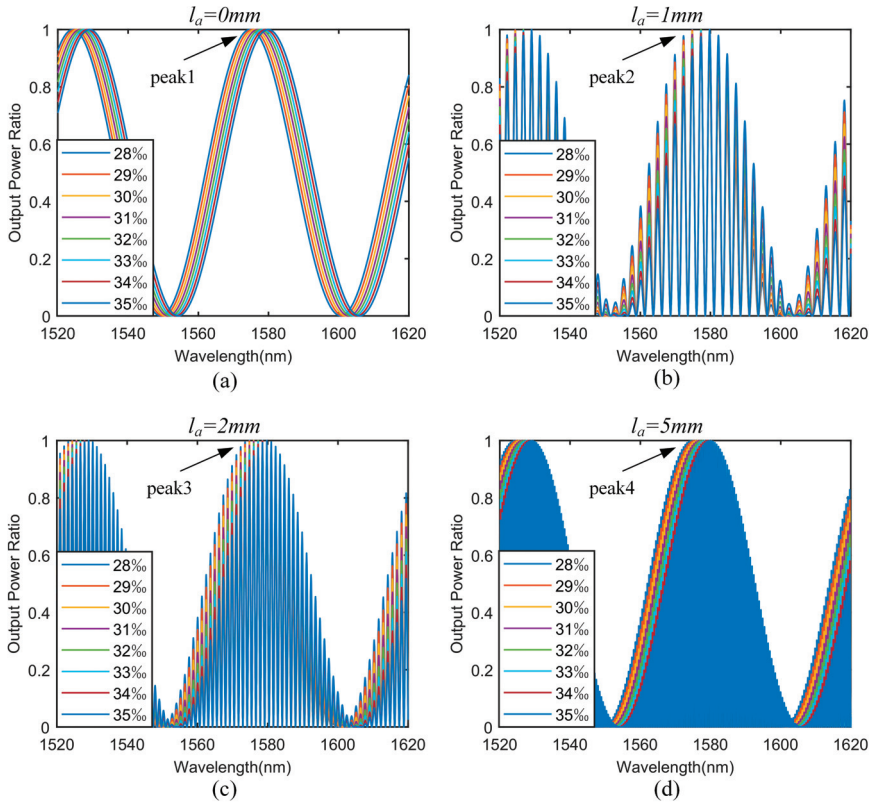

Figure 2. The simulation output spectra with salinities for OMCI arm difference (**a**) $l_a = 0$ mm, (**b**) $l_a = 1$ mm, (**c**) $l_a = 2$ mm, and (**d**) $l_a = 5$ mm.

In fact, when a light source with different wavelengths (broadband source) injects to OMCI, the output intensity corresponding to each wavelength is the superimposed output effect after interference, and the phase difference of the interferometer corresponding to different wavelengths is different, so the output light intensity at each wavelength is different (corresponding to the optical path difference of the interferometer and the wavelength filtering characteristics of the OMC). It means that the reflection spectrum of OMCI will present an intensity envelope signal related to the OMC coupling characteristics, as well as "interference fringe" (intensity periodic oscillations) related to the optical path difference of the interferometer. This "interference" reflects the output result of the interference intensity caused by the phase difference of the interferometer at different wavelengths, rather than the traditional meaning of interference. In salinity sensing applications, the filtering characteristics of OMCI play a major role, and sensing is achieved by tracking reflection spectra with environmental salinity changes.

Figure 3a shows the detail of the peak1 of the output spectra near 1576 nm with the salinities when the OMCI is equal arm. It can be seen from the figure that the output spectra of OMCI red-shift as the salinity increases. By monitoring the drift of specific wavelength (peak), the salinity response

sensitivity of the OMCI is 318 pm/‰. Moreover, when the two arms of OMCI are not equal, the output spectra with the variation of salinity also red-shift, and the salinity sensing response can be realized by tracking the extreme point of the interference peak. However, it should be noted that when the difference value of the OMCI arm is small, the output characteristic interference spectra will be very sparse. When the wavelength shift caused by the change of seawater salinity is less than the interference peak spacing, it will not be accurately monitored and will read the drift of the maximum point of the interference peak, which will cause a large error of data reading. The problem can be clearly seen from Figure 3b, which partially details that the change of the OMCI-specific spectra with the difference of salinity under the arm is 3 mm.
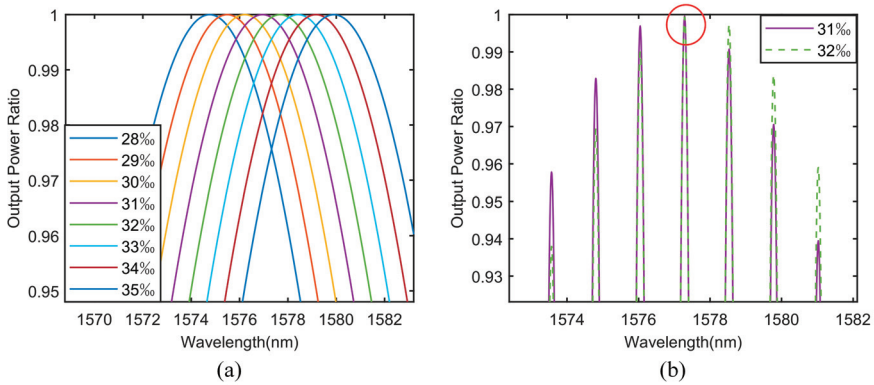
Figure 3. Details of the output spectra with salinity (**a**) at peak1 with arm difference $l_a = 0$ mm, and (**b**) at peak2 with arm difference $l_a = 3$ mm.

For the sake of further analyzing the effect of the OMCI interferometer arm difference on the data reading error of the salinity sensing response, we tracked and analyzed the characteristic spectra of OMCIs in salinity sensing with different arm differences. The calculation results are shown in Figure 4; when the OMCI is equal arm, there is no interference peak in its output spectrum, so there is no wavelength drift error that directly reads the wavelength offset corresponding to the extreme point. As shown in Figure 4b,c, the data reading error of the salinity sensing response is large under the small arm difference, and the fitting effect is not obvious (low R^2). In addition, as can be seen from Figure 4d, the fitting result of the sensing response data is closer to the zero arm difference as the OMCI arm difference increases; that is, the error is getting smaller.

From the above analysis, if the OMCI structure designed in this paper chooses 0 arm difference or a larger arm difference, the error of signal demodulation can be reduced. In practice, however, it is more difficult to manufacture an interferometer with 0 arm difference. The output spectrum interference peaks of OMCI with large arm difference are relatively dense, which imposes higher precision reading requirements on the demodulation equipment (OSA), and it is easy to bring other environmental noise, thereby reducing the system's signal-to-noise ratio. Therefore, in the practical salinity sensing application of OMCI, it is more appropriate to keep the OMCI arm difference within 5–30 mm.
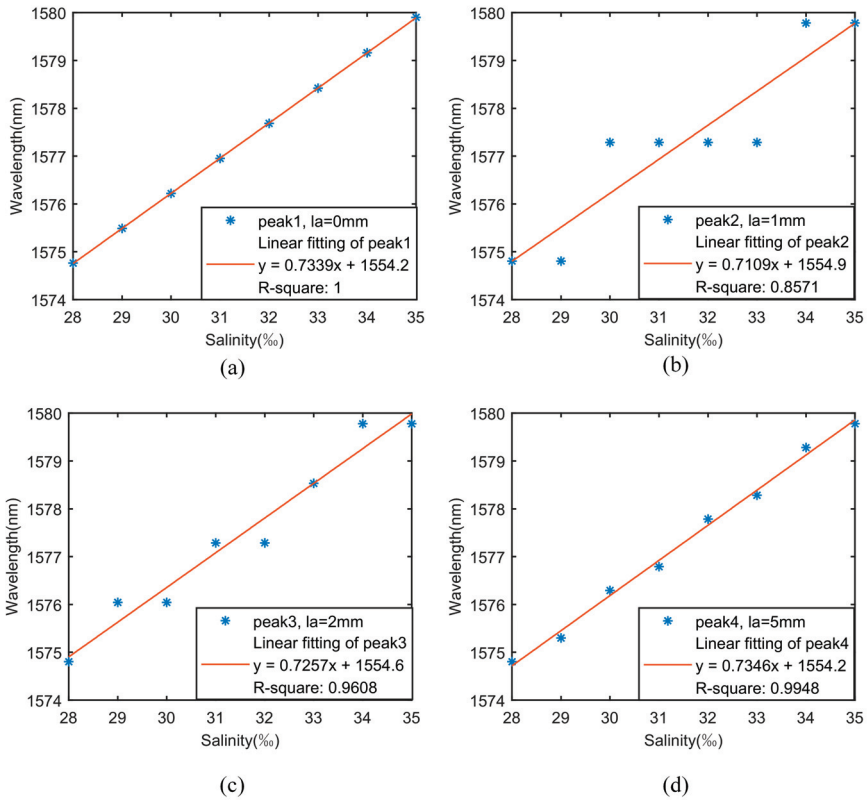
Figure 4. The fitting lines of interference peak wavelength shift with salinities under the arm difference (**a**) $l_a = 0$ mm, (**b**) $l_a = 1$ mm, (**c**) $l_a = 2$ mm, and (**d**) $l_a = 5$ mm.

For almost all sensor applications, improving the signal-to-noise ratio of the device is an effective means to reduce detection errors. It is found from Figure 5 that the the sensing sensitivity of OMCI structure can be improved by reducing the uniform waist radius r of OM. We tracked the specific wavelengths of peak1', peak2', and peak3'; the linear results are shown in Figure 6. The red line (guideline) in the picture represents the three peaks' drift under zero arm difference. We can find that the result is closer to the guideline as the sensitivity rises. That is, when the wavelength drift with salinities is much larger than the interference peak spacing, the detection error will be greatly reduced. Therefore, if the manufacturing process conditions permit, the OM radius r should be reduced as much as possible to improve sensor performance. The length L of the OMCI waist region has little effect on sensitivity, but directly determines the output spectral characteristics (number of specific wavelengths) [30]. In addition, multiple specific wavelengths can realize multi-parameter sensing, so in practical engineering applications, device parameters should be selected reasonably according to requirements.
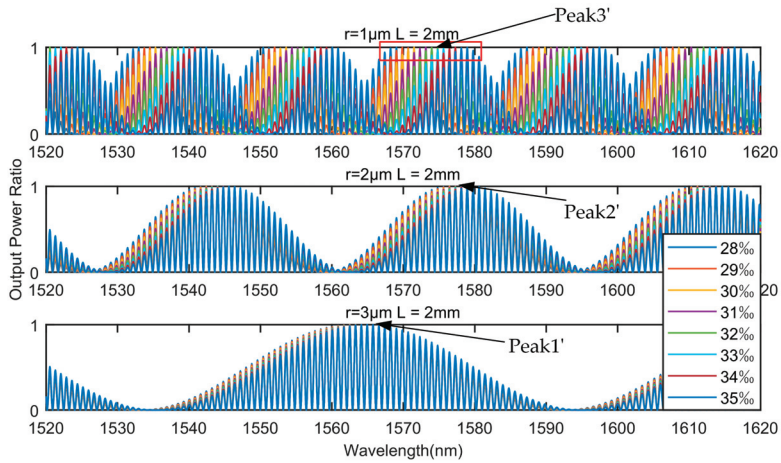
Figure 5. The results of simulation output spectra with OMCI waist length of 2 mm, arm difference of 3 mm and OM radius of 1, 2, and 3 μm, respectively, for the salinity range of 28–35‰.
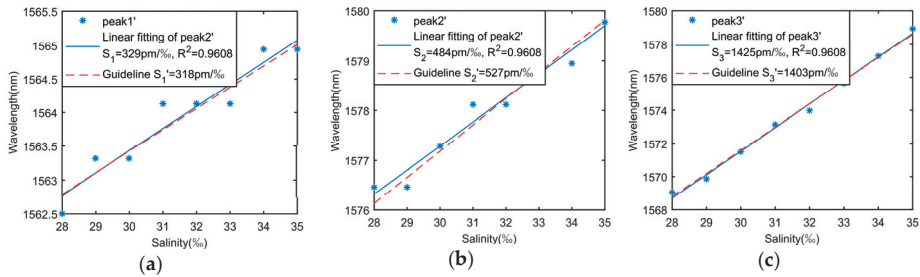

Figure 6. Linear fitting result of peaks. The red lines represent the peak wavelengths' shift under an arm difference of zero; (**a**) linear fitting of peak1′, (**b**) linear fitting of peak2′ and (**c**) linear fitting of peak3′.

3. Experimental Results

We established an experimental system in order to fully verify the foregoing theoretical analysis results and grasp the salinity sensing characteristics of OMCI. As shown in Figure 7, it consists of an ASE broadband light source (1520–1620 nm), an optical spectrum analyzer (OSA, 600–1700 nm, Q8384, ADVANTEST, resolution 0.01 nm), a CTD system (Midas, VALEPORT), a water tank, a signal processing computer, etc. Port1 of the OMCI is connected to the ASE light source, and the output signal from Port2 is sent into the OSA. The electrical CTD system is used for calibrating and comparing the salinity tests. The salinity measuring experimental setup is shown in Figure 7b.

In the sanility experiment, we first used an OMCI sample with the uniform waist length L of approximately 7 mm; the radius of the microfiber was 1.55 μm, and the lengths of the two arms of the interferometer were about L1 = 2.0 m, L2 = 2.006 m. The water tank capacity was about 4 L. The seawater samples were blended with NaCl crystals and pure water. Firstly, the salinity of the seawater samples was adjusted to 23.8‰, and the centration of the seawater samples was then changed by adding pure water with the aim of avoiding exothermic impact when the NaCl crystals were dissolved in water. About 200–300 mL of pure water was added and stirred evenly each time; at the same time, the electrical CTD system was used to monitor the seawater salinity and temperature changes (the impact of temperature has been eliminated). The data was recorded after the salinity became stable

and the output spectrum no longer shifted. Figure 8a,b show that the red shifted at the sensing dips as the salinity increased from 16.6‰ to 23.8‰.
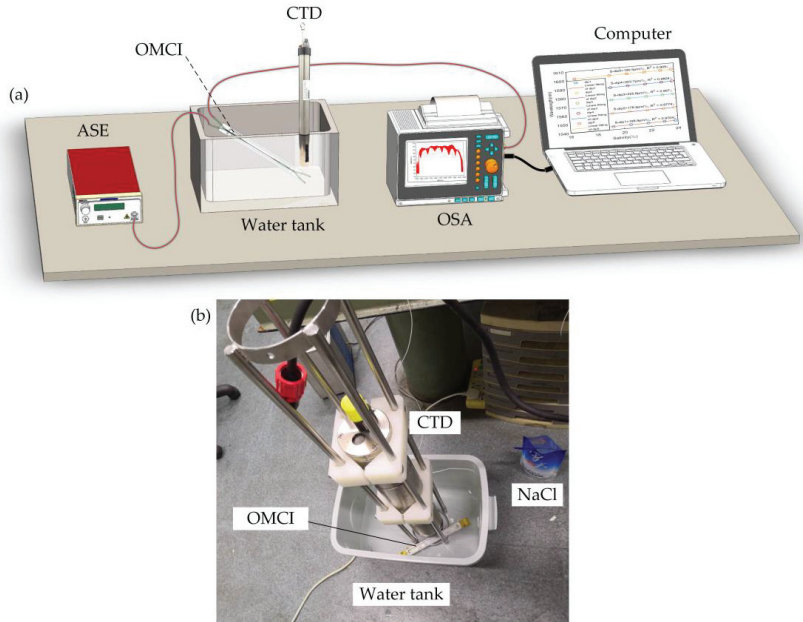

Figure 7. (**a**) The schematic diagram of the experimental system, and (**b**) the salinity measuring experimental setup.
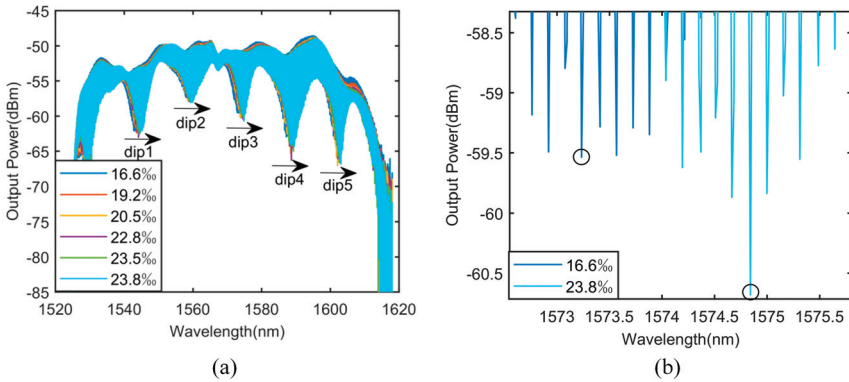

Figure 8. (**a**) The output spectra at different salinities with L = 7 mm, r = 1.55, l_a = 6 mm. (**b**) Detail of output spectra near dip3.

To estimate the sensitivities, we tracked five dips in output spectra, and the dip values at different salinities are shown in Figure 9. The fitting results show that the salinity sensitivity responses of OMCI in different specific wavelengths are: S_{dip1} = 198.9 pm/‰, S_{dip2} = 178.5 pm/‰, S_{dip3} = 225.8 pm/‰. S_{dip4} = 303.7 pm/‰, S_{dip5} = 190.5 pm/‰. Under the condition of 0.01 nm resolution of OSA, the salinity resolution of the OMCI sample is less than 0.03‰. The minimum dynamic range of the dip3 wavelength is 13.97 nm, allowing the salinity to vary by 46.1‰. In the global sea area, the average

salinity is 35‰. From the Baltic Sea with the lowest salinity to the Red Sea with the highest salinity, the range is about 7.4–40‰ [31,32]. Therefore, the dynamic range of the salinity response of the experimental sample of the OMCI sensor is applicable to the practical measurement requirements of salinity in most sea areas.
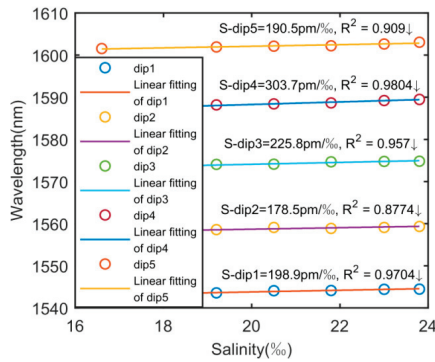

Figure 9. Relationships between the specific wavelengths and the salinities.

The above simulation results show that the OMCI salinity sensing under small arm difference will bring a large specific wavelength drift error; that is, the data fitting degree of the dip wavelength drift is bad. To verify this feature, we adjust the arm difference of the above OMCI sample to $l_a = 1$ mm. The output spectra (partial) at different salinities are shown in Figure 10a. There is a large interference peak spacing, with a width of about 2100 pm, in the output characteristic spectrum. Figure 10b shows the salinity response sensitivity and fitting results at different dips. It can be seen from the figure that the data reading error of this sample is large (the minimum R^2 is about 0.027), which is consistent with the previous theoretical analysis; that is, there is large detection error under the small arm difference. Therefore, the OMCI sample with large arm difference should be selected to make the sensor obtain more accurate sensing results. It should be noted that the signal intensity at the dips of the OMCI characteristic spectrum is weak. Because of the groundnoise, there are large data reading errors for salinity sensing detection by tracking the dips' wavelengths and low signal-to-noise ratios. Therefore, it is more reasonable to track the peaks of the characteristic OMCI spectrum to achieve higher precision salinity sensor detection.
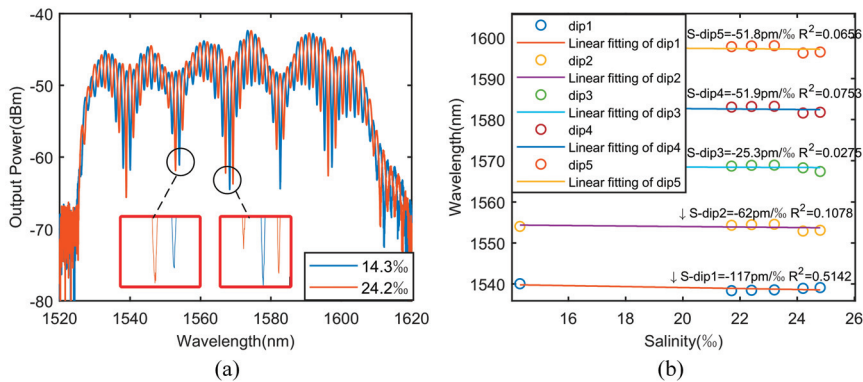

Figure 10. After adjusting arm difference $l_a = 1$, (**a**) the output spectrum (partial) at different salinities, and (**b**) relationships between the characteristic wavelengths and the salinities.

4. Discussion

The waist region of OMCI can respond to salinity and temperature simultaneously. There is a proven solution to eliminate the effects of cross-sensitivity; that is, tracking two sensing dips and constructing a salinity and temperature sensitivity matrix, then performing inversion calculations [12,22,24], as shown in Equation (6). In addition, the two arms of the interferometer only respond to temperature; tracking the distance of two adjacent interference peaks can realize this sensitivity to temperature. In view of this, the temperature sensitivity of the interferometer can compensate for the temperature sensitivity of the OMCI's waist region; we have analyzed this feature in detail in previous work [31].

$$
\begin{bmatrix} \Delta\lambda_{dip1} \\ \Delta\lambda_{dip2} \end{bmatrix} = \begin{bmatrix} S_{S1} S_{T1} \\ S_{S2} S_{T2} \end{bmatrix} \begin{bmatrix} \Delta S \\ \Delta T \end{bmatrix} \tag{6}
$$

According to the above results, it shows excellent salinity sensing performance by reasonably setting the parameters of OMCI sensor. Comparing other salinity sensors, for example, the salinity sensors based on optical reflection have high sensitivity, but their prism systems are complicated and difficult to apply to harsh marine environments. The structure of the fiber grating salinity sensor is relatively simple, but its sensitivity is generally low. There is a sensitivity of around 50–200 pm/‰ with the SPR sensor, However, what matters is that the metal film should be coated effectively. As far as we know, most interference structures are complex although some of them can reach high sensitivity. As we all know, fiber optic sensors are immune to electromagnetic interference, but most of them are sensitive to temperature; in practical application, ways of eliminating the effects of cross-sensitivity should be considered. The sensor designed in this paper not only has high sensitivity, a compact structure to encapsulate it, and ease of manufacturing, but also has special advantages for temperature self-compensation.

5. Conclusions

In summary, a novel seawater salinity sensor based on the structure of optical microfiber coupler interferometer is proposed. The results show that the output spectra of OMCI red-shift as salinity increases, and the salinity response sensitivity reaches 303.7 pm/‰. The experiment is consistent with the theoretical analysis. In addition, we discussed the relationship between the OMCI arm difference and the wavelength drift error. When the arm difference is small, the interference peak of the output spectrum is relatively sparse. Moreover, there is an error between the dip wavelength in the output spectrum and the dip wavelength in the envelope (0 arm difference), and the smaller the arm difference, the greater the error. At the same time, when the sensitivity is low (that is, wavelength drift is much smaller than the interference peak spacing), the error is more obvious. Therefore, this paper proposes three improvement suggestions: firstly, controlling the OMCI arm difference to zero; secondly, controlling the OMCI arm difference to 5–30 mm; third, reducing the OM radius *r* to improve the sensor's signal-to-noise ratio. In practical applications, the latter two schemes are easier to implement. This OMCI salinity sensor meets the needs of salinity testing in most sea areas. It provides good research ideas and alternative technical solutions for the development of practical optical fiber salinity sensors.

Conflicts of Interest: The authors declare no conflict of interest.

References

1. Fofonoff, N.P. Physical properties of seawater: A new salinity scale and equation of state for seawater. *J. Geophys. Res.* **1985**, *90*, 3332. [CrossRef]
2. Gentleman, D.J.; Booksh, K.S. Determining salinity using a multimode fiber optic surface plasmon resonance dip-probe. *Talanta* **2006**, *68*, 504–515. [CrossRef] [PubMed]
3. Nathan, A.J.; Scobell, A. *Salinity: Environment-Plants-Molecules*; Springer: Berlin, Germany, 2012; Volume 91, ISBN 9788578110796.
4. Durack, P.J.; Wijffels, S.E.; Matear, R.J. Ocean salinities reveal strong global water cycle intensification during 1950 to 2000. *Science* **2012**, *336*, 455–458. [CrossRef]
5. Díaz-Herrera, N.; Esteban, O.; Navarrete, M.C.; Le Haitre, M.; Gonzalez-Cano, A. In situ salinity measurements in seawater with a fibre-optic probe. *Meas. Sci. Technol.* **2006**, *17*, 2227–2232. [CrossRef]
6. Liao, Y.; Wang, J.; Yang, H.; Wang, X.; Wang, S. Salinity sensing based on microfiber knot resonator. *Sens. Actuators A Phys.* **2015**, *233*, 22–25. [CrossRef]
7. Cox, R.A.; Culkin, F.; Riley, J.P. The electrical conductivity/chlorinity relationship in natural sea water. *Deep. Res. Oceanogr. Abstr.* **1967**, *14*, 203–220. [CrossRef]
8. Qian, Y.; Zhao, Y.; Wu, Q.L.; Yang, Y. Review of salinity measurement technology based on optical fiber sensor. *Sens. Actuators B Chem.* **2018**, *260*, 86–105. [CrossRef]
9. Huang, H.; Yu, Y.; Zhou, L.; Tao, Y.; Yang, J.; Zhang, Z. Whispering gallery modes in a microsphere attached to a side-polished fiber and their application for Magnetic field sensing. *Opt. Commun.* **2020**, *478*, 126366. [CrossRef]
10. Huang, H.; Zhang, Z.; Yu, Y.; Zhou, L.; Tao, Y.; Li, G. A Highly Magnetic Field Sensitive Photonic Crystal. *Sensors* **2020**, *20*, 5193. [CrossRef]
11. Yang, L.; Luo, J.; Xu, Y.; Zhang, Z.; Dong, Z. A Distributed dual consensus admm based on partition for dc-dopf with carbon emission trading. *IEEE Trans. Ind. Inform.* **2020**, *16*, 1858–1872. [CrossRef]
12. Hou, Y.; Wang, J.; Wang, X.; Liao, Y.; Yang, L.; Cai, E.; Wang, S. Simultaneous Measurement of Pressure and Temperature in Seawater with PDMS Sealed Microfiber Mach-Zehnder Interferometer. *J. Lightwave Technol.* **2020**. [CrossRef]
13. Yang, H.Z.; Qiao, X.G.; Lim, K.S.; Harun, S.W.; Chong, W.Y.; Islam, M.R.; Ahmad, H. Optical fiber sensing of salinity and liquid level. *IEEE Photonics Technol. Lett.* **2014**, *26*, 1742–1745. [CrossRef]
14. Rahman, H.A.; Harun, S.W.; Yasin, M.; Ahmad, H. Fiber-optic salinity sensor using fiber-optic displacement measurement with flat and concave mirror. *IEEE J. Sel. Top. Quantum Electron.* **2012**, *18*, 1529–1533. [CrossRef]
15. Cong, J.; Zhang, X.; Chen, K.; Xu, J. Fiber optic Bragg grating sensor based on hydrogels for measuring salinity. *Sens. Actuators, B Chem.* **2002**, *87*, 487–490. [CrossRef]
16. Men, L.; Lu, P.; Chen, Q. A multiplexed fiber Bragg grating sensor for simultaneous salinity and temperature measurement. *J. Appl. Phys.* **2008**, *103*, 053107. [CrossRef]
17. Wang, Y.-J.; Dai, X.; Zhao, Q.; Li, F.; Gao, X.; Bo, B.-X. Based on fiber grating the high sensitivity all optical fiber CTD. In Proceedings of the OFS2012 22nd International Conference on Optical Fiber Sensors, Beijing, China, 14–19 October 2012; Volume 8421.
18. Sharma, A.K.; Mohr, G.J. On the application of different bimetallic alloy nanoparticle combinations in fiber optic surface plasmon resonance salinity sensor and its performance optimization against thermal effects. *J. Nanosci. Nanotechnol.* **2010**, *10*, 3145–3154. [CrossRef]
19. Jaddoa, M.F.; Jasim, A.A.; Razak, M.Z.A.; Harun, S.W.; Ahmad, H. Highly responsive NaCl detector based on inline microfiber Mach-Zehnder interferometer. *Sens. Actuators A Phys.* **2016**, *237*, 56–61. [CrossRef]
20. Wang, X.; Wang, J.; Wang, S.S.; Liao, Y.P. Fiber-Optic Salinity Sensing with a Panda-Microfiber-Based Multimode Interferometer. *J. Lightwave Technol.* **2017**, *35*, 5086–5091. [CrossRef]
21. Lou, J.; Tong, L.; Ye, Z. Modeling of silica nanowires for optical sensing. *Opt. Express* **2005**, *13*, 2135. [CrossRef]
22. Wang, S.; Yang, H.; Liao, Y.; Wang, X.; Wang, J. High-Sensitivity Salinity and Temperature Sensing in Seawater Based on a Microfiber Directional Coupler. *IEEE Photonics J.* **2016**, *8*. [CrossRef]
23. Wang, S.; Liao, Y.; Yang, H.; Wang, X.; Wang, J. Modeling seawater salinity and temperature sensing based on directional coupler assembled by polyimide-coated micro/nanofibers. *Appl. Opt.* **2015**, *54*, 10283. [CrossRef] [PubMed]

24. Yu, Y.; Bian, Q.; Lu, Y.; Zhang, X.; Yang, J.; Liang, L. High Sensitivity All Optical Fiber Conductivity-Temperature-Depth (CTD) Sensing Based on an Optical Microfiber Coupler (OMC). *J. Lightwave Technol.* **2019**, *37*, 2739–2747. [CrossRef]

25. Cao, L.; Yu, Y.; Xiao, M.; Yang, J. High sensitivity conductivity-temperature-depth sensing based on an optical microfiber coupler combined fiber loop. *Chin. Opt. Lett.* **2020**, *18*, 011202. [CrossRef]

26. Yu, Y.; Bian, Q.; Zhang, N.; Lu, Y.; Zhang, X.; Yang, J. Investigation on an all-optical intensity modulator based on an optical microfiber coupler. *Chin. Opt. Lett.* **2018**, *16*, 040605.

27. Yu, Y.; Zhang, X.; Song, Z.; Wang, J.; Meng, Z. Precise control of the optical microfiber tapering process based on monitoring of intermodal interference. *Appl. Opt.* **2014**, *53*, 8222. [CrossRef]

28. Birks, T.A.; Li, Y.W. The Shape of Fiber Tapers. *J. Lightwave Technol.* **1992**, *10*, 432–438. [CrossRef]

29. Quan, X.; Fry, E.S. Empirical equation for the index of refraction of seawater. *Appl. Opt.* **1995**, *34*, 3477. [CrossRef]

30. Zhou, L.; Yu, Y.; Cao, L.; Huang, H.; Tao, Y.; Zhang, Z.; Wang, J.; Yang, J.; Zhang, Z. Fabrication and characterization of seawater temperature sensor with self-calibration based on optical microfiber coupler interferometer. *Appl. Sci.* **2020**, *10*, 6018. [CrossRef]

31. Meier, H.E.M.; Kauker, F. Sensitivity of the Baltic Sea salinity to the freshwater supply. *Clim. Res.* **2003**, *24*, 231–242. [CrossRef]

32. Beal, L.M.; Ffield, A.; Gordon, A.L. Spreading of Red Sea overflow waters in the Indian Ocean. *J. Geophys. Res. Ocean.* **2000**, *105*, 8549–8564. [CrossRef]

Article

Giant Displacement Sensitivity Using Push-Pull Method in Interferometry

Paulo Robalinho and Orlando Frazão *

INESC TEC—Institute for Systems and Computer Engineering, Technology and Science,
Rua do Campo Alegre 687, 4169-007 Porto, Portugal; paulo.robalinho@inesctec.pt
* Correspondence: orlando.frazao@inesctec.pt

Abstract: We present a giant sensitivity displacement sensor combining the push-pull method and enhanced Vernier effect. The displacement sensor consists in two interferometers that are composed by two cleaved standard optical fibers coupled by a 3 dB coupler and combined with a double-sided mirror. The push pull-method is applied to the mirror creating a symmetrical change to the length of each interferometer. Furthermore, we demonstrate that the Vernier effect has a maximum sensitivity of two-fold that obtained with a single interferometer. The combination of the push-pull method and the Vernier effect in the displacement sensors allows a sensitivity of 60 ± 1 nm/µm when compared with a single interferometer working in the same free spectral range. In addition, exploring the maximum performance of the displacement sensors, a sensitivity of 254 ± 6 nm/µm is achieved, presenting a M-factor of 1071 and $M_{Vernier}$ of 1.9 corresponding to a resolution of 79 pm. This new solution allows the implementation of giant-sensitive displacement measurement for a wide range of applications.

Keywords: optical fiber sensor; cleaved fiber; Vernier effect; optical interferometer

1. Introduction

With the evolution of technology, the impact of sensors on human life has increased. The significant impact of optical systems is due to the emergence of fiber optics in 1960 [1]. The features such as low attenuation and insensitivity to electromagnetic fields have allowed optical systems to replace electronic communications. In addition, they have enabled the design of ultra-sensitive optical sensors with applicability in nanotechnology [2].

The cleaved-tip optical sensors are the simplest [3]. When used alone, they are only intensity sensors. However, when they are coupled to reflective surfaces [4] or when coatings are deposited on the tip [5], in addition to the intensity operation, they can also operate at wavelength because they allow the implementation of Fabry–Perot interferometers (FPI) [6]. The operation of an FPI is unidirectional where, initially, part of the beam is reflected, and another part is transmitted forming two beams. The transmitted beam is then reflected travelling a distance that is twice the length of the interferometer. Finally, the two beams overlap resulting in the interference pattern. Although in certain areas there are sensory architectures with higher sensitivity and the possibility of multiple measurements [7–9], the cleaved-tip sensors are the easiest to control and manufacture in addition to covering a higher number of research areas.

Despite the vast advances in the development of optical sensors, it was only in 2011 that the Vernier effect was applied in interferometry [10]. This phenomenon is based on the optical waves beat where two waves appear, the envelope and the carrier [11]. Normally, measurements are based on the envelope wave because it shows the highest sensitivity. In the case of interferometry, the effect is in the wavelength dimension, so spectral optical waves are used.

Currently there are several interferometric displacement sensors. From these, the Mach–Zehnder with a sensitivity of 1.53 nm/µm [12] stands out for a wide range. For

a narrow range, the application of surface plasmon resonance (SPR) with a sensitivity of 10.32 nm/µm for a micrometric range [13] and a sensitivity of 31.45 nm/nm for a nanometric range [14] stand out. Recently a new strain sensor architecture based on a push-pull deformation method was reported [15].

In this work, the enhanced Vernier effect combined with the push-pull method is presented. This sensor consists of two FPIs formed by two cleaved tips and a mirror. The signal from the two interferometers are overlapped by means of a 3 dB fiber coupler, resulting the Vernier effect. In this research, the sensitivity of the single interferometer is compared with the sensitivity of the enhanced Vernier effect envelope, both with the same free spectral range (FSR). In addition, it also presents the results regarding the maximization of displacement sensors with enhanced Vernier effect.

2. Materials and Methods

The Vernier effect consists on the overlapping of two optical waves, a concept similar to the beat of two sound waves [16]. This optical phenomenon results in the formation of two new waves: the envelope and the carrier. Usually, optical sensors are based on the traditional Vernier effect, where one of the interferometers is referenced and another is the sensing probe. However, in this paper, the enhanced Vernier effect is presented, and it uses two sensing interferometers which move in opposite directions [17]. One of the major problems with this type of Vernier effect is the lack of sensors with symmetrical sensitivities. Thus arises the application of the push-pull method in interferometry, allowing symmetrical variations of two equal interferometers. This results in two sensors with symmetric sensitivities allowing the maximization of the enhanced Vernier effect [15].

The architecture of the two interferometers is presented in Figure 1 and it is composed by two cleaved fibers and a double-sided reflecting surface. The two interferometers are linked together with a 3 dB coupler. The operating method consists in dividing the light beam into two beams that through the cleaved fibers and the reflecting surface form two Fabry–Perot interferometers (FPIs).
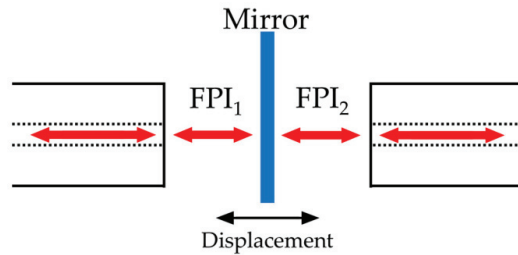

Figure 1. Sensor architecture concept.

The optical signal of the two interferometers is overlapped by means of the coupler forming the output signal of the sensor. The intensity of a FPI can be written as:

$$I_{FPI} = [A\cos(\Delta\phi) + I_0]^2 \tag{1}$$

where $\Delta\phi = \pi n L/\lambda$, n is the refractive index, L is the interferometer length, λ is the wavelength and I_0 is the difference in intensity of the optical paths. If the optical signal is coupled between fibers, a $\pi/2$ phase must be added to $\Delta\phi$. Thus, the sensor output signal is described by:

$$I_{Ve} = \left[2\cos\left(\frac{\Delta\phi_1 - \Delta\phi_2}{2}\right)\cos\left(\frac{\Delta\phi_1 + \Delta\phi_2}{2} + \frac{\pi}{2}\right) + I_0\right]^2 \tag{2}$$

where the indices 1 and 2 allow identify the two interferometers, the components $\Delta\phi_1$ − $\Delta\phi_2$ and $\Delta\phi_1 + \Delta\phi_2$ correspond to the envelope and the carrier, respectively. Figure 2 presents the simulation of Equation (2) with two cavities-one with 500 μm and the other with 600 μm-and a refraction index of 1.00027316. The length of the interferometers can be written as $L = L_0 + \Delta L$, where L_0 is the initial length and ΔL is the mirror displacement. Therefore, taking into account that the interferometers are submitted to a symmetric displacement, Equation (2) can be rewritten as follows:

$$I_{Ve} = \left[2\cos(\gamma[2\Delta L])\cos\left(\gamma[L_{01} + L_{02}] + \frac{\pi}{2}\right) + I_0\right]^2 \tag{3}$$

where $\gamma = \pi n/2\lambda$. As can be seen, the envelope of the enhanced Vernier effect has a sensitivity two-fold that of the one achieved for a single FPI. Furthermore, the envelope does not depend on the length of the interferometers allowing the result of ultra-sensitive displacement sensors with macroscopic FPIs to be replicated.
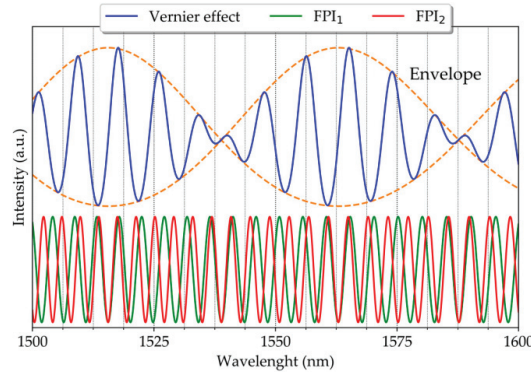

Figure 2. Vernier effect simulation.

To evaluate the efficiency of the implementation of the Vernier effect, the *M*-factor is considered and is given by [16]:

$$M = \frac{\Delta\lambda_{env}}{\Delta\lambda_1} \tag{4}$$

where $\Delta\lambda_{env}$ is the free spectral range (FSR) of the envelope and $\Delta\lambda_1$ is the FSR of a single interferometer. With the appearance of the enhanced Vernier effect, new factors have emerged to evaluate the performance of the Vernier effect [18]:

$$M_{sens} = \frac{sens_{env}}{sens_{carr}} \tag{5}$$

where $sens_{env}$ and $sens_{carr}$ are the envelope and the carrier sensitivities, respectively,

$$M_{FSR} = \frac{\Delta\lambda_{env}}{\Delta\lambda_{carr}} \tag{6}$$

where $\Delta\lambda_{carr}$ is the *FSR* of the carrier and,

$$M_{Vernier} = \frac{M_{sens}}{M_{FSR}} \tag{7}$$

where $M_{Vernier}$ is = 1 for the traditional Vernier effect, < 1 for reduced case and > 1 for the enhanced case.

3. Results

The setup used to characterize the sensor is shown in Figure 3. The mechanical part consists of a double-sided reflective silver surface coupled to a piezoelectric with a displacement of 180.0 ± 0.2 nm/V. Also, a standard optical fiber (SMF28), an erbium broadband source, centered at 1550 nm and a bandwidth of 90 nm, and an optical spectral analyzer (OSA, "YOKOGAWA AQ5370C") with a resolution of 0.02 nm, were used. All the splices in the system were made with a conventional splice machine ("Sumitomo Electric—Type-72C", Osaka, Japan). The overlap of the interferometers signals is obtained with a 3 dB fiber coupler. The fiber cleavage was performed by "Fiber Cleaver FC-6RS" which provides a cleavage angle of less than $1°$ (Figure 3c).
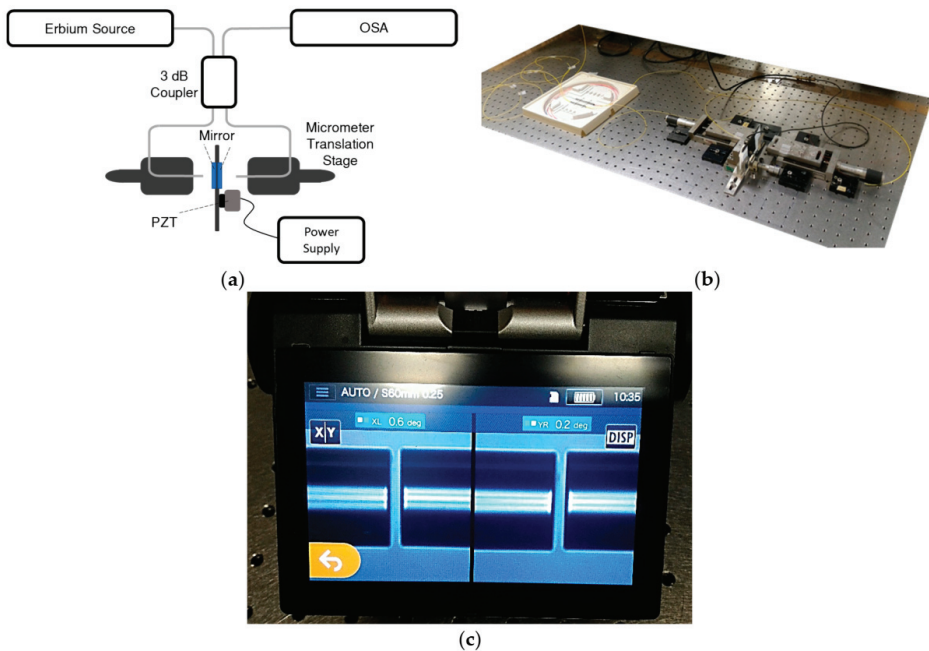

Figure 3. Experimental setup: (**a**) scheme, (**b**) picture, and (**c**) fibers cleavage angle obtained with "Sumitomo Electric—Type-72C".

The sensor characterization involved nano-step measurement provided by the piezoelectric device. To determine the efficiency of the displacement sensor, a single interferometer with a length of 73 ± 2 μm was initially developed, which allowed only three fringes in the bandwidth supplied by the erbium source (Figure 4a) to be obtained. Varying the distance between the fiber and the reflecting surface resulted in Figure 4b where a sensitivity of 29.2 ± 0.3 nm/μm with a r^2 of 0.9995 was obtained.

Following, the Vernier effect was investigated. Since the accuracy of the envelope measurement increases with the increase of the carrier frequency, the sensitivity of a single interferometer with a length of 15.4 ± 0.5 mm was first studied (Figure 5), where a sensitivity of 0.95 ± 0.05 nm/μm with a r^2 of 0.995 was achieved. Thus, the interferometers used to generate the Vernier effect have a lower sensitivity than the reference single interferometer. In this case, the FSR is 0.07 nm.

Now, a second fiber has been added allowing to obtain the Vernier effect. Although both interferometers have the same length (15.4 ± 0.5 mm), they differ by a value close to 70 μm. Hence an envelope with only three fringes appears (Figure 6). This last feature is important because it allows us to compare the envelope of this sensor with the first singular interferometer that is present in this paper.
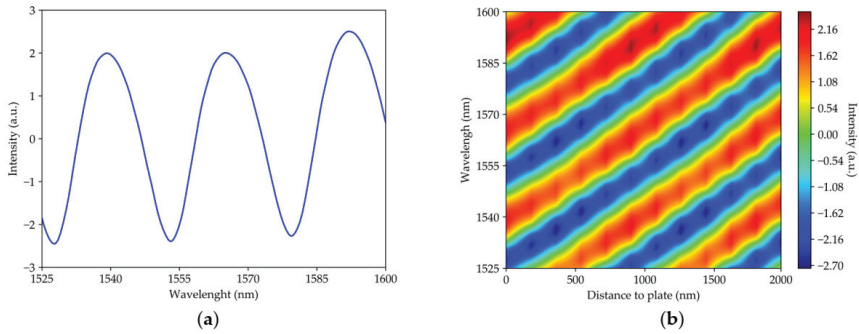
Figure 4. The single interferometer with a length of 73 ± 2 μm: (**a**) Spectrum at the beginning of measurements and (**b**) intensity as a function of the distance between the optical fiber and the reflecting surface and as a function of wavelength.

Figure 5. The single interferometer with a length of 15.4 ± 0.5 mm: (**a**) spectrum at the beginning of measurements and (**b**) intensity as a function of the distance between the optical fiber and the reflecting surface and as a function of wavelength.

Figure 6. The two interferometers with a length of 15.4 ± 0.5 mm: (**a**) spectrum at the beginning of measurements and (**b**) intensity as a function of the distance between the optical fiber and the reflecting surface and as a function of wavelength.
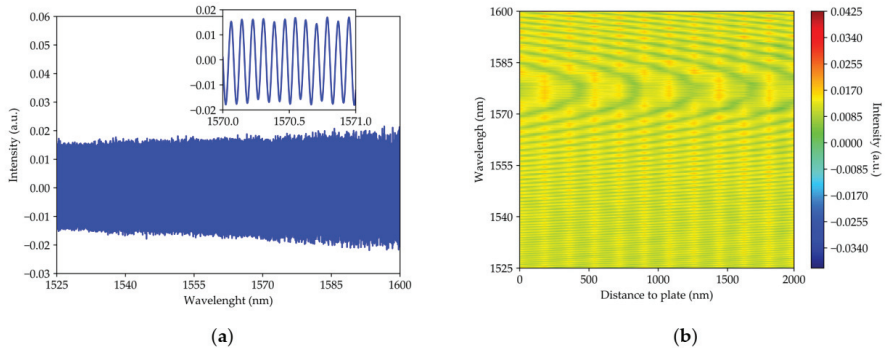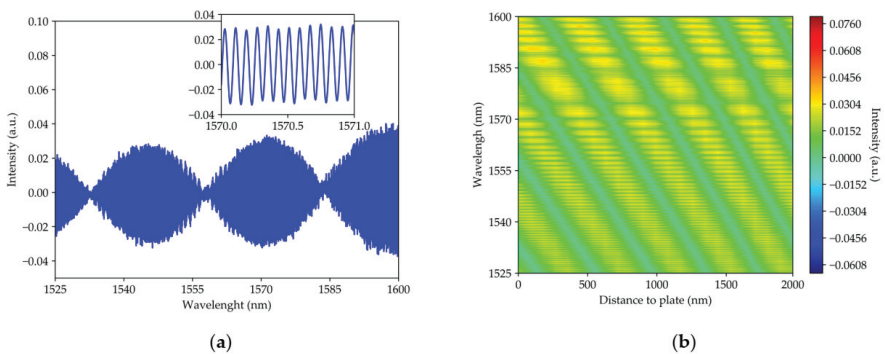
In this case, the envelope sensitivity was 60 ± 1 nm/μm with a r^2 of 0.998 (which is shown in Figure 8) and the carrier had a negligible sensitivity. The envelope sensitivity was two-fold that obtained by the reference single interferometer. the *FSR* for the envelope and carrier was 18 nm and 0.07 nm, respectively. Therefore, the *M*-factor is 257, $M_{sens} = 360$, $M_{FSR} = 257$, $M_{Vernier} = 1.4$.

The last characterization was to optimize the proposed setup in order to obtain the maximum sensitivity of this configuration. In this case, we used two interferometers with a length of 6.1 ± 0.2 mm each and by reducing the difference between the two interferometers, an envelope with only one fringe was achieved, as depicted in Figure 7. The sensitivity obtained was 254 ± 6 nm/µm with an r^2 of 0.9990 (which is shown in Figure 8) for the envelope, and 0.160 ± 0.005 nm/µm with a r^2 of 0.992 for the carrier. Also, the *FSR* for the envelope and the carrier was 75 nm 0.09 nm respectively. Therefore, the *M*-factor was 1071, $M_{sens} = 1587$, $M_{FSR} = 833$, $M_{Vernier} = 1.9$. Table 1 summarizes all the values.
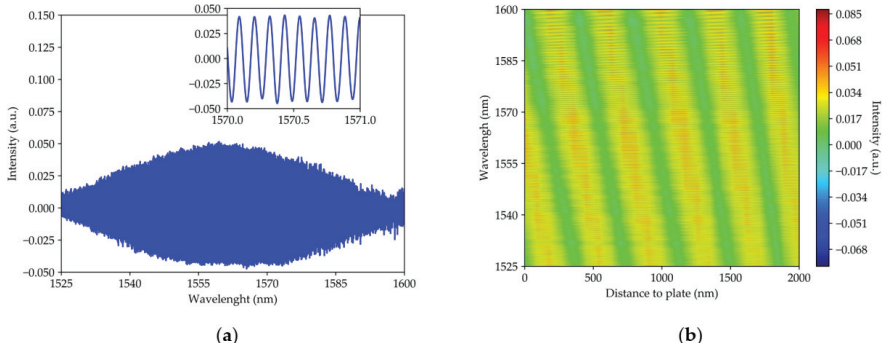

Figure 7. The two interferometers with a length of 6.1 ± 0.2 mm: (**a**) spectrum at the beginning of measurements, and (**b**) intensity as a function of distance to the reflecting surface and as a function of wavelength.
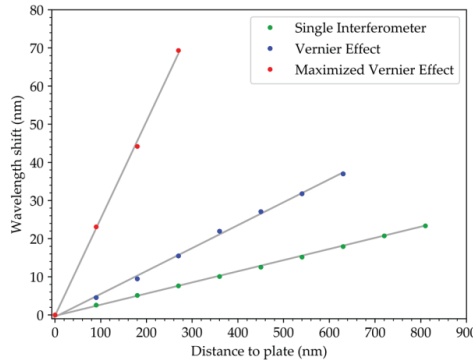

Figure 8. Wavelength shift for a single interferometer, the Vernier effect compared to single interferometer and the Vernier effect maximized. The error bars associated with each value are the same dimension as the geometry of the point that represents it.

Table 1. Parameters values that characterize the implementation of the enhanced Vernier effect maximized.

	Sensitivity	r^2	*FSR*
Envelope	254 ± 6 nm/µm	0.9990	75 nm
Carrier	0.160 ± 0.005 nm/µm	0.992	0.09 nm
***M*-factor**	M_{sens}	M_{FSR}	$M_{Vernier}$
1071	1587	833	1.9

4. Discussion

Figure 8 presents the comparison of the different sensitivities obtained in each case. As can be seen, the displacement sensitivity of the two interferometers with the Vernier effect (60 ± 1 nm/μm) is two-fold the one obtained with the single interferometer (29.2 ± 0.3 nm/ μm), with the same FSR. In addition, when the two interferometers are optimized, the maximum sensitivity obtained is 254 ± 6 nm/μm corresponding to an *M*-factor of 1071 and a $M_{Vernier}$ of 1.9. Therefore, the sensor using the enhanced Vernier effect was more efficient than the traditional Vernier effect besides the fact that the maximum sensitivity obtained was 24 times higher than the SPR-based sensor for a micrometric range [13]. Furthermore, the Vernier effect allows a sensor whose implementation is easier to be obtained because the performance depends on the relation between the interferometers and not on the specific length of each FPI. Thus, it is possible to develop giant sensitivities in ranges where the sensitivity of a single interferometer is low.

5. Conclusions

This research compares the sensitivity of a single FPI and the Vernier effect performed with two FPIs for the same number of fringes. The results reveal that the Vernier effect envelope, where 60 ± 1 nm/μm is achieved, has twice the sensitivity of the single FPI, 29.2 ± 0.3 nm/ μm. Moreover, with the optimization of the system, an envelope sensitivity of 254 ± 6 nm/μm with *M*-factor of 1071 and a $M_{Vernier}$ of 1.9 was obtained and corresponded to a resolution of 79 pm (considering the spectral resolution of 0.02 nm). In addition, the sensitivity of the Vernier effect envelope depends only on the relationship between interferometers, which allows problems in the production of ultra-sensitive sensors to be overcome as well as the same sensitivity for any distance of the fibers to the reflecting surface to be observed. This new displacement sensor architecture allows the implementation of giant-sensitive non evasive measurements with high relevance in areas such as micro and nano manufacturing and biology.

References

1. Kapany, N. Fiber optics. *Sci. Am.* **1960**, *203*, 72–81. [CrossRef]
2. M-Hernández, M.E.; Goicoechea, J.; Arregui, F.J. Hg^{2+} Optical Fiber Sensor Based on LSPR Generated by Gold Nanoparticles Embedded in LBL Nano-Assembled Coatings. *Sensors* **2019**, *19*, 4906. [CrossRef] [PubMed]
3. Maciak, E. Low-Coherence Interferometric Fiber Optic Sensor for Humidity Monitoring Based on Nafion® Thin Film. *Sensors* **2019**, *19*, 629. [CrossRef] [PubMed]
4. Alayli, Y.; Topçu, S.; Wang, D.; Dib, R.; Chassagne, L. Applications of a high accuracy optical fiber displacement sensor to vibrometry and profilometry. *Sens. Actuators A Phys.* **2004**, *116*, 85–90. [CrossRef]
5. Tabassum, S.; Wang, Y.; Qu, J.; Wang, Q.; Oren, S.; Weber, R.J.; Lu, M.; Kumar, R.; Dong, L. Patterning of Nanophotonic Structures at Optical Fiber Tip for Refractive Index Sensing. In Proceedings of the 2016 IEEE SENSORS, Orlando, FL, USA, 30 October–3 November 2016; p. 16597373. [CrossRef]
6. Costa, G.K.B.; Gouvêa, P.M.P.; Soares, L.M.B.; Pereira, J.M.B.; Favero, F.; Braga, A.M.B.; Palffy-Muhoray, P.; Bruno, A.C.; Carvalho, I.C.S. In-fiber Fabry-Perot interferometer for strain and magnetic field sensing. *Opt. Express* **2016**, *24*, 14690–14696. [CrossRef] [PubMed]

7. Hu, T.; Zhao, Y.; Song, A.-N. Fiber optic SPR sensor for refractive index and temperature measurement based on MMF-FBG-MMF structure. *Sens. Actuators B Chem.* **2016**, *237*, 521–525. [CrossRef]
8. Yao, T.; Pu, S.; Zhao, Y.; Li, Y. Ultrasensitive refractive index sensor based on parallel-connected dual Fabry-Perot interferometers with Vernier effect. *Sens. Actuators A Phys.* **2019**, *290*, 14–19. [CrossRef]
9. Liang, L.; Li, M.; Liu, N.; Sun, H.; Rong, Q.; Hu, M. A high-sensitivity optical fiber relative humidity sensor based on microsphere WGM resonator. *Opt. Fiber Technol.* **2018**, *45*, 415–418. [CrossRef]
10. Zhang, X.; Ren, L.; Wu, X.; Li, H.; Liu, L.; Xu, L. Coupled optofluidic ring laser for ultrahigh-sensitive sensing. *Opt. Express* **2011**, *19*, 22242–22247. [CrossRef] [PubMed]
11. Liu, Y.; Li, X.; Zhang, Y.-N.; Zhao, Y. Fiber-optic sensors based on Vernier effect. *Measurement* **2021**, *167*, 108451. [CrossRef]
12. Chen, J.; Zhou, J.; Yuan, X. M–Z Interferometer Constructed by Two S-Bend Fibers for Displacement and Force Measurements. *IEEE Photonics Technol. Lett.* **2014**, *26*, 837–840. [CrossRef]
13. Zhu, Z.; Liu, L.; Liu, Z.; Zhang, Y.; Zhang, Y. High-precision micro-displacement optical-fiber sensor based on surface plasmon resonance. *Opt. Lett.* **2017**, *42*, 10. [CrossRef] [PubMed]
14. Wang, X.-M.; Zhao, C.-L.; Wang, Y.-R.; Shen, C.-Y.; Dong, X.-Y. A Highly Sensitive Fibre-Optic Nano-Displacement Sensor Based on Surface Plasmon Resonance. *J. Light. Technol.* **2016**, *34*, 2324–2330. [CrossRef]
15. Robalinho, P.; Gomes, A.D.; Frazão, O. Colossal enhancement of strain sensitivity using the push-pull deformation method. *IEEE Sens. J.* **2020**, *1*. [CrossRef]
16. Gomes, A.D.; Ferreira, M.S.; Bierlich, J.; Kobelke, J.; Rothhardt, M.; Bartel, H.; Frazão, O. Optical Harmonic Vernier Effect: A New Tool for High Performance Interferometric Fiber Sensors. *Sensor* **2019**, *19*, 5431. [CrossRef] [PubMed]
17. Li, J.; Zhang, M.; Wan, M.; Lin, C.; Huang, S.; Liu, C.; He, Q.; Qiu, X.; Fang, X. Ultrasensitive refractive index sensor based on enhanced Vernier effect through cascaded fiber core-offset pairs. *Opt. Express* **2020**, *28*, 4145–4155. [CrossRef] [PubMed]
18. Robalinho, P.; Gomes, A.; Frazão, O. High Enhancement Strain Sensor Based on Vernier Effect Using 2-Fiber Loop Mirrors. *IEEE Photonics Technol. Lett.* **2020**, *32*, 1139–1142. [CrossRef]

Communication

Glycerol–Water Solution-Assisted Mach–Zehnder Temperature Sensor in Specialty Fiber with Two Cores and One Channel

Haiming Qiu [1,†], Chunyu Zhao [1,†], Xuehao Hu [1,2,*], Haijin Chen [1], Qianqing Yu [3], Zhenggang Lian [3] and Hang Qu [1,2]

[1] Research Center for Advanced Optics and Photoelectronics, Department of Physics, College of Science, Shantou University, Shantou 515063, China; 19hmqiu@stu.edu.cn (H.Q.); 19cyzhao@stu.edu.cn (C.Z.); 18hjchen1@stu.edu.cn (H.C.); haqux@stu.edu.cn (H.Q.)
[2] Key Laboratory of Intelligent Manufacturing Technology of MOE, Shantou University, Shantou 515063, China
[3] Yangtze Optical Electronics Co., Ltd., East Lake Hi-Tech Developzone, Wuhan 430205, China; yuqianqing@yoec.com.cn (Q.Y.); lianzhenggang@yoec.com.cn (Z.L.)
* Correspondence: xhhu3@stu.edu.cn
† The first two authors contributed equally to this paper.

Abstract: In this paper, we propose an in-fiber Mach–Zehnder temperature sensor based on a dual-core fiber with an eccentric core and a central core. The latter one is beside a fluidic channel embedded in the fiber. The effective refractive index of the guided mode in the central core could be influenced by the glycerol–water solution filled in the fluidic channel. Thus, the transmitted spectrum of the sensor is shifted as a function of temperature. By monitoring the selected spectral dip shifts, an experimental sensitivity of 2.77 nm/°C is obtained in the range of 25 to 40 °C for a solution length of 15 cm. To further improve the temperature sensitivity, the solution length is increased up to 29.5 cm, and a higher sensitivity of 5.69 nm/°C is achieved in the same temperature range. The experimental results agree well with the theoretical ones. The proposed sensor has good robustness and stability, which makes it promising for applications of high precision temperature monitoring.

Keywords: fiber optics sensors; dual-core fiber; interferometer; temperature sensing

1. Introduction

Optical fibers sensors (OFSs) have been extensively investigated and utilized for decades due to numerous advantages, such as high sensitivity, high compactness, corrosion resistance, anti-electromagnetic interference and remote monitoring. Based on these advantages, OFSs are popular for temperature, strain, refractive index, curvature and humidity measurements. In this paper, we focus on temperature sensing using OFSs, which have been realized by different types of structures and mechanisms, such as fiber Bragg gratings (FBGs) [1–4], long period gratings (LPGs) [5–8], Fabry–Perot (F-P) fiber interferometers [9–12] and Mach–Zehnder (M-Z) fiber interferometers [13–16], in the last 20 years. Fiber grating-based sensors normally operate by recording the variations of the resonance wavelength, which corresponds to thermally induced grating pitch and refractive index changes. Thus, grating-based OFSs normally have lower temperature sensitivities because of the relatively low thermo-optic coefficient and thermal expansion coefficient of the fiber material of silica. For example, Dong et al. produced an FBG in a D-shaped fiber with a temperature sensitivity of 28.7 pm/°C [1]. Hu et al. achieved a higher temperature of ~50 pm/°C by using poly(methyl methacrylate) (PMMA)-based polymer FBGs [4]. Han et al. obtained different temperature sensitivities of 130 pm/°C and 115 pm/°C based on LPGs in a standard single-mode fiber and in a single-mode double-clad fiber, respectively [5]. Theodosiou et al. first inscribed LPGs in a multi-mode cyclic transparent optical polymer (CYTOP) fiber using a femtosecond laser. The temperature sensitivity was found to be 704 pm/°C in the temperature range 42–67 °C [6]. Shu et al.

reported a simple fabrication of LPGs in the conventional B-Ge co-doped fiber with a high sensitivity of 2.75 nm/°C [7]. Colaço et al. produced an arc-induced LPG in the B-Ge co-doped fiber in the dispersion turning point. The highest refractive index sensitivity obtained was −720 nm/RIU in the 1.33–1.41 refractive index range. This technique may potentially be applied for temperature measurement [8]. We note that grating-based sensors usually had relatively low sensitivities, which were typically smaller than 1 nm/°C. Thus, these sensors are not quite suitable for high-precision temperature measurements.

Compared to fiber grating-based sensors, interferometric OFSs normally operate with fiber refractive index modulations as a function of temperature variations, consequently shifting the resonant wavelengths in transmitted spectra. For example, Wang et al. proposed a high temperature sensor based on an F-P fiber interferometer. A sapphire wafer served as an F-P cavity fixed at the end face of the sapphire fiber encapsulated in a sleeve to improve structural stability. It had a large temperature measurement range of 25–1550 °C with a sensitivity of 32.5 pm/°C at 1550 °C [9]. Li et al. proposed an F-P fiber interferometer composed of a microfiber, a single-mode fiber, a silica glass capillary, and polydimethylsiloxane (PDMS) sol. The experimental sensitivity reached up to 6.386 nm/°C in the range 42 to 54 °C [10]. Though high temperature sensitivity was obtained, fabrication of this sensor required a tricky cleaving process at the microfiber end and complicated integration procedures.

For M-Z fiber interferometers, the propagating light in the fiber is normally separated into two or more routes or coupled to different modes, and afterward the separated light from different routes or modes recombines to generate interferometric amplitude spectra, which shift as a function of temperature. Geng et al. fabricated an M-Z fiber interferometer consisting of two concatenated waist-enlarged fusion bitapers, which were fabricated simply by fiber cleaving and fusion splicing. The sensitivity was 0.070 nm/°C [13]. Also based on the taper method, Wang et al. sandwiched a thin core fiber between two single mode fibers to develop an M-Z fiber interferometer with a temperature sensitivity of 0.065 nm/°C. To improve the temperature sensitivity, Gao et al. reported a single-mode-capillary-single-mode prototype using the core offset splicing technique. After filling the refractive index matching liquid with a large thermo-optic coefficient, the sensitivity was improved to 21.2 nm/°C [14]. However, the mechanical strength of this sensor is quite low due to a small fusion splice area. Zhao et al. presented a single-mode-multi-core-single-mode structure M-Z fiber interferometer by simply using a fiber splicing technique. The temperature sensitivity was 0.131 nm/°C [15]. In addition, Ma et al. proposed a high-performance temperature sensor based on the mode-coupling principle using a selectively filled solid-core photonic crystal fiber with a central air-bore. A high sensitivity of −6.02 nm/°C was obtained with a resolution of 3.32×10^{-3} °C in the range from −80 to 90 °C [16].

In this paper, combining both advantages of the refractive index matching liquid and the multi-core fiber, we propose an M-Z fiber interferometer based on a dual-core fiber (DCF), in which one core is in the center of the fiber, while the other eccentric one locates between the central core and the cladding surface. Additionally, a fluidic channel is embedded in the fiber right beside the central core but far from the other core. Based on this structure, liquid analytes could infiltrate the fluidic channel along the entire fiber for different parameter sensing applications, such as refractive index, magnetic field and temperature. Their sensitivity could be enhanced simply by increasing the effective fiber length. Here, we propose to use this DCF as a sensing platform to record variations in environmental temperatures in real-time. A non-toxic glycerol–water solution with high thermo-optic coefficients is filled in the fluidic channel with different lengths. The concentration of the solution is optimized to be close to the fiber core to improve the temperature sensitivity. Because of the large distance between the two cores, two single-mode fiber (SMF) pigtails are fusion spliced to the DCF via multi-mode fibers (MMFs), so that the guided modes in the dual cores can be excited, and then the guided light could recombine in the outlet single-mode fiber. Afterward, temperature modulations change

the refractive index of the glycerol–water solution in the channel, consequently varying the effective refractive index of the guided mode in the central core. Thus, the transmitted spectra with resonances generated by interference shift as a function of the surrounding temperature. Spectral simulations with resonances versus temperatures are carried out using the Finite Element Method (FEM) method. Based on different fiber lengths (shorter fiber length: 20 cm with a solution length of 15 cm in the channel, longer fiber length: 36.5 cm with a solution length of 29.5 cm in the channel), the temperature measurements are characterized in the same range of 25–40 °C. For the shorter fiber, a linear fitting of spectral shift with respect to temperature suggests a sensitivity of 2.77 nm/°C, while for the longer counterpart, a sensitivity of 5.69 nm/°C is obtained. Both the experimental and simulation results in both sensors coincide well. The robustness sensor presented in this work can be fabricated easily without fiber tapering or a laser micromachining technique. The temperate sensitivity is fiber length dependent, and thus sensitivity can be further improved by filling more glycerol–water solution in the fiber channel. Moreover, the whole fiber sensor device can be coiled with high compactness.

2. Fabrication of DCF

Firstly, a high-purity silica glass rod (HPSGR) with a diameter of 50 mm was needed, and then two holes ~3.1 mm in diameter were drilled in the middle and 1/4 diameter positions of this HPSGR. Secondly, two core rods with a diameter of 3 mm obtained by doping germanium in silica were inserted into the two drilled holes, and then they were fused together by a collapse process with oxyhydrogen flame. Thirdly, a hole 12 mm in diameter was drilled on the other side of the central hole, so that the hole and the two cores were in the same line, and the edge distance between the hole and the central core is 1 mm. Finally, the DCF with a cladding diameter of ~125 μm was drawn by a commercial fiber drawing tower at Yangtze Optical Electronics, Co. Ltd. The schematic of the fiber manufacturing process is shown in Figure 1. The diameters of the central core, the eccentric core and the hole are ~8.1, ~9.2, and ~36 μm, respectively. The center-to-center distance between the central core and the eccentric core is 30 μm, and the edge distance between the central core and the hole is 1.15 μm.
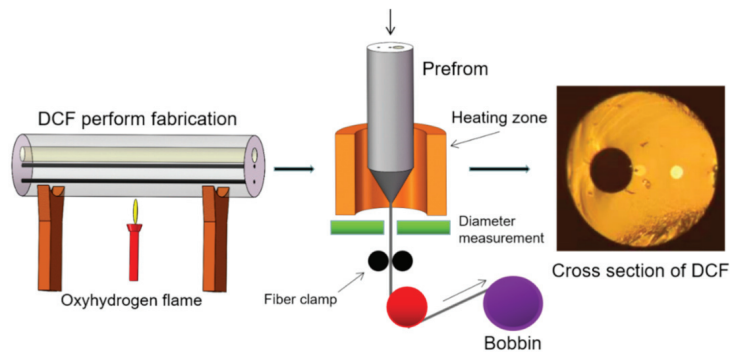
Figure 1. Schematic of the fabrication process of the dual-core fiber (DCF).

3. Operation Principle of the Sensor

The mechanism of the M-Z fiber interferometer sensor based on a DCF can be explained as follows. When the coherent laser beam is coupled to the two cores, guided modes in both cores are excited and propagate independently. Then, light from two cores is recombined in the single-mode fiber to generate interference transmitted spectra. Temperature-induced variations in the effective refractive index of the center-core modes

change the phase difference among the modes guided by the two cores. The output spectral intensity of the transmitted light I_{output} can be expressed as:

$$I_{output} = I_{cc} + I_{ec} + 2\sqrt{I_{cc}I_{ec}} \cos(\Delta\varphi), \tag{1}$$

where I_{cc} and I_{ec} represent the intensities of the transmitted beams from the center core and the eccentric one, respectively, and $\Delta\varphi$ represents the phase difference between the two propagating beams in both cores, and is expressed as:

$$\Delta\varphi = \frac{2\pi\left(L_{air}\Delta n_{air}^{eff} + L_{solution}\Delta n_{solution}^{eff}\right)}{\lambda}, \tag{2}$$

where λ is the operating wavelength in vacuum, and L_{air} and $L_{solution}$ are the length of the DCF channel filled with air and glycerol–water solution, respectively. $\Delta n_{air}^{eff} = n_{air,cc}^{eff} - n_{air,ec}^{eff}$ represents the effective refractive index difference between modes propagating in the center core and in the eccentric core for the DCF section without glycerol–water solution filled in the channel, while $\Delta n_{solution}^{eff} = n_{solution,cc}^{eff} - n_{solution,ec}^{eff}$ is the counterpart for the DCF section filled with glycerol–water solution. On the basis of Equations (1) and (2), the transmitted spectra of the sensor denote periodical intensity modulations, and the central wavelength λ_m of the m-order interference dip can be defined as:

$$\lambda_m = \frac{2(L_{air}\Delta n_{air}^{eff} + L_{solution}\Delta n_{solution}^{eff})}{2m+1}, \tag{3}$$

where m is an integer. The central wavelength is a function of effective refractive index and fiber lengths with and without glycerol–water solution. The latter is influenced by surrounding temperatures. The thermo-optic coefficients of water and pure glycerol are $-1.5 \times 10^{-4}/°C$ and $-2.3 \times 10^{-4}/°C$, respectively [17], with an estimated average value of $-2.2 \times 10^{-4}/°C$ according to the composition of glycerol–water solution (glycerol mass fraction 85.9%, refractive index 1.45 @ 589 nm) used in this work. However, the counterparts of silica and air are $9.2 \times 10^{-6}/°C$ [18] and $-9.8 \times 10^{-7}/°C$ [19], respectively, which are much smaller. Thus, temperature-induced refractive index changes for $\Delta n_{air,cc}^{eff}$ $\Delta n_{air,ec}^{eff}$ and $\Delta n_{solution,ec}^{eff}$ can be omitted, and when surrounding temperature changes, the refractive index of the glycerol–water solution varies, which dominantly affects the effective refractive index $\Delta n_{solution,cc}^{eff}$ of the modes propagating in the central core beside the solution because the guided mode in the core has partial modal overlap with the solution. Oppositely, the effective indices of the modes in the eccentric core and in the central core without the surrounding solution cannot be influenced due to a non-existent of modal overlap. As a result, temperature variations induce an effective refractive index change for the central core beside the solution $\Delta n_{solution,cc}^{eff}$ and further result in the shifts of the spectral dips, which is the main mechanism for this presented M-Z fiber interference sensor. According to Equation (3), the temperature sensitivity can be deduced as follows:

$$S = \frac{d\lambda_m}{dT} \approx \frac{2L_{solution}}{2m+1} \cdot \frac{d\left(\Delta n_{solution}^{eff}\right)}{dT} \approx \frac{2L_{solution}}{2m+1} \cdot \frac{dn_{solution,cc}^{eff}}{dT}. \tag{4}$$

According to the classic perturbation theory [20], changes of effective refractive index of the guided mode in the central core are related to surrounding temperature variations, expressed as:

$$\delta n_{solution,cc}^{eff} \approx f \cdot \delta n_{solution} = f \cdot \alpha \cdot \delta T, \tag{5}$$

where α is the thermo-optic coefficient of the glycerol–water solution; f is power overlap factor of the central core modes in the solution, which is expressed as:

$$f = \frac{\iint_{solution} Re(E_x H_y^* - E_y H_x^*) dxdy}{\iint_{total} Re(E_x H_y^* - E_y H_x^*) dxdy},$$ (6)

where $E_{x/y}$ and $H_{x/y}$ refer to the electric and magnetic field in two orthodox directions in the fiber cross-sectional plane. According to Equations (4)–(6), the sensitivity of this sensor can be enhanced by increasing the length of the liquid filled in the fiber channel and the thermo-optic coefficient of the solution and reducing the refractive index difference between the solution and the central core in order to enhance the factor f. Therefore, we choose the glycerol–water solution as a thermally sensitive liquid filled in the fiber channel mainly for two reasons. First, it has a relatively high thermo-optic coefficient. Second, it has a measured refractive index of 1.45, which is close to yet somehow smaller than that of the fiber core, which ensures a high f factor. According to Equation (3), the free spectrum range (FSR) can be defined as:

$$FSR = |\lambda_{m+1} - \lambda_m| \approx \left| \frac{\lambda_m^2}{(L_{air} \Delta n_{air}^{eff} + L_{solution} \Delta n_{solution}^{eff})} \right|.$$ (7)

4. Experimental and Numerical Results

To fabricate this temperature sensor, an SMF pigtail with a core and cladding diameter of 8.2 and 125 mm, respectively, was first spliced with a short piece of MMF, which has a core and cladding diameter of 105 and 125 mm, respectively, using a fusion splicer (FSM-100M, Fujikura). Meanwhile, the prepared glycerol–water solution was infiltrated into the fluidic channel of the DCF by capillary effect. The effective sensing length of the DCF corresponds to the length of the glycerol–water solution in the fiber channel, which was confirmed by observing the solution–air interface in the fluidic channel using an optical microscope, as was shown in Figure 2a. Then, the end of the DCF filled with the solution was hung vertically so that the solution was moved to the center of the DCF along the fiber channel by gravity to avoid any negative influence on the DCF–MMF connectorization in the following fusion splice process. Due to the existence of the MMF with an optimized length of ~1 cm between the SMF and the DCF, the SMF–MMF–DCF structure enables the light to be coupled into the dual cores. In order to verify the propagating modes in the cores, a supercontinuum light source in the range 480–2200 nm (YSL Photonics, SC-5-FC) was launched to the SMF pigtail of the SMF–MMF–DCF structure, and then the output end-face of the DCF was visualized by using a $20\times$ objective and an infrared camera (Ghopto, GH-SWU2), as shown in Figure 2b. We found that LP_{01} modes were excited and thus propagated in the central core and in the eccentric core, respectively. After the mode verification, the other end of the DCF was fusion spliced to another MMF–SMF structure. Finally, the whole sensor structure SMF–MMF–DCF–MMF–SMF was built (Figure 3) without any air gap in the middle of the liquid filled in the channel and then twined with a diameter of 3 cm to form a compact sensing device. An optical spectral analyzer (OSA) (Anritsu MS9740A) was used to record the spectrum evolution with respect to temperature. The temperature characterization in the range (25−40 °C) was conducted with an interval of 1 °C. The twined fiber was stuck to the surface of a temperature-controlled breadboard (Thorlabs, PTC1, 15−45 °C) tightly by tapes. The temperature stability of this temperature-controlled breadboard is 0.1 °C, and the temperature readout resolution is $\pm$ 0.001 °C.

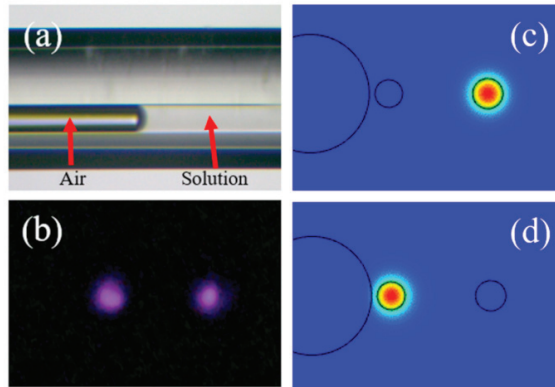**Figure 2.** (**a**) Interface between the glycerol–water solution and the air in the channel of the DCF; (**b**) Guided modes of DCF experimentally visualized by an infrared camera; (**c**) LP$_{01}$ mode simulation in the eccentric core in the solution-filled DCF; (**d**) LP$_{01}$ mode simulation in the central core in the solution-filled DCF.
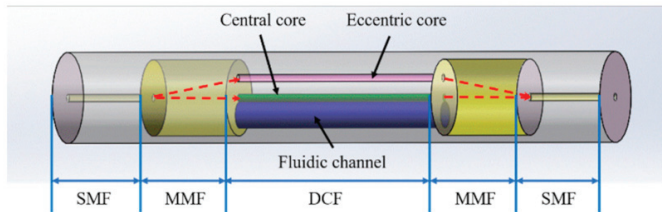

Figure 3. Schematic illustration of the SMF–MMF–DCF–MMF–SMF structure of the temperature sensor. SMF—single-mode fiber, MMF—multi-mode fiber.

For the shorter fiber, the transmitted spectrum of this sensor shows a red shift as the temperature increases. With the initial temperature of 25 °C, the spectral dip at ~1628 nm was selected and then traced for temperature measurement, as shown in Figure 4a. Besides the selected dip, the maximal extinction ratio of each spectrum and the FSR were measured to be ~9 dB and ~22 nm, respectively. The quasi-linear dip evolution versus temperature was shown in Figure 4b. The experimental sensitivity of the sensor was calculated to be 2.77 $\pm$ 0.08 nm/°C. The nonlinear effect showing lower temperature sensitivity at higher temperature is attributed to the decreasing f factor, as the refractive index difference between the liquid and the central core increases, when temperature rises. It is worth mentioning that a more economical broad-band source (BBS) at the C+L band can be used instead of the supercontinuum used in this work, if we follow spectral resonance dips within the C+L band.

We used Comsol 5.0 to numerically simulate the guided modes in the DCF. Considering material dispersion at the spectrum range, the refractive index of the Ge-doped cores was set as 1.4485 [21], while the index of silica cladding is 0.006 lower. The refractive index of the glycerol–water solution was set to 1.439 [22]. The effective refractive index of the LP$_{01}$ mode, $n^{eff}_{solution,ec}$ in the eccentric core in the solution-filled DCF segment is ~1.4455 (Figure 2c), while the effective index of the LP$_{01}$ mode, $n^{eff}_{solution,cc}$, in the central core of the same segment is ~1.4450 (Figure 2d). The effective refractive index of the LP$_{01}$ mode, $n^{eff}_{air,ec}$, in the eccentric core in the air-filled DCF segment is ~1.4455, while the effective refractive index of the LP$_{01}$ mode, $n^{eff}_{air,cc}$, is ~1.4448 in the central core of the same segment. According to Equation (7), the FSR was calculated to be ~22 nm with, $L_{air} = 5 \, cm$,

$L_{solution} = 15\ cm$. The simulated result matches well with the experimental counterpart. Based on these parameters and Equation (3), the integer m was calculated to be -75 for the spectral dip at ~1632 nm. Furthermore, considering the thermo-optic coefficient of the glycerol–water solution ($-2.2 \times 10^{-4}/°C$) and silica ($9.2 \times 10^{-6}/°C$), we could simulate the effective refractive index of each mode with different temperatures, and then calculate the corresponding shifts of the selected spectral dip at ~1632 nm with the same m value of -75. The simulated spectral dip shift as a function of temperature and its linear fit is shown in Figure 4b with a temperature sensitivity of 2.93 ± 0.05 nm/°C. The spectral evolution and the sensitivity are similar to the experimental results.

Figure 4. (**a**) Partial transmitted spectrum evolution of the sensor measured in the temperature range of 25 to 29 °C. The length of the infiltrated glycerol–water solution is 15 cm; (**b**) experimental and simulated wavelength shift of the spectral dip at ~1628 nm as a function of temperature in the range of 25 to 40 °C.

To further improve the temperature sensitivity, the length of the DCF channel filled with the glycerol–water solution was increased to 29.5 cm with a total DCF length of 36.5 cm. The sensor structure is the same as that of the shorter one. The transmitted spectra of the sensor were measured in the temperature range of 25−40 °C with a temperature interval of 1 °C, as shown in Figure 5a.
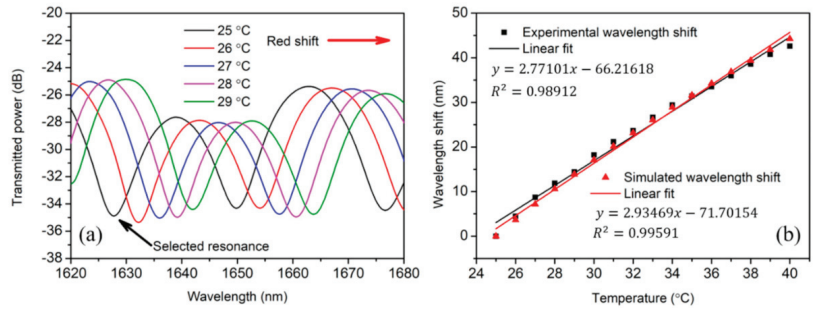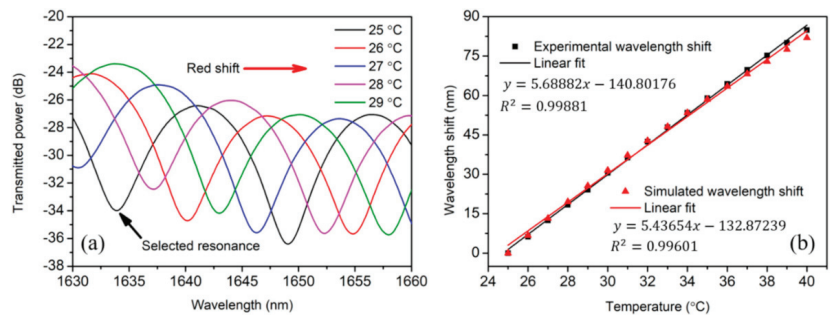

Figure 5. (**a**) Partial transmitted spectrum evolution of the sensor measured in the temperature range of 25 to 29 °C. The length of the infiltrated glycerol–water solution is 29.5 cm; (**b**) experimental and simulated wavelength shift of the spectral dip at ~1634 nm as a function of temperature in the range of 25 to 40 °C.

The maximum extinction ratio of each spectrum was measured to be ~10 dB, and the FSR was ~15 nm. The transmitted spectrum of the sensor also shows a red shift as the temperature increases. By following the initial spectral dip shift at ~1634 nm, an experimental sensitivity of 5.69 ± 0.05 nm/°C was obtained, as shown in Figure 5b. By using the similar effective refractive indices ($n_{solution,ec}^{eff}$, $n_{solution,cc}^{eff}$, $n_{air,ec}^{eff}$, $n_{air,cc}^{eff}$) of the

guided modes as the former ones, we calculated the FSR to be ~15 nm, which also coincides well with the experimental result. Moreover, the integer $m = -113$ for the selected spectral resonance at ~1638 nm was obtained. Then, the effective refractive index of the guided modes at different temperatures was calculated, and the calculated variations of the selected spectral dip at ~1638 nm with a linear fit were also shown in Figure 5b. The simulated temperature sensitivity was calculated to be 5.44 ± 0.09 nm/°C, also similar to the experimental result.

5. Conclusions

In conclusion, we proposed an in-fiber Mach–Zehnder temperature sensor with a structure of SMF–MMF–DCF–MMF–SMF. The sensor operating principle is based on the interference of the two propagating modes in the dual cores. The eccentric core serves as a reference arm, while the central core adjacent to the fluidic channel filled with glycerol–water solution works as a sensing arm. Thus, the interfered transmitted spectrum of the sensor shifts as a function of temperature. Both experiments and numerical simulations were carried out to characterize the temperature sensor. For the 20-cm-long DCF infiltrated with 15-cm-long glycerol–water solution, the experimental sensitivity of 2.77 nm/°C was obtained in the range of 25 to 40 °C. For the 36.5-cm-long DCF infiltrated with 29.5-cm-long solution, a higher sensitivity of 5.69 nm/°C was achieved in the range of 25 to 40 °C. The experimental results coincided well with the simulated counterparts. The proposed sensor has good robustness and stability. We believe that this sensing regime may be potentially used for high precision temperature measurements as well as detection of other parameters, such as liquid or gas refractive index or magnetic field, thanks to the presence of the fluidic channel.

References

1. Dong, Y.; Xiao, S.; Wu, B.; Xiao, H.; Jian, S. Refractive index and temperature sensor based on D-Shaped fiber combined with a fiber Bragg grating. *IEEE Sens. J.* **2019**, *19*, 1362–1367. [CrossRef]
2. Hirayama, N.; Sano, Y. Fiber Bragg grating temperature sensor for practical use. *ISA Trans.* **2000**, *39*, 169–173. [CrossRef]
3. Zhang, B.; Kahrizi, M. High-temperature resistance fiber Bragg grating temperature sensor fabrication. *IEEE Sens. J.* **2007**, *7*, 586–591. [CrossRef]
4. Hu, X.; Pun, C.F.J.; Tam, H.Y.; Mégret, P.; Caucheteur, C. Highly reflective Bragg gratings in slightly etched step-index polymer optical fiber. *Opt. Express* **2014**, *22*, 18807–18817. [CrossRef]
5. Qu, H.; Lan, X.; Huang, J.; Kaur, A.; Wei, T.; Gao, Z.; Xiao, H. Long-period grating inscribed on concatenated double-clad and single-clad fiber for simultaneous measurement of temperature and refractive index. *IEEE Photon. Technol. Lett.* **2012**, *24*, 1130–1132.
6. Theodosiou, A.; Min, R.; Leal-Junior, A.; Ioannou, A.; Frizera, A.; Pontes, M.; Marques, C.; Kalli, K. Long period grating in a multimode cyclic transparent optical polymer fiber inscribed using a femtosecond laser. *Opt. Lett.* **2019**, *44*, 5346–5349. [CrossRef]

7. Shu, X.; Allsop, T.; Gwandu, B.; Zhang, L.; Bennion, I. High-temperature sensitivity of long-period gratings in B-Ge codoped fiber. *IEEE Photon. Technol. Lett.* **2001**, *13*, 818–820.
8. Colaço, C.; Caldas, P.; Villar, I.D.; Chibante, R.; Rego, G. Arc-induced long-period fiber gratings in the dispersion turning points. *J. Light. Technol.* **2016**, *34*, 4584–4590. [CrossRef]
9. Wang, B.; Niu, Y.; Zheng, S.; Yin, Y.; Ding, M. A High temperature sensor based on sapphire fiber Fabry-Perot interferometer. *IEEE Photonics Technol. Lett.* **2020**, *32*, 89–92. [CrossRef]
10. Li, J.; Li, Z.; Yang, J.; Zhang, Y.; Ren, C. Microfiber Fabry-Perot interferometer used as a temperature sensor and an optical modulator. *Opt. Laser. Technol.* **2020**, *129*, 106296. [CrossRef]
11. Zhao, L.; Zhang, Y.; Chen, Y.; Wang, J. Composite cavity fiber tip Fabry-Perot interferometer for high temperature sensing. *Opt. Fiber Technol.* **2019**, *50*, 31–35. [CrossRef]
12. Domínguez-Flores, C.E.; Monzón-Hernández, D.; Moreno-Basulto, J.I.; Rodríguez-Quiroz, O.; Minkovich, V.P.; López-Cortés, D.; Hernández-Romano, I. Real-time temperature sensor based on in-fiber Fabry–Perot interferometer embedded in a resin. *J. Light. Technol.* **2019**, *37*, 1084–1090. [CrossRef]
13. Geng, Y.; Li, X.; Tan, X.; Deng, Y.; Yu, Y. High-sensitivity Mach–Zehnder interferometric temperature fiber sensor based on a waist-enlarged fusion bitaper. *IEEE Sens. J.* **2011**, *11*, 2891–2894. [CrossRef]
14. Gao, S.; Ji, C.; Ning, Q.; Chen, W.; Li, J. High-sensitive Mach-Zehnder interferometric temperature fiber-optic sensor based on core-offset splicing technique. *Opt. Fiber Technol.* **2020**, *56*, 102202. [CrossRef]
15. Zhao, Z.; Tang, M.; Fu, S.; Liu, S.; Wei, H.; Cheng, Y.; Tong, W.; Shum, P.P.; Liu, D. All-solid multi-core fiber-based multipath Mach–Zehnder interferometer for temperature sensing. *Appl. Phys. B* **2013**, *112*, 491–497. [CrossRef]
16. Ma, J.; Yu, H.H.; Jiang, X.; Jiang, D.S. High-performance temperature sensing using a selectively filled solid-core photonic crystal fiber with a central air-bore. *Opt. Express* **2017**, *25*, 9406–9415. [CrossRef]
17. Cao, Z.; Jiang, L.; Wang, S.; Wang, M.; Liu, D.; Wang, P.; Zhang, F.; Lu, Y. All-glass extrinsic Fabry–Perot interferometer thermo-optic coefficient sensor based on a capillary bridged two fiber ends. *Appl. Opt.* **2015**, *54*, 2371–2375. [CrossRef]
18. Chang, S.; Hsu, C.C.; Huang, T.H.; Chuang, W.C.; Tsai, Y.S.; Shieh, J.Y.; Leung, C.Y. Heterodyne interferometric measurement of the thermo-optic coefficient of single mode fiber. *Chin. J. Phys.* **2000**, *38*, 437–442.
19. Bauld, R.; Choi, D.Y.W.; Bazylewski, P.; Divigalpitiya, R.; Fanchini, G. Thermo-optical characterization and thermal properties of graphene–polymer composites: A review. *J. Mater. Chem. C* **2017**, *6*, 2901–2904. [CrossRef]
20. Qu, H.; Skorobogatiy, M. Resonant bio- and chemical sensors using low-refractive-index-contrast liquid-core Bragg fibers. *Sens. Actuators B Chem.* **2012**, *161*, 261–268. [CrossRef]
21. Rodney, W.S.; Spindler, R.J. Index of refraction of fused quartz glass for ultraviolet, visible, and infrared wavelengths. *J. Opt. Soc. Am.* **1954**, *44*, 677–679. [CrossRef]
22. Rheims, J.; Köser, J.; Wriedt, T. Refractive-index measurements in the near-IR using an Abbe refractometer. *Meas. Sci. Technol.* **1997**, *8*, 601–605. [CrossRef]

Akinetic Swept-Source Master–Slave-Enhanced Optical Coherence Tomography

Manuel J. Marques [1,*], Ramona Cernat [1], Jason Ensher [2], Adrian Bradu [1] and Adrian Podoleanu [1]

[1]   Applied Optics Group, Division of Natural Sciences, School of Physical Sciences, University of Kent, Canterbury CT2 7NH, UK; R.Cernat@kent.ac.uk (R.C.); A.Bradu@kent.ac.uk (A.B.); ap11@kent.ac.uk (A.P.)

[2]   Insight Photonic Solutions, Inc., 2650 Crescent Drive, Ste. 201, Lafayette, CO 80026, USA; jensher@sweptlaser.com

[*]   Correspondence: M.J.Marques@kent.ac.uk; Tel.: +44-1227-823772

Abstract: This paper presents a different approach for processing the signal from interferometers driven by swept sources that exhibit non-linear tuning during stable time intervals. Such sources are, for example, those commercialised by Insight, which are electrically tunable and akinetic. These Insight sources use a calibration procedure to skip frequencies already included in a spectral sweep, i.e., a process of "clearing the spectrum". For the first time, the suitability of the Master–Slave (MS) procedure is evaluated as an alternative to the conventional calibration procedure for such sources. Here, the MS process is applied to the intact, raw interferogram spectrum delivered by an optical coherence tomography (OCT) system. Two modalities are investigated to implement the MS processing, based on (i) digital generation of the Master signals using the OCT interferometer and (ii) down-conversion using a second interferometer driven by the same swept source. The latter allows near-coherence-limited operation at a large axial range (>80 mm), without the need for a high sampling rate digitiser card to cope with the large frequency spectrum generated, which can exceed several GHz. In both cases, the depth information is recovered with some limitations as described in the text.

Keywords: optical coherence tomography; low-coherence interferometry; large-scale imaging

1. Introduction

Optical Coherence Tomography (OCT) is an established, non-invasive imaging modality, which uses low-coherence interferometry to obtain three-dimensional representations of translucent media. Having made its debut in ophthalmology, OCT is now widely used across many different medical imaging fields as well as for non-destructive testing [1]. OCT imaging can be achieved with both time- and frequency-domain detection, with the latter presenting significant improvements in imaging speed and noise performance over the former [2]. Frequency-domain detection in OCT can be implemented by either (a) sampling the output optical spectrum of the OCT interferometer driven by a broadband source using a spectrometer (spectral-domain OCT) or (b) sweeping a narrow frequency emission tuned within a wide spectral band and measuring the signal with a point photo-detector (swept source OCT).

One of the main strengths of swept-source OCT is the larger axial imaging range than can be found in spectral-domain OCT systems, enabled by the long instantaneous coherence length of the swept source. Recently reported swept-source implementations [3,4] demonstrated coherence lengths on the order of meters. However, swept-source OCT still lags behind spectral-domain OCT with respect to phase stability. Electrically tunable, all-semiconductor optical sources, such as the monolithic cavity one developed by Insight (Lafayette, CO, USA) employed in this work, are akinetic by nature, making them less prone to phase instabilities [5], while achieving long instantaneous coherence lengths (over 200 mm). Moreover, their tuning rate and tuning range can easily be reconfigured by

93

electronically changing the driving signal, allowing extra flexibility and high sweeping rates (over 600 kHz), meaning that the source has been successfully used in a number of previous studies [5–8].

The electrical tuning procedure employed by the swept source employed in this study is based on Vernier tuning of multiple sections within an all-semiconductor laser structure. Using this tuning mechanism, the laser may be swept over a wide wavelength range in a single longitudinal laser mode, with a linear sweep of optical frequency versus time within valid regions of the sweep. Although this procedure has its benefits, there are short (<10 ns), sporadic periods during the sweep where the optical frequency is not swept linearly as shown in Figure 1, corresponding to invalid data regions. These time periods repeat deterministically and therefore can be identified during the calibration routine prepared for each source and subsequentially eliminated. The laser generates a data-valid vector (DVV), which specifies the samples of the time-record that are valid, while the invalid data (which may account for 25% of the total samples in a 100 kHz spectral sweep) are removed from the output interferogram prior to the depth profile (A-scan) generation. An advantage of the akinetic source is that the valid data are already *k*-space linearised, meaning that once the invalid data are removed, no further k-space resampling or optical *k*-clock is needed prior to data processing. However, the removal procedure requires (i) a strict synchronous clock (provided by the control electronics in the optical source) and (ii) robust communication between the source and the digitising hardware to transfer the DVV after each source self-calibration.
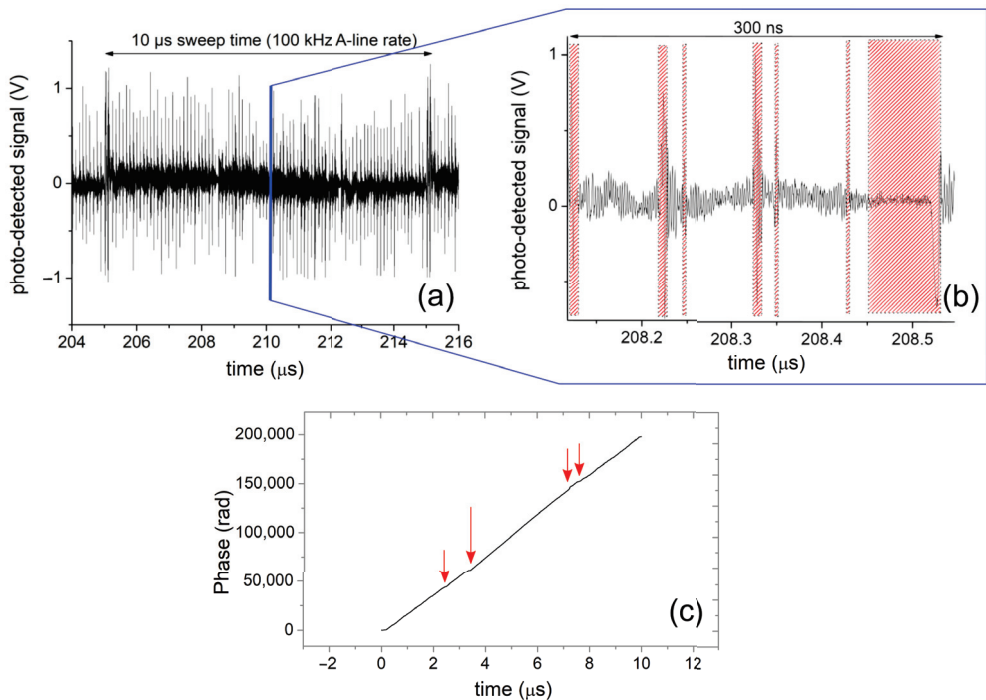
Figure 1. (**a**) Channelled spectrum as acquired from the photo-detector in the OCT system with the optical source used in this study. (**b**) Zoomed version of (**a**), with the shaded regions denoting the portions of time when the optical frequency is not swept linearly, which are invalid and therefore removed based on the information carried by the data valid vector. (**c**) Phase of the interferogram (trimmed to one cycle) represented in (**a**), showing discontinuities (red arrows) pertaining to the portions of time when the optical frequency is not swept linearly.

Master–Slave OCT [9] (MS–OCT) processes the raw OCT data differently. Instead of employing a Fast-Fourier Transform (FFT), MS–OCT performs a comparison of the raw OCT data against either: (i) pre-recorded (or pre-generated) spectra for all axial positions considered [10] or (ii) against "live" spectra provided in real-time by a several optical interferometers using the down-conversion Master–Slave procedure [11] detailed below. Effectively, MS–OCT implements a "calibration" of the system that makes the whole operation tolerant to both the non-linear sweeping [9] as well as to the dispersion left uncompensated in the interferometer [12], enabling swept-source operation without a *k*-clock [13]. The Vernier tuning enables linear frequency sweeping in time; however, within the sweep there are short, deterministically located regions where the tuning is not linear with the optical frequency. This represents a different set of challenges from those tackled by the MS-based methods in the literature, hence the subject of this paper.

One aspect that is common to all SS-OCT implementations is that the resulting interferometric signal needs to be digitised in order to be processed and the resulting OCT volume rendered. In SS-OCT, the desire or need to image at greater depths demands a larger coherence length for the swept source. The larger the axial range, the higher the sampling rates of the data acquisition system, which drives up costs and electrical power consumption. Furthermore, if the frequency exceeds several GHz, the dynamic range suffers as the available digitizer bit depths for higher sampling rates are 8–10 bit only.

Beyond employing high-speed digitizer cards, other approaches have been reported, such as circular ranging by Siddiqui et al. [14] (the same method improved by Lippok and Vakoc in 2020 [15]) and Chun et al. [16]. This method takes advantage of the aliasing intervals to "unfold" the imaging domain whilst maintaining a lower sampling rate. While this method is advantageous in terms of obtaining a single-shot depth profile, it relies on having single surfaces with no multiple interfaces across the entire "unfolded" imaging range.

Recently, Podoleanu et al. [11] have reported a novel variant of MS–OCT processing, where unlike in the previous MS–OCT paper, the Master and Slave interferometers are two separate physical entities. The comparison operation between the signals returned by them is carried out by using an analogue broadband mixer, prior to digitisation, to mix the signals. The resulting signal is effectively down-converted to frequencies within the order of magnitude of the sweep frequency, enabling the use of lower-speed digitiser cards to acquire the signal and carry out the remainder of operations (signal conditioning and image rendering) digitally.

In this communication, the suitability of MS–OCT is investigated for processing the signal delivered by an OCT interferometer when driven by an electrically tunable, akinetic swept source presenting non-linearities throughout the sweep. In a short preliminary study [17], a demonstration was performed of two of the possibilities of using the MS methods. Here, we expand to more modalities, as presented, and document details of procedures, calibrations, and results, compared with conventional modalities in terms of axial resolution and axial range.

If MS–OCT is proven suitable as a processing method, then a Vernier tuning principle could be used in a simpler manner: there would be no need for a DVV-based correction and, ultimately, no need for an external clock (synchronous with the optical source), thus somewhat simplifying the overall system. Unlike earlier studies with the MS–OCT method, here we compare against a "Master" mask that contains a few non-linearly tuned intervals in the spectrum, which are otherwise eliminated by the DVV calibration. When using the MS–OCT procedure, the entire photo-detected signal is compared against itself; i.e., the signal contains the intervals otherwise eliminated by the DVV correction. We also evaluate the use of the down-conversion OCT method [11], which would bypass the need for both DVV correction (including the synchronous clock) and a high-speed digitiser card to cope with the large frequency of the photo-detected signal. Due to the comparison of spectra that is fundamental to MS–OCT, some tolerance to distorted spectral behaviour should also be expected.

2. Materials and Methods

Throughout this study, an optical source from Insight (model SLE-101) [18], with a sweep rate of 100 kHz and the maximum tuning range setting (roughly 90 nm), centred at $\lambda_0 = 1.31\,\mu m$, is employed.

At the sample clock frequency setting used (400 MHz), a maximum of 4000 sampling points are enabled at a source sweep duty cycle of 100%. Due to the presence of the invalid regions in the tuned spectrum, the DVV returns useful data within a duty cycle of 70% only. During this study, two separate interferometric setups were employed, which are schematically represented in Figure 2a,b.
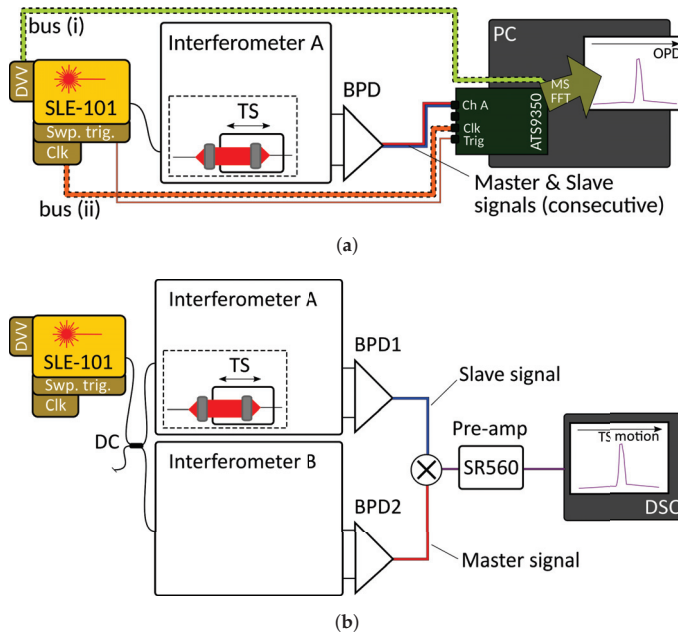
Figure 2. Schematic diagrams of the two interferometric configurations used with the electrically tunable akinetic optical source throughout this study. (**a**) Single interferometer configuration, illuminated by the Insight akinetic source SLE-101, driving a balanced photo-detector BPD. (**b**) Dual interferometer configuration to implement the down-conversion MS–OCT method.

In the first case, as shown in Figure 2a, MS–OCT processing is explored in a single interferometer configuration with a recirculating reference path, following the procedures described by Rivet et al. [10]. Bus (i) carries the DVV produced during the source's self-calibration, and bus (ii) synchronises the acquisition clock from the digitiser board (ATS9350) with that of the optical source. As shown by the large green arrow in Figure 2a, Master–Slave (MS) or FFT processing can be implemented on the PC. An electronically adjustable translation stage TS (Newport M-VP-25XA) is used to vary the optical path difference (OPD) in the reference arm. The resulting interferometric signal is detected by a balanced photo-detector unit (Insight BPD-1, cut-off frequency 400 MHz) and digitised using an AlazarTech ATS9350 board (12-bit digitisation bit depth, maximum sampling rate 500 MS/s). For the digitisation procedure, it is possible to use the clock signal provided by the optical source (represented as bus (ii) in Figure 2a), or the built-in hardware clock from the AlazarTech digitiser card (asynchronous clock operation). The DVV correction (bus (i)) is only possible with synchronous clock operation.

In the second case, schematically represented in Figure 2b, the down-conversion OCT (DC-OCT) Master–Slave method [11] was employed on a long axial range (>100 mm)-swept source-based system. To achieve this goal, an additional optical interferometer, Interferometer B (Master) was set up with the same optical path difference as Interferometer A presented above (Slave), both having 80 mm of SMF-28e fibre in their reference arms, which introduces an optical path difference of ≈120 mm; these two interferometers were both fed by the Insight source using a 60/40 fused fibre-based directional coupler DC, as depicted in Figure 2b. The outputs of each interferometer are photo-detected by balanced photo-detectors BPD1 (Insight BPD-1) and BPD2 (Thorlabs model PDB481C, AC-coupled, bandwidth 30 kHz–1 GHz). The resulting electrical signals from either photo-detector are high-pass-filtered (Thorlabs, model EF513, 6.7 MHz cutoff frequency, not shown in diagram) and directed to a RF frequency mixer, shown as a circled X in the diagram in Figure 2b (Minicircuits, model ZFM-4, operating bandwidth 5–1250 MHz). Its output is first low-pass filtered and amplified (Stanford Research low-noise pre-amplifier, model SR560) and then displayed by a digital storage oscilloscope, DSO (LeCroy model LC534A), running at a sample rate of ∼25 kS/s. To produce an A-scan in this case, the OPD of Interferometer A is varied whilst the DSO reads the filtered output of the pre-amplifier and displays it against time on its screen.

At this very large OPD of ≈120 mm, the frequency of the photo-detected signal exceeds 600 MHz. The Nyquist limit of the digitiser board used earlier in the study is 250 MHz (if working with the asynchronous clock of the digitiser board), therefore, the board is not able to sample the resulting interferogram.

2.1. Channelled Spectrum Processing for MS–OCT

To evaluate MS–OCT processing in a single interferometer configuration (Figure 2a), the procedure demonstrated in Rivet et al. [10] is employed, allowing masks to be synthesised from a small set of experimentally acquired channelled spectra. This procedure is schematically represented in Figure 3a. Briefly, during the Master step, a small number of channelled spectra are acquired for several OPD settings and used to infer a pair of system model calibration functions (g and h). These two functions can then be used to render an arbitrary number of complex-valued Master signals, which are then compared against the real-valued channeled spectra acquired during the Slave step, finally generating the full A-scan profile.

While the procedure was successfully validated when the interferograms were DVV-corrected (as one would normally use the Insight source), it failed otherwise. This is expected, due to the discontinuities in the phase of the interferogram, as evidenced by the plot in Figure 1c. Moreover, as shown later in Section 3, the frequency spectrum of the interferogram acquired with no DVV correction presents multiple peaks due to the aforementioned discontinuities; since the generation of masks requires a channeled spectrum whose variation in peak density with wavenumber is monotonic, it was not possible to infer the system model calibration functions g and h, as per Figure 3a, and ultimately the complex-valued Master signals. This is not a failure of the MS principle, but rather of the specific algorithm to synthesise masks from experimentally acquired spectra for different OPD values, which has been successfully employed so far on other commercial swept sources.

Instead, a hybrid operation mode was implemented (HyMS–OCT), comprising portions of the original MS–OCT concept [9] but employing complex-valued spectra (as explained in a subsequent paper on MS–OCT, where masks are complex-valued, for which reason such a MS–OCT version denominated CMS–OCT [10]) to enhance the tolerance to phase fluctuations [10].

The hybrid procedure is described diagrammatically in Figure 3b. To obtain an A-scan for a single reflector, the procedure is split into two stages, the Master and the respective Slave. In the Master stage, the reference arm length was varied over the depth range under study using the translation stage TS, whilst constantly retrieving the Master signals,

which were then Hilbert-transformed (producing complex-valued spectra) and stored in the computer's memory. Following this, in the Slave stage, the object under test, considered here a mirror, was positioned in the middle of the depth range under study, and a single Slave signal was acquired. This signal was then compared against the set of Master signals by means of a matrix multiplication, as described in Bradu et al. [19] and the result of these comparisons plotted against the TS position, thus generating an A-scan.
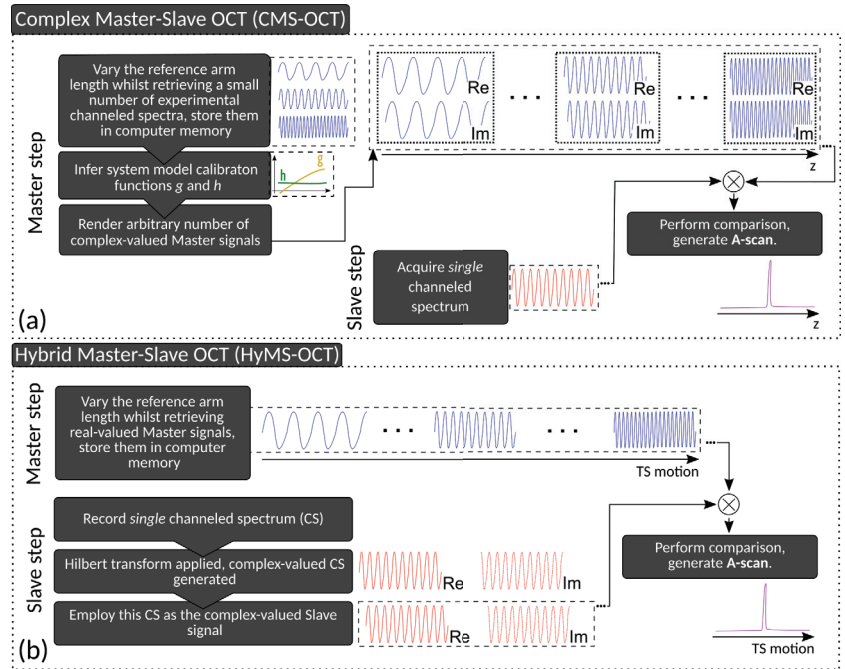
Figure 3. (**a**) Simplified description of the Complex Master–Slave OCT procedure presented in Rivet et al. [10]; (**b**) Diagrammatic description of the hybrid HyMS–OCT method to perform MS–OCT processing of the non-DVV-corrected interferograms retrieved with the akinetic swept source system used in this study.

3. Results

Firstly, a frequency characterisation of the interferogram with a single interferometer configuration was performed, for the case where the DVV correction is applied versus the case where the DVV correction is not applied, for two OPD values (2.55 mm and 17.55 mm), as shown in Figure 4. When the DVV correction is not applied, the invalid signal regions present within the interferometric signal introduce additional frequencies; therefore the red traces in both plots display multiple peaks. These additional frequencies, when not eliminated, degrade the A-scan and also axially move the main A-scan peak from its "true" location.

For the first part of the study, described in Section 3.1, the single interferometer configuration (Figure 2a) with a single reflector in the object arm was used, thus generating a single modulation frequency in the interferogram. In the second part of the study (Section 3.2), the dual interferometer configuration of Figure 2b was used, with single reflectors employed as samples in the object arms of either interferometer.
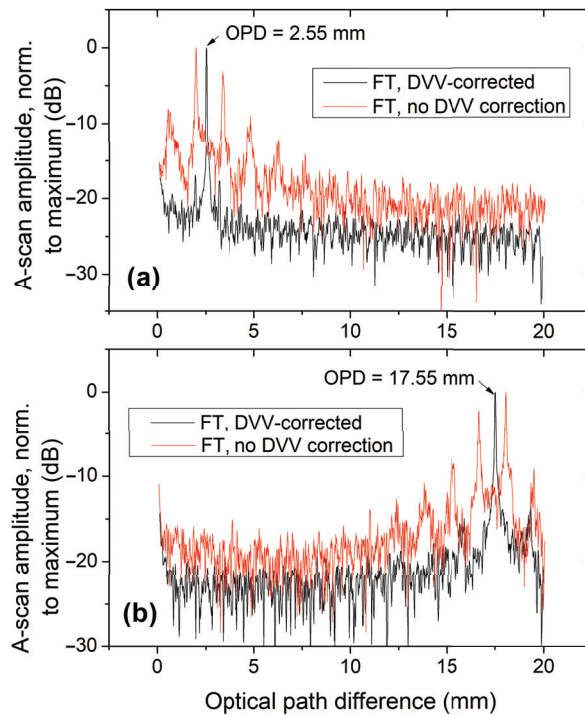
Figure 4. Comparison of A-scans obtained for two separate OPD values by Fourier-transforming the interferogram ((**a**) −2.55 mm; (**b**) −17.55 mm), with (black trace) and without (red trace) DVV correction. Data normalized to the maximum value in each data set, and the logarithmic dB scale on all A-scan profiles was computed with $10 \times \log_{10}(\tilde{A})$, where $\tilde{A}$ is the normalized A-scan profile.

3.1. Complex Master–Slave/Hybrid Master–Slave Operation with Pre-Stored Masks

As mentioned in Section 2.1, any attempts to use the CMS–OCT method described in [10] on any non-DVV-corrected data have proven unsuccessful. The method did work on DVV-corrected interferograms, and the full width at half-maximum (FWHM) for the A-scan peaks was approximately 11.7 μm. The transform-limited peak width was also measured as 11.6 μm, following the procedure described in Appendix C of Reference [10]. This procedure removes all non-linearities present in the phase, preserving only the spectral shape of the signal; therefore, it yields the minimum width attainable by the system for the tuning range specified.

To study the suitability of the MS–OCT method in non-DVV-corrected cases, complex-valued Master masks were generated using the HyMS–OCT method described in Section 2.1, and compared against a single Slave signal. Similar OPD values to those in Figure 4, of 2.55 mm and 17.55 mm, were used here, representing a "short" and "large" OPD depth range, respectively. This HyMS–OCT method was evaluated for three sampling/processing protocols as follows:

1. Interferogram corrected with the DVV data, having been sampled with the source's 400 MHz clock signal (both (i) and (ii) buses connected to the digitiser in Figure 2a);
2. Interferogram not corrected with the DVV data, but still sampled with the source's 400 MHz clock signal (bus (ii) only in Figure 2a connected);
3. Interferogram sampled with the digitiser card's built-in clock signal (500 MHz). Due to the asynchronous operation, the DVV correction is not possible (both (i) and (ii) buses in Figure 2a disconnected).

For these three sampling/processing protocols, A-scans were obtained by comparing the Slave signal corresponding to a reflector placed in the middle of the depth range intervals under study (corresponding to a "short" 2.55 mm and "large" 17.55 mm OPD range, both spanning 1 mm) against a pre-recorded, complex-valued set of Master signals recorded over the same depth range interval, using a matrix multiplication, as described in Bradu et al. [19]. The result of these comparisons is plotted against the TS position, thus generating A-scan profiles as depicted in Figure 5a,b alongside those obtained by Fourier transforming the DVV-corrected interferograms.

As Figure 5a,b show, the A-scan profiles obtained with the HyMS–OCT method on all sampling/processing protocols are very similar, both in terms of peak width and S/N ratio. In other words, the HyMS–OCT method works equally well with DVV-corrected and DVV-uncorrected data.

The location of the A-scan peaks obtained with the FT processing differs slightly from those obtained with the HyMS–OCT due to the different manner the OPD coordinate is determined: in the FT processing, the full A-scan profile needs to be mapped to the distance coordinate by taking several position measurements and interpolating the distance between them, which introduced some imprecision. In the HyMS–OCT processing, each Master signal is directly mapped to a single position of the TS, effectively providing an absolute calibration of each depth point.
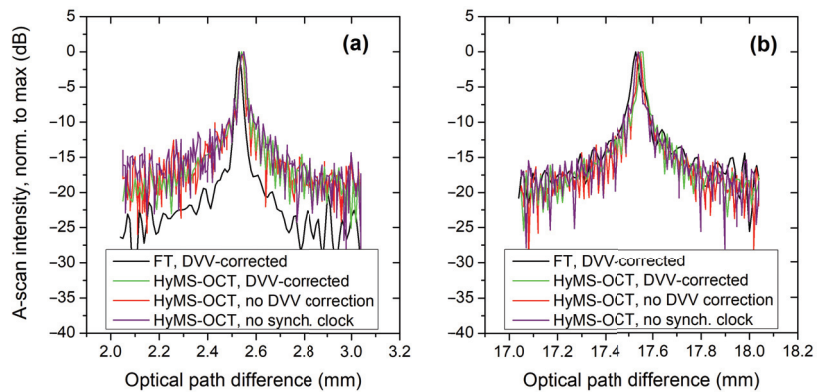
Figure 5. A-scans for three sampling cases as detailed in the insets taken at small (≈2–3 mm) (**a**) and large (≈17–18 mm) (**b**) OPD values with the HyMS–OCT method for the different sampling cases considered. The conventional procedure, the Fourier transform of the DVV-corrected interferogram, is plotted in black in both graphs.

The FWHM of all peaks plotted in Figure 5 are listed in Tables 1 and 2, and their corresponding signal-to-noise ratio values in Table 3 and in the second column of Table 2. These contain the FHWM peak values from the DVV-corrected interferograms and from the non-DVV corrected ones, respectively.

Regarding the peak width values obtained with the FFT method, it is clear that for the two OPD values considered, larger widths than the expected transform-limited value are obtained. For the larger OPD value (≈17.5 mm), the peak width is significantly larger, and a depth-dependent widening is observed. Since the interferometer used in this study was not fully compensated for material dispersion between its two arms, this result is to be expected. This depth-dependent widening is not observed in the results obtained with either CMS–OCT or HyMS–OCT since the MS–OCT method automatically compensates [12] for any material dispersion imbalance in the system.

Table 1. Full-width at half-maximum values of the A-scan peaks (in µm) for the methods evaluated for a short (2.55 mm) and a large (17.55 mm) OPD value, employing DVV-corrected data. No spectral windowing was employed in any of interferograms used to obtain these A-scan peaks.

Method / Sampling Protocol	Transform-Limited	FFT (No Dispersion Compensation)		CMS–OCT		HyMS–OCT	
DVV-corrected, 400 MHz source clock	11.6	12.37 ± 0.89	(short)	11.72 ± 0.08	(short)	12.40	(short)
		16.07 ± 1.79	(large)	11.27 ± 0.87	(large)	12.35	(large)

Table 2. Full-width at half-maximum values of the A-scan peaks (in µm) and their respective signal-to-noise ratio (SNR) values (in dB) for the HyMS–OCT method, employing data sampled without DVV correction. No spectral windowing was employed in any of the interferograms used to obtain these A-scan peaks.

Sampling Protocol	Peak Width (µm)	SNR (dB)
no DVV correction, 400 MHz source clock	12.57 (short) 12.47 (large)	19.6 (short) 22.4 (large)
asynchronous operation, 500 MHz clock from digitiser	14.82 (short) 14.64 (large)	18.3 (short) 20.8 (large)

Table 3. Signal-to-noise ratios (SNR) of the A-scan peaks (in dB) for the methods evaluated for a short (2.55 mm) and a large (17.55 mm) OPD value, employing DVV-corrected data. No spectral windowing was employed in any of interferograms used to obtain these A-scan peaks.

Method / Sampling Protocol	Transform-Limited	FFT (No Dispersion Compensation)		CMS–OCT		HyMS–OCT	
DVV-corrected, 400 MHz source clock	n/a	26.7	(short)	18.6	(short)	19.8	(short)
		18.6	(large)	19.4	(large)	21.0	(large)

The CMS method employing synthesised complex-valued masks provides the closest peak width value to the transform-limited width (the ground truth), differing by less than 100 nm in the short OPD case.

The last column of Table 1 and the middle column of Table 2 relate to peak width values obtained using the HyMS–OCT method employing pre-recorded Master masks, as described in Section 2.1. In this case, the peak width was estimated from a shorter run of the TS (500 points over a travel range of ≈300 µm, centred at the relevant OPD where the Slave signal was acquired). The larger values (when compared with those obtained for the CMS–OCT method employing synthesised complex-valued masks) may be due to the precision limitations of the mechanical translation stage encoder, and the settling time allowed for each individual position recording of the channelled spectra. Still, it is clear that no depth-dependent peak widening is observed when using the HyMS–OCT method, as shown in Tables 1 and 2. For most cases, the peak widths are smaller than those obtained with the FFT method.

In Table 2, the peak widths for the HyMS–OCT under asynchronous clock operation between source and digitizer are only slightly larger (by ≈2 µm) than the other two cases obtained with the same processing method; this is due to the fact that the digitiser used has fixed, pre-set clock settings that do not match the clock signal frequency used in the other two cases (400 MHz). In this particular case, the maximum clock frequency allowed by the digitiser card, 500 MHz, was used, but the number of sampled points was kept constant. This has an impact in terms of the sampled region of the spectrum, with the digitised spectral range not fully covering the sweep range of the source, which was expected to negatively impact the axial resolution measured.

We present the signal-to-noise ratio (SNR) values for the A-scan peaks in Figure 5a,b in Tables 2 and 3. These SNR values should be interpreted with some reservation, as they represent single run events and no average or detailed noise analysis was performed. Data employed in the SNR calculations were collected in separate events. This may explain some variations in the values presented. To avoid signal saturation, a different attenuation of the reference power was applied when switching from one regime to another, which was maintained consistently for measurements on each regime for different OPD values, for instance, but not when switching between regimes.

In both Tables 2 and 3, the larger the OPD value for both CMS–OCT and HyMS–OCT methods, the larger the SNR, despite the system sensitivity decreasing with OPD, showing that noise decreases at a higher rate than the sensitivity when moving to larger RF frequency values. There might be other noise components with larger strength at smaller RF frequency values (shallow OPD values) that may explain this. As far as the FFT case, the noise floor lies more than 5 dB below the noise floor of the other three traces at short OPD values. The trend of S/N noise with OPD cannot be commented on for the FFT data as no dispersion compensation was applied.

To study the applicability of the HyMS–OCT method to large axial range measurements, an A-scan was produced over the full range of OPD values allowed by the sampling clock from the digitiser card for the locations where the two Slave signals were previously recorded. This behaviour was tested for the case with asynchronous clock operation between source and digitiser (operating at 500 MHz, which translates into ≈21 mm of depth range, with 18 mm of it represented in the plot). The resulting A-scans were compared against those obtained from FFT processing of the interferogram, with and without DVV correction. These results are shown in Figure 6.

As expected, if the non-DVV-corrected interferogram is processed using the FFT method, not only is there a rise in the noise floor level, but also the appearance of satellite peaks, whose heights are comparable to those of the main interferometric peak, as has already been shown in Figure 4. The trace corresponding to the non-DVV corrected, HyMS–OCT-processed interferogram also presents some residual satellite peaks, although these are significantly reduced when compared to those present in the non-DVV-corrected, FFT-processed trace, being attenuated by more than 10 dB.

The noise floor behaviour mimics what was presented before: the DVV-corrected interferogram, when processed using the FFT method, possesses a lower noise floor (by about 5 dB) when compared to the same data processed using the HyMS–OCT method (without DVV correction, and without using the clock signal from the source). However at a larger OPD value, closer to the sampling limit of the digitiser, the difference between the noise floor of the DVV-corrected, FFT-processed interferogram and that processed using the HyMS–OCT method is not significant, possibly due to the fact that no dispersion compensation was applied on the FFT-processed data, as mentioned earlier.

No S/N ratio value is presented for the coherence limited peak in Table 3, as this is obtained from the envelope of the spectrum, that is similar to that obtained from the reference or sample wave only. In other words, we cannot associate a separate signal or noise measurement to this procedure (signal in OCT is measured with both waves on and noise with the sample wave obstructed).

Since the primary concern with this study was to assess any peak width degradation when using any of the methods evaluated, no spectral windowing was applied to any of the interferograms processed, which may explain the existence of side-lobes in some of the A-scans presented in Figures 4–6.
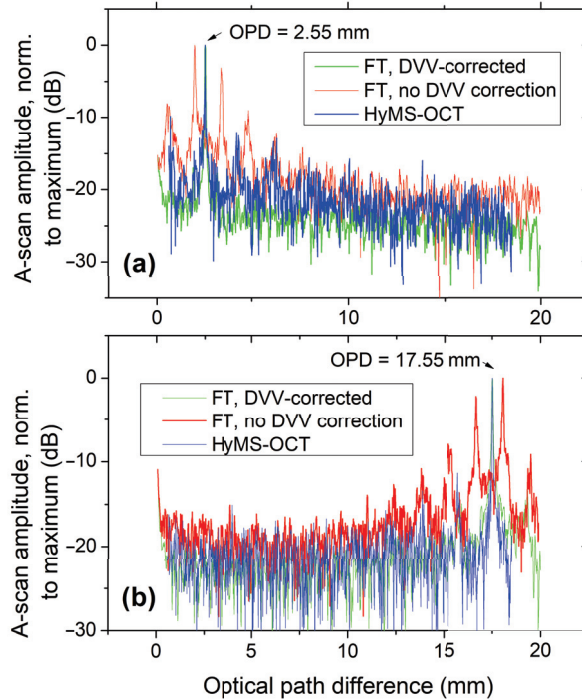
Figure 6. A-scan comparison between the FT method (on both DVV and non-DVV corrected interferograms) and the HyMS–OCT method (asynchronous clock case, no DVV correction), for a total OPD value scan range of 18 mm. Arrows depict the corresponding OPD at which the Slave signal was acquired for the two sub-figures ((**a**) −2.55 mm; (**b**) −17.55 mm), and also the OPD values of the interferograms subject to FT processing.

3.2. Down-Conversion (DC) OCT Implementation with Two Physical Interferometers

To evaluate the axial resolution with the DC-OCT method, the OPD in one of the two interferometers is scanned mechanically using the TS in Interferometer A, as presented in Section 2. This leads to the graph in Figure 7. This is not, however, the way the DC-OCT method is normally used, where no mechanical depth scanning is applied; as demonstrated by Podoleanu et al. [11], DC-OCT allows the production of constant depth images of the object under study (*en-face* images) by setting both interferometers to the same optical path difference and comparing the channelled spectra of similar modulation.

The second interrogating interferometer performs real-time generation of the mask, therefore operating as an Optical Master. In contrast, in all previous MS papers, masks were generated electrically and/or numerically by Electronic Masters, and then stored in the PC memory.

A down-conversion factor N can be calculated as the ratio between the frequency of the photo-detected signal for the maximum OPD recoverable and the frequency of the processor performing the down-conversion (composed of the mixer and the low-pass filter). Considering the Nyquist limit, this should be at least twice the sweep frequency value, therefore giving a value of $N = \dfrac{600\,\text{MHz}}{200\,\text{kHz}} = 3000$. This means that by using DC-OCT, the bandwidth of photo-detected signal was reduced by a factor of 3000. The A-scan peak obtained using the down-conversion method exhibits a width of $\approx$14 µm, slightly larger than the expected 11.6 µm.
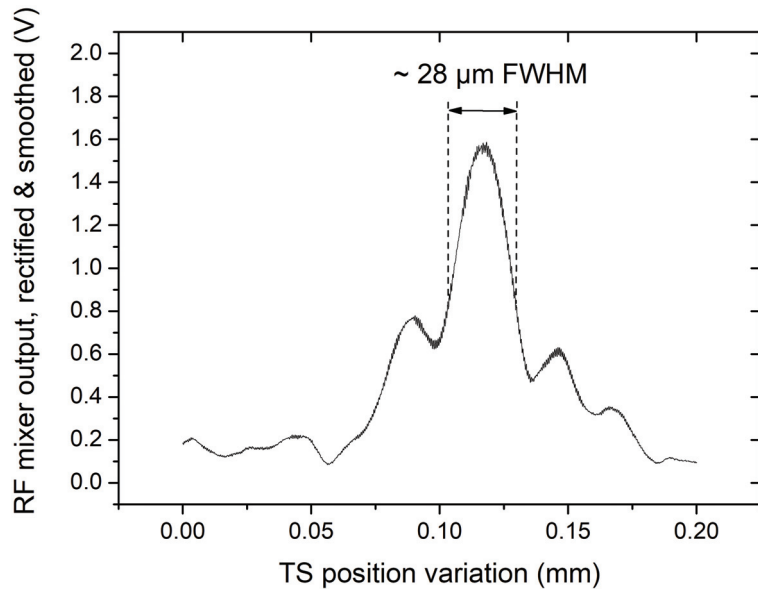
Figure 7. A-scan obtained with the down-conversion procedure, with the Master interferometer having an OPD value of ∼80 mm, and the reference arm of the Slave interferometer being mechanically scanned over a range of 200 μm at ∼80 mm OPD. The main peak has a FWHM of ∼28 μm, which corresponds to an axial resolution of ∼14 μm due to the double-pass interferometer configuration.

4. Discussion and Conclusions

This study has evaluated the suitability of three versions of the MS–OCT method to decode interferograms, delivered by an interferometer driven by an electrically tunable (Vernier tuning) swept source that presents invalid regions throughout its tuning. The three MS–OCT versions are as follows: (i) using pre-synthesised, complex-valued masks (CMS–OCT); (ii) a hybrid (HyMS–OCT) modality, where multiple Master masks are generated by multiple stepped OPD changes and compared against a complex-valued Slave signal; and (iii) a DC-OCT version. As demonstrated, both (ii) and (iii) methods can be used with some success, even when interferograms are not corrected by the manufacturer's DVV. The CMS–OCT method with pre-synthesised masks can only work with DVV-corrected spectra. Therefore, the MS–OCT methods present a suitable alternative for the signal processing of OCT systems driven by swept sources employing a similar tuning modality as that of the Insight source used in this study. If the use of a DVV correction can be eliminated, as allowed by both (ii) and (iii) methods, signal processing is simplified with an overall cost advantage for the whole OCT system. A summary of the advantages (and disadvantages) of the approaches presented in this study is shown in Table 4.

One of the advantages of the electrically tunable source used in this study is its long axial range, which can be on the order of tens of centimetres or more; in order to digitise such interferograms, ultra-fast digitiser cards with multi-GHz sampling clocks are needed. However, if the DC procedure presented in this study (and detailed by Podoleanu et al. [11]) is used, one can do without the digitiser card altogether. In effect, this has also been demonstrated in this study, where an A-scan taken at an OPD value of 80 mm is obtained, which would have otherwise been impossible to obtain with the ATS-9350 digitiser card, as the 80 mm OPD corresponds to a dominant channelled spectrum frequency of more than 200 MHz over the digitiser's aliasing limit. This conclusion can be scaled to larger frequency sweeping rates, exceeding tens of MHz, where the DC procedure would allow processing of tens of GHz-frequency signals using digitisers with sampling rates in the range of the sweeping rate.

Table 4. Summary of positive and negative aspects of using the MS–OCT method with the akinetic, electrically tunable swept source employed in this study.

Advantages	Disadvantages
• No need to use the source's sampling clock, which relaxes the restrictions in the choice of digitiser card; • Tolerance to dispersion in the system, with no need to carry out a separate operation; • Direct *en-face* imaging: multiple *en-faces* (CMS/HyMS–OCT), single, unrestricted depth *en-face* (DC-OCT); • Using DC-OCT lowers the sampling rate of the digitiser, where the maximum achievable depth is only set by the photo-detector bandwidth.	• HyMS–OCT can only run with pre-recorded masks (mask synthesising is not possible *at present*); • In HyMS–OCT, Masks need to be acquired by mechanically changing the OPD on the Master interferometer (but these can be stored and re-used); • Noise penalty in the system when the DVV is not used; • DC-OCT requires an interferometer for each depth; the front-end electronics for each balanced photo-detector and the mixer need to have high enough bandwidth to handle the carrier frequency.

As demonstrated, the method described by Rivet et al. [10] to pre-synthesise the Master signals for the CMS–OCT procedure is only applicable to the case where the DVV correction is applied. However, the DVV correction and external clock sampling only address one of the issues encountered with SS-OCT, that of securing linear sweeping. The other issue is the dispersion in the interferometer. The MS calibration addresses both non-linear sweeping and dispersion. Therefore, when compared with the conventional usage case of these optical sources (DVV correction followed by FT), the MS procedure presented here offers some benefit, in the sense that it is tolerant to dispersion in the system [12]. This is demonstrated in Table 1 by the improvement in the peak width brought by the CMS–OCT with synthesised masks when compared against that obtained by simple FFT.

The HyMS–OCT procedure with non-DVV-corrected interferograms was made working with pre-recorded spectra. A similar approach was used in the earlier MS–OCT implementations [9,12], and while it worked well enough for the demonstrations, it has a negative impact on the flexibility and usability of the system, as a large number of masks need to be collected. The procedure for synthesising the masks from a small sub-set of channelled spectra, however, can potentially be upgraded to something more tolerant of the extra frequency terms (e.g., by suppressing the satellite terms during capture using band-pass filtering). More research will need to be carried out with regards to this aspect.

Running the HyMS–OCT procedure on non-DVV-corrected data appears to raise the noise floor, especially when imaging at lower OPD values; moreover, some satellite terms, similar to those observed when Fourier-transforming a non-DVV-corrected interferogram, also appear in the A-scan, albeit significantly attenuated. This could pose a problem, especially if low-bit-depth digitiser cards are used, as they will present lower dynamic range in the digitisation. Still, bypassing the requirement for DVV correction means that the need for synchronous sampling operation between source and digitiser is eliminated, with potential cost savings and additional flexibility. For example, with a sufficiently large sampling rate digitiser, OPD values beyond the limit introduced by the source clock can be accessed, as has already been demonstrated in Marques et al. [13].

In the second part of this study, the operation of this optical source without the need for a high-speed digitiser was also investigated, by means of the down-conversion OCT method [11]. By using two near-identical optical interferometers and mixing their output interferograms with an analogue RF mixer, long-range operation at an OPD value of 120 mm is demonstrated. When compared with the results from the first part of our study, the axial resolution obtained was not significantly deteriorated. Indeed, it actually presented a >2 µm improvement over the width measured for DVV-corrected, FT-processed data at 17 mm.

The peak width is, however, slightly larger than all results obtained using the CMS/HyMS–OCT procedures. This is explained by some dispersion difference between the two optical interferometers. Moreover, it was not possible to perform any spectral windowing on these time-based signals, which can also explain the presence of side-lobes in the A-scan.

The peak contrast is also significantly reduced, to less than 10 dB, compared with the ≈20 dB obtained with the CMS/HyMS–OCT procedures. The bandwidth of the Insight BPD-1 (employed in the Slave interferometer), narrower than the Thorlabs photo-detector employed in the Master interferometer, explains the lower peak contrast at large OPD values.

This is only a constructive disadvantage due to the non-availability of two 1 GHz balanced photo-detectors. Even so, DC-OCT is worth pursuing due to the lowering of the signal processing bandwidth to levels comparable to the sweeping frequency. This allows a low-cost route via low-cost digitizers, a procedure that also enables real-time delivery capability of *en-face* views, as when using ultra-high-speed digitizers, the amount of data is so high that it needs to be buffered locally before being transferred out of the digitizer for post-acquisition. The more important disadvantage of DC-OCT is the need for a second high-speed, large-bandwidth photo-detector unit.

In summary, Master–Slave OCT (both in its HyMS–OCT and DC-OCT guises) offers some simplification over the conventional DVV-based invalid region removal procedure, allowing the user to employ both the valid and invalid regions, as long as a reference interferometer (Master) signal is available (either pre-stored at a Master step or as a physical interferometer as in the down-conversion case). Another advantage of the MS approach is that it may enable better analysis of phase errors, particularly at higher imaging depths. These phase errors may occur around the invalid-to-valid transitions due to slight imperfections in the discontinuity resolution with the DVV or simply due to a change in the performance of the laser over time or ambient temperature.

Author Contributions: Conceptualization, A.P. and M.J.M.; methodology, A.P. and M.J.M.; software, M.J.M. and A.B.; validation, M.J.M. and R.C.; formal analysis, M.J.M.; investigation, M.J.M. and R.C.; resources, A.P. and J.E.; data curation, M.J.M.; writing—original draft preparation, M.J.M.; writing—review and editing, M.J.M., R.C., J.E., A.B., and A.P.; visualization, M.J.M.; supervision, A.P. and A.B.; project administration, A.P.; funding acquisition, A.P. and A.B. All authors have read and agreed to the published version of the manuscript.

Conflicts of Interest: A.P. and A.B. are inventors of patents: US10760893 and US9383187 in the name of the University of Kent. R.C. and M.J.M., no conflicts of interest. J.E. is the chief technological officer (CTO) and executive vice-president (EVP) of Insight Photonic Solutions, Inc. The funders had no role in the design of the study; in the collection, analyses, or interpretation of data; in the writing of the manuscript, or in the decision to publish the results.

References

1. Swanson, E.A. OCT Technology Transfer and the OCT Market. In *Optical Coherence Tomography: Technology and Applications*; Drexler, W., Fujimoto, J.G., Eds.; Springer International Publishing: Cham, Switzerland, 2015; pp. 2529–2571. [CrossRef]
2. Leitgeb, R.; Hitzenberger, C.; Fercher, A. Performance of fourier domain vs. time domain optical coherence tomography. *Opt. Express* **2003**, *11*, 889. [CrossRef] [PubMed]
3. Minneman, M.P.; Ensher, J.; Crawford, M.; Derickson, D. All-Semiconductor High-Speed Akinetic Swept-Source for OCT. In *Optical Sensors and Biophotonics*; Paper 831116; Optical Society of America: Shanghai, China, 2011; p. 831116. [CrossRef]
4. Wang, Z.; Potsaid, B.; Chen, L.; Doerr, C.; Lee, H.C.; Nielson, T.; Jayaraman, V.; Cable, A.E.; Swanson, E.; Fujimoto, J.G. Cubic meter volume optical coherence tomography. *Optica* **2016**, *3*, 1496. [CrossRef] [PubMed]

5. Park, J.; Carbajal, E.F.; Chen, X.; Oghalai, J.S.; Applegate, B.E. Phase-sensitive optical coherence tomography using an Vernier-tuned distributed Bragg reflector swept laser in the mouse middle ear. *Opt. Lett.* **2014**, *39*, 6233–6236. [CrossRef] [PubMed]
6. MacDougall, D.; Farrell, J.; Brown, J.; Bance, M.; Adamson, R. Long-range, wide-field swept-source optical coherence tomography with GPU accelerated digital lock-in Doppler vibrography for real-time, middle ear diagnostics. *Biomed. Opt. Express* **2016**, *7*, 4621–4635. [CrossRef] [PubMed]
7. Song, S.; Xu, J.; Wang, R.K. Long-range and wide field of view optical coherence tomography for in vivo 3D imaging of large volume object based on akinetic programmable swept source. *Biomed. Opt. Express* **2016**, *7*, 4734–4748. [CrossRef] [PubMed]
8. Salas, M.; Augustin, M.; Felberer, F.; Wartak, A.; Laslandes, M.; Ginner, L.; Niederleithner, M.; Ensher, J.; Minneman, M.P.; Leitgeb, R.A.; et al. Compact akinetic swept source optical coherence tomography angiography at 1060 nm supporting a wide field of view and adaptive optics imaging modes of the posterior eye. *Biomed. Opt. Express* **2018**, *9*, 1871–1892. [CrossRef] [PubMed]
9. Podoleanu, A.G.; Bradu, A. Master–slave interferometry for parallel spectral domain interferometry sensing and versatile 3D optical coherence tomography. *Opt. Express* **2013**, *21*, 19324. [CrossRef] [PubMed]
10. Rivet, S.; Maria, M.; Bradu, A.; Feuchter, T.; Leick, L.; Podoleanu, A. Complex master slave interferometry. *Opt. Express* **2016**, *24*, 2885. [CrossRef] [PubMed]
11. Podoleanu, A.; Cernat, R.; Bradu, A. Down-conversion en-face optical coherence tomography. *Biomed. Opt. Express* **2019**, *10*, 772. [CrossRef] [PubMed]
12. Bradu, A.; Maria, M.; Podoleanu, A.G. Demonstration of tolerance to dispersion of master/slave interferometry. *Opt. Express* **2015**, *23*, 14148. [CrossRef] [PubMed]
13. Marques, M.J.; Rivet, S.; Bradu, A.; Podoleanu, A. Complex master-slave for long axial range swept-source optical coherence tomography. *OSA Contin.* **2018**, *1*, 1251. [CrossRef]
14. Siddiqui, M.; Nam, A.S.; Tozburun, S.; Lippok, N.; Blatter, C.; Vakoc, B.J. High-speed optical coherence tomography by circular interferometric ranging. *Nat. Photonics* **2018**, *12*, 111–116. [CrossRef] [PubMed]
15. Lippok, N.; Lippok, N.; Vakoc, B.J.; Vakoc, B.J.; Vakoc, B.J. Resolving absolute depth in circular-ranging optical coherence tomography by using a degenerate frequency comb. *Opt. Lett.* **2020**, *45*, 371–374. [CrossRef] [PubMed]
16. Chun, S.K.; Jang, H.; Cho, S.W.; Park, N.S.; Kim, C.S. Unfolding displacement measurement method for the aliasing interferometer signal of a wavelength-comb-swept laser. *Opt. Express* **2018**, *26*, 5789–5799. [CrossRef] [PubMed]
17. Marques, M.J.; Cernat, R.; Ensher, J.; Bradu, A.; Podoleanu, A. Master-slave principle applied to an electrically tunable swept source-OCT system. In *Optical Coherence Tomography and Coherence Domain Optical Methods in Biomedicine XXIV*; International Society for Optics and Photonics: San Francisco, CA, USA, 2020; Volume 11228, p. 112280D. [CrossRef]
18. Insight Akinetic Swept Lasers Enabling OCT and SS-OCT Angiography | Insight. Available online: https://www.sweptlaser.com/content/insight-akinetic-swept-lasers-enabling-oct-and-ss-oct-angiography (accessed on 27 May 2020).
19. Bradu, A.; Rivet, S.; Podoleanu, A. Master/slave interferometry – ideal tool for coherence revival swept source optical coherence tomography. *Biomed. Opt. Express* **2016**, *7*, 2453. [CrossRef] [PubMed]

Comparison of Pulse Wave Signal Monitoring Techniques with Different Fiber-Optic Interferometric Sensing Elements

Nikolai Ushakov *, Aleksandr Markvart, Daria Kulik and Leonid Liokumovich

Institute of Physics, Nanotechnology and Telecommunications, Peter the Great St. Petersburg Polytechnic University, 195251 St. Petersburg, Russia; markvart_aa@spbstu.ru (A.M.); kulik.dd@edu.spbstu.ru (D.K.); leonid@spbstu.ru (L.L.)

* Correspondence: n.ushakoff@spbstu.ru

Abstract: Pulse wave (PW) measurement is a highly prominent technique, used in biomedical diagnostics. Development of novel PW sensors with increased accuracy and reduced susceptibility to motion artifacts will pave the way to more advanced healthcare technologies. This paper reports on a comparison of performance of fiber optic pulse wave sensors, based on Fabry–Perot interferometer, fiber Bragg grating, optical coherence tomography (OCT) and singlemode-multimode-singlemode intermodal interferometer. Their performance was tested in terms of signal to noise ratio, repeatability of demodulated signals and suitability of demodulated signals for extraction of information about direct and reflected waves. It was revealed that the OCT approach of PW monitoring provided the best demodulated signal quality and was most robust against motion artifacts. Advantages and drawbacks of all compared PW measurement approaches in terms of practical questions, such as multiplexing capabilities and abilities to be interrogated by portable hardware are discussed.

Keywords: optical fiber sensor; biomedical sensor; optical coherence tomography; intermodal interferometer; singlemode-multimode-singlemode; Fabry–Perot interferometer; fiber Bragg grating; pulse wave; spectral interferometry

1. Introduction

Biomedical applications of optical sensing and imaging techniques draw great attention in terms of academic research towards further technological advancements, commercialization of practical devices and search for new applications. Recently, an increasing number of such chronic diseases as diseases of the cardiovascular system, connective tissue dysplasia, diabetes mellitus and others have become very widespread. At the same time, timely diagnosis is the most important stage of treatment and prevention of complications. One of the widely used methods for diagnosing these diseases is pulse wave analysis [1–3], which allows to estimate stiffness of arterial walls and according to it, the state of the cardiovascular system. The advantages of this method include non-invasiveness, high diagnostic confidence, and potential ease of implementation. Typically, high-precision setups for recording pulse wave (PW) signals are stationary and are available only in medical institutions. The examples of such devices include SphygmoCor (Atcor Medical, Sydney, Australia), Complior (Artech Medical, Pantin, France), and others [4,5]. The main factors limiting their implementation in personal and portable devices is their high cost and sensitivity to body movements, which can significantly distort the recorded signals. On the other hand, the development and implementation of portable and personal medical devices based on the registration and processing of pulse wave signals will make it possible to diagnose the above diseases at the earliest stage, significantly facilitating and increasing the effectiveness of their treatment.

A cost-effective solution to PW signal acquisition is offered by photoplethysmography (PPG) [6–8], that detects the change of light intensity transmitted through or scattered from a biological tissue as a response to change of blood volume in blood vessels.

109

Typically, small vessels such as capillaries are monitored [8,9], however, the original (arterial) pulse wave becomes distorted when coupled from arterial walls to capillary walls, limiting the measurement accuracy. Moreover, PPG is reported to be susceptible to motion artifacts [10,11]. With that in mind, state-of-the-art PPG systems are not ideally suited for high-precision medical inspection, hence, some alternatives might be highly relevant.

Fiber optic sensors are excellent candidates to measure pulse wave signals due to their bio-compatibility, immunity to electromagnetic interference, small footprint of the sensing element, extremely high achievable accuracy and resolution. Several recent papers report the approaches for cardiac monitoring [12–14] and pulse wave measurement [15–20] by means of fiber Bragg gratings (FBG) and Fabry–Perot interferometric (FPI) sensors. A comparison of FBG sensors inscribed in silica and polymer fibers has been reported in [17], with a clear advantage of polymer FBG in terms of achieved resolution. However, humidity sensitivity of polymer optical fiber sensors [21] may lead to undesirable effects in biomedical sensors due to sweating. However, when attached to the skin, such sensors may be subject to uneven deformations, which will distort the shape of their spectral transfer function and reduce the accuracy of the measurements [22,23]. Parasitic sensors deformation may also lead to motion artifacts, deteriorating measurement accuracy.

One way of solving the problem of motion artifacts is increasing the mechanical rigidity of the sensing element. However, for such a weak measurand as pulse wave, this will degrade the sensitivity and might lead to distorted shape of the measured signal. Another solution to the motion artifacts problem might be a sensor, suited for sensing of complex geometries by means of an increased number of variables that can be extracted from the sensor signal. An example of such a sensor is a fiber-optic intermodal interferometer, based on singlemode-multimode-singlemode structure (SMS) [24–27]. In these sensors, a short section of multimode fiber (MMF) is spliced between two singlemode fibers (SMF). Depending on the splicing parameters and type of the multimode fiber, from several to tens of modes are excited in the multimode fiber. After propagation in the MMF section, these modes are coupled to the fundamental mode of the second SMF, leading to intermode interference signal, which encodes the perturbations of the MMF section. Typically, SMS interference signal consists of several interference components, which OPDs, depending on the sensor structure, are related to different perturbations. In addition to the ability of multi-parameter sensing and suppression of cross-talk induced by physical quantities not being measured [24,28], SMS sensors also offer higher strain sensitivities than FBG sensors [26].

Multimode optical fiber sensors are commonly used for multiparameter sensing [29]. An example of simultaneous strain, bending and torsion sensing with a single FBG inscribed in a polymer fiber has been reported in [30]. An example of simultaneous heart rate and breathing rate measurement, demonstrating low susceptibility to motion artefacts is reported in [31,32], wherein the effect of reduced body motion sensitivity was attained by incorporating polymer fiber Bragg grating sensors into a smart textile according to well-defined geometric pattern.

However, mechanical coupling between the pulse wave and even the tiniest fiber-optic sensor unavoidably leads to at least some distortions of the measured signal. Therefore, imaging methods of PW monitoring are considered to be the most advantageous [33]. Optical coherence tomography (OCT) is one of the most prominent approaches of biomedical imaging, enabling to provide a 3-dimensional images of tissues. The basic step of OCT imaging is the so-called A-scan, or axial depth profile of reflection, calculated as the Fourier transform of the measured optical reflection spectrum [34]. 2-dimensional projections and 3-dimensional tomograms are computed by combining the A-scans.

Non-invasive nature of OCT measurements as well as high spatial resolution and ability to perform fast measurements dictated the success of OCT for medical diagnostics. OCT is most widely used in ophthalmology [35–37], as well as endoscopic imaging [38–40], tissue characterization [41,42] and other applications. Initially proposed in the 1980-s [35] originating from white-light interferometry [43], it rapidly matured and became a clinically

accepted tool in 2000-s due to proposal of spectral-domain OCT and in particular swept-source OCT [34,44] and technological advancement of required optical components.

Moreover, phase-sensitive OCT (φ-OCT) [45,46] is able to measure sub-nanometer displacements of tissues, providing a powerful platform for measuring PW signals with ultimate signal-to-noise ratio (SNR). Up to date, OCT was only reported to be used for PW measurement in retinal arteries [47–49] and relatively small arteries in fingers [50,51], which do not bring much information for cardiovascular system assessment in general due to their peripheral position [33,52].

The aim of the current paper is to compare the performance of fiber-optic sensors with various sensing mechanisms for the task of noninvasive pulse wave monitoring in major arteries (demonstrated on carotid, subclavian and radial arteries). The compared sensing approaches include FPI, FBG, φ-OCT as well as SMS interferometer. The obtained pulse wave signals were compared on the basis of signal to noise ratio, repeatability and robustness against motion artefacts. It is, to the best of our knowledge, the first comparative study of several types of optical fiber sensors for pulse wave measurement. Advantages and drawbacks of the investigated approaches in terms of signal quality and practical aspects of sensors implementation are discussed. We believe that the reported work will lead to better understanding of applicability of different types of OFS and will pave the way to their widespread use in healthcare.

2. Interrogation Setup and Sensors Description

All compared sensing approaches (FPI, FBG, φ-OCT and SMS) typically utilize spectral interrogation for signal readout. In order to perform an adequate comparison of approaches' performance, the same interrogation setup was used to acquire optical spectra. It consists of Ibsen I-MON USB512 spectrometer (spectrum measurement interval was [1.51; 1.595] μm, variable integration time from 10 μs to 100 μs, spectra acquisition rate up to 3 kHz) and Exalos EXS210066-01 SLED (output power up to 5 mW, central wavelength 1.55 μm, –6 dB spectral width 160 nm, flat-top spectrum shape, the most uniform part coincides with the spectrometer measurement range) installed on Exalos EBD5000 driver board. A photo of interrogation setup is shown in Figure 1a.
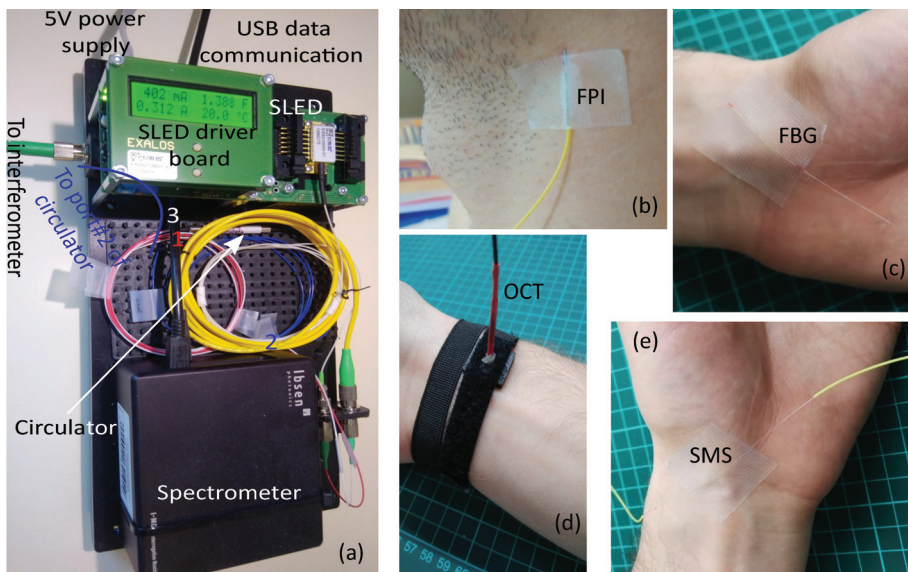

Figure 1. Photo of interrogation setup (**a**) and examples of FPI (**b**), FBG (**c**), OCT (**d**) and SMS (**e**) pulse wave sensors fixed over subject's artery. (**a**,**b**) are reproduced from [20].

Depending on the tested sensing element, integration time was varied from 10 μs for FBG and SMS sensors, to 50 μs for FPI and OCT sensors. Output optical power of the SLED was controlled from about 2 mW for FBG and SMS sensors to 5 mW for FPI and OCT sensors by adjusting the operating current. Different parameters of the interrogation system were used in order to match the span of acquired optical spectra to the dynamic range of the spectrometer's analog to digital converter. Details of sensing elements and interrogation system configuration for each of the sensing approaches are listed in subsections below.

2.1. Fabry–Perot Interferometric Pulse Wave Sensor

In the case of Fabry–Perot interferometric sensing element, spectra reflected from the sensing element were acquired and further demodulated. The sensing element was connected to the interrogation hardware via optical circulator, as shown schematically in Figure 2a. The sensing element was formed by the end faces of two optical fibers, mated inside a glass capillary. The lead-in fiber was conventional SMF-28 one, while the second fiber was coreless Thorlabs FG125LA fiber, the use of which allowed us to suppress parasitic interference components, originating from light reflection off its far end face. The inner diameter of the capillary was about 130 μm, outer—300 μm, the length was about 1 cm. The fibers were glued at the ends of capillary, the length of the air gap between their end faces was about 57 μm. A metal string about 200 μm in diameter was also glued to the capillary and the SMF fiber 900 μm jacket to increase the mechanical robustness of the sensor.
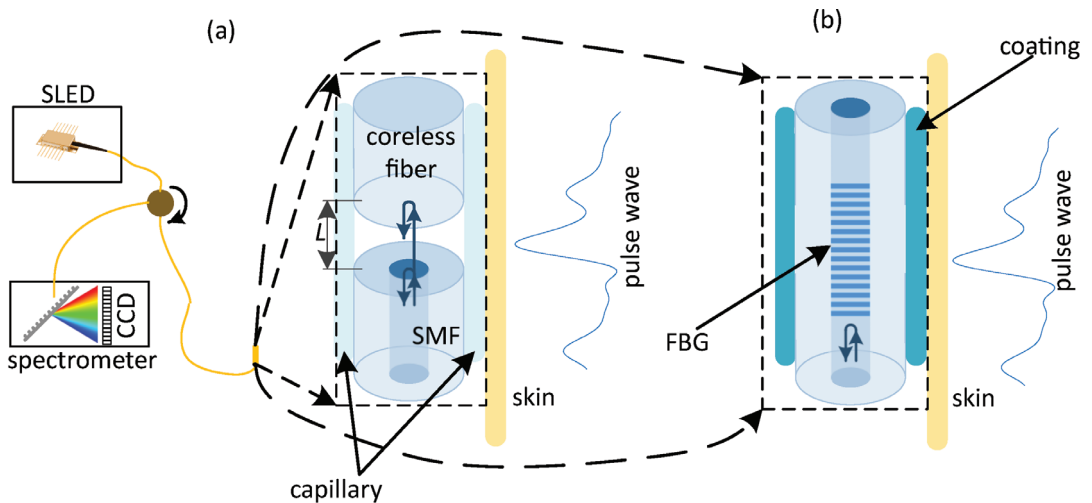

Figure 2. Schematic illustration of sensing setups for FPI (**a**) and FBG (**b**) pulse wave sensors.

The sensor was fixed to the skin of the subject, whose pulse wave signal was measured with the use of a flexible adhesive tape over an artery at a point with the most pronounced pulse sensible using fingertips as shown in Figure 1b for carotid artery. No adhesive was added between the skin and the sensor. The sensing principle of such a FPI pulse wave sensor relies upon coupling of the pulse wave to the mechanical perturbation of the sensing element, causing the change of the air gap between the fibers. More details on the FPI pulse wave sensor can be found in our previous paper on this topic [20].

2.2. Fiber Bragg Grating Based Pulse Wave Sensor

Fiber Bragg grating is a section of optical fiber with periodic modulation of its refractive index. At each bound of areas with different refractive indexes, the incident optical wave is reflected according to the Fresnel's law. When the period of refractive index mod-

ulation is a multiple of half of the incident light wavelength, all reflected waves add in phase and due to their constructive interference nearly 100% reflectivity can be achieved, while at other wavelengths such interference does not happen and FBG transmits light. Therefore, the reflection spectrum of an FBG has a form of a sharp peak, which position shifts when mechanical perturbation is applied.

The same as for the FPI sensor, the spectra reflected from the FBG were acquired using an optical circulator, as shown schematically in Figure 2c. The FBG was inscribed in a SMF-28 fiber using a KrF excimer laser system with 248 nm wavelength and a phase mask. The central wavelength of the inscribed FBG was 1540 nm and peak reflectivity about 98%. The length of the grating was about 1 cm. Protective UV-cured epoxy acrylate coating with 250 μm diameter was applied to the fiber in order to reduce fragility of the sensor.

The sensor was fixed to skin of the subject, whose pulse wave signal was measured with a flexible adhesive tape over an artery at a point with the most pronounced pulse sensible using fingertips as shown in Figure 1b for radial artery. No adhesive was added between the skin and the sensor. Thanks to smaller weight than the FPI sensor, higher sensitivity could be expected for the FBG sensor, however, it might in fact degrade due to mechanical damping induced by the protective coating.

2.3. Phase-Sensitive Optical Coherence Tomography Pulse Wave Sensor

Typically, OCT systems feature a lens, focusing the probing light in a small spot. However, such lenses are quite bulky and can not be robustly fixed over the investigated artery. On the other hand, in order to accurately measure the pulse wave signal, it is advisable to somehow fix the OCT sensing probe above the investigated artery. Therefore, we have chosen to equip the proposed system with a fiber tip probe, similar to those already used in common-path OCT [53,54]. Its advantages are the small footprint of the OCT probe and insensitivity to any perturbations of the lead-in fiber since the interference occurs between the light reflected from the fiber end, which acts as a reference and the light waves reflected at the bounds of different tissue types. This results in optical path differences (OPD) of interference components being unambiguously related to the depth without the need for any calibration and path length alignment.

Due to the small mode field diameter (MFD) of conventional single-mode fiber (10.4 μm at 1.55 μm wavelength), there is a large divergence angle of the output light. In the OCT system this will result in decreased SNR and sensing range. In order to increase the system performance, the single-mode fiber was terminated with a short section (about 2 mm) of graded-index multimode fiber (MMF), spliced to the lead-in SMF fiber. As a result, primarily the fundamental mode of MMF was excited, having larger MFD (16 μm at 1.55 μm wavelength), which helped to decrease the beam divergence inside the tissue. Neglecting the light scattering inside the tissue and adopting a simple model of Gaussian beam propagation, the fraction of light intensity η that is coupled back to the fiber can be estimated as [55]

$$\eta(w) = \frac{(\pi n w^2)^2}{(8L\lambda)^2 + (\pi n w^2)^2},$$ (1)

where L is the distance the light travelled in the tissue before being reflected, λ is light wavelength, n is the mean refractive index of the tissue and w is mode field diameter. The use of MMF for terminating the OCT system also causes light loss due to the mode diameter mismatch, however, in case of relatively large imaging distances the decreased beam divergence due to larger output MFD has greater influence on the increase of reflected intensity. The overall figure of merit (FoM) of using the MMF termination can be evaluated as a ratio of coupling efficiencies $\eta(w_{MMF})$ and $\eta(w_{SMF})$ multiplied by the areas of SMF and MMF modes

$$FoM = \frac{\eta(w_{MMF})}{\eta(w_{SMF})} \cdot \frac{w_{SMF}^2}{w_{MMF}^2}.$$ (2)

The FoM values greater than 1 indicate the conditions under which the intensity of light reflected from the tissue is greater in case of MMF termination than in case of simple SMF probe. The dependency of figure of merit on the imaging distance L is shown in Figure 3b in case of wavelength $\lambda = 1.55$ μm, tissue refractive index $n=1.4$ (which is in accordance with the reported data for epidermis refractive index near 1.55 μm [56]), $w_{SMF} = 10.4$ μm, $w_{MMF} = 16$ μm, where it can be seen that the use of MMF termination is effective in case of imaging depth $L > 100$ μm.
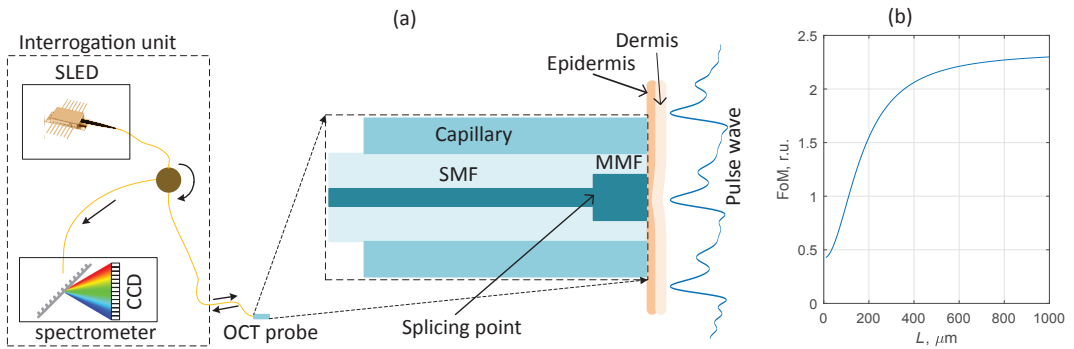

Figure 3. Schematic illustration of the proposed OCT pulse wave sensing system (**a**) and dependence of figure of merit on the imaging depth (**b**).

In order to increase the mechanical robustness of the OCT probe, the fibers were packaged in a glass capillary with inner diameter ~ 140 μm, outer diameter ~ 2 mm and about 5 cm long. The lead-in SMF fiber in the 900 μm jacket was glued to the capillary and protected with a thermally shrinking tube. The fibers were spliced using Jilong KL-280 fiber splicer.

Similarly to the FPI sensor, the spectrum reflected from the OCT probe was measured and further analyzed. The proposed common-path OCT system is schematically depicted in Figure 3a. During pulse wave measurement at the radial artery, the OCT probe was fixed on the wrist using a flexible strap as shown in Figure 1d. During the measurements at carotid and subclavian arteries, the OCT probe was leaned against the skin and held by hand, which did not cause any noticeable signal artifacts.

In contrast to the rest of the pulse wave sensing approaches studied in the current paper, the sensing principle of φ-OCT sensor did not rely on any mechanical coupling between the pulse wave and the sensing element. In turn, this method was based on the properties of biological tissues, namely on different refractive indexes of epidermis and dermis [56,57], which resulted in clearly observable reflection at their bound. Due to elasticity of biological tissues, the position of this bound with respect to the end face of the OCT probe changed according to the shape of the pulse wave signal. Finally, this change was monitored using phase-sensitive demodulation of the acquired OCT signal.

Because of large attenuation of IR light in spectral range around 1.55 μm by water, contained in biological tissues, the reflection at epidermis-dermis bound mainly contributed to the acquired OCT signals. Additional reflection took place at the bound between stratum corneum and epidermis due to the difference of their refractive indexes. However, since the thickness of stratum corneum was quite small (about 10–15 μm), OPD of the corresponding interference component was small and this component was observed as a slowly oscillating signal component, as in Figure 4b. All lightwaves reflected deeper in dermis could be resolved because of strong attenuation of light with the used spectral range.
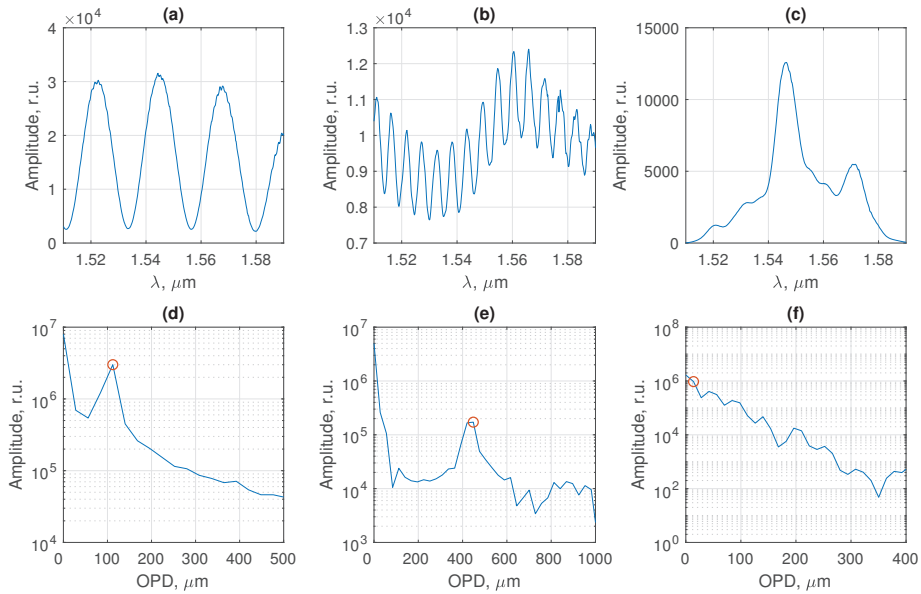
Figure 4. Examples of optical spectra and their FFTs of FPI (**a**,**d**); OCT (**b**,**e**) and SMS (**c**,**e**) sensors. Horizontal scales in (**d**–**f**) correspond to optical path length in air (note that OPD of FPI and OCT system is doubled air gap and tissue depth, respectively). Circles in (**d**–**f**) indicate FFT samples, from which phase the target signal was calculated.

Such choice of spectral range might be advantageous in terms of the laser safety as only the tissues close to the surface will be heated, while heat dissipation for the surface tissues is much more efficient than for the deep ones. Moreover, harmfullness of infrared radiation is verified through active use of 1540 and 1550 nm lasers in cosmetology [58]. Due to wide spread of OCT imaging techniques, their safety also has been extensively studied in large cohorts of patients, showing no hazards related to IR radiation exposure [59].

2.4. Singlemode-Multimode-Singlemode Interferometric Pulse Wave Sensor

As opposed to sensors described in the previous subsections, when spectral interrogation of SMS sensors is performed, sensors transmission spectra are acquired and processed. Therefore, the scheme of interrogation setup was slightly modified, with the sensor becoming the direct connection between the light source and the spectrometer, as depicted in Figure 5. The SMS sensor was fabricated using Jilong KL-280 fiber splicer. The multimode section consisted of a 5 cm long step-index Thorlabs FG050LGA fiber. At both ends, it was spliced to SMF-28 patchcords. For the sake of mechanical strength of the sensor, protective coating (PC) was left on the MMF and was applied to the splicing points. The reason for using step-index fiber is greater values of phase delays and therefore ability to obtain spectral interference signal with at least several oscillation periods in case of shorter MMF section as compared to graded-index fiber, which is important for practical applications of such sensors.
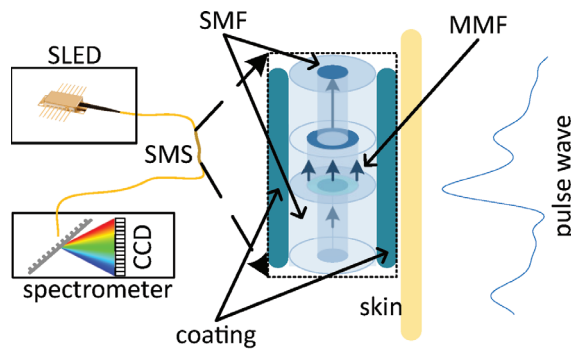
Figure 5. Schematic illustration of sensing setups for SMS pulse wave sensor.

The sensor was fixed to skin of the subject, whose pulse wave signal was measured with a flexible adhesive tape over an artery at a point with the most pronounced pulse sensible using fingertips as shown in Figure 1e for radial artery. No adhesive was added between the skin and the sensor. The physical principle of such a sensor relies on mechanical perturbation of the MMF section caused by the pulse wave and consequently induced intermodal phase delays, resulting in a change of acquired spectral interference signal.

3. Interferometric and Pulse Wave Signal Processing

The measured optical spectra were stored on the personal computer, to which the spectrometer was connected via USB protocol and further processed in Matlab. FBG signal was demodulated by fitting measured spectra with Gaussian functions as was done in [60,61] with its position, width and amplitude being fit parameters. It was shown in [61] that such the FBG demodulation approach is nearly optimal in terms of demodulated signal noise.

Demodulation of FPI, φ-OCT and SMS sensors was performed using FFT-based phase calculation, as it is often done in case of spectral interferometry [20,27,62]. Prior to calculating FFT, the measured optical spectrum was interpolated so that spectra samples corresponded to uniform spacing of optical frequency, not the wavelength. In this case interferometer OPD directly corresponded to fringe oscillation frequency, hence resulting in minimal broadening of FFT peaks [63]. Additionally, a Blackman window was applied to the optical spectrum before FFT calculation in order to mitigate the cross-talk between different interference components [64]. In φ-OCT, the phase (or argument) of a given sample of a complex-valued Fourier transform of the optical spectrum provides the information about the phase of the lightwaves reflected in a given position. Since the axial spatial resolution δL of OCT system as limited by the width of the measured optical spectrum, this calculated phase was an average over the waves reflected within a layer of δL width, centered around the bound of tissue layers with different refractive indexes. This way, sub-nanometer displacements of various layers in the inspected tissue could be accurately measured, with the resulting displacement resolution determined by the signal-to-noise ratio of the measured optical spectrum.

For FPI and φ-OCT sensors the phase of the most prominent interference components (marked with circles in Figure 4d,e, which corresponded to FPI cavity and reflections between the OCT probe end face and the bound between epidermis and dermis were used to form the resultant signal. Optical spectra and their FFTs for FPI and OCT sensors (OCT sensor was installed over radial artery) are shown in Figure 4a,b,d,e, respectively. In case of SMS sensor the choice was less obvious since, as can be seen in Figure 4c,f, optical spectrum of the SMS sensor contains a great number of interference components, which was expected for the SMS sensor with a step-index multimode section. Obviously, different harmonic components of the SMS optical spectrum corresponded to interference of MMF modes of different orders. This potentially led to different responses of these components' phases to the PW signal. In this work, we used the phase of the first sample of SMS spectra

FFT (the 0-th sample corresponds to the constant component) as the main demodulated signal for the SMS sensor (marked with circle in Figure 4f) due to its greatest magnitude and therefore, highest achievable SNR of the demodulated signal.

Temporal evolution of the measured vibration signal in interferometric sensors can be observed as a sequence of the measured phase samples. In case of relatively large dynamic range of the vibration signal (if the phase variation of the reflected lightwave is greater than 2π), phase unwrapping [65] must be applied in order to remove the discontinuities of the measured signal. Since the raw phase signal can contain a quasi-static component, caused by breathing, body movements, temperature changes, etc., a high-pass finite impulse response (FIR) filter with stop frequency 0.4 Hz and pass frequency 0.75 Hz was designed and used for phase signal processing.

After the above-mentioned processing of interference signals, pulse wave signals measured with different sensors were obtained. The comparison of sensors performance was carried out according to the following metrics of the pulse wave signal quality: signal to noise ratio (SNR); proportion of successfully extracted pulse wave signal features (PEPWF), such as wave peaks and wave feet; correlation of repetitive pulse wave intervals (CPWI); repeatability of PW interval decomposition features (RPWDF).

The above-mentioned quality metrics were calculated in the following manner: SNR was introduced as a ratio of standard deviation of high-pass filtered signal and white noise level, evaluated from high-pass filtered signal according to [66].

Pulse wave signal features such as wave foot and forward wave peak extraction was performed by one of the algorithms described in [6] (the one developed by *C. Orphanidou*). The algorithm was slightly modified in order to enable successful processing of signals measured from subjects with arterial pulse amplification. The details on algorithm modification and realization details can be found in [20]. Prior to feature extraction PW signal was filtered with a low-pass filter with cut-off frequency 10 Hz. The PEPWF metric was introduced as a ratio of a number of successfully retrieved wave foot and forward wave peak pairs to the total number of pulse wave intervals.

After the pulse wave intervals were successfully identified, it was possible to evaluate the repeatability of PW sensors operation by comparing the waveforms of repetitively measured PW intervals. In order to do that, the signals were divided into intervals corresponding to single pulse waves. The starting points were chosen as the boundaries of the pulse wave slopes. To eliminate the influence of the heart rate on the measurement results, each PW interval was interpolated. As a result, each interval contained the same number of samples, and the sampling rate was normalized on the pulse period. After interpolation, cross-correlation functions of all combinations of pulse wave intervals, identified in the analyzed signal were calculated. The maximal values of these cross-correlation functions were found, their mean value was used as a CPWI metric.

Relatively complex shape of typical PW signal (examples measured at radial and carotid arteries are shown in Figure 6) is due to superposition of direct pulse wave and several reflected waves. While CPWI metric reflects the repeatability of the whole shape of PW interval, more detailed analysis involving feature extraction can provide more quantitative information about PW propagation and sensor performance. In the current paper, we adopted the feature extraction approach, based on approximation of each PW interval by a superposition of six Gaussian functions of a form

$$f(t_0, w, A) = A\exp(-(t - t_0)^2/(w^2)), \tag{3}$$

where t_0, w and A are arrival time, width and amplitude of each wave, respectively. Similar multi-Gaussian models were used to describe PW signals in [7,67] and references therein. As a result, each interval was described by 18 parameters (amplitude, position and width of the Gaussian peaks). Initial approximations and restrictions on the values of the approximation parameters were chosen in such a way that the Gaussian functions corresponded to direct and reflected waves in the pulse wave signal, hence providing meaningful physical interpretation of the analyzed PW signals. Pulse wave interval

examples measured using the FPI sensor at the radial artery and at the carotid artery, as well as their approximations by a six-Gaussian model are shown in Figure 6a,b. According to humans' anatomy, the first reflected wave corresponded to the juncture between thoracic and abdominal aorta, and the second reflected wave to the juncture between the abdominal aorta and common iliac arteries [68,69].

Limiting our analysis to quantities with clear physical interpretation, we considered several RPWDF metrics, introduced using the following Gaussian functions parameters:

- standard deviations of delays of the first two reflected waves with respect to the direct wave (denoted as $RPWDF_{t_i}$, $i = 1, 2$);
- standard deviations of widths of the direct and the first two reflected waves (denoted as $RPWDF_{w_i}$, i from 0 to 2);
- ratio of standard deviations of the first two reflected waves' amplitudes and the corresponding direct wave's amplitude (denoted as $RPWDF_{A_i}$, $i = 1, 2$).
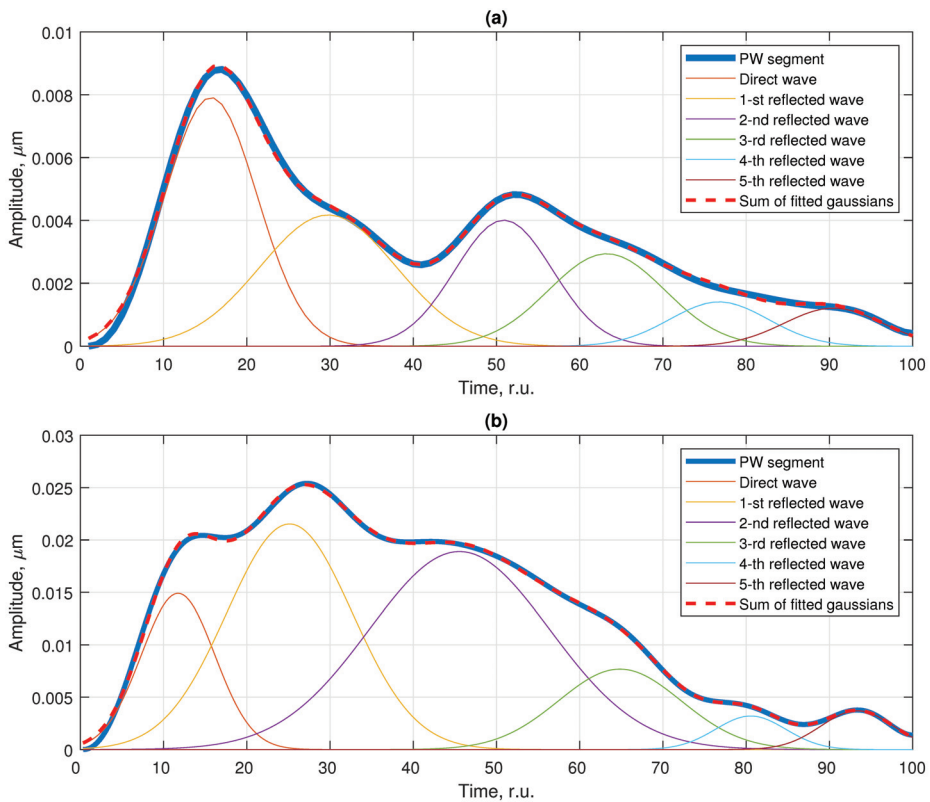

Figure 6. Examples of PW signal intervals measured at radial (**a**) and carotid (**b**) arteries and their approximations by a superposition of Gaussian functions, comprising a superposition into direct and reflected waves.

4. Experimental Results

The developed system was tested through measuring the pulse wave signals at different arteries, namely, radial, carotid and subclavian. Four individuals participated in the study: a 32-year-old man (Subject I), 26-year-old man (Subject II), 21-year-old woman (Subject III) and a 64-year-old woman (Subject IV). This allowed to demonstrate the system performance via registration of pulse wave signals with different properties. All participants were comprehensively informed about the experimental procedure and gave written

consent before the experiment, which was conducted according to the declaration of Helsinki and approved by the institutional ethics committee.

For each subject, pulse wave signal measurements were performed with each sensing element in 2 min sessions with resting periods between the sessions. The subjects were in a seated position and tried to be as still as possible. Sensing elements were applied as mentioned in Sections 2.1–2.4 at points above the arteries, in which the pulse wave sensed by fingertips was the strongest.

PW signals were demodulated as described in Section 3 using FFT-based phase calculation for interferometric sensors and using Gaussian fitting for the FBG sensor. The above-described metrics were calculated for all PW signals. The variation of the obtained values over different subjects and different arteries did not exceed 5%, so the averaged values were used for comparison of different sensing elements. Such comparison is presented in Table 1, numbers in bold show the best values.

Table 1. Comparison of pulse wave signals measured with different sensors. Best scores are shown in bold. Green text color shows the values that deviate not greater than 5% from the best score, orange text color—values which deviation from the best score is between 5% and 25%, red text color—values which deviation from the best score is greater than 25%.

	FPI	FBG	OCT	SMS
SNR, dB	65	30	**69**	40
PEPWF, %	99	95	**100**	78
CPWI average, r.u.	0.91	**0.96**	**0.96**	0.81
CPWI σ, r.u.	0.07	0.05	**0.03**	0.12
$RPWDF_{t_1}$, ms	16	**7**	**7**	62
$RPWDF_{t_2}$, ms	17	**12**	14	57
$RPWDF_{w_0}$, ms	4.6	9	**3**	19.6
$RPWDF_{w_1}$, ms	10.6	8.5	**6.1**	16.9
$RPWDF_{w_2}$, ms	25.6	**14.7**	22.5	26.4
$RPWDF_{A_1}$, r.u	0.27	**0.14**	0.15	0.5
$RPWDF_{A_2}$, r.u	0.23	**0.21**	0.37	0.57

One of the most important characteristics of any measured signal is signal to noise ratio. In terms of this metric, the best performance was demonstrated by optical coherence tomography (69 dB) and Fabry–Perot interferometer (65 dB). Another objective metric, characterizing signal quality is the amount of signal features, extracted from the measured PW signal using some already validated algorithm, denoted as PEPWF. In this case, three approaches (FPI, FBG and OCT) demonstrated comparable performance, with slight advantage of OCT and FPI over the FBG sensor (100% and 99% versus 95%).

The rest of the introduced metrics demonstrated the reliability of the compared approaches by demonstrating the repeatability of the measured PW signals. Assuming that, for a subject being in a relaxed and calm state and not performing any physical exercises, the shape of the pulse wave signal remains constant, it is possible to compare the shapes of repetitively measured PW intervals and draw conclusions about sensors' performance on this basis. In order to do that, the above-mentioned interpolation of the PW intervals was performed, which eliminated the influence of heart rate variability [70] on signal shape repeatability. For correct results, the length of the analyzed PW signal on the one hand had to be much longer than the pulse period, so that a sufficient number of PW intervals was compared, and on the other hand had to be not long enough so that cardiovascular system state (influenced by fasting, mental stress, etc.) remained the same. Again, the OCT approach demonstrated the best results, with the average cross-correlation of PW

intervals (CPWI average metric) of 0.96 and standard deviation (CPWI σ metric) of 0.03. FBG sensor demonstrated the same average cross-correlation, but slightly greater standard deviation of 0.05. A similar picture with the best scores achieved by OCT and FBG sensors could be observed in terms of PW signal features obtained via pulse wave decomposition into direct and reflected waves (RPWDF parameters).

For every sensor, it is important to ensure that the cross-sensitivity to physical quantities that are not the subject of interest. In our case, the main value of interest is sensor deformation (or change of epidermis optical path difference for the OCT approach), caused by the pulse wave. On the other hand, such processes as body temperature change, breathing and body movement can lead to undesired artefacts of the demodulated signal.

For the OCT pulse wave sensing approach, temperature fluctuations resulted in practically no cross-talk since it could only be induced by the epidermis temperature change. However, due to the thermoregulation function of the human body [71,72], skin temperature change occurs slowly and within a finite temperature range. Therefore, any temperature-induced epidermis OPD change is filtered out before the feature extraction procedure and does not result in any influence on the measured pulse wave signal. A similar conclusion can safely be drawn for FBG and FPI sensors—due to their close contact with the skin, high thermal conductivity of silica glass and the compactness of optical fibers, ambient temperature induced only a slight quasi-static component of sensors' signals, which was completely removed by the high-pass filter, used for signal processing. Anyway, the temperature stability of the FPI sensor might be made even better with the use of specially designed temperature-compensating sensing element constructions [73,74]. However, the situation might be slightly different for the SMS sensor, in which the change of temperature can cause intermode phase shifts different from the ones induced by the PW signal, resulting in sensor response nonlinearity.

The effect of sensors cooling on the demodulated PW signal was tested in a separate experiment, in which Subject II participated. After the sensor was applied to the wrist above the radial artery, the sensor was cooled by putting the arm out of the laboratory window. The outside temperature at that moment was about 10 degrees Celsius, leading to sensor cooling. All tested sensors except for the SMS showed no change of demodulated PW signal shape: after filtering out the quasi-static component, the signal shape and signal metrics remained the same. However, cooling of the SMS sensor led to significant change of demodulated signal shape, which is shown in Figure 7. This experiment also validated the repeatability of sensors performance after its reapplication.

Breathing during the PW measurement causes amplitude and frequency modulation of the demodulated signal, as well as adds some low-frequency component due to physiological factors [75]. The low-frequency component is the most detrimental of these effects in terms of further signal processing, however, it is completely removed with the use of high-pass filter, applied to the signal before the feature extraction. The remaining amplitude and frequency modulation of the measured PW signals can be observed in Figures 7 and in 8a,c,e,g.

An additional experiment was performed in order to estimate the susceptibility of different sensors to motion artifacts. Only Subject I participated in this additional study. Sensors were attached to skin over the radial artery near the wrist, as described above. The subject was repetitively squeezing his palm into fist and releasing it with periodicity about 10 s. For each sensor, the PW measurements were performed for 2 min with short rests between the measurements. As can be seen in Figure 8, there were notable motion artifacts and change of the shape of demodulated signal. However, this effect was much stronger for FBG, FPI and SMS sensors than for the OCT sensor. A comparison of the obtained results can be found in Table 2.
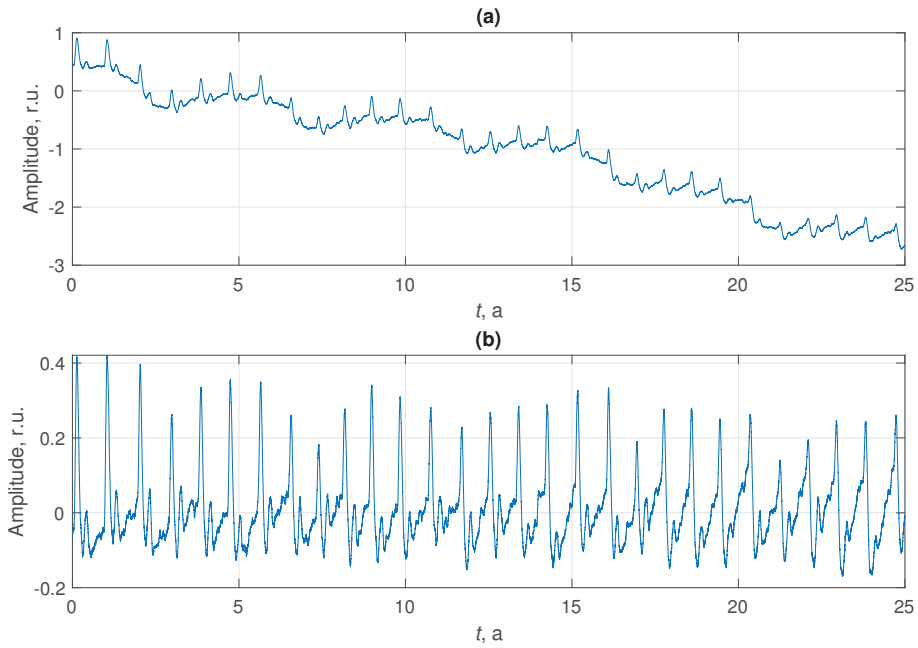
Figure 7. Fragment of PW signal measured at radial artery of Subject II with SMS sensor during sensor cooling. (**a**) raw signal, (**b**) high-pass filtered signal.

Table 2. Comparison of pulse wave signals measured with different sensors. Measurements were performed at the radial artery with palm movement. Best scores are shown in bold. Green text color shows the values that deviate not greater than 5% from the best score, orange text color—values which deviation from the best score is between 5% and 25%, red text color—values which deviation from the best score is greater than 25%.

	FPI	FBG	OCT	SMS
SNR, dB	65	30	**69**	40
PEPWF, %	79	30	**88**	7
CPWI average, r.u.	0.72	0.59	**0.76**	0.6
CPWI σ, r.u.	**0.14**	0.17	0.15	0.20
RPWDF$_{t_1}$, ms	15	20	**11**	16
RPWDF$_{t_2}$, ms	22	27	**18**	23
RPWDF$_{w_0}$, ms	9.6	11.5	**5.8**	9.2
RPWDF$_{w_1}$, ms	10.7	7.8	**6.3**	9.9
RPWDF$_{w_2}$, ms	11.4	9.4	12.4	**7.6**
RPWDF$_{A_1}$, r.u	0.39	0.42	**0.28**	0.35
RPWDF$_{A_2}$, r.u	0.53	0.38	0.46	**0.34**

However, unlike FBG and FPI sensors, the signal of the SMS sensor became considerably distorted only on a relatively short time interval, corresponding to the most rapid palm movement (the corresponding motion artefact can be seen in Figure 8h at time interval

121

around 6–7 s). However, outside of the motion artifact area, the signal correlated with typical PW shape very well, except for the inverted shape before the 4-th s. Additionally, some fluctuations of PW signal measured with the SMS sensor were present even without any deliberate movements. This indicated nonlinear response of the SMS sensor with simple FFT-based interrogation to the pulse wave.
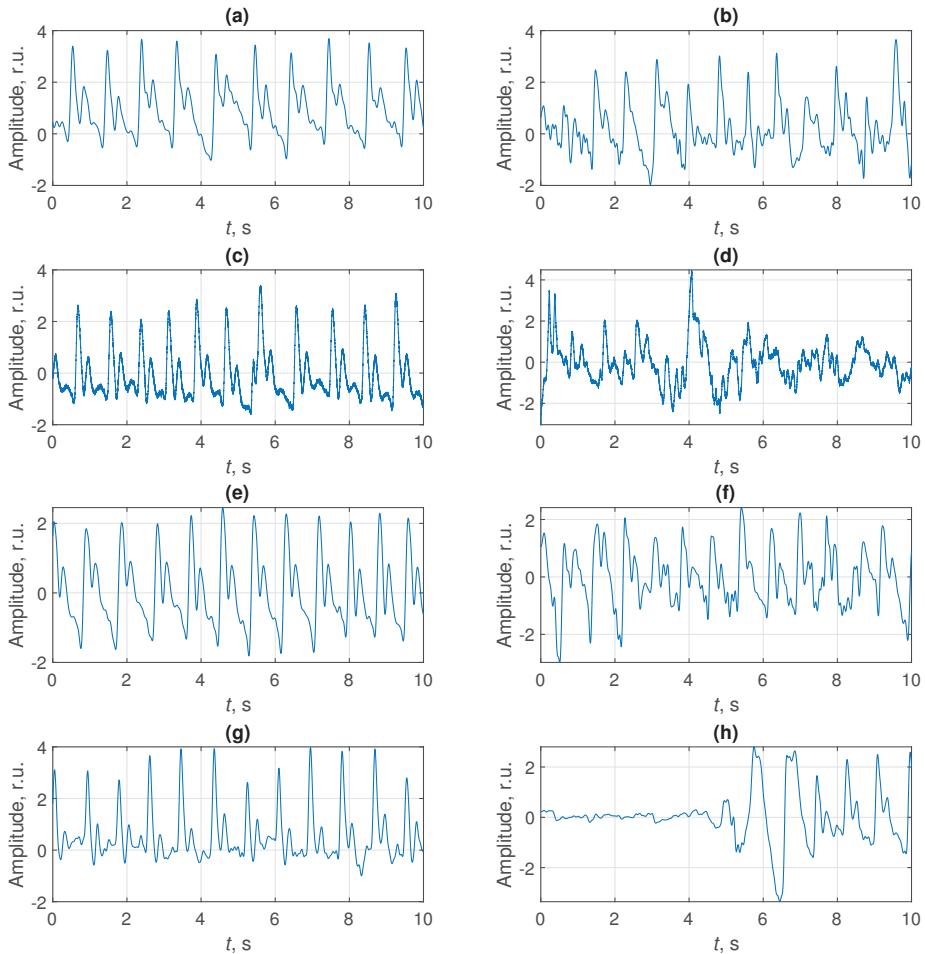

Figure 8. Examples of PW signals measured at radial artery of Subject I using FPI (**a,b**) FBG (**c,d**), OCT (**e,f**) and SMS (**g,h**) sensors in case of still posture (**a,c,e,g**) and palm movement (**b,d,f,h**).

As can be seen in Tables 1 and 2, there was no obvious winner when the subject was not moving, with OCT method having most of the best metrics and FBG and FPI being close in some of the metrics. However, the PW measurements on radial artery during hand movement revealed the clear advantage of the OCT approach compared to the rest compared ones.

Reproducibility of sensors characteristics was verified through an additional experiment, for which separate sensing elements with similar properties to those mentioned in Sections 2.1–2.4 were used. Subject II participated in this additional experiment, no deliberate body movements were made. The calculated signal metrics were very close to

those reported in Table 1, with the difference not exceeding 5% for SNR, PEPWF and CPWI metrics and reaching up to about 10% for some of the RPWDF metrics.

5. Discussion

The results reported in Section 4 demonstrate that the small footprint of the sensor and absence of mechanical coupling between the measured signal and the sensing element are key ingredients for a minimally distorted PW signal. Although spectral interferometric demodulation provides the lowest noises, FPI sensor performance in terms of repeatability is slightly worse than the FBG one, presumably due to greater footprint and non constant mechanical coupling between the pulse wave and the sensor. Nevertheless, an additional experiment performed when the subject made palm movements, showed that the OCT sensor has superior performance in terms of motion artifacts reduction as compared to the rest tested sensors. The main cause for that is the more direct sensing mechanism of the φ-OCT approach—in contrast to FPI, FBG and SMS, it does not rely on mechanical deformation of the sensing element caused by the pulse wave. Instead, the φ-OCT approach directly monitors the displacement of biological tissues, which are induced by the pulse wave propagation. This is the main reason for high SNR and measurement repeatability, achieved by the φ-OCT approach.

Along with the sensors' measurement performance, their ability to be implemented in a portable format, be interrogated by cost-effective hardware and be integrated into modern gadgets is vital for their evolution from laboratory prototypes to commercial products, demanded by healthcare and sport industries. In this regard, there are two important limitations on the interrogation hardware: the use of a spatially incoherent light source, such as LED, which are much more cost-effective than SLED or ASE sources; and low spectral resolution of the optical spectrometer used to acquire sensors' spectra. Another important property is an ability to simultaneously interrogate several multiplexed sensing elements.

Regarding the desirable ability to work with spatially incoherent light, it, in turn, leads to the requirement of only multimode fibers being used in the whole fiber system since it is fundamentally impossible to efficiently couple spatially incoherent light into singlemode optical fiber [76]. This immediately leads to the problem of modal noise [61] that can give rise to parasitic interference signals, which will affect sensor resolution. However, smartphone-based interrogation of FPI [77,78] and FBG [61] sensors has already been successfully demonstrated. All-multimode sensors equivalent to SMS are definitely possible, with intermode interference used for sensing taking place in a largely multimode fiber, sandwiched between two MMFs with smaller number of propagating modes. OCT in all-multimode systems has already been experimentally demonstrated [79], paving the way for its use with portable devices.

Spectral resolution of an optical spectrometer used for sensor interrogation must be in accordance with the width of the sensor's spectrum features, such as reflection peak of FBG or interference fringes of interference sensors. FPI sensors offer the greatest flexibility in this regard, with periods of spectral interference signals ranging from tens of nanometers in case of short-cavity FPIs, allowing to use spectrometers with sufficiently low spectral resolutions of around several nanometers. Typically, the width of the FBG reflection spectrum is about 100–200 pm, therefore, requiring the use of spectrometers with relatively high spectral resolution for correct spectra measurement. However, gratings inscribed in multimode fibers exhibit complex multipeak spectra and therefore are typically chirped in order to obtain a single spectral feature, resulting in a several nm-width reflection peak [61], requiring spectral resolution of spectrometer about 1 nm. This, however, leads to a decrease of achievable measurement resolution and therefore, will result in further decrease of SNR, which, as shown above, even with FBG inscribed in SMF is not quite high. Sensors based on intermodal interference typically have rather complex spectra with fine spectral features, sometimes used for signal demodulation [24]. However, as shown in Sections 3 and 4, the signal of an SMS sensor was obtained from

the interference component, corresponding to the lower-order modes interference. This interference signal component has a large oscillation period and therefore can be acquired using a spectrometer with low spectral resolution (on the order of 10–20 nm). Finally, since the φ-OCT approach proposed for PW measurement relies on demodulation of phase of a lightwave, reflected from the bound between epidermis and dermis, and is realized using a common-path scheme, it is crucial that the interference signal with OPD equal to doubled optical length of epidermis is acquired without distortions. As follows from the known values of epidermis thickness and refractive index as well as from the obtained data, OPD of such interferometer is about 400 μm. This corresponds to a period of OCT spectrum oscillations about 5 nm, requiring spectral resolution of spectrometer not less than 1–2 nm, which is realizable even with smartphone-based spectrometers [61,80].

In terms of multiplexing capacity, FBG sensors with the use of the wavelength-division multiplexing approach have an obvious advantage. For example, with the spectrometer used in our work with 85 nm spectral span, FBG spectral spacing of 1.5 nm, it is possible to simultaneously interrogate up to 56 multiplexed sensors. FPI sensors also offer multiplexing abilities, typically realized through spatial frequency-division multiplexing (SFDM), sometimes also referred to as OPD-domain multiplexing. Multiplexing tens of FPI sensors is technically possible, but will either require the use of a light source with a relatively high intensity or will result in reduced resolution [81]. Multiplexed OCT systems have already been demonstrated [82,83] with a principle that is similar to SFDM. Limiting factor for multiplexing of OCT probes will be imaging depth and spectral resolution of the spectrometer. In our case of imaging depth up to about 400 μm and spectral resolution of about 200 nm (with corresponding effective coherence length 6 mm and maximal imaging depth of a single probe system of 3 mm) it leads to potentially up to about 6–7 multiplexed probes. To the best of our knowledge, multiplexing of SMS sensors has not been reported yet, although in principle, it can be performed with the SFDM approach as well.

Other practical aspects of such sensing systems include repeatability of sensing characteristics, as well as reproducibility of characteristics of sensing elements and their fabrication cost. Repeatability mainly depends on mechanical coupling between the pulse wave and the sensing element, therefore, the OCT approach has a clear advantage, even despite its small area and seemingly higher requirement to sensor alignment. However, since there is no adhesive used to fix the OCT probe on skin, it is easy to manually adjust it while observing the demodulated signal in order to achieve the highest amplitude. An SMS sensor could also have some advantage in point thanks to its greater length and therefore, greater chance of coincidence of its section with the area of maximal sensitivity. However, this could not be observed in the current study due to the sensor nonlinearity.

In terms of reproducibility, fabrication of FPI sensor of the configuration used in our work is the simplest one in terms of required equipment, requiring a fiber stripper, a fiber cleaver, capillary cleaver (it can also be cleaved manually), glue and equipment for inserting cleaved fibers into capillary (the latter can be performed manually by a trained person). In terms of sensor characteristics reproducibility, the most crucial point is the flatness and cleavage angles of fiber end faces [84,85], which can be monitored right after the cleavage using a conventional optical microscope. For FBG sensor reproducibility of its characteristics solely depends on the grating inscription setup and recoating process and typically is quite high. Reproducibility of the proposed φ-OCT PW monitoring technique depends primarily on the difference between epidermis and dermis refractive index values, which is consistent within several independent studies [86–88]. The properties of the sensing element mainly influence the amplitude of the demodulated PW signal. Nevertheless, their reproducibility is quite high in case of high quality fiber cleaver and splicer used to produce the sensing element. Reproducibility of SMS sensor characteristics might be the most problematic at the moment due to the above-mentioned sensor nonlinearity. However, its fabrication is not much more complicated than for FPI and OCT sensors, requiring four fiber cleavages and two splices. From the current point, it is hard to predict the cost of sensing elements, however, we believe that for all of them it would be on the same order

of magnitude, since higher cost of grating inscription hardware required to produce FBG sensor is compensated by greater amount of required manual production operations (fiber cleaving, splicing) for FPI, OCT and SMS sensors. Anyway, sensing elements cost still might be several times lower than the cost of even the simplest interrogation hardware.

The above-mentioned parameters of the compared sensing configurations are listed in Table 3. To summarize, we believe that the φ-OCT approach of pulse wave monitoring may be of the greatest interest for the use in applications where the highest measurement accuracy is needed: medical research and cardiovascular clinics. At the same time, FPI sensors might be most well-suited for use in personal and portable devices since, as follows from the obtained results and the analysis above, they offer a compromise between signal quality and repeatability on the one hand and can be multiplexed, interrogated by simple and cost-effective hardware and demonstrate very weak temperature cross-sensitivity on the other hand. According to the reported results, the main drawbacks of the FBG sensor are relatively low SNR and susceptibility to motion artefacts. However, both of these problems can be solved by the use of FBGs inscribed in polymer fibers, which are also compatible with low-cost interrogation hardware, making them a tight concurrent of FPI sensors, which, according to our study, turn out to be preferable. The use of SMS sensors for pulse wave monitoring and other biomedical tasks may also be prominent if more advanced signal processing algorithms based on detailed analysis of mode propagation in the MMF section are developed.

Table 3. Comparison of technical properties of the investigated sensors. σ_{SPEC}—spectral resolution, N_{MULT}—number of multiplexed sensors.

	FPI	FBG	OCT	SMS
Required σ_{SPEC}, nm	<10–20	0.1	1–2	<10–20
N_{MULT}	<10–20	<50–60	<6–8	?
Limiting factor of N_{MULT}	σ_{SPEC}	Spectral range	σ_{SPEC}	σ_{SPEC}, number of modes
MMF compatibility	+	+, but reduces resolution	+	possible
Signal quality rank, still	3	2	1	4
Signal quality rank, movement	2	3	1	4

6. Conclusions

The paper reports on a comparative study of four pulse wave fiber-optic sensors, based on Fabry–Perot interferometer, fiber Bragg grating, optical coherence tomography and singlemode-multimode-singlemode intermodal interferometer. In order to compare the sensors performance, several metrics, evaluating the quality of the obtained PW signals were proposed. According to the scores produced by the proposed metrics, the OCT approach turned out to be the most advantageous. Additional experiment, involving PW measurement of a moving subject also showed that the OCT approach is the most robust against the motion artifacts among the compared ones. However, as follows from the analysis presented in discussion, FPI sensors, having slightly lower scores, are better suited for implementation of portable sensing systems. In turn, the OCT approach of pulse wave monitoring can be successfully implemented for more unique tasks, such as scientific research of pulse wave propagation and cardiovascular system function and be used in specialized clinics.

It should be further noted that configurations of FPI [16,19] and FBG [18,89,90] pulse wave sensors, different from the ones used in our study, have been reported, which might demonstrate different sensing characteristics. Performance of the φ-OCT approach can be further increased by incorporating micro- and nano-optics for higher light confinement and reduction of light loss inside biological tissues [38,91,92].

References

1. Peltokangas, M.; Vehkaoja, A.; Verho, J.; Mattila, V.M.; Romsi, P.; Lekkala, J.; Oksala, N. Age Dependence of Arterial Pulse Wave Parameters Extracted From Dynamic Blood Pressure and Blood Volume Pulse Waves. *IEEE J. Biomed. Health Inform.* **2017**, *21*, 142–149. [CrossRef]
2. Townsend, R.R. Arterial Stiffness: Recommendations and Standardization. *Pulse* **2016**, *4*, 3–7. [CrossRef]
3. Laurent, S.; Cockcroft, J.; Van Bortel, L.; Boutouyrie, P.; Giannattasio, C.; Hayoz, D.; Pannier, B.; Vlachopoulos, C.; Wilkinson, I.; Struijker-Boudier, H. Expert consensus document on arterial stiffness: Methodological issues and clinical applications. *Eur. Heart J.* **2006**, *27*, 2588–2605. [CrossRef]
4. Pereira, T.; Correia, C.; Cardoso, J. Novel methods for pulse wave velocity measurement. *J. Med. Biol. Eng.* **2015**, *35*, 555–565. [CrossRef]
5. Salvi, P. *Pulse Waves: How Vascular Hemodynamics Affects Blood Pressure*, 2nd ed.; Springer: New York, NY, USA, 2017; p. 221.
6. Charlton, P.H.; Bonnici, T.; Tarassenko, L.; Clifton, D.A.; Beale, R.; Watkinson, P.J. An assessment of algorithms to estimate respiratory rate from the electrocardiogram and photoplethysmogram. *Physiol. Meas.* **2016**, *37*, 610–626. [CrossRef] [PubMed]
7. Couceiro, R.; Carvalho, P.; Paiva, R.P.; Henriques, J.; Quintal, I.; Antunes, M.; Muehlsteff, J.; Eickholt, C.; Brinkmeyer, C.; Kelm, M.; et al. Assessment of cardiovascular function from multi-Gaussian fitting of a finger photoplethysmogram. *Physiol. Meas.* **2015**, *36*, 1801–1825. [CrossRef]
8. Schäfer, A.; Vagedes, J. How accurate is pulse rate variability as an estimate of heart rate variability? A review on studies comparing photoplethysmographic technology with an electrocardiogram. *Int. J. Cardiol.* **2013**, *166*, 15–29. [CrossRef]
9. Moço, A.V.; Stuijk, S.; De Haan, G. New insights into the origin of remote PPG signals in visible light and infrared. *Sci. Rep.* **2018**, *8*, 8501. [CrossRef]
10. Elgendi, M. On the Analysis of Fingertip Photoplethysmogram Signals. *Curr. Cardiol. Rev.* **2012**, *8*, 14–25. [CrossRef] [PubMed]
11. Couceiro, R.; Carvalho, P.; Paiva, R.P.; Henriques, J.; Muehlsteff, J. Detection of motion artifact patterns in photoplethysmographic signals based on time and period domain analysis. *Physiol. Meas.* **2014**, *35*, 2369–2388. [CrossRef] [PubMed]
12. Katayama, K.; Chino, S.; Kurasawa, S.; Koyama, S.; Ishizawa, H.; Fujimoto, K. Classification of Pulse Wave Signal Measured by FBG Sensor for Vascular Age and Arteriosclerosis Estimation. *IEEE Sens. J.* **2020**, *20*, 2485–2491. [CrossRef]
13. Lo Presti, D.; Massaroni, C.; D'Abbraccio, J.; Massari, L.; Caponero, M.; Longo, U.G.; Formica, D.; Oddo, C.M.; Schena, E. Wearable system based on flexible FBG for respiratory and cardiac monitoring. *IEEE Sens. J.* **2019**, *19*, 7391–7398. [CrossRef]
14. Dziuda, L.; Skibniewski, F.W.; Krej, M.; Lewandowski, J. Monitoring respiration and cardiac activity using fiber Bragg grating-based sensor. *IEEE Trans. Biomed. Eng.* **2012**, *59*, 1934–1942. [CrossRef] [PubMed]
15. Kurasawa, S.; Koyama, S.; Ishizawa, H.; Fujimoto, K.; Chino, S. Verification of non-invasive blood glucose measurement method based on pulse wave signal detected by FBG sensor system. *Sensors* **2017**, *17*, 2702. [CrossRef]
16. Domingues, M.F.; Tavares, C.; Alberto, N.; Radwan, A.; André, P.; Antunes, P. High Rate Dynamic Monitoring with Fabry–Perot Interferometric Sensors: An Alternative Interrogation Technique Targeting Biomedical Applications. *Sensors* **2019**, *19*, 4744. [CrossRef] [PubMed]
17. Haseda, Y.; Bonefacino, J.; Tam, H.Y.; Chino, S.; Koyama, S.; Ishizawa, H. Measurement of Pulse Wave Signals and Blood Pressure by a Plastic Optical Fiber FBG Sensor. *Sensors* **2019**, *19*, 5088. [CrossRef] [PubMed]
18. Leitão, C.; Antunes, P.; André, P.; Pinto, J.L.; Bastos, J.M. Central arterial pulse waveform acquisition with a portable pen-like optical fiber sensor. *Blood Press. Monit.* **2015**, *20*, 43–46. [CrossRef]
19. Wang, J.; Liu, K.; Sun, Q.; Ni, X.; Ai, F.; Wang, S.; Yan, Z.; Liu, D. Diaphragm-based optical fiber sensor for pulse wave monitoring and cardiovascular diseases diagnosis. *J. Bio.* **2019**, *12*, 1–10. [CrossRef] [PubMed]

20. Ushakov, N.A. Markvart, A.A.; Liokumovich, L.B. Pulse Wave Velocity Measurement with Multiplexed Fiber Optic Fabry-Perot Interferometric Sensors. *IEEE Sens. J.* **2020**, *20*, 11302–11312. [CrossRef]

21. Theodosiou, A.; Kalli, K. Recent trends and advances of fibre Bragg grating sensors in CYTOP polymer optical fibres. *Opt. Fiber Technol.* **2020**, *54*, 102079. [CrossRef]

22. Ushakov, N.A.; Liokumovich, L.B. Abrupt $\lambda/2$ demodulation errors in spectral interferometry: origins and suppression. *IEEE Photonics Technol. Lett.* **2020**, *32*, 1159–1162. [CrossRef]

23. Zhang, W.; Lei, X.; Chen, W.; Xu, H.; Wang, A. Modeling of spectral changes in bent fiber Bragg gratings. *Opt. Lett.* **2015**, *40*, 3260. [CrossRef] [PubMed]

24. Silva, S.; Frazão, O.; Viegas, J.; Ferreira, L.A.; Araújo, F.M.; Malcata, F.X.; Santos, J.L. Temperature and strain-independent curvature sensor based on a singlemode/multimode fiber optic structure. *Meas. Sci. Technol.* **2011**, *22*, 085201. [CrossRef]

25. Wu, Q.; Hatta, A.M.; Wang, P.; Semenova, Y.; Farrell, G. Use of a Bent Single SMS Fiber Structure for Simultaneous Measurement of Displacement and Temperature Sensing. *IEEE Photonics Technol. Lett.* **2011**, *23*, 130–132. [CrossRef]

26. Lu, C.; Su, J.; Dong, X.; Sun, T.; Grattan, K.T.V. Simultaneous Measurement of Strain and Temperature With a Few-Mode Fiber-Based Sensor. *J. Light. Technol.* **2018**, *36*, 2796–2802. [CrossRef]

27. Cardona-Maya, Y.; Socorro, A.B.; Del Villar, I.; Cruz, J.L.; Corres, J.M.; Botero-Cadavid, J.F. Label-free wavelength and phase detection based SMS fiber immunosensors optimized with cladding etching. *Sens. Actuators B Chem.* **2018**, *265*, 10–19. [CrossRef]

28. Wang, P.; Zhang, S.; Wang, R.; Farrell, G.; Zhang, M.; Geng, T.; Lewis, E.; Tian, K. Temperature-insensitive refractometer based on an RI-modulated singlemode-multimode-singlemode fibre structure. *Opt. Express* **2019**, *27*, 13754. [CrossRef] [PubMed]

29. Pevec, S.; Donlagić, D. Multiparameter fiber-optic sensors: A review. *Opt. Eng.* **2019**, *58*, 1. [CrossRef]

30. Leal-Junior, A.G.; Theodosiou, A.; Diaz, C.R.; Marques, C.; Pontes, M.J.; Kalli, K.; Frizera, A. Simultaneous measurement of axial strain, bending and torsion with a single fiber bragg grating in CYTOP fiber. *J. Light. Technol.* **2019**, *37*, 971–980. [CrossRef]

31. Leal-Junior, A.G.; Díaz, C.R.; Leitão, C.; Pontes, M.J.; Marques, C.; Frizera, A. Polymer optical fiber-based sensor for simultaneous measurement of breath and heart rate under dynamic movements. *Opt. Laser Technol.* **2019**, *109*, 429–436. [CrossRef]

32. Leal-Junior, A.G.; Diaz, C.R.; Jimenez, M.F.; Leitao, C.; Marques, C.; Pontes, M.J.; Frizera, A. Polymer Optical Fiber-Based Sensor System for Smart Walker Instrumentation and Health Assessment. *IEEE Sens. J.* **2019**, *19*, 567–574. [CrossRef]

33. Segers, P.; Rietzschel, E.R.; Chirinos, J.A. How to Measure Arterial Stiffness in Humans. *Arterioscler. Thromb. Vasc. Biol.* **2020**, *40*, 1034–1043. [CrossRef] [PubMed]

34. Leitgeb, R.A. En face optical coherence tomography: A technology review [Invited]. *Biomed. Opt. Express* **2019**, *10*, 2177. [CrossRef] [PubMed]

35. Fercher, A.F.; Mengedoht, K.; Werner, W. Eye-length measurement by interferometry with partially coherent light. *Opt. Lett.* **1988**, *13*, 186. [CrossRef] [PubMed]

36. Azimipour, M.; Migacz, J.V.; Zawadzki, R.J.; Werner, J.S.; Jonnal, R.S. Functional retinal imaging using adaptive optics swept-source OCT at 16 MHz. *Optica* **2019**, *6*, 300. [CrossRef]

37. de Moura, J.; Vidal, P.L.; Novo, J.; Rouco, J.; Penedo, M.G.; Ortega, M. Intraretinal Fluid Pattern Characterization in Optical Coherence Tomography Images. *Sensors* **2020**, *20*, 2004. [CrossRef]

38. Pahlevaninezhad, H.; Khorasaninejad, M.; Huang, Y.W.; Shi, Z.; Hariri, L.P.; Adams, D.C.; Ding, V.; Zhu, A.; Qiu, C.W.; Capasso, F.; et al. Nano-optic endoscope for high-resolution optical coherence tomography in vivo. *Nat. Photonics* **2018**, *12*, 540–547. [CrossRef]

39. Tearney, G.J.; Brezinski, M.E.; Bouma, B.E.; Boppart, S.A.; Pitris, C.; Southern, J.F.; Fujimoto, J.G. In vivo endoscopic optical biopsy with optical coherence tomography. *Science* **1997**, *276*, 2037–2039. [CrossRef]

40. Wang, J.; Tao, K.; Zhu, W.; Jiang, J.; Liu, T. A FBG-OCT catheter to reconstruct vascular shape in intravascular optical coherence tomography. *IEEE Photonics Technol. Lett.* **2019**, *31*, 701–704. [CrossRef]

41. Gan, Y.; Fleming, C.P. Extracting three-dimensional orientation and tractography of myofibers using optical coherence tomography. *Biomed. Opt. Express* **2013**, *4*, 2150–2165. [CrossRef]

42. Li, Q.; Karnowski, K.; Untracht, G.; Noble, P.B.; Cense, B.; Villiger, M.; Sampson, D.D. Vectorial birefringence imaging by optical coherence microscopy for assessing fibrillar microstructures in the cornea and limbus. *Biomed. Opt. Express* **2020**, *11*, 1122–1138. [CrossRef]

43. Podoleanu, A.G. Fiber Optics, from Sensing to Non Invasive High Resolution Medical Imaging. *J. Light. Technol.* **2010**, *28*, 624–640. [CrossRef]

44. De Boer, J.F.; Leitgeb, R.; Wojtkowski, M. Twenty-five years of optical coherence tomography: The paradigm shift in sensitivity and speed provided by Fourier domain OCT [Invited]. *Biomed. Opt. Express* **2017**, *8*, 3248–3280. [CrossRef]

45. Tang, P.; Li, Y.; Rakymzhan, A.; Xie, Z.; Wang, R.K. Measurement and visualization of stimulus-evoked tissue dynamics in mouse barrel cortex using phase-sensitive optical coherence tomography. *Biomed. Opt. Express* **2020**, *11*, 699. [CrossRef]

46. Li, P.; Shen, T.T.; Johnstone, M.; Wang, R.K. Pulsatile motion of the trabecular meshwork in healthy human subjects quantified by phase-sensitive optical coherence tomography. *Biomed. Opt. Express* **2013**, *4*, 2051. [CrossRef] [PubMed]

47. Dion, C.; Singh, K.; Ozaki, T.; Lesk, M.R.; Costantino, S. Analysis of Pulsatile Retinal Movements by Spectral-Domain Low-Coherence Interferometry: Influence of Age and Glaucoma on the Pulse Wave. *PLoS ONE* **2013**, *8*, e54207. [CrossRef] [PubMed]

48. Spahr, H.; Hillmann, D.; Hain, C.; Pfäffle, C.; Sudkamp, H.; Franke, G.; Hüttmann, G. Imaging pulse wave propagation in human retinal vessels using full-field swept-source optical coherence tomography. *Opt. Lett.* **2015**, *40*, 4771. [CrossRef] [PubMed]

49. Li, Q.; Li, L.; Fan, S.; Dai, C.; Chai, X.; Zhou, C. Retinal pulse wave velocity measurement using spectral-domain optical coherence tomography. *J. Bio.* **2018**, *11*, e201700163. [CrossRef]

50. Kuwabara, M.; Fuji, T.; Ohrni, M.; Haruna, M. Dynamic optical coherence tomography of small arteries and veins of human fingers. *Appl. Phys. Express* **2008**, *1*, 0580011–0580013. [CrossRef]

51. Zhao, Y.; Chen, Z.; Saxer, C.; Xiang, S.; de Boer, J.F.; Nelson, J.S. Phase-resolved optical coherence tomography and optical Doppler tomography for imaging blood flow in human skin with fast scanning speed and high velocity sensitivity. *Opt. Lett.* **2000**, *25*, 114. [CrossRef]

52. Salvi, P.; Scalise, F.; Rovina, M.; Moretti, F.; Salvi, L.; Grillo, A.; Gao, L.; Baldi, C.; Faini, A.; Furlanis, G.; et al. Noninvasive Estimation of Aortic Stiffness Through Different Approaches: Comparison with Intra-Aortic Recordings. *Hypertension* **2019**, *74*, 117–129. [CrossRef] [PubMed]

53. Vakhtin, A.B.; Kane, D.J.; Wood, W.R.; Peterson, K.A. Common-path interferometer for frequency-domain optical coherence tomography. *Appl. Opt.* **2003**, *42*, 6953. [CrossRef] [PubMed]

54. Wang, C.; Zhang, Q.; Wang, Y.; Zhang, X.; Zhang, L. Long-range common-path spectral domain optical coherence tomography. *Opt. Express* **2019**, *27*, 12483. [CrossRef] [PubMed]

55. Ushakov, N.A.; Liokumovich, L.B. Resolution limits of extrinsic Fabry–Perot interferometric displacement sensors utilizing wavelength scanning interrogation. *Appl. Opt.* **2014**, *53*, 5092–5099. [CrossRef]

56. Ding, H.; Lu, J.Q.; Wooden, W.A.; Kragel, P.J.; Hu, X.H. Refractive indices of human skin tissues at eight wavelengths and estimated dispersion relations between 300 and 1600 nm. *Phys. Med. Biol.* **2006**, *51*, 1479–1489. [CrossRef]

57. Lister, T.; Wright, P.A.; Chappell, P.H. Optical properties of human skin. *J. Biomed. Opt.* **2012**, *17*, 0909011. [CrossRef]

58. Modena, D.A.O.; Miranda, A.C.G.; Grecco, C.; Liebano, R.E.; Cordeiro, R.C.T.; Guidi, R.M. Efficacy, safety, and guidelines of application of the fractional ablative laser erbium YAG 2940 nm and non-ablative laser erbium glass in rejuvenation, skin spots, and acne in different skin phototypes: A systematic review. *Lasers Med. Sci.* **2020**, *35*, 1877–1888. [CrossRef]

59. Van der Sijde, J.N.; Karanasos, A.; van Ditzhuijzen, N.S.; Okamura, T.; van Geuns, R.J.; Valgimigli, M.; Ligthart, J.M.; Witberg, K.T.; Wemelsfelder, S.; Fam, J.M.; et al. Safety of optical coherence tomography in daily practice: A comparison with intravascular ultrasound. *Eur. Heart J. Cardiovasc. Imaging* **2016**, *18*, jew037. [CrossRef]

60. Mizragi, V.; Sipe, J.E. Optical properties of photosensitive fiber phase gratings. *J. Light. Technol.* **1993**, *11*, 1513–1517. [CrossRef]

61. Markvart, A.; Liokumovich, L.B.; Medvedev, I.; Ushakov, N. Smartphone-Based Interrogation of a Chirped FBG Strain Sensor Inscribed in a Multimode Fiber. *J. Light. Technol.* **2021**, *39*, 282–289. [CrossRef]

62. Subhash, H.M.; Choudhury, N.; Chen, F.; Wang, R.K.; Jacques, S.L.; Nuttall, A.L. Depth-resolved dual-beamlet vibrometry based on Fourier domain low coherence interferometry. *J. Biomed. Opt.* **2013**, *18*, 1. [CrossRef] [PubMed]

63. Ushakov, N.; Liokumovich, L. Measurement of dynamic interferometer baseline perturbations by means of wavelength-scanning interferometry. *Opt. Eng.* **2014**, *53*, 114103. [CrossRef]

64. Harris, F.J. On the Use of Windows for Harmonic Analysis with the Discrete Fourier Transform. *Proc. IEEE* **1978**, *66*, 51–83. [CrossRef]

65. Itoh, K. Analysis of the phase unwrapping algorithm. *Appl. Opt.* **1982**, *21*, 2470. [CrossRef] [PubMed]

66. Ushakov, N.A.; Liokumovich, L.B. Signal Processing Approach for Spectral Interferometry Immune to $\lambda/2$ Errors. *IEEE Photonics Technol. Lett.* **2019**, *31*, 1483–1486. [CrossRef]

67. Rubins, U. Finger and ear photoplethysmogram waveform analysis by fitting with Gaussians. *Med. Biol. Eng. Comput.* **2008**, *46*, 1271–1276. [CrossRef] [PubMed]

68. Ting, C.T.; Chang, M.S.; Wang, S.P.; Chiang, B.N.; Yin, F.C.P. Regional pulse wave velocities in hypertensive and normotensive humans. *Cardiovasc. Res.* **1990**, *24*, 865–872. [CrossRef] [PubMed]

69. Latham, R.D.; Westerhof, N.; Sipkema, P.; Rubal, B.J.; Reuderink, P.; Murgo, J.P. Regional wave travel and reflections along the human aorta: A study with six simultaneous micromanometric pressures. *Circulation* **1985**, *72*, 1257–1269. [CrossRef]

70. Malik, M.; John Camm, A.; Thomas Bigger, J.; Breithardt, G.; Cerutti, S.; Cohen, R.J.; Coumel, P.; Fallen, E.L.; Kennedy, H.L.; Kleiger, R.E.; et al. Heart rate variability: Standards of measurement, physiological interpretation, and clinical use. *Circulation* **1996**, *93*, 1043–1065. [CrossRef]

71. Romanovsky, A.A. Skin temperature: Its role in thermoregulation. *Acta Physiol.* **2014**, *210*, 498–507. [CrossRef]

72. Charkoudian, N. Skin blood flow in adult human thermoregulation: How it works, when it does not, and why. *Mayo Clin. Proc.* **2003**, *78*, 603–612. [CrossRef]

73. Qing Chen, M.; Ming Wei, H.; Zhao, Y.; Hua Lei, X.; Krishnaswamy, S. Temperature insensitive air-cavity Fabry-Perot gas pressure sensor based on core-offset fusion of hollow-core fibers. *Sens. Actuators A Phys.* **2019**, *298*, 111589. [CrossRef]

74. Wang, Z.; Jiang, Y.; Peng, H.; Ma, X.; Cui, L. A temperature-compensated fibre optic extrinsic Fabry–Perot interferometric displacement sensor for fault measurement in geomechanics. *Meas. Sci. Technol.* **2013**, *24*, 025104. [CrossRef]

75. Charlton, P.H.; Birrenkott, D.A.; Bonnici, T.; Pimentel, M.A.; Johnson, A.E.; Alastruey, J.; Tarassenko, L.; Watkinson, P.J.; Beale, R.; Clifton, D.A. Breathing Rate Estimation from the Electrocardiogram and Photoplethysmogram: A Review. *IEEE Rev. Biomed. Eng.* **2018**, *11*, 2–20. [CrossRef] [PubMed]

76. Salem, M.; Agrawal, G.P. Effects of coherence and polarization on the coupling of stochastic electromagnetic beams into optical fibers. *J. Opt. Soc. Am. A* **2009**, *26*, 2452–2458. [CrossRef] [PubMed]

77. Markvart, A.; Liokumovich, L.; Medvedev, I.; Ushakov, N. Continuous Hue-Based Self-Calibration of a Smartphone Spectrometer Applied to Optical Fiber Fabry-Perot Sensor Interrogation. *Sensors* **2020**, *20*, 6304. [CrossRef]
78. Pan, T.; Cao, W.; Wang, M. TiO2 thin film temperature sensor monitored by smartphone. *Opt. Fiber Technol.* **2018**, *45*, 359–362. [CrossRef]
79. Lee, S.Y.; Hui, P.C.; Bouma, B.; Villiger, M. Single-shot depth profiling by spatio-temporal encoding with a multimode fiber. *Opt. Express* **2020**, *28*, 1124. [CrossRef]
80. Wilkes, T.C.; McGonigle, A.J.S.; Willmott, J.R.; Pering, T.D.; Cook, J.M. Low-cost 3D printed 1 nm resolution smartphone sensor-based spectrometer: Instrument design and application in ultraviolet spectroscopy. *Opt. Lett.* **2017**, *42*, 4323. [CrossRef]
81. Ushakov, N.A.; Liokumovich, L.B. Multiplexed Extrinsic Fiber Fabry-Perot Interferometric Sensors: Resolution Limits. *J. Light. Technol.* **2015**, *33*, 1683–1690. [CrossRef]
82. Yi, L.; Sun, L.; Zou, M.; Hou, B. Dual-Channel Spectral Domain Optical Coherence Tomography Based on a Single Spectrometer Using Compressive Sensing. *Sensors* **2019**, *19*, 4006. [CrossRef]
83. Li, Q.; Karnowski, K.; Noble, P.B.; Cairncross, A.; James, A.; Villiger, M.; Sampson, D.D. Robust reconstruction of local optic axis orientation with fiber-based polarization-sensitive optical coherence tomography. *Biomed. Opt. Express* **2018**, *9*, 5437. [CrossRef] [PubMed]
84. Wilkinson, P.R.; Pratt, J.R. Analytical model for low finesse, external cavity, fiber Fabry-Perot interferometers including multiple reflections and angular misalignment. *Appl. Opt.* **2011**, *50*, 4671–4680. [CrossRef]
85. Yang, Y.; Zhang, H.; Cao, G.; Zhao, H.; Cheng, Y. Influence of surface errors on the performance of EFPI based on GRIN lenses. *Optik* **2014**, *125*, 3564–3568. [CrossRef]
86. Tuchin, V.V.; Utz, S.R.; Yaroslavsky, I.V. Tissue optics, light distribution, and. *Opt. Eng.* **1994**, *33*, 3178–3188. [CrossRef]
87. Tearney, G.J.; Brezinski, M.E.; Bouma, B.E.; Hee, M.R.; Southern, J.F.; Fujimoto, J.G. Determination of the refractive index of highly scattering human tissue by optical coherence tomography. *Opt. Lett.* **1995**, *20*, 2258. [CrossRef] [PubMed]
88. Lai, J.C.; Zhang, Y.Y.; Li, Z.H.; Jiang, H.J.; He, A.Z. Complex refractive index measurement of biological tissues by attenuated total reflection ellipsometry. *Appl. Opt.* **2010**, *49*, 3235–3238. [CrossRef] [PubMed]
89. Sharath, U.; Sukreet, R.; Apoorva, G.; Asokan, S. Blood pressure evaluation using sphygmomanometry assisted by arterial pulse waveform detection by fiber Bragg grating pulse device. *J. Biomed. Opt.* **2013**, *18*, 067010. [CrossRef] [PubMed]
90. Jia, D.; Chao, J.; Li, S.; Zhang, H.; Yan, Y.; Liu, T.; Sun, Y. A Fiber Bragg Grating Sensor for Radial Artery Pulse Waveform Measurement. *IEEE Trans. Biomed. Eng.* **2018**, *65*, 839–846. [CrossRef]
91. Bo, E.; Luo, Y.; Chen, S.; Liu, X.; Wang, N.; Ge, X.; Wang, X.; Chen, S.; Chen, S.; Li, J.; et al. Depth-of-focus extension in optical coherence tomography via multiple aperture synthesis. *Optica* **2017**, *4*, 701. [CrossRef]
92. Tan, K.M.; Mazilu, M.; Chow, T.H.; Lee, W.M.; Taguichi, K.; Ng, B.K.; Sibbett, W.; Herrington, C.S.; Brown, C.A.; Dholakia, K. In-fiber common-path optical coherence tomography using a conical-tip fiber. *Opt. Express* **2009**, *17*, 2375–2384. [CrossRef] [PubMed]

New Methods to Seismic Monitoring: Laboratory Comparative Study of Michelson Fiber-Optic Interferometer and Pneumatic Measurement Systems

Martin Stolarik [1], Jan Nedoma [2,*], Radek Martinek [3], Stanislav Kepak [2], Eva Hrubesova [1], Miroslav Pinka [1] and Jakub Kolarik [3]

[1] Department of Geotechnics and Underground Engineering, Faculty of Civil Engineering, VSB-Technical University of Ostrava, Ludvika Podeste 1875/17, 708 33 Ostrava-Poruba, Czech Republic; martin.stolarik@vsb.cz (M.S.); eva.hrubesova@vsb.cz (E.H.); miroslav.pinka@vsb.cz (M.P.)

[2] Department of Telecommunications, Faculty of Electrical Engineering and Computer Science, VSB-Technical University of Ostrava, 17. listopadu 15, 708 33 Ostrava-Poruba, Czech Republic; stanislav.kepak@vsb.cz

[3] Department of Cybernetics and Biomedical Engineering, Faculty of Electrical Engineering and Computer Science, VSB-Technical University of Ostrava, 17. listopadu 15, 708 33 Ostrava-Poruba, Czech Republic; radek.martinek@vsb.cz (R.M.); jakub.kolarik@vsb.cz (J.K.)

* Correspondence: jan.nedoma@vsb.cz

Abstract: New possibilities of vibration monitoring can be found in completely different physical approaches, where all measuring technology is currently based on sensors in the electrical domain. This paper presents two different promising alternative approaches to vibration measurement, specifically in the field of fiber-optics and pneumatic sensors. The proposed solution uses a Michelson fiber-optic interferometer designed without polarization fading and with operationally passive demodulation technique using three mutually phase-shifted optical outputs. Experimentally developed sensor systems for the registration of anthropogenic seismic phenomena were complemented by standard instrumentation for measuring seismicity used as a standard. The measurement was performed under simplified conditions using a calibrated stroke as a source of dynamic loading. In addition to alternative systems, the paper also presents the results of recalculation of the measured values in a time domain and basic relationships for the conversion to basic units derived from the SI (International System of Units) system and used internationally in the field of seismic engineering. The results presented demonstrate that even systems operating on a different physical principle have great potential to replace the existing seismic devices. The correlation coefficients for both sensory devices were high (above 0.9) and the average deviations from the measured values of the amplitude of the oscillation velocity did not exceed the value of 0.02, neither with the fiber-optic or pneumatic sensor.

Keywords: seismic measurement; dynamic impact; dynamic response; interferometric sensor; pneumatic sensor

1. Introduction

Monitoring of vibrations from anthropogenic sources is becoming increasingly important, mainly due to the mass development of transport and construction–reconstruction in urban areas, where heavy construction equipment is used. Hence, effective low-cost, low-power, low-complexity methods for monitoring the dynamic response of buildings are intensively sought, which will transmit information about seismic or acoustic load continuously and in real time.

In the field of seismic engineering, when monitoring vibrations from anthropogenic sources, measuring technology based on sensors in the electrical domain has been used for several decades to measure the dynamic response of the rock environment as well as the dynamic response of the structure. Currently, standard seismic instrumentation

131

consisting of a digital station and a three-component piezoelectric velocity seismometer is used to monitor dynamic effects [1]. In the dynamically developing 21st century, however, new progressive solutions are being sought in this area as well; these solutions can be found, for example, in other physical principles than those that have been used so far. Sensory technologies based on other physical principles form a new alternative method of monitoring both seismic (dynamic) effects and acoustic (all-in-one) effects, with high added value. The main advantages of these technologies are small size, electrical passivity and immunity to electromagnetic interference, the simple internal structure, high mechanical resistance, the possibility of use in extreme conditions (humidity, extreme temperatures, explosive environments, oil industry, nuclear power plants, etc.) or also a significantly lower price. In recent years, there has also been considerable progress in the area of advanced methods of digital signal processing and work with Big Data. It is one of the fastest growing scientific disciplines and it is obvious that these progressive methods will penetrate the field of seismic monitoring. These new DSP (Digital Signal Processing) methods can make measurements more accurate, provide new measurement functions, etc. Modern digital signal processing methods have now been used in many areas and industries, and current practice suggests that the same trend will continue in the future. For the practical application of these progressive methods in real applications, among other things, both theoretical and applied research of the new as well existing methods are needed. Some application areas of these new approaches are not yet very developed and, in some fields, including the area of seismic monitoring, they are completely missing. It can be expected that new methods of seismic monitoring will enable the development of progressive techniques that are not yet very developed in this area, such as the use of artificial intelligence and machine learning techniques to predict, creation of seismic and acoustic maps of analyzed areas, linking with other smart cities entities, etc.

However, before the routine field deployment of similar equipment in common seismic engineering tasks, such as monitoring the dynamic response of the building structure and rock mass from various sources [2–7], it is first necessary to experimentally verify whether the equipment being developed is able to detect vibrations to the extent and accuracy required for engineering practice (Table 1). For this purpose, several successful experiments with different sources of vibration have been conducted in situ [8–10]. These experiments, when confronted with common instrumentation for seismic monitoring, proved the applicability of the devices tested and being developed for given tasks, specifically in a wide range of applications, with excellent agreement both in time (length of seismic events, detection of specific maxima) and the frequency domain (predominant frequency content, identical frequency peaks). The next logical step was to verify, at the experimental level, the possibility of recalculation of the measurements units in the time domain, so that new devices could be a direct alternative to commercially used systems. The paper is going to present such a laboratory experiment with finding of basic relationship for an interferometric sensor and a pneumatic sensor using a calibrated stroke in simplified conditions. A calibrated and certified standard seismic station with a velocity sensor installed was used as a reference standard.

The following sections will present State Of-the-Art , Methods, Experimental Setup, Results of Experiments, Discussion and Conclusions.

Table 1. Examples of anthropogenic vibrations [6].

Type of Dynamic Load	Distance from Dynamic Source (m)	Peak Particle Velocity (PPV) (mm/s)
Road traffic	2–6	0.4–0.1
Heavy lorry-poor road	8–3	0.8–0.1
Train	2–12	1.8–0.1
TBM in soil	2–20	3.5–0.15
Bulldozer	4–30	4–0.15
Pipe-bursting mole	4–30	6–0.4
TBM in rock	6–10	5–0.1
Plate compactor	1–6	10–25
Pile driving	6–12	5–0.3
1 kg dynamite	6–80	90–1.5
Explosive demolition (14 storey tower)	6–14	5–0.5

2. State-of-the-Art

In this part, the issue of vibration measurement with standard seismic instrumentation will be introduced, as well as alternative approaches to vibration measurement using developed sensors.

2.1. Commercially Used Seismic Instrumentation

Many manufacturers around the world produce seismic vibration monitoring stations, which are used for seismic monitoring purposes in engineering practice. These stations are manufactured as compact, or are supplied separately with an evaluation unit and a seismic sensor.

As a standard, these stations are used to measure vibrations to dynamically assess the response of a building structure due to anthropogenic sources. These sources include both wheeled and rail transport (tram transport especially in the urban area) as well as all construction technology generating vibrations, which are mostly inextricably connected with construction processes, especially with foundation of buildings and subsoil modification. Blasting work carried out in the vicinity of urban areas, whether it is large-scale blasting work in mining processes on the surface and underground, as well as blasting work as one of the work cycles in tunnel excavation, is a stand-alone issue. Here, these stations are then deployed as a necessary part of geotechnical monitoring, where, based on the measurement results, excavation and tunnelling procedures are optimized, thus reducing negative impacts on the environment. In general, vibrations from all these sources are called technical seismicity. The character of the recording in the time domain is subsequently dependent on the source of the dynamic load, which is a rapidly dampened seismic impulse or a longer-lasting shock.

Seismic sensors detect and measure ground vibration by means of the movement of a magnet suspended in a surrounding by a coil of wire. According to the Lenz Law of physics, a current is induced in the surrounding coil in a proportion to the velocity of the magnet movement with respect to the coil. The electronics in the monitor then measures this current, converts it to ground motion velocities and stores the raw data in the memory. Each of the three directions perpendicular to one another (longitudinal or radial, transverse, and vertical) has its own separate measuring coil in the transducer head, since the vibrations often differ significantly along the different measurement directions.

Standard seismic stations used for monitoring vibrations from anthropogenic sources have a common frequency range in the range from 2 to 200 Hz with respect to the sensor type. The mechanical principle of the measurement itself is the main disadvantage of these devices, since they are very sensitive to manipulation. The sensors as such are not immune to electromagnetic interference and, unlike the newly designed sensory technologies, do not withstand the long-term effects of extreme climatic conditions.

2.2. Experimentally Developed Sensor Systems

Sensory technologies based on optical fibers are an alternative method of monitoring seismic (dynamic) effects with a high added value. The fundamental advantages of fiber-optic sensors include small size, electrical passivity, resistance to electromagnetic interference (EMI) and low optical attenuation (measuring point can be separated from the evaluation optoelectronics). For high-precision measurements fiber-optic interferometers (such as Mach–Zehnder, Sagnac, Michelson, or Fabry–Perot) are the best choice. Interferometers are well known for their ability of making precision measurements of optical path difference between two fiber arms caused by a refractive index change in the interferometer arm or physical displacement [11]. Other technologies such as fiber gratings have limited frequency range, so the acoustic measurements are easier to implement in the case of interferometers. Below is a summary of current research in the field of optical sensing technology applicable in seismic measurements and with emphasis on interferometers.

The current state of knowledge mentions the use of optical interferometers in the area of seismic measuring about two decades ago [12]. However, these interferometers used interference in free space, not in optical fibers. Optical fiber configurations did not begin to appear until later. As one of the first fiber-optic approach within interferometric seismic measuring Sagnac interferometers [13] were described. Sagnac interferometer enables measuring even with the use of less coherent radiation sources contrary to other types of interferometers. The ability to measure rotation during seismic activity proved interesting but without further application, their main domain is still gyroscopes. An example of possible sensor design is [14]. The sensor is in the form of a cylinder on which a coil of optical fiber is wound. The cylinder is then immersed in a second larger cylinder full of water. The fiber length used in the Sagnac interferometer was only about 30 m long, yet the authors were able to sense the vibrations generated within the experiment.

Seismic stations can be substituted by another fiber-optic sensors operating on the principle of acceleration detection [15] such as Fabry–Perot, Mach–Zehnder or Michelson interferometers. Sensors with these types of interferometers can be constructed as tri-axial [16]. They can be characterized with the output intensity modulation measurable with regular optical power detectors. Design issues of all-fiber interferometric seismometers are discussed in [17].

The authors of [18] describe a simple seismometer based on a Mach–Zehnder interferometer. The designers were facing a phase drift of the sensor, which they successfully solved by actively controlling the operating point using a piezoelement in the arm of the interferometer. However, this solution is no longer completely optically passive and requires active electronic control, which is a considerable disadvantage. The resonant frequency of the resultant sensor is relatively low (60 Hz), which is also not practical in terms of calibrating the sensor frequency response. These issues were overcome in our setup using passive optical demodulation as described in [19] and a sensor design with short optical fibers in the interferometer arms.

The demonstration of in-fiber Fabry–Perot interferometer with fiber Bragg grating mirrors (FBG-FPI) is described in [20]. The sensor can monitor a wide range of vibration frequencies and therefore can be applicable in monitoring of seismic responses.

A distributed fiber-optic sensing technology called DAS or DVS (Distributed Acoustic/Vibration Sensing) was also presented as an alternate approach [21]. The principle uses Rayleigh's backscattering for scanning interferences over the entire length of the optical fiber acting as the sensor. Resulting acoustic and vibration signals at any point of the monitored fiber length have no parallel in the conventional measuring technology. The downside is the impossibility of measuring of wave direction at the measuring point and very high price of the evaluation units. For these reasons, it has not been put into practice yet and is used rather on an experimental basis. In [22] the authors deal with the use of DAS for the measurement of underground propagation of acoustic and vibration waves, is an example of a successful application in practice, but, for surface measurements, this method is not entirely suitable.

In case of non-fiber interferometric approach of measuring, several interesting studies can be mentioned. The authors of [23] provided results describing the monitoring system of bridge statics and dynamic vibrations. Two different camera types were used to monitor the response of a bridge to a passing train. Image processing techniques (pattern matching, edge detection, and digital image correlation) were used for the analysis of the acquired images. Results were compared to reference measurements obtained by single point measurements using the laser interferometer. The laser interferometer sensors can provide a method for observing low-frequency ground motion on seismic, geodetic, and intermediate time scales, as described by the authors of [24]. Comparison of individual interferometers with respect to the description of the sensor design, and the advantages and disadvantages are shown in Table 2.

Table 2. Table of comparison of fiber-optic methods of vibration measurement.

Method	Description of the Sensor Design	Advantages	Disadvantages
Mach–Zehnder [17,18]	short section of fiber in the arms of the interferometer, two fiber couplers	small size, low radiation source requirements (ordinary laser diodes are sufficient), dynamic range	high phase drift setting the lower limit for frequency measurement, polarization drift
Michelson [16]	short section of fiber in the arms of the interferometer, a fiber coupler and a circulator or an isolator, termination with a reflecting element	small size, low radiation source requirements (ordinary laser diodes are sufficient), dynamic range	high phase drift setting the lower limit for frequency measurement
Fabry–Perot [20]	a minuscule dimension of the resonator formed between two reflecting surfaces	minuscule dimensions, small phase drift, high sensitivity	small dynamic range, high requirements for radiation source coherence
Sagnac [14,15]	long section of the fiber in the interferometer, a fiber coupler and a circulator or an isolator	linearity of frequency response, very low requirements for radiation source coherence, small phase drift	large size, the sensitivity increases with the frequency—not entirely suitable for measuring vibrations
FBG [25]	a pre-stressed fiber grating attached to the monitored structure	very small size, remote evaluation, the temperature drift can be compensated by a second sensor	spectral evaluation unit, limited frequency range
DAS or DVS [21,22]	measurement of back reflection interference spatially along the entire length of the optical fiber (acting as a sensor)	a unique measurement method—thousands of virtual point sensors along the entire fiber	extremely high price of evaluation units

A unique pneumatic sensory device was also employed in the experiments using other physical approaches to vibration measurement. The first instruments used to measure vibrations historically consisted mainly of weights suspended on a cable or a spring, and these, using their inertia, were able to detect slight movements of the earth due to seismic waves. The device, which is historically close in principle to the presented solution, is called a geophone. However, the pneumatic sensor does not detect movement by direct contact of the armature from the permanent magnet inserted in the coil, but uses a pressure sensor to measure the change in sound pressure inside the closed tube. This innovative method was a by-product of experiments in which dilatation was measured using a similar pneumatic system in a strong magnetic field, where standard sensors designed for this type of measurement could not be used. This device is still unparalleled in its research field and thus has not a non-commonly used and defined name. The device is, by its principle, similar to closed-hose presence detectors [26–28]. In contrast, this application does not depend on deformation, and its subsequent pressure changes, under the weight of the

measured object. The presented device measures vibrations, which are propagated by material surrounding the pressure tube.

A partly similar topic can be found in publications examining the manifestation of changes in closed tube-based vibration measurement [29–31]. The authors analyze vibrations produced by changes in flow, pressure, and density of the medium propagated by the tubes. This gives them a better understanding of the process that takes place inside the pressure tube, in contrast to our measurement, which focuses on the detection of external excitations passing into the tube.

3. Methods

In this section, will be presented specific devices that have been used for experimental vibration measurements, therefore standard seismic station, fiber-optic interferometric system and pneumatic system.

3.1. Seismic Equipment BRS32

The BRS32 seismic station is one of the most widely used seismic stations in Central Europe; it is used for the purposes of seismic monitoring in engineering practice. BRS32 is, therefore, a universal seismic station, used for measurements both with battery power in field conditions for short-term measurements and for long-term seismic monitoring with connection to the electrical network and the possibility of remote data transmission. The compact station contains a three-component seismic velocity geophone. USB interface is used for all settings. The frequency range of the internal geophone (depending on the type of installed geophone) is between 0.5 Hz and 80 Hz at the dynamics of up to 120 dB. Sampling frequency is 250 Hz. The device, after switching on is automatically connected to the Global Positioning System (GPS) signal. The measurement coordinates are saved and the time is synchronized. The battery lasts more than 48 hours. BRS32 is very compact with simple control. Use of this device is in all application in the field of natural and induced seismicity. Internal geophones can be selected during the production. Two types are the most used: Dutch SM6-3D with frequency range 4.5 to 100 Hz and German LE3D Lennartz with frequency range 1 to 80 Hz [32]. Geophone SM6-3D has been installed in the device used. The seismic station BRS32 is serially manufactured in the Czech Republic by Arenal s.r.o., it is calibrated according to the relevant standards, and certified.

3.2. Fiber-Optic Interferometric System Being Developed for Seismic Monitoring

Fiber-optic sensors can be divided into several basic categories, wherein one of them includes phase-modulated sensors. Phase-modulated sensors compare the phase of the radiation source (light) in a measurement fiber to a reference fiber in a device called an interferometer. In other words, the relative phase change between two light waves is measured. Phase-modulated sensors are one of the most sensitive principles known, with large dynamic range suitable for various applications.

The phase delay of light due to passing through the optical fiber section ϕ is given by relation (1), where n_0 is the refractive index of the fiber core, l represents the fiber length and λ the wavelength of the radiation source used. A change in the fiber length l or the refractive index of the core of the measuring fiber n_0 causes a phase change that can be described as follows (2).

$$\phi = kn_0l = \frac{2\pi n_0 l}{\lambda} \tag{1}$$

$$\phi + \Delta\phi = \frac{2\pi}{\lambda}(n_0l + n_0\Delta l + l\Delta n_0) \tag{2}$$

The external conditions can affect the characteristics of light waves within the optical fiber one of them being the phase delay. The optical fiber is sensitive to the mechanical stress (the expansion or compression) acting in the fiber axis which is based on the theory of elasticity. The mechanical stress results in the changes of the refractive indices of the

fiber core and cladding, the fiber length and the fiber core diameter [33]. Interferometer translates these mechanical changes into optical intensity changes measurable by regular optical power detectors. The interferometric sensor output can be described by (3), where C is the mean value of the optical intensity, A is the amplitude of the variation of the optical intensity, and $\Delta\phi(t)$ is the phase difference between the interferometer arms.

$$I(t) = C + A\cos(\Delta\phi(t)) \tag{3}$$

Since several known fiber-optic connections lead to wave interference, it was necessary to choose the most suitable one for solving the issue of vibration measurement. Eventually, the connection of the Michelson interferometer, which uses two short sections of fibers terminated by a reflective element, such as a mirror, became the most suitable one. This type of interferometer is not very sensitive to changes in the wavelength of the radiation source, assuming a balanced fiber length of the interferometer arms, is compact because it requires only short sections of optical fibers in the sensor, has as large dynamic range as the Mach–Zehnder interferometer, and is fairly sensitive to low-frequency vibrations and acoustic signals [33].

The basic connection of the fiber-optic Michelson interferometer (MI) is determined by fiber optical symmetrical 2 × 2 coupler which has two input and two output ports. An optical radiation source is connected at the input port and is supplemented by an isolator, to suppress the back reflections. The short fiber sections at the outputs form the measurement and reference arms of the interferometer. The fibers are terminated with mirrors and the output signal is transmitted by the same coupling element to the photodetector via the second input port, see Figure 1.
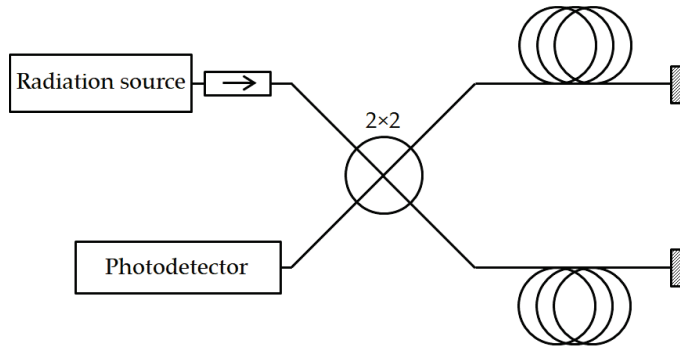
Figure 1. A basic connection of the Michelson interferometer.

To determine the value of $\Delta\phi(t)$, a demodulation technique is essential to perform the measurements. The operational passivity of the so-called homodyne demodulation [34] is advantageous in the sensor construction as it uses a 3 × 3 coupler instead of 2 × 2 and therefore having phase-shifted signal outputs, which can be described by the following Equations (4)–(6), where δ_i is 3 × 3 coupler phase asymmetry.

$$u_1 = C_1 + A_1 \cos\left(\Delta\phi(t) - \frac{2\pi}{3} - \delta_1(t)\right) \tag{4}$$

$$u_2 = C_2 + A_2 \cos(\Delta\phi(t)) \tag{5}$$

$$u_3 = C_3 + A_3 \cos\left(\Delta\phi(t) + \frac{2\pi}{3} + \delta_2(t)\right) \tag{6}$$

In the first step, the DC offset C_i and modulation amplitude A_i are equalized for all channels, C_i is set to 0 and A_i is set to 1. Subsequently, following Formula (7) can be applied [35]. The demodulation can be performed digitally with harmonic arctangent function.

$$\tan \Delta\phi(t) = \frac{\sqrt{3}(u_2 - u_3)}{u_2 + u_3 - 2u_1} \tag{7}$$

The unwrapped phase difference can be continuously measured in real time with basically no limit to its measuring range. The accuracy and amplitude limit of phase difference is given by the photodetector bandwidth and sampling rate. For the particular application, single MHz photodetector and 100 kS/s sampling rate is well above the expected measured vibration frequency and amplitude range. The entire connection of the actual measuring system with the interferometer is shown in Figure 2.
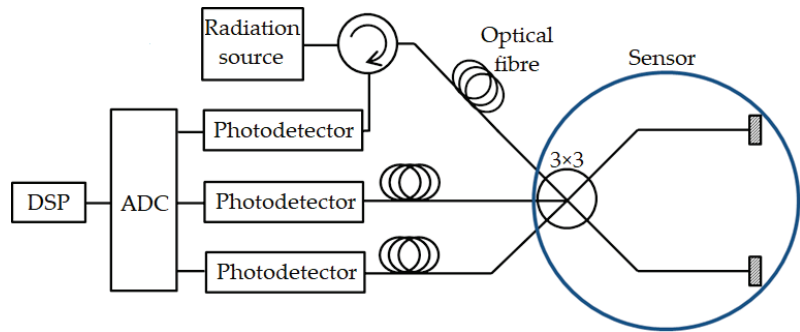
Figure 2. Connection of the sensor system with the fiber-optic interferometer.

The radiation source is a narrow-spectrum laser diode operating at a wavelength of 1550 nm with an output power of 3 mW. An optical three-port circulator separating the forward and reverse directions is connected to the laser output. This circulator can be located just behind the diode, behind the connecting optical cable, or be a part of the sensor, but is typically located just behind the radiation source, thereby saving one fiber in the cable connecting the optoelectronics and the sensor itself. The sensor then consists only of a 3 × 3 coupling element with even ratio and a measuring and reference fiber terminated with fiber mirrors, e.g., Newport F-FRM. Three output signals are fed to InGaAs photodetectors, the electrical output of which is connected to a measuring card (A/D converter). The ADC used is the 9222 module in the cDAQ-9181 chassis made by National Instruments. The signals are further processed by software (passive demodulation, filtering, spectral analysis).

The sensor design incorporates a waterproof aluminum box measuring 253 × 159 × 72 mm. A three-meter single-mode fiber in primary protection was affixed to the bottom of the box using epoxy resin (hard material with a high Young's modulus of elasticity, for good vibration transmission). Shorter fiber lengths provide lower sensitivity, while longer lengths limit the lower cut-off frequency of the sensor due to the still present slow drift of the sensors. The drift comes from several imperfections, such as finite polarization extinction ratio of passive optical components and fibers, radiation source wavelength stability but mainly due to the small temporal variation of temperature. The length of three meters is the compromise value for both. A vertical vibration then uniformly applies mechanical stress perpendicular to the fiber axis. A reference arm of the same length and a fiber coupler were then loosely placed in the acoustic insulating foam to minimize the transmission of vertical vibrations to the other arm [36]; in addition, this arm was made in a higher degree of protection with a 3 mm jacket further reducing the amount of vibration affecting the fiber length and core refractive index. Optical connectors for connecting

the optical cable or fibers were built into the front panel. An example of the complete connection of the Fiber-optic interferometric system is shown in Figure 3.
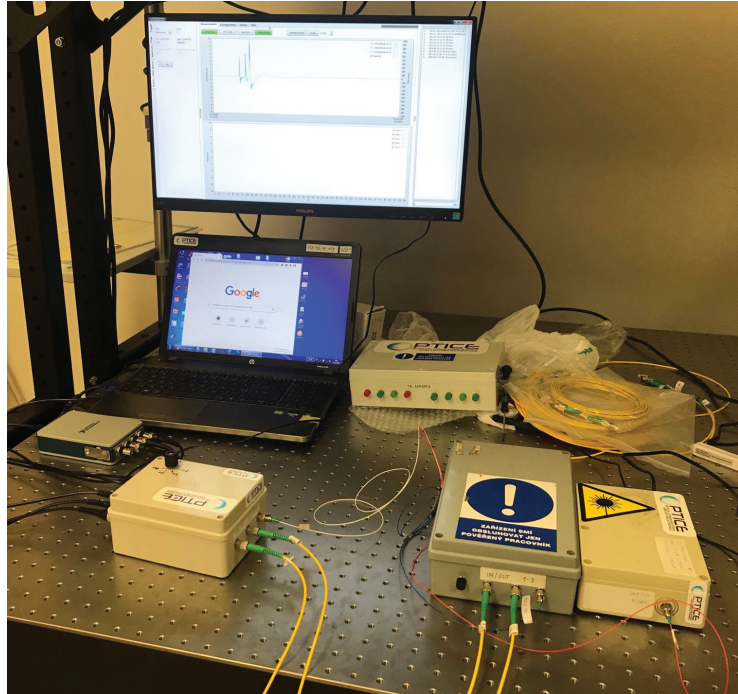

Figure 3. Example of connection of the fiber-optic interferometer and the sensor system.

3.3. Pneumatic System Being Developed for Seismic Monitoring

The device works as a converter of mechanical vibrations propagated by the surrounding material to a change in the sound pressure, which is sensed by a pressure sensor. The device consists of a flexible polyvinyl chloride (PVC) tube, which is in direct contact with a pad through which the desired signal is propagated. The tube is sealed on both sides, specifically with a microphone on one side and a seal on the other one. The surface of the tube acts as a membrane that is dilated by seismic/mechanical waves, thus changing the volume of the tube. A system sealed in this manner has, at a constant temperature, a direct relationship between the volume and the pressure of the gas enclosed within the tube, so this system works as a converter of physical quantities (Figure 4).
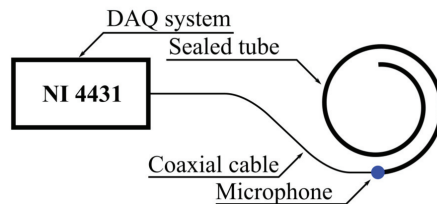
Figure 4. Diagram of the pneumatic system.

This system is resistant to ambient acoustic interference. According to the previous experiment in which the signal inside and outside the tube was sensed, the measurement showed that the attenuation of the signal measured with a wobble frequency of up to

2.5 kHz was 20 to 40 dB [37]. Furthermore, it was found that despite the self-supporting PVC pipes, there were changes in the measured signal due to sudden changes in the ambient pressure, e.g., when opening the doors or windows. In the case of industrial use, it would be necessary to bury this sensor, cover it with sand or place it in a box with a constant pressure to prevent the influence of changes in the ambient pressure on the measured signal. These error signals appear to be short-term extremes, but in the case of evaluating seismic activity at critical points, they could be evaluated as a hazardous condition.

Previous experiments have also confirmed that this system measures more easily mechanical vibration propagated through materials with acoustic impedance similar to the tube material rather than through ambient air. In the case of using a material with similar acoustic impedance, this results in minimal reflection of the passing wave and the highest signal gain.

Due to its low construction costs, the measuring system is suitable for outdoor use or for incorporation into the building structure. The sensitive part of the measuring system, a soft tube with the advantage of a PVC material, is resistant to electromagnetic influences, mechanical and chemical damage, so it can be used even in places where standard sensors could be harmed or affected. An example of the complete connection of the pneumatic system is shown in Figure 5.
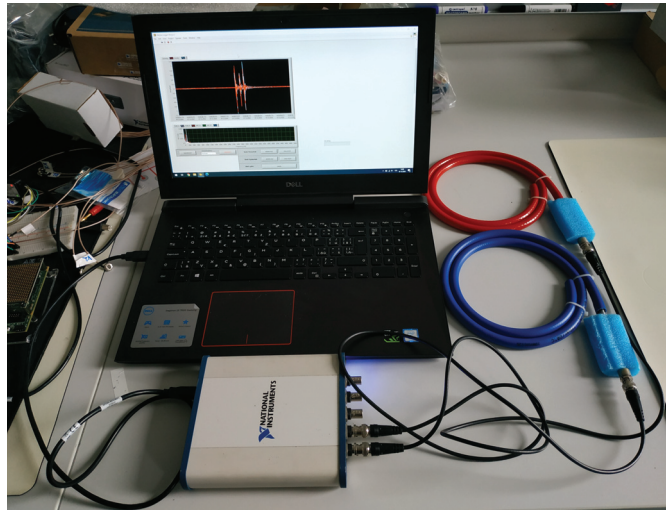
Figure 5. Example of connection of the pneumatic system.

4. Experimental Setup

The experiment was conducted in the heavy laboratories of the Faculty of Civil Engineering, VSB-Technical University of Ostrava, on a massive, poured concrete floor in the basement of the building. Two BRS32 seismic stations, two experimentally developed interferometers for vibration measurement, five pneumatic sensors and one tri-axial accelerometer were used throughout the experiment (not all results from all devices from this comparative measurement are presented in this paper). For further processing, for the purposes of this publication, data from only one BRS32 seismic station, one interferometric sensor and one pneumatic sensor (marked in red) were used. The distance of the sensors from the source of the calibrated stroke was 0.5 m (Figure 6a), or 1.0 m (Figure 6b), or 1.5 m (Figure 6c). The diagram of the entire calibration experiment is shown in Figure 7.
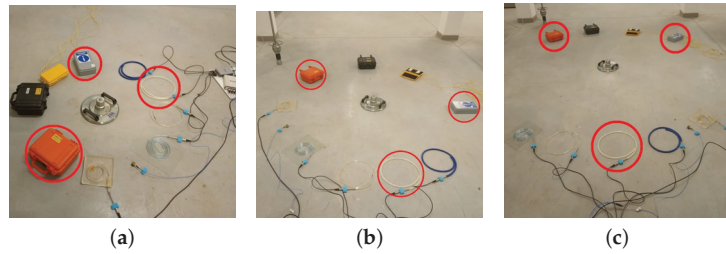
Figure 6. Comparative experiment (the alternative types of the sensors being developed presented in this paper are marked in red): (**a**) a distance of 0.5 m from the calibrated stroke; (**b**) a distance of 1.0 m from the calibrated stroke; (**c**) a distance of 1.5 m from the calibrated stroke.
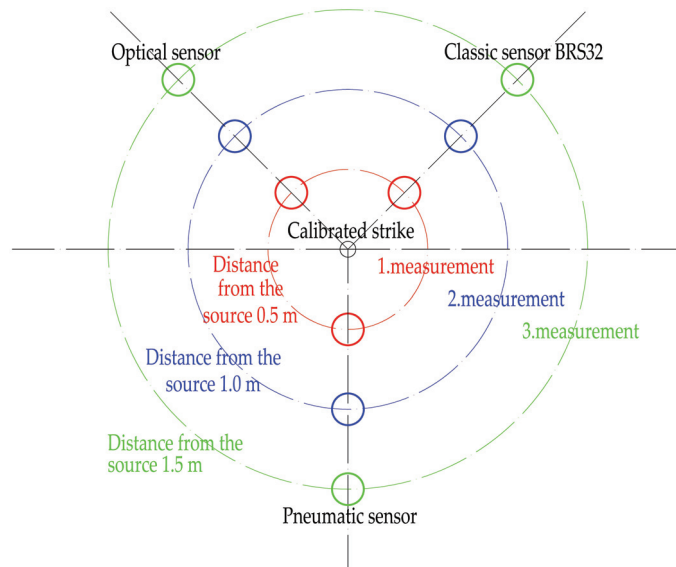

Figure 7. Diagram of the entire comparative experiment.

The source of the calibrated stroke consisted of a drop weight weighing 10 kg and falling from a height of 0.7 m on a circular impact plate with a diameter of 0.3 m and a weight of 5 kg. The induced impulse of force of the weight is 7.1 kN and the duration of the impulse is 45 ms.

In each stage of the measurement, at a distance of 0.5 m to 1.5 m, 100 strokes were performed. A time delay of at least 5 s was allowed between each stroke. After each stroke, the recordings from the experimental sensors were stored and marked with the appropriate time according to GPS for the purpose of unambiguous identification. The BRS32 seismic station was started in a continuous recording mode, which is synchronized with GPS.

5. Results of Experiments

In the following section, the results from experimental measurements in the time domain, which were obtained both from the BRS32 seismic station and from both sensory devices being developed, will be presented and described in detail.

Figure 8 shows a time recording of the calibrated stroke at a distance of 1 m from the BRS32 seismic station. The horizontal axis represents GPS time, while the vertical axis represents amplitude of the oscillation velocity [mm.s^{-1}]. A calibrated stroke was recorded at time "T". After a rapid and sharp increase to the maximum, there was very quick

attenuation. This is a typical manifestation of such an isolated dynamic phenomenon in the time domain. In general, seismic station BRS32 records in three perpendicular directions (vertical, horizontal radial and horizontal transversal). The comparative experiment was simplified with dynamic impulse in vertical direction, in the near zone also we can expect the main dynamic response in vertical direction, thus only the vertical component was compared with experimentally developed devices.
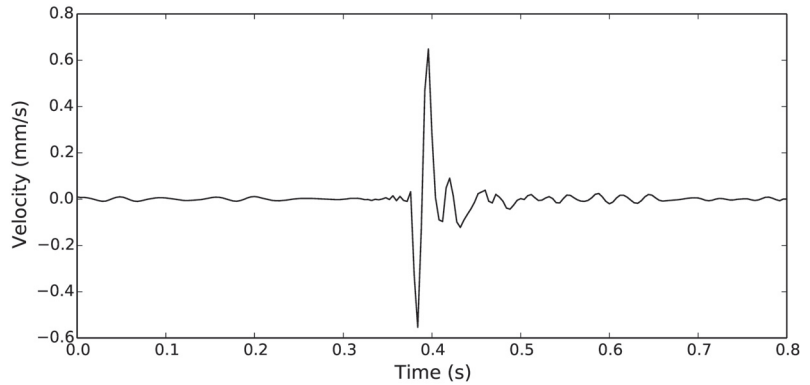
Figure 8. Time recording of the calibrated stroke at a distance of 1 m from the BRS32 seismic station.

Figure 9 shows a time recording of one calibrated stroke at a distance of 1 m from the interferometric sensor being developed. The horizontal axis represents time, while the vertical axis represents phase response [Deg]. A calibrated stroke was recorded at time "T". After a rapid and sharp increase to the maximum, there was very quick attenuation and at time T + 0.045 s a second impulse of a very similar nature was recorded, only with a lower maximum. The first maximum is a manifestation of the impact of the drop weight on the circular impact plate, the second maximum is a manifestation of the plate in contact with the concrete base. The time difference between the two maxima corresponds exactly to the impact time of the drop weight, which is 45 ms. This is a phenomenon that can be observed when placing the place on a relatively very rigid layer (e.g., a concrete floor). If the plate is placed on a less solid surface (e.g., soil) then the second maximum is significantly smaller.
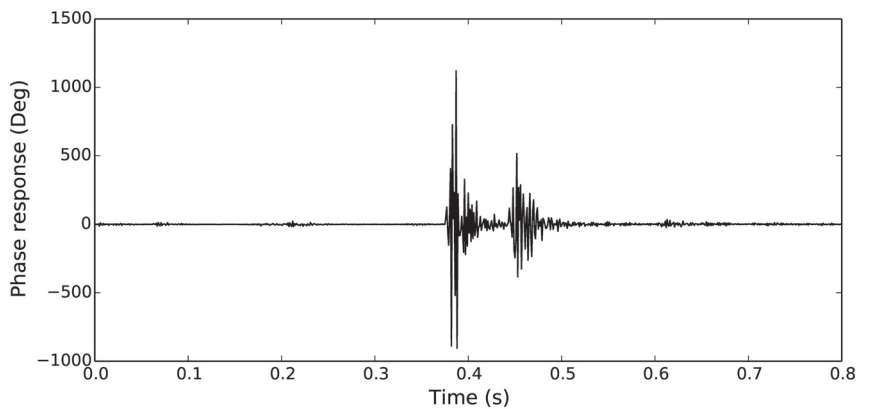
Figure 9. Time recording of a calibrated stroke at a distance of 1 m from the interferometric sensor being developed.

Figure 10 shows a time recording of one calibrated stroke at a distance of 1 m from the pneumatic sensor being developed. The horizontal axis represents time, while the

vertical axis represents pressure [Pa]. A calibrated stroke was recorded at time "T". After a rapid and sharp increase to the maximum, there was attenuation, but before the pulse was completely attenuated, so, at time T + 0.045 s, a second impulse of a very similar nature was recorded again, and again only with a lower maximum. The first maximum is, as with the interferometric sensor, a manifestation of the impact of the falling weight on the circular impact plate; only this manifestation was not so quickly attenuated, which is related to the construction of the pneumatic sensor; and the second maximum is again a manifestation of the plate in contact with the base. As with the previous recording, the time difference is 45 ms.
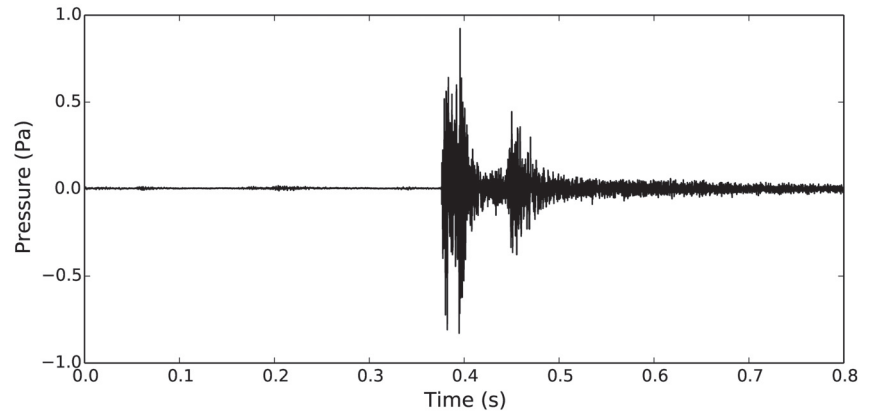
Figure 10. Time recording of one calibrated stroke at a distance of 1 m from the pneumatic sensor being developed.

Time recordings from all 300 strokes at distances of 0.5 m, 1.0 m and 1.5 m were always of the same nature for the BRS32 seismic station as well as for both sensory devices being developed, both in terms of the length of each phenomenon and in terms of the size of the maxima. As the distance from the calibrated stroke increased, only the maxima measured decreased.

6. Basic Recalculation of Measured Values between Fiber-optic Interferometric Sensor and Pneumatic Sensor, Respectively and Seismic Station

To the finding of the mathematical relationship between the values of optical measurement system and the oscillation velocity measurements, an analysis of the subsets of the measured data for each distance and each dynamic stroke was first performed. From each of the two corresponding partial recordings of the oscillation velocity and the phase response for a certain distance and a certain stroke, we obtain a pair of values, which correspond to the absolute maxima of these two recordings mentioned. Maxima are not exactly at the same time. This does not allow neither an environment of experiment, nor a completely different design of sensors working on other physical principles and with a different sampling frequency. By merging the results of the primarily processed subsets, we then receive a global set of results—maximum values obtained by optical measurement (independent variable in the regression analysis) and corresponding maximum absolute values of oscillation velocity (dependent variable in the regression function). Using the least squares method, the regression function with the highest coefficient of determination R^2, was determined. In this case, a linear regression function was the best:

$$v = a + bx \qquad (8)$$

v—amplitude of the oscillation velocity,

x—maximum phase response obtained from optical measurements,

a, b—constants.

In the case of the finding of the mathematical relationship between the results of pneumatic measurements and the measurement of oscillation velocity, an analogous approach was applied to determine the optimal shape of the regression function with the highest determination coefficient R^2. The exponential regression curve is the best:

$$v = a \times exp(bx) \tag{9}$$

v—amplitude of the oscillation velocity,

x—maximum value of pneumatic measurements,

a, b—constants.

The results of both mathematical relationships for the optical interferometer and the seismic station, and the pneumatic sensor and the seismic station are presented in Figures 11 and 12, respectively. Both dependences show a very high correlation coefficient R^2. Table 3 then summarizes the main results from the entire experiment, i.e., the correlation relations for both sensory devices being developed, the relevant correlation coefficients and the deviations from the measured values of the amplitude of the oscillation velocity obtained from the seismic station.
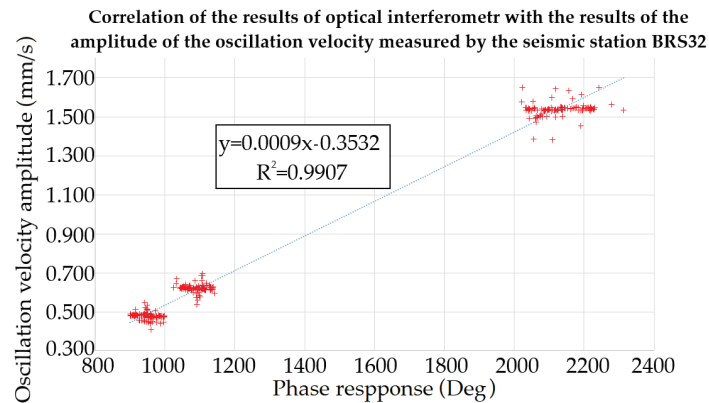
Figure 11. Mathematical relationship for the optical interferometer.
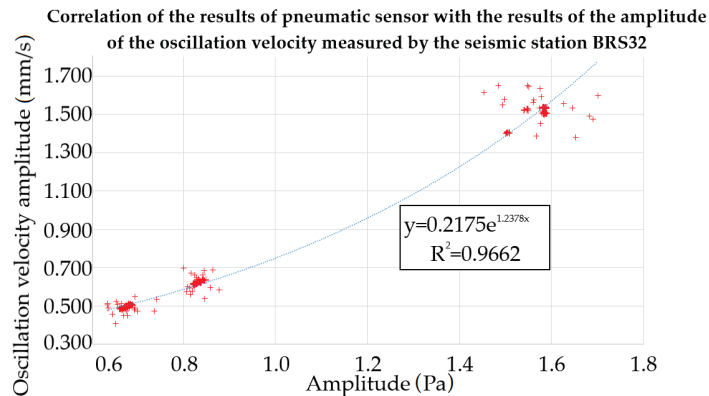
Figure 12. Mathematical relationship for the pneumatic sensor.

Table 3. Summary results of data mathematical processing of the comparative measurement of the optical interferometer system and the pneumatic system.

	Seismic Station / Optical Interferometer	Seismic Station / Pneumatic Sensor
Correlation equation	y = 0.0009x − 0.3532	v = 0.2175 * EXP(1.2378x)
Correlation coefficient R^2	0.9907	0.9662
Average deviation from the measured values of velocity amplitude (mm/s)	0.022	0.002
Max. deviation from the measured values of velocity amplitude (mm/s)	0.203	0.301

7. Discussion

This paper describes the first basic laboratory experiment with the finding of the mathematical relationship between the measured values of the alternative sensory devices being developed working on a different physical principle than it is still common in the field of vibration measurement. The comparative measurements were performed in simplified conditions. In these conditions, all measuring instrumentation was placed as well as the source of vibrations, which was placed on a homogeneous base at a relatively small mutual distance. However, in conventional in situ measurements, the distances are significantly greater, in the order of tens to hundreds of meters, and the environment in which the vibrations propagate is always fairly heterogeneous. Likewise, a calibrated stroke is the simplest form of a possible source of vibrations, where commonly monitored vibrations have a much more complex character. Climate conditions will certainly be another, not insignificant factor influencing the measurement results. In contrast, it is also possible to perform the entire comparative process in a much more sophisticated manner, using a vibrating table in a vacuum chamber, which will be the next step in the research. Similarly, the next step of the research will include verification of the currently obtained correlation equations outside the laboratory, in situ, on seismic phenomena caused by, for example, transport, construction equipment or blasting work.

The team of author has already started this experimental verification of laboratory-obtained correlation equations by means of pilot measurements of vibrations from tram transport.

One of the main benefits of alternative systems may be, among other things, the higher explanatory power of measurement without human access to the monitored site, i.e., shortening the necessary downtime or unavailability time only for the period necessary for instrumentation installation. The indisputable advantage of the alternative fiber-optic solution is the possibility of control monitoring in areas with interfering electromagnetic fields (increased safety), the possibility of measuring without access to the monitored site, data acquisition to streamline the design of monitored structures, minimizing risks in construction and operation. The users may also benefit from the access to the measurement data evaluated in an almost online mode. The synergy of the aforementioned aspects may increase the ability of the contractor to accurately and operatively respond to the direct consequences of the work being carried out on the environment and the built-up area—it will be possible to optimize blasting, the material used, to implement maximum procedures, thus achieving greater efficiency, safety and reduction of the impact of construction on the environment in contrast to the contractors offering their work in conjunction with the currently used conventional measuring systems.

The degree of sensitivity of the sensors being developed was an interesting item of verification resulting from this comparative measurement, which is demonstrated by capturing even the secondary manifestation of the impact of the weight. Capturing the reflection of the plate from stiffer subsoil by an interferometric, or pneumatic, sensory device is enabled due to a significantly higher sampling frequency. The original sampling

rate for interferometric signal was 100 kHz to make the demodulation with maximum precision. The original pre-demodulation sampling rate is always much higher. After the signal processing (demodulation) the phase response was down sampled to 1 kHz for the comparison and display. Pneumatic sensor has sampling frequency 10.24 kHz. For the BRS32 seismic station, the sampling frequency is 250 Hz, which is a commonly used sampling frequency for monitoring and subsequent analysis of seismic loading in engineering practice. The pneumatic and interferometric sensor being developed offers a higher frequency range and, as a result, it is sampled at higher frequencies, which can enable a much more detailed analysis of the seismic recording.

Regarding common engineering practice, the results are very interesting, because technical standards (e.g., [38]) state the limit values of effective velocity in tenths, while we achieved the average deviation from the measured values of the amplitude of the oscillation velocity of 0.022 and even 0.002 for the optical interferometer and the pneumatic sensor respectively.

8. Conclusions

The primary benefit of this paper is to present new alternative sensor systems suitable for seismic monitoring and the results of data mathematical processing. This experimental comparative study took place in simplified conditions and a total of 300 seismic phenomena were processed and evaluated in the time domain. All phenomena captured were of similar nature in the time domain.

Correlation equations in a general form were created for both sensory devices being developed, specifically $v = a + bx$ for the fiber-optic sensor and $v = a \times exp(bx)$ for the pneumatic sensor. Correlation coefficients R^2 for both equations were high, 0.9907 for the optic fiber sensor and 0.9662 for the pneumatic sensor. The average deviations from the measured values of the amplitude of the oscillation velocity were very low, specifically 0.022 for the optic fiber sensor and 0.002 for the pneumatic sensor.

This initial basic laboratory comparative study showed that even with the use of a completely different physical principle, it is possible to find a very cost-effective alternative method for the purpose of measuring vibrations, but so far only in simplified conditions. Results of this experimental measurement has shown that both the fiber-optic sensor and the pneumatic sensor are able to replace a standard seismic device while using a given solution and input boundary conditions.

Author Contributions: M.S., J.N., R.M., J.K. and S.K. proposed the system idea and edited the manuscript. S.K., M.S., J.N., R.M., E.H, J.K. and M.P. developed, tested, and validated the data. J.N., S.K., M.F., R.M., M.S. and J.K. wrote the manuscript. S.K., M.S., R.M., E.H. and J.N. critically evaluated the quality of the research data and experimental methods used to generate/acquire them, as well as the soundness/validity of the scientific and engineering techniques, wrote the manuscript, and performed its final edits. All authors have read and agreed to the published version of the manuscript.

Institutional Review Board Statement: Not applicable.

Informed Consent Statement: Not applicable.

Data Availability Statement: This study did not report any data.

Conflicts of Interest: The authors declare no conflict of interest.

References

1. Scheeper, P.; Gulløv, J.O.; Kofoed, L.M. A piezoelectric triaxial accelerometer. *J. Micromech. Microeng.* **1996**, *6*, 131–133. [CrossRef]
2. Jiang, N.; Gao, T.; Zhou, C.; Luo, X. Effect of excavation blasting vibration on adjacent buried gas pipeline in a metro tunnel. *Tunn. Undergr. Space Technol.* **2018**, *81*, 590–601. [CrossRef]
3. Czech, K.; Gosk, W. Analysis of the Vibration Propagation Induced by Pulling out of Sheet Pile Wall in a Close Neighbourhood of Existing Buildings. *Procedia Eng.* **2016**, *143*, 1460–1467. [CrossRef]
4. Xiao, Y.J.; Chen, F.Q.; Lin, L.Q. Study of ground vibration and vibration isolation due to sleeve of cast-in-place piles installed by vibratory driving. *Yantu Lixue/Rock Soil Mech.* **2017**, *38*, 705–713. [CrossRef]
5. Varughese, A.; Kumar, R. Vibration monitoring for surface compaction—A case study. *Water Energy Int.* **2017**, *59*, 56–59.
6. Hiller, D.M.; Crabb, G.I. Groundborne Vibration Caused by Mechanised Construction Works. *Noise Vib. Worldw.* **2001**, *32*, 9–14. [CrossRef]
7. Zou, C.; Wang, Y.; Wang, P.; Guo, J. Measurement of ground and nearby building vibration and noise induced by trains in a metro depot. *Sci. Total Environ.* **2015**, *536*, 761–773. [CrossRef]
8. Nedoma, J.; Stolarik, M.; Fajkus, M.; Pinka, M.; Hejduk, S. Use of Fiber-Optic Sensors for the Detection of the Rail Vehicles and Monitoring of the Rock Mass Dynamic Response Due to Railway Rolling Stock for the Civil Engineering Needs. *Appl. Sci.* **2019**, *9*, 134. [CrossRef]
9. Nedoma, J.; Stolarik, M.; Kepak, S.; Pinka, M.; Martinek, R.; Frnda, J.; Fridrich, M. Alternative Approaches to Measurement of Ground Vibrations Due to the Vibratory Roller: A Pilot Study. *Sensors* **2019**, *19*, 5420. [CrossRef]
10. Kepak, S.; Stolarik, M.; Nedoma, J.; Martinek, R.; Kolarik, J.; Pinka, M. Alternative Approaches to Vibration Measurement Due to the Blasting Operation: A Pilot Study. *Sensors* **2019**, *19*, 4084. [CrossRef]
11. Lopez-Higuera, J.M. *Handbook of Optical Fibre Sensing Technology*; Wiley: New York, NY, USA, 2002.
12. Nesterov, V.; Nasonkin, V. Characteristics of orientation of long-baseline laser interferometry seismic deformographs. *Geophys. J.* **1997**, *16*, 561–568.
13. Teisseyre, R.; Majewski, E.; Takeo, M.; Schreiber, K.; Stedman, G.; Igel, H.; Flaws, A. *Ring Laser Gyroscopes as Rotation Sensors for Seismic Wave Studies*; Springer: Berlin/Heidelberg, Germany, 2006; doi:10.1007/3-540-31337-029. [CrossRef]
14. Grigorie, T.; Adochiei, I.; Adochiei, F. Trends in the development of miniature optical accelerometers. *Int. Multidiscip. Sci. GeoConf. Surv. Geol. Min. Ecol. Manag.* **2014**, *1*, 197–204.
15. Liang, T.C.; Lin, Y.L. A fiber-optic sensor for the ground vibration detection. *Opt. Commun.* **2013**, *306*, 190–197. [CrossRef]
16. Zumberge, M.; Berger, J.; Hatfield, W.; Wielandt, E. A Three-Component Borehole Optical Seismic and Geodetic Sensor. *Bull. Seismol. Soc. Am.* **2018**, *108*, 2022–2031. [CrossRef]
17. Brown, D.A. Fiber optic accelerometers and seismometers. In *AIP Conference Proceedings*; AIP: College Park, MD, USA, 1996; pp. 260–273. doi:10.1063/1.50341. [CrossRef]
18. Kamenev, O.T.; Kulchin, Y.N.; Petrov, Y.S.; Khiznyak, R.V.; Romashko, R.V. Fiber-optic seismometer on the basis of Mach-Zehnder interferometer. *Sens. Actuators A Phys.* **2016**, *244*, 133–137. [CrossRef]
19. Papp, B.; Donno, D.; Martin, J.E.; Hartog, A.H. A study of the geophysical response of distributed fibre optic acoustic sensors through laboratory-scale experiments. *Geophys. Prospect.* **2016**, *65*, 1186–1204. [CrossRef]
20. Wada, A.; Ikuma, K.; Tanaka, S.; Takahashi, N. Experimental investigation of dynamic characteristics of wavelength of DFB-LD for FBG-FPI vibration sensor based on wavelength-to-time mapping. In Proceedings of the OFS2012 22nd International Conference on Optical Fiber Sensors, Beijing, China, 14–19 October 2012; Volume 8421, pp. 820–823. [CrossRef]
21. Papp, B.; Donno, D.; Martin, J.; Hartog, A. Fundamentals of Vibration Sensing with Distributed Fibre Optic Sensors through Downscaled Experiments. In Proceedings of the 76th EAGE Conference and Exhibition 2014, Amsterdam, The Netherlands, 16–19 June 2014; p. 622. [CrossRef]
22. Zaanen, L.V.; Bona, A.; Correa, J.; Tertyshnikov, K.; Dean, T.; Pevzner, R. A comparison of borehole seismic receivers. In *SEG Technical Program Expanded Abstracts 2017*; Society of Exploration Geophysicists (SEG): Houston, TX, USA, 2017; pp. 5974–5978. [CrossRef]
23. Busca, G.; Cigada, A.; Mazzoleni, P.; Zappa, E. Vibration Monitoring of Multiple Bridge Points by Means of a Unique Vision-Based Measuring System. *Exp. Mech.* **2013**, *54*, 255–271. [CrossRef]
24. Araya, A.; Takamori, A.; Morii, W.; Miyo, K.; Ohashi, M.; Hayama, K.; Uchiyama, T.; Miyoki, S.; Saito, Y. Design and operation of a 1500-m laser strainmeter installed at an underground site in Kamioka, Japan. *Earth Planets Space* **2017**, *69*. [CrossRef]
25. Guo, T.; Zhang, T.; Li, Y.; Qiao, X. Highly Sensitive FBG Seismometer With a 3D-Printed Hexagonal Configuration. *J. Light. Technol.* **2020**, *38*, 4588–4595. [CrossRef]
26. Reed, J.W.; Colquitt, R. Acoustic Pulse Transfer System for Event Counting. U.S. Patent No. 7,022,925, 4 April 2006.
27. Newmeyer, R. Sensor for Vehicular Traffic Data Accumulating Systems. U.S. Patent No. 3,949,355, 6 April 1976.
28. Tyburski, R. Roadway Sensor Systems. U.S. Patent No. 3,949,355, 12 September 1995.
29. Enoksson, P.; Stemme, G.; Stemme, E. Fluid density sensor based on resonance vibration. *Sens. Actuators A Phys.* **1995**, *47*, 327–331. [CrossRef]
30. Krantz, W.B.; Bilodeau, R.R.; Voorhees, M.E.; Elgas, R.J. Use of axial membrane vibrations to enhance mass transfer in a hollow tube oxygenator. *J. Membr. Sci.* **1997**, *124*, 283–299. [CrossRef]

31. Whitmore, S.A.; Wilson, M.D. Wiener Deconvolution for Reconstruction of Pneumatically Attenuated Pressure Signals. *AIAA J.* **2011**, *49*, 890–897. [CrossRef]
32. Broz, M.; Strunc, J.; Malek, J.; Linda, M. New generation seismological datalogger BRS32-USB and its application in induced seismicity monitoring. *EGRSE* **2014**, *XXI/1*, 35–47.
33. Krohn, D.A.; MacDougall, T.W.; Mendez, A. *Fiber Optic Sensors: Fundamentals and Applications*; Society of Photo-Optical Instrumentation Engineers (SPIE): Bellingham, WA, USA, 2014; doi:10.1117/3.1002910. [CrossRef]
34. Udd, E.; Spillman, W.B. *Fiber Optic Sensors: An Introduction for Engineers and Scientists*, 2nd ed.; Wiley: Hoboken, NJ, USA, 2011.
35. Todd, M.; Johnson, G.; Chang, C. Passive, light intensity-independent interferometric method for fibre Bragg grating interrogation. *Electron. Lett.* **1999**, *35*, 1970.:19991328. [CrossRef]
36. Kepak, S.; Cubik, J.; Doricak, J.; Vasinek, V.; Siska, P.; Liner, A.; Papes, M. The arms arrangement influence on the sensitivity of Mach–Zehnder fiber optic interferometer. In *Optical Sensors 2013*; Baldini, F., Homola, J., Lieberman, R.A., Eds.; International Society for Optics and Photonics, SPIE: Washington, DC, USA, 2013; Volume 8774, pp. 249–256. [CrossRef]
37. Kolarik, J.; Kahankova, R.; Brablik, J.; Martinek, R. Comparison of SCG and ECG Based Cardiac Activity Monitoring in Laboratory Conditions. *IFAC-PapersOnLine* **2019**, *52*, 550–555. [CrossRef]
38. European-standard. *CSN 73 0040: Loads of Technical Structures by Technical Seismicity*; Technical Report; Czech Office for Standards, Metrology and Testing: Prague, Czech Republic, 1996. (In Czech)

Article

Interferometric Instrument for Thickness Measurement on Blown Films

Michele Norgia * and Alessandro Pesatori

Politecnico di Milano, Dipartimento di Elettronica e Informazione e Bioingegneria (DEIB),
Piazza Leonardo da Vinci 32, 20133 Milano, Italy; alessandro.pesatori@polimi.it
* Correspondence: michele.norgia@polimi.it

Abstract: Real-time measurement of plastic film thickness during production is extremely important to guarantee planarity of the final film. Standard techniques are based on capacitive measurements, in close contact with the film. These techniques require continuous calibration and temperature compensation, while their contact can damage the film. Different optical contactless techniques are described in literature, but none has found application to real production, due to the strong vibration of the films. We propose a new structure of low-coherence fiber interferometer able to measure blown film thickness during productions. The novel fiber-optic setup is a cross between an autocorrelator and a white light interferometer, taking the advantages of both approaches.

1. Introduction

Plastic films are used in countless applications, from normal bags, food containers, packaging or other varied uses. The manufacturing technique is based on blown film extrusion [1], realized through large cylindrical bubbles (1–2 m of diameter), see, for example, the photo in Figure 1. At the top of the system, the bubble is cut to be then wound on a roller. Through the dosers, it is possible to manage the composition of the plastic film, while its thickness depends on the height of what is called the "freeze-line": the point where the plastic solidifies and the bubble stops expanding.

Figure 1. Photo of a bubble for plastic film extrusion. Bubble diameter is 1.5 m.

To realize a flat film, without swelling, the thickness of the bubble must be extremely uniform. In addition, there are numerous applications where a minimum thickness should be guaranteed, that is why the temperature at the beginning of the bubble is controlled accurately through a number of valves opening a jet of cold air. The thickness control cannot work properly in open loop, so a real-time measurement performed during the bubble growth is essential. Online gauging systems are used to provide automatic feedback control on the valves. Considering the bubble extrusion, it is impossible to access the inner film face during the extrusion, therefore, the thickness measurement must be obtained just from one side. This requirement excludes some standard techniques, such as absorption methods of light [2] or radiations [3], or simple distance measurements from both sides [4]. The classic technique from one side is based on capacitive gauging systems. The bubble is scanned using a circular slide and the sensor must keep a deep contact with the film to allow capacitive sensing [5]. This approach, even if extensively adopted, is limited by some problems. First of all, it gives a relative measurement because of troubles in holding calibration. To obtain the absolute thickness value, if the density is known, the gravimetric control is the normal choice. Considering that the film is quite hot, the change of temperature after the touch of the film induces a transient which is very difficult to compensate. Another problem arises with multilayers of film: if one layer has a dielectric constant quite higher than the others, the capacitive sensor calibration is lost if the percentages of the different layers vary. Finally, contact measurement often leaves a slight mark on the film during its movement, and for some film applications, it could be unsightly.

Some non-contact techniques are proposed for film gauging from one side, such as optical confocal methods or laser triangulation [2]. These techniques allow to have source and detector on the same side of the plastic film, however, the low intensity with which the beam focused on the second interface reaches the photodetector often does not allow to distinguish the signal from the noise of the measurement system. Other optical methods are based on low-coherence interferometry [6], a well-known technique used for Optical Coherence Tomography (OCT) [7–11]. In this paper, we present a modified fiber-optic low-coherence interferometer, able to work directly on a plastic bubble during extrusion, thanks to high-speed scanning and high depth of measurement field.

2. Materials and Methods

A low-coherence interferometer is based on the interference of an optical source, characterized by a limited coherence: the interference happens only when two beating optical beams have a path difference lower that the coherence length L_c [6]. For light sources with a Gaussian spectrum, the coherence length is equal to:

$$L_c = \frac{2 \ln(2)}{\pi} \cdot \left(\frac{\lambda_0^2}{\Delta \lambda} \right) \tag{1}$$

where $\Delta \lambda$ is the spectral linewidth of the optical source and λ_0 is its central wavelength. In classical low-coherence interferometer, the reference arm is constituted by a movable mirror to perform the spatial scanning: as the optical path difference varies, there will be interference between the recombined beams and, consequently, the classical function of periodic interference with sinusoidal trend. Since the source coherence is low, the fringes have a periodicity $\lambda/2$ as in a normal interferometer, but they are modulated in amplitude by the coherence function. For a source with Gaussian spectrum, also the coherence function is Gaussian. Figure 2 shows the intensity measured at the receiver of the output branch of a Michelson interferometer [2] when a source with coherence length L_c is used to measure the thickness d of a plastic film, with refractive index n, and the reference mirror is moved at speed v. The delay measurement between the pulses with Gaussian envelopes is a measurement of the thickness d of the plastic films, obtained by Equation (2):

$$d = \frac{v}{n} \bar{t}, \tag{2}$$

where $\bar{t}$ is the time distance between the two pulses.
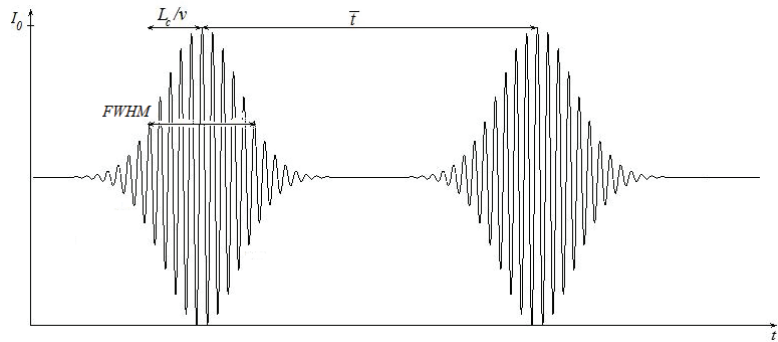

Figure 2. Photodetector interference figures in a Michelson interferometer with a low-coherence source when measuring a plastic film.

As evident from Figure 2, the coherence length limits the spatial resolution of the thickness measurement.

For measurement on real bubble for blown film, we decided to implement an all-fiber configuration for the low-coherence interferometer. Figure 3 shows the scheme of the first prototype realized for this particular application.
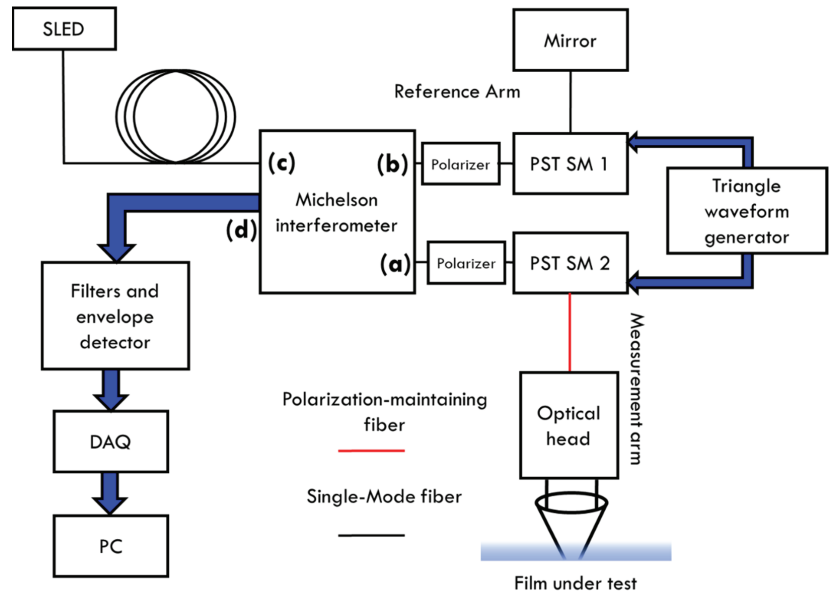
Figure 3. Scheme of the first prototype of low-coherence interferometer. SLED is superluminescent diode; DAQ is Data Acquisition card; PST SM is Piezo Stretcher with Single Mode fiber; PC is Personal Computer: (**a**) is measurement output; (**b**) is reference output; (**c**) is SLED input; (**d**) is electrical output.

The low-coherence light source (EXS1320-2111, EXALOS) is a superluminescent diode (SLED) with optical fiber output, at $\lambda_0 = 1315$ nm, $\Delta\lambda = 60$ nm corresponding to about

12 μm of coherence length. It is fed to an all-fiber Michelson interferometer (model INT-MSI-1300, THORLABS). Its scheme is described in Figure 4.
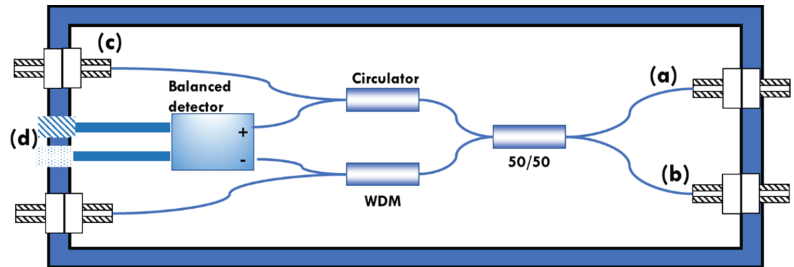
Figure 4. Scheme of the commercial all-fiber Michelson interferometer. (**a**) is measurement output; (**b**) is reference output; (**c**) is SLED input; (**d**) is electrical output.

The circulator couples the optical power incident at circulator ports, through the directional coupler (50/50), into the measurement (a) and reference branches (b). The reflections of the two branches recombine in the coupler and are directed to the two photodiodes. The interferometer makes the difference between the photodiodes signals, implementing a balanced detection. Compared to the classic solution, this system with circulator exploits doubles the power, in addition to considerably reducing the common mode components and avoiding back-reflection to the source, very dangerous for a superluminescent diode. The interferometer is also equipped with a wavelength division multiplexer (WDM) for an input in the visible region (a red laser typically), to better see the measurement spot.

The reference branch is equipped with a fiber stretcher (PZ2 Fiber Stretchers, OPTIPHASE) to modulate the length of the optical path, in order to perform a spatial scan along the axis of the measuring branch without having to physically move the mirror of the reference branch. Other scanning methods are available, but they require the movement of some optical and mechanical element, thus reducing the reliability and average life of the device, especially in the case of continuous operation of the system. Other than this, we experimentally found that the scanning frequencies should be higher than 150 Hz, to minimize the errors induced by film vibrations on real bubbles. This scanning rate is difficult to realize with a mechanical mirror. Fiber stretcher is driven by a triangular wave generator and a subsequent high voltage amplifier. After traveling through the two branches, the optical signal reflected returns to the inside of the interferometer where the interference is acquired by a photodetector. The driving voltage of the fiber stretcher must be carefully studied, to obtain a spatial scanning which allows the observation of the interference fringes due to the two plastic film interfaces: air-plastic and plastic-air. It must also be taken into account that any non-linearity in the scan translates into a non-linearity of the measurement. The equivalent speed of the mirror of the reference branch, which depends on the driving parameters of the fiber stretcher, determines the frequency of the fringes and the bandwidth of the electrical signal output from the interferometer. In fact, the following relationships hold true:

$$f_{fringes} = \frac{2 \cdot v_{mirror}}{\lambda_0}, \tag{3}$$

$$\Delta f = 2 \cdot v_{mirror} \frac{\Delta \lambda}{\lambda_0^2}, \tag{4}$$

where $f_{fringes}$ is the frequency of the fringes of the signal leaving the interferometric block, Δf is the width of its frequency spectrum, $\cdot v_{mirror}$ is the equivalent speed of the mirror on the reference branch, λ_0 is the central wavelength of the light source and $\Delta \lambda$ is the width of the emission spectrum.

For the prototype made, the PZ2 model of Optiphase was chosen as fiber stretcher, which includes both the piezoelectric cylinder and the fiber suitable for wavelengths between 1200 nm and 1600 nm. It can be controlled with voltages between ±400 V with a fiber extension factor of 3.8 μm for each applied volt. Considering then that the refractive index of the optical fiber is equal to 1.45, there is an effective variation of the optical path of about 5.5 μm for each applied volt. This value is not exact, because when the fiber is stretched, the effective refractive index decreases correspondingly, that is why the system will need a calibration, described in Section 3.1. From the electric point of view, it exhibits a strong resonance at 18 kHz; for lower frequency, it can be modeled as a purely capacitive 100 nF load. It is necessary to operate at frequencies much lower than 18 kHz to avoid oscillations due to resonance. It is also important to avoid abrupt transitions in the driving voltage, so as not to stimulate spontaneous oscillations of the system.

Figure 5 shows the periodic modulating wave, digitally designed to have a linear scan on both directions, but smoothed in order to reduce drastically its high-frequency harmonics. The voltage is generated by the analog output of a microcontroller, with main frequency of 180 Hz.
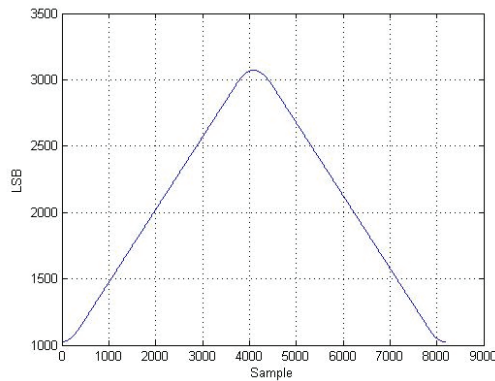
Figure 5. Modulating wave, digitally generated with smoothed edges to not exciting fiber stretcher piezo resonances (18 kHz). LSB is the number of Less Significant Bit, read by the microcontroller to generate the output wave.

The modulating wave is finally amplified at high voltage by a custom-made amplifier. Figure 6 shows the driving wave applied to the fiber stretcher, attenuated by a 1/31 divider.
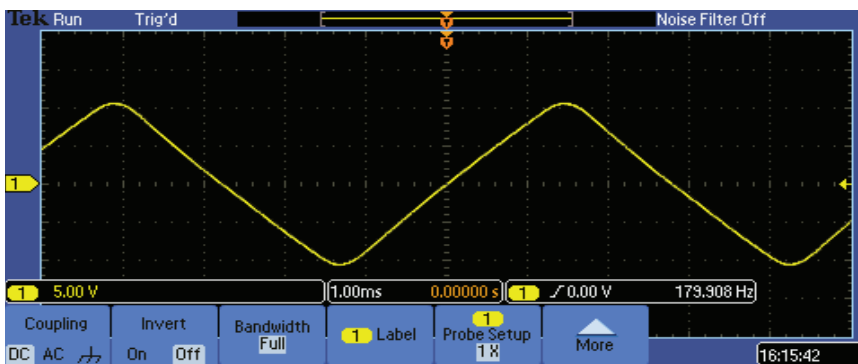
Figure 6. Detail of the waveform output from the amplifier and applied to the fiber stretcher, scaled by a factor of 1/31. Amplitude scale: 5 V/division. Horizontal scale: 1 ms/division.

Figure 7 shows its spectrum; the cancellation of harmonics above 2 kHz is evident.
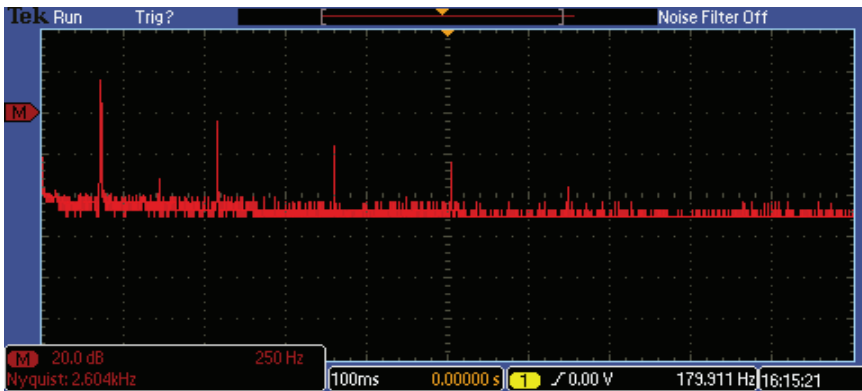
Figure 7. Spectrum of the signal applied to the fiber stretcher. All disturbances above 2 kHz are canceled to avoid fiber stretcher resonances. Amplitude scale: 20 dB/division. Horizontal scale: 250 Hz/division.

The output signal from the Michelson interferometer consists of interference fringes with a Gaussian envelope. The frequency of these fringes, given by Equation (3), is equal to about 2.4 MHz. To filter at this frequency, an active second order band-pass filter was chosen, inspired by band-pass configuration of the Sallen–Key cell. Next, electronics is an envelope detector and a final low-pass filter. The output signal is acquired by a DAQ-card (model NI 6251) and processed by a PC via LabVIEW.

The last section of the instrument is the optical head, connected through a polarization maintaining fiber, to minimize polarization variation while moving the head. Light is collimated and focused on the plastic film, as shown in Figure 8.
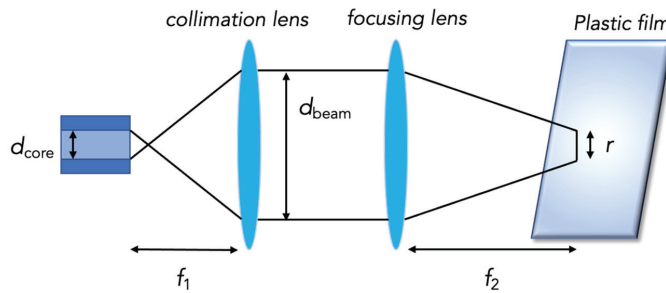
Figure 8. Optical head: collimation optics and beam focusing.

The collimator is the F240APC-C model by Thorlabs, working at $\lambda = 1310$ nm, with a focal length $f_1 = 8$ mm and a numerical aperture of 0.50. In this way, as indicated by the collimator specifications, a collimated beam of about 1.4 mm in diameter is obtained. It is focused by a biconvex lens with focal length $f_2 = 25$ mm, thus obtaining a transversal resolution r equal to:

$$r = \frac{4\lambda_0}{\pi} \frac{f}{d_{beam}} = \frac{4 \times 1310 \text{ nm}}{\pi} \cdot \frac{25 \text{ mm}}{1.4 \text{ mm}} \cong 30 \text{ μm,} \tag{5}$$

where d_{beam} is the diameter of the light beam after its collimation. As can be seen from Figure 8, the transverse resolution, r, represents the width of the beam focused on the measurand. The choice of these lenses made it possible to obtain a depth of focus D_{focus}

of about 1 mm. The depth of focus is the distance from the focus point, where average intensity has decreased by a factor 2, and it is given by:

$$D_{focus} = \frac{\pi r^2}{2\lambda}.$$

(6)

With the depth of focus of 1 mm, the instrument can provide acceptable signals within ± 2 mm of dynamics. This means that it is sufficient to keep the surface of the bubble within these at 4 mm around the focus distance f_2 = 25 mm to obtain a correct measurement. From a practical point of view, this means that the measuring system requires a relatively slow bubble follower. The focal length chosen for the focusing lens represents a good compromise between retroreflected power collected and depth of focus obtained. Another factor to be considered is the sensitivity to the incident angle of the light, that in theory should be perpendicular to the film surface. With a focal length of 25 mm and a collimated beam diameter of 1.4 mm, there are ± 1.6 degrees of tolerance for the alignment, to still achieve some reflected signal. The error in thickness measurement for this kind of misalignment is absolutely negligible (it is a cosine error lower than 10^{-3}): the problem related to misalignment is only signal fading; if the sensor can see the signal, the measurement value is correct. Finally, the distance between the collimating lens and the focusing lens must be such that the overall length of the measuring branch equals that of the reference branch, to obtain the maximum output signal when the fiber stretcher is in the rest condition.

The last part of the first prototype consists in two polarization controllers, placed in both measurement and reference arm, to change the light polarization in the fiber, to avoid a different path for the two main polarizations in the fiber. If not well controlled, the two paths of different polarizations generate 2 measurement peaks for every surface, significantly worsening the resolution of the instrument. This control in laboratory condition is easily obtained manually, but it is not stable in the real environment, due to strong temperature variations (plastic bubble is at high temperature, and ambient temperature around the bubble can easily exceed 40 degrees).

The problem of light polarization for these kind of interferometers is well known. A standard solution is given by a different scheme, the auto-correlator [12], shown in Figure 9. This scheme measures the beating frequencies between the reflection of the two surfaces, instead of the ones between a mirror and a single surface. It has the great advantage to not require two measurement branches of the same length and it is insensitive to polarization effect, thanks to the Faraday mirrors. The main drawback is the requirement of strong light reflection from the target surface because internal mirror light reflection is much higher than the surface reflection. This requirement forces to work only with a strong focusing of the measurement beam on the target, and it makes it not possible to reach an instrument depth of focus of 4 mm.

In order to keep the advantages of the low-coherence interferometer (Figure 3) adding the absence of sensitivity to polarization, typical of auto-correlator, we propose a novel scheme, shown in Figure 10. The main difference from the traditional one, Figure 3, is the addition of a Faraday mirror on the reference branch, and a Faraday rotator on the measurement branch, close to the optical head. Another difference is the use of a single fiber stretcher, which proved sufficient for the application, considering 4 mm of depth of focus.
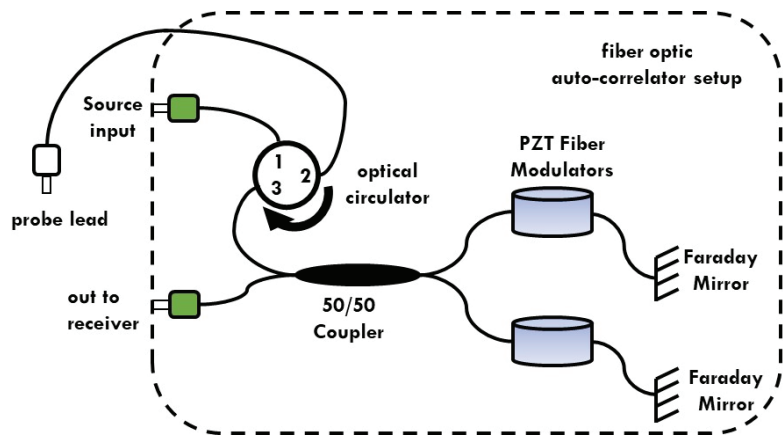
Figure 9. Scheme of an all-fiber autocorrelator for thickness measurement: the beating happens between the reflections from the two film surfaces.
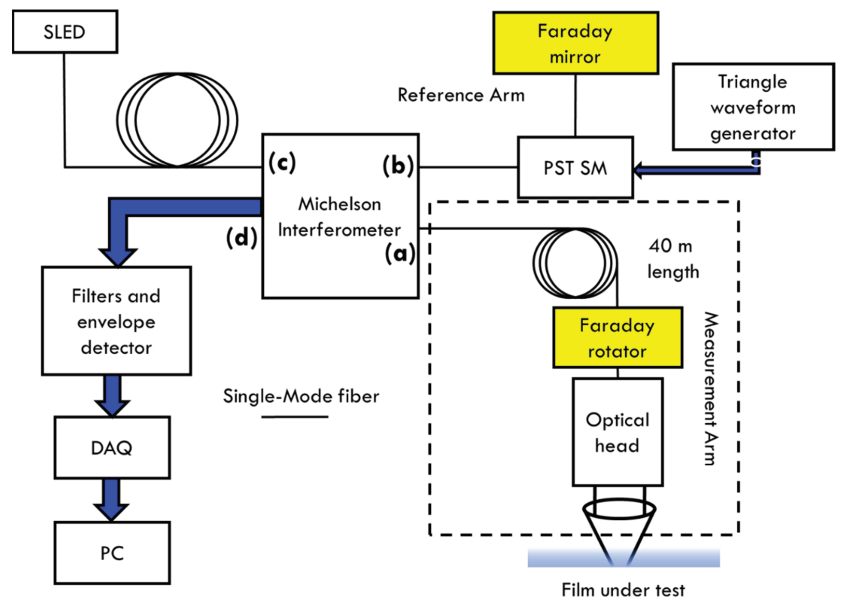

Figure 10. Final set-up of low-coherence interferometer, with Faraday mirror and rotator, to solve polarization problems. SLED is superluminescent diode; DAQ is Data Acquisition card; PST SM is Piezo Stretcher with Single Mode fiber; PC is Personal Computer. (**a**) is measurement output; (**b**) is reference output; (**c**) is SLED input; (**d**) is electrical output (same labels of Figures 3 and 4).

Faraday rotator is an optical device that rotates the polarization of the light flowing in it by exploiting the Faraday effect, the result of a ferromagnetic resonance [13]. This resonance causes the decomposition of the waves into two rays with reverse circular polarization which propagate at different speeds (circular birefringence). Due to the difference in propagation speeds, at the end of the medium, the two rays recombine with a sharp phase difference which results in a rotation of the angle of the polarization plane. The light exiting Faraday rotator will be rotated 45° with respect to the input polarization.

Subsequently, this light will reach the plastic film and will be reflected. Passing again through the Faraday rotator, it will be rotated by another 45° so that the return light is orthogonal to the outward one. In this way, the polarization changes along the fiber are canceled during the return journey, because for every input polarization state, the sum of the round trip remains a constant path. The same happens for the Faraday mirror, inserted in the reference branch, able to compensate for the polarization problems, also due to the birefringence induced by the fiber stretcher [14].

The final prototype shows a complete insensitivity to polarization problems, maintaining the excellent performance of the first prototype. Figure 11 shows an example of an acquired signal while measuring a transparent film, together with the triangular modulating wave.
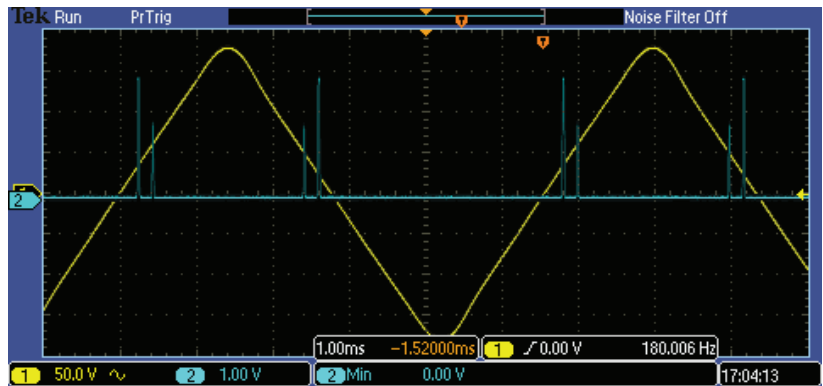
Figure 11. Acquired signal (light blue signal) while measuring a transparent film, together with the smoothed triangular modulating wave (yellow signal). Amplitude scale: 50 V/division for triangular wave; 1 V/division for acquired signal. Horizontal scale: 1 ms/division.

3. Results

The prototype instrument elaborates acquired signals for obtaining the more accurate thickness measurement. Figure 12 shows an example of raw signal acquired while measuring a transparent plastic film, with nominal thickness of 50 μm. In the figure, the two couple of peaks are evident, corresponding to the ascendant and descendant phases of the triangular modulation. Time distance between two peaks is proportional to the film thickness.

With regards to the amplitude variability of every peak, we have to note that the peak's amplitude depends on the angular alignment of the sensor, on the parallelism of the two surfaces, and also on the absolute distance (the relative position with respect to the focus). For these reasons, in every measurement, we can see different amplitudes, which are also relative between the peaks corresponding to the two surfaces. To pass from time measurements to thickness measurement, an instrument calibration is required, as described in the later paragraph.
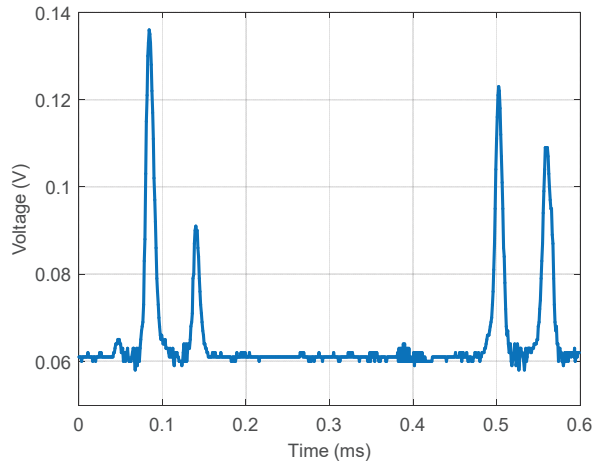
Figure 12. Raw signal acquired for a transparent film; nominal thickness 50 µm.

3.1. Calibration

The calibration of the instrument was carried out using a single interface target (aluminum wall), moved by a micrometric slide. In this way, the instrument measures only one peak. The calibration curve is reported in Figure 13: the final range is higher than 4 mm, linearity is guaranteed on all the range and the sensitivity in air is about 1.5 mm/ms. When measuring plastic films, the refractive index *n* should be considered. For the types of plastic normally employed (for example, polyethylene), it is around 1.5.
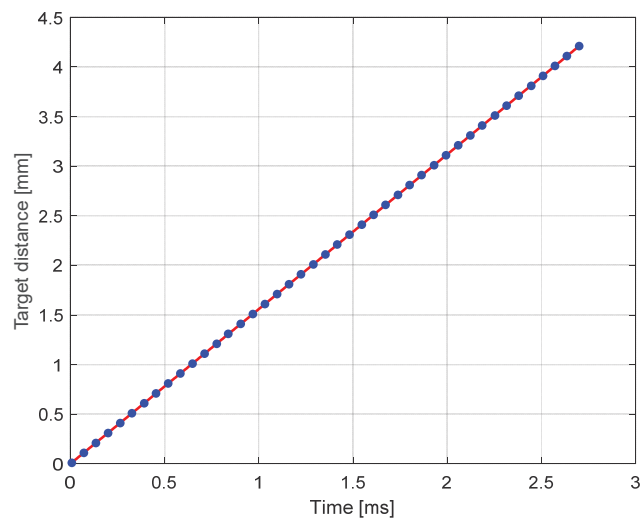
Figure 13. Calibration of low-coherence interferometer (in air). Dots represent measured data while the line is the linear fitting curve. The measurement range of about 4 mm is centered at 25 mm from the output lens (see Figure 8).

3.2. Average Algorithm

The algorithm for calculating film thickness requires an input signal as clean as possible, without disturbances caused by bubble vibrations or by the presence of dyes.

For this reason, 10 forward spatial scans are acquired before evaluating the thickness. Subsequently, these scans are aligned since the first peak (recognized with a parabolic regression technique), and then averaged to obtain a signal as independent as possible from the vibrations. The same procedure is carried out with the return spatial scans.

In Figure 14a, we see the trend of 10 forward scans aligned based on the first peak. Due to the vibrations, they will not all be perfectly alike; however, the distance between the peaks, which indicates the thickness of the plastic film, will be kept constant. By averaging the 10 scans, we can eliminate noise and disturbances, as we can see in Figure 14b.

(**a**)

(**b**)
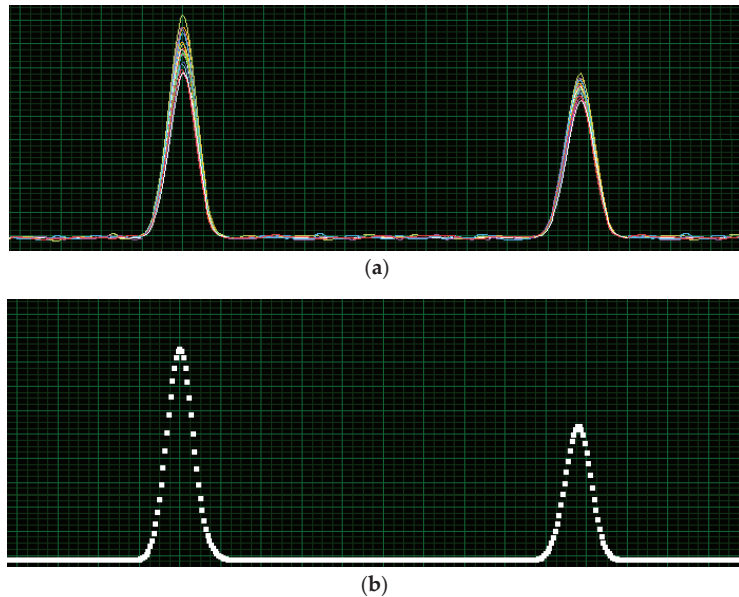
Figure 14. (**a**) Ten subsequent acquisitions, aligned on the first peak. Amplitude scale: 100 mV/division. Horizontal scale: 10 μm/division; (**b**) Average of the acquisitions from Figure 14a. Amplitude scale: 100 mV/division. Horizontal scale: 10 μm/division.

Several algorithms have been tested for the best localization of the peaks: optimal filters, correlation with Gaussian functions, center of gravity. It was noted that the best accuracy and repeatability performances were obtained with a parabolic regression algorithm, applied to 8 points around the maximum. This algorithm has the advantage of being extremely simple and can be easily implemented even on a microcontroller: the analytical solution of linear regression is applied to the derivative of the curve, and the zero of the signal derivative corresponds to the maximum of the peak.

3.3. Measurement on A Real Plant

The instrument was initially mounted on a fixed location in front of the bubble. The normal vibrations of the bubble do not exceed the 4 mm range of the instrument, so it was possible to carry out a continuous measurement of the film thickness. A very first version of the instrument, modulated at 20 Hz, did not exhibit a stable measurement, while the actual prototype, at 180 Hz, show a series of measurements that move in the measurement range, but once realigned on the first peak, they show a variation of a few micrometers, practically negligible after the 10 averages. Figure 15 shows the two measures during rise and fall of the triangular wave, for 80 μm transparent film. Horizontal scale is already calibrated in micrometers. The measured peaks now are not perfectly symmetric, because the vibration changes the peak position (the scanning speed is much higher than

the vibration speed, but there is still an influence). By averaging 10 measurements, this effect is strongly reduced, but there is still a contribution on the measurement accuracy: the measured standard deviation is about 0.1 μm in laboratory conditions, while on real bubble, it is between 1 μm and 2 μm, depending on the bubble vibration.
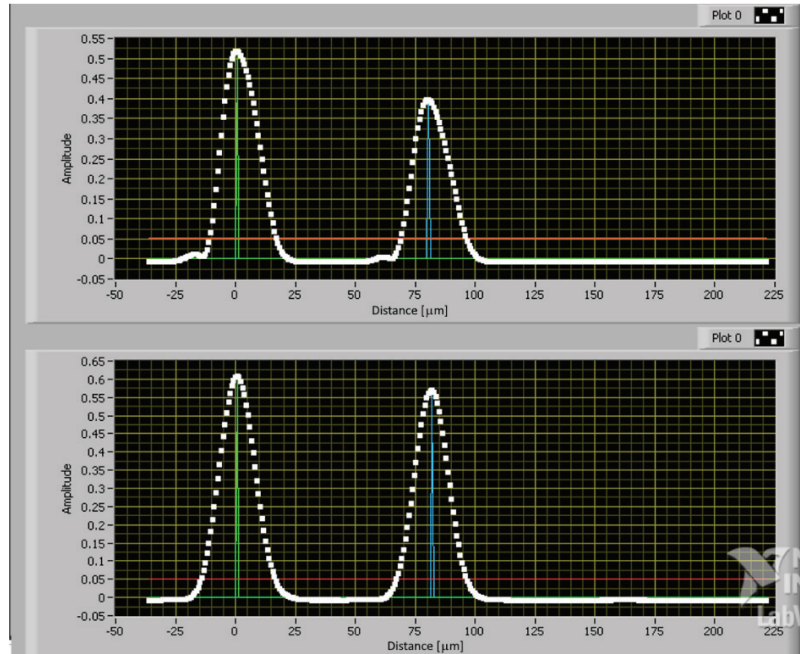

Figure 15. LabVIEW screenshot of the measurement acquired on a real bubble in a working plant, for a transparent film with thickness 80 μm, during rise (**top**) and fall (**bottom**) of the triangular wave. Amplitude scale: 50 mV/division. Horizontal scale: 25 μm/division. The two vertical lines indicate the position of the peaks, localized by the parabolic regression algorithm.

After a series of positive results on real bubbles, the instrument was mounted on the rotating structure of a commercial capacitive sensor. In this case, the measurement is easier because the contact sensor dampens the natural vibrations of the bubble. In any case, comparable measurement results were obtained by releasing the capacitive sensor (bubble free to vibrate). The comparison of thickness measurement from capacitive and optical sensors is reported in Figure 16: Figure 16a shows the measurement for a transparent film with nominal thickness of 80 μm, as a function of the angle of the rotating stage; Figure 16b shows the measurements acquired during a change of film thickness. The capacitive sensor was automatically disconnected during the change. The small thermal drift of its measurement while touching the film (at angle 180°) is also evident.
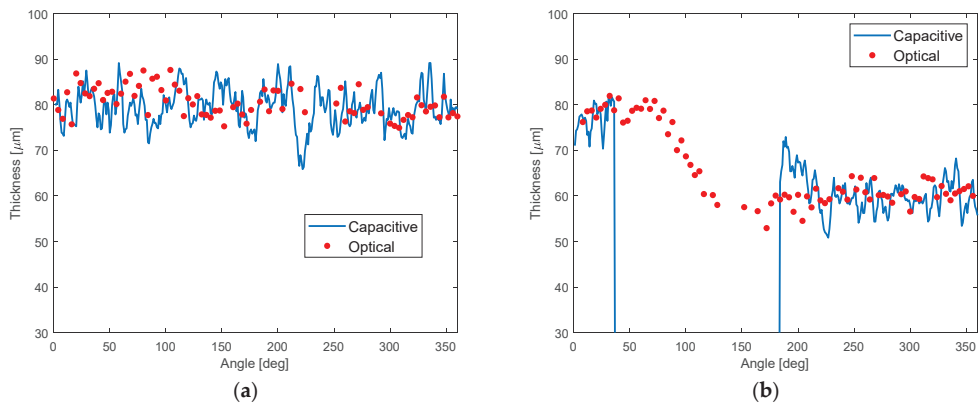
Figure 16. Measured thickness during rotation around the bubble. Comparison of capacitive and optical measurements: (**a**) Constant thickness; (**b**) Measurement during a change of film thickness, from 80 μm to 60 μm.

4. Discussion

The proposed instrument for contactless thickness measurement is based on a modified low-coherence interferometer. It is realized in an all-fiber configuration, in order to take advantage of the high modulation speed of piezo stretcher, mandatory for measuring on a real bubble, vibrating at a frequency of a few hertz. In order to overcome the polarization problems induced by the optical fiber, standard techniques for thickness measurement are based on autocorrelation: the beating interference is given between the reflections of the two surfaces of the film. This technique exhibits good results in laboratory conditions, but it is not adequate to application in a real plant, because it requires strong focusing on the film, in order to get enough back-reflection. In this way, the depth of focus is too limited to include bubble vibrations. Our proposal is based on a standard low-coherence interferometer, enriched by two faraday rotators, able to compensate for the fiber birefringence, even if time-variant. To our knowledge, this configuration is original. The designed depth of focus is about 4 mm, coherent with the scanning range. From a measurement campaign on a real plant, the range proved to be adequate to compensate for bubbles' vibrations, considering the measurement frequency of 180 Hz.

With reference to performance, the instrument has a resolution lower than 1 μm, limited by the coherence length of the source (about 12 μm) improved by the parabolic regression on the peaks. The standard deviation, at a measurement rate of 180 Hz, in laboratory condition is about 0.1 μm, while on real bubble, it is between 1 μm and 2 μm, depending on the vibration conditions (function of the film thickness). Minimum measurable thickness is about 20 μm. As expected from theory, we cannot see any measurement error due to incident angle variation, with an angle tolerance of about ±1.6 degrees to still obtain some reflected signal: the error is a cosine function of the angle and it is negligible for this misalignment (lower than 10^{-3}). The main problem of misalignment is signal fading: on real bubble, the sensor should be carefully aligned to be perpendicular to the film surface, by looking at the signal amplitude. Experiments have shown rapid distance variations due to bubble vibrations, but small angular misalignment. On tens of measurement on real plants, we have noticed no signal fading due to misalignment.

In conclusion, the proposed instrument is a possible substitute for capacitive sensors, as these performances are adequate for the specific measuring application of plastic films.

Institutional Review Board Statement: Not applicable.

Informed Consent Statement: Not applicable.

Conflicts of Interest: The authors declare no conflict of interest.

References

1. Wagner, J.R.; Mount, E.M.; Giles, H.F. Blown Film. In *Extrusion*, 2nd ed.; Wagner, J.R., Mount, E.M., Giles, H.F., William, A., Eds.; ASM International: Oxford, UK, 2014; Volume 3, pp. 539–549.
2. Donati, S. *Electro.-Optical Instrumentation: Sensing and Measuring with Lasers*, 1st ed.; Prentice Hall: Hoboken, NJ, USA, 2004.
3. Gutiérrez, R.M. Thin film thickness measurement with triple gas electron multiplier detector by 55Fe radiation transmission and background detection using energy distribution analysis. *Instrum. Sci. Technol.* **2020**, *48*, 539–549.
4. Piegari, A.; Masetti, E. Thin film thickness measurement: A comparison of various techniques. *Thin Solid Films* **1985**, *124*, 249–257. [CrossRef]
5. Cai, L.; Tan, Y.G.; Wei, Q. On-line thickness measurement of thin film based on neural network. In *Applied Mechanics and Materials*; Trans Tech Publications Ltd.: Kapellweg, Switzerland, 2014; Volume 484, pp. 307–310.
6. Rao, Y.-J.; Jackson, D.A. Recent progress in fibre optic low-coherence interferometry. *Meas. Sci. Technol.* **1996**, *7*, 981–999. [CrossRef]
7. Aumann, S.; Donner, S.; Fischer, J.; Müller, F. Optical Coherence Tomography (OCT): Principle and Technical Realization. In *High Resolution Imaging in Microscopy and Ophthalmology*; Bille, J., Ed.; Springer: Cham, Switzerland, 2019. [CrossRef]
8. Huang, D.; Swanson, E.A.; Lin, C.P.; Schuman, J.S.; Stinson, W.G.; Chang, W.; Hee, M.R.; Flotte, T.; Gregory, K.; Puliafito, C.A. Optical coherence tomography. *Science* **1991**, *254*, 1178–1181. [CrossRef] [PubMed]
9. Fercher, A.F.; Drexler, W.; Hitzenberger, C.K.; Lasser, T. Optical coherence tomography-principles and applications. *Rep. Prog. Phys.* **2003**, *66*, 239. [CrossRef]
10. Bouma, B.E.; Tearney, G.J. *Handbook of Optical Coherence Tomography*, 1st ed.; CRC Press: Boca Raton, FL, USA, 2001.
11. Drexler, W.; Fujimoto, J.G. *Optical Coherence Tomography*, 2nd ed.; Springer: Berlin, Germany, 2015.
12. Walecki, W.J.; Szondy, F. Fiber optics low-coherence IR interferometry for defense sensors manufacturing. In *Photonic Microdevices/Microstructures for Sensing*; Society of Photo Optical: Bellingham, WA, USA, 2009.
13. Shiraishi, K.; Sugaya, S.; Kawakami, S. Fiber Faraday rotator. *Appl. Opt.* **1984**, *23*, 1103–1106. [CrossRef] [PubMed]
14. Lagorceix, H.; Reynaud, F. Birefringent effect measurement and compensation in a highly birefringent fiber optical path modulator. *Opt. Commun.* **1995**, *118*, 235–240. [CrossRef]

Measurement of Focal Length and Radius of Curvature for Spherical Lenses and Mirrors by Using Digital-Grating Moiré Effect

Chien-Yuan Han [1], Wen-Tai Lo [2], Kun-Huang Chen [3], Ju-Yi Lee [4], Chien-Hung Yeh [2] and Jing-Heng Chen [2,*]

[1] Department of Electro-Optical Engineering, National United University, No. 2, Lienda, Nanshi Li, Miaoli 36063, Taiwan; cyhan@nuu.edu.tw
[2] Department of Photonics, Feng Chia University, No. 100, Wenhwa Rd., Seatwen, Taichung 40724, Taiwan; fcum0405954@alumni.fcu.edu.tw (W.-T.L.); yehch@fcu.edu.tw (C.-H.Y.)
[3] Department of Electrical Engineering, Feng Chia University, No. 100, Wenhwa Rd., Seatwen, Taichung 40724, Taiwan; chenkh@fcu.edu.tw
[4] Department of Mechanical Engineering, National Central University, No. 300, Zhongda Rd., Zhongli District, Taoyuan 320317, Taiwan; juyilee@ncu.edu.tw
* Correspondence: jhchen@fcu.edu.tw; Tel.: +886-4-2451-7250 (ext. 5093); Fax: +886-4-2451-0182

Abstract: This paper proposes the use of digital-grating moiré effect for measuring the focal lengths and radius of curvatures of biconvex and biconcave spherical simple lenses and spherical mirrors. Based on Fresnel diffraction, the equation for the electric field of propagated light passing through the test samples was derived. Through digital image post processing, the recorded intensity on an observation screen was superimposed on a digital grating to generate a moiré pattern. On substituting the slant angle of the moiré pattern into the derived equation, the focal lengths and radius of curvatures could be determined. The experimental results successfully demonstrated the feasibility of the proposed method; the percent errors for focal length and radius of curvature measurement were less than 0.5%. The measurement uncertainty was analyzed and the correctness of the derived equation was confirmed through simulation. Because of the use of digital image post processing, the proposed method has advantages such as a simple set up, easy operation, high stability, high accuracy, and low cost. Thus, the method has considerable potential in relevant application.

Keywords: moiré effects; diffraction theory; lenses; mirrors; digital image processing

1. Introduction

Focal length and radius of curvature, the most important parameters of spherical lenses and mirrors, have been widely used to design optical systems and commercial electro-optical products. The measurement of focal length and radius of curvature is necessary to ensure the quality and performance of lenses and mirrors. Methods such as nodal slide and image magnification have been proposed for these measurements [1]. These methods have been successfully applied to measure the lenses with short focal lengths or large numerical apertures. Modern methods mainly use the Talbot effect and moiré technique to measure focal length [2–8]. In both these methods, two Ronchi gratings are required. After the test light passes through the test lens and mirror, the magnified self-image of the first grating is superimposed on the second grating to generate moiré fringes. By rotating one grating with respect to the other, the slant angle of the moiré fringes can be used to estimate to the curvature and focal length of the test samples. However, the rotation of the grating can introduce mechanical vibrations. In addition, two gratings are required; therefore, measurement using these two methods is complex and time-consuming. Digital image post processing, a recent trend in relevant applications, has several advantages [9,10]. The technique proposed by Angelis et al. for the automated analysis of moiré fringes for accurate measurement of the focal length of lenses is based on the fast Fourier transform

(FFT) and least-squares fit methods [11]. Lee proposed a Talbot interferometry-based digital image method for measuring the focal length of lenses without using moiré fringes. In this method, only one grating is required and the original Fourier transform is used to access the spectrum beyond the limitations of the usual fast Fourier transform [12]. However, using the original Fourier transform can be time-consuming.

In this paper, a method based on digital-grating moiré effect is proposed for measuring the focal lengths and radius of curvatures of spherical lenses and mirrors. The measurement system consists of a test light source, a Ronchi grating, a digital camera, and a personal computer. Based on Fresnel diffraction, the electric fields of the test light at various positions and the intensity at an observation screen were derived using the kernel equation for the method. After the test light passed through the grating and sample, the light intensity was projected on the observation screen and captured by the digital camera. This light intensity was superimposed on a digital grating to generate a moiré fringe. Using the slant angle of the moiré fringe, the focal length and radius of curvature of the test sample were determined. To demonstrate the feasibility of the proposed method, the focal lengths of three convex mirrors and two concave lenses were measured. The measurement percent errors for the focal lengths and radius of curvatures were less than 0.5%. Because the method applied digital image post processing, only a single digital image was required to be captured during measurement. Therefore, this method is time saving and free of mechanical vibrations. In addition, only one grating is required in this method. Consequently, this method has merits such as a simple establishment, easy operation, high stability, high accuracy, and low cost. Thus, it has considerable potential in relevant applications.

2. Principles

Figure 1a,b schematically represent the measurements for the reflection spherical mirrors and transmission spherical lenses (bi-convex or bi-concave), respectively. To facilitate understanding, an x–y–z coordinate system is introduced in the figures. A collimated and expanded laser beam with a wavelength of λ passes through the Ronchi grating (G), located at (x_0, y_0); the transmittance of the grating can be written as

$$t_0(x_0, y_0) = \frac{1}{2}(1 + \cos \frac{2\pi x_0}{p_1}),\tag{1}$$

where p_1 is the period of the grating in the x–direction. The electric field behind the grating is denoted as $U_0 (x_0, y_0, 0)$ (at $z = 0$) and the intensity can be expressed as

$$I_0 = |U_0(x_0, y_0, 0)|^2 = \frac{1}{4}(1 + 2\cos\frac{2\pi x_0}{p_1} + \cos^2\frac{2\pi x_0}{p_1}),\tag{2}$$
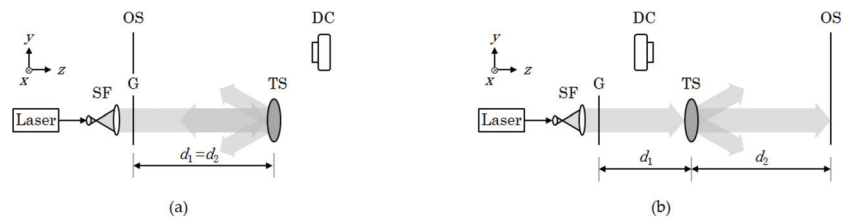

Figure 1. Schematic of the measurement setup for (**a**) reflection and (**b**) transmission samples. SF, spatial light filter; G, Ronchi grating; TS, test sample; OS, observation screen; DC, digital camera.

According to Fresnel diffraction, the electric field U_1 (x_1, y_1, d_1) of the test light reaching the test sample (TS) after propagating a distance of d_1 can be expressed as

$$U_1(x_1, y_1, d_1) = \frac{e^{jkd_1}}{j\lambda d_1} \int \int_{-\infty}^{\infty} t_0(x_0, y_0) e^{j\frac{k}{2d_1}[(x_1-x_0)^2+(y_1-y_0)^2]} dx_0 dy_0. \tag{3}$$

Meanwhile, the transmittance of the test sample, t_1 (x_1, y_1), can be expressed as [13]

$$t_1(x_1, y_1) = e^{-j\frac{k}{2f}(x_1^2+y_1^2)}, \tag{4}$$

where $k = 2\pi n/\lambda$ is the propagation number, n is the refractive index of the environmental medium, and f is the focal length of the test sample. For converging lenses or concave mirrors, the focal length has a positive sign. By contrast, for diverging lenses or convex mirrors, the focal length has a negative sign.

As shown in Figure 1a,b, respectively, the reflected and transmitted electric field U_1' can be written as

$$U_1'(x_1, y_1, d_1) = \frac{e^{jkd_1}}{j\lambda d_1} \int \int_{-\infty}^{\infty} t_0(x_0, y_0) e^{j\frac{k}{2d_1}[(x_1-x_0)^2+(y_1-y_0)^2]} e^{-j\frac{k}{2f}(x_1^2+y_1^2)} dx_0 dy_0. \tag{5}$$

Again, the test light travels an additional distance of propagation d_2 and reaches the observation screen (OS), as shown in Figure 1a,b, respectively. According to Fresnel diffraction, the electric field of the test light on the observation screen can be written as

$$U_2(x_2, y_2, d_2) = \frac{e^{jkd_2}}{j\lambda d_2} \int \int_{-\infty}^{\infty} U_1'(x_1, y_1, d_1) e^{j\frac{k}{2d_2}[(x_2-x_1)^2+(y_2-y_1)^2]} dx_1 dy_1. \tag{6}$$

With extensive substitution, Equation (6) can be expressed as [13]

$$U_2(x_2, y_2, d_2) = \frac{1}{2} \left\{ 1 + \cos\left[2\pi \frac{x_2}{p_1\left(1 - \frac{d_2}{f}\right)}\right] \times \exp\left[-j\frac{\pi\lambda d_1}{p_1^2}\left(\frac{\frac{1}{d_1} - \frac{1}{f} + \frac{1}{d_2}}{\frac{1}{d_2} - \frac{1}{f}}\right)\right] \right\}. \tag{7}$$

Accordingly, the intensity on the observation screen, recorded using a digital camera (DC), can be expressed as follows:

$$I(x_2, y_2, d_2) = |U_2(x_2, y_2, d_2)|^2 = \frac{1}{4}\left\{1 + 2\cos\frac{2\pi x_2}{p_1(1-\frac{d_2}{f})}\cos\frac{\pi\lambda d_1}{p_1^2}\left(\frac{\frac{1}{d_1}-\frac{1}{f}+\frac{1}{d_2}}{\frac{1}{d_2}-\frac{1}{f}}\right) + \cos^2\frac{2\pi x_2}{p_1(1-\frac{d_2}{f})}\right\}. \tag{8}$$

The captured intensity with a period of mp_1 and a grating vector $K_1 = (2\pi/mp_1)\hat{i}$ is superimposed on a digital grating with a period of p_2 and a grating vector $K_2 = (2\pi\cos\theta/p_2)\hat{i} - (2\pi\sin\theta/p_2)\hat{j}$, as shown in Figure 2. The value of p_2 is determined by the captured pattern described in Equation (8) and is set as $p_2 \cong mp_1$. Therefore, a moiré pattern with a slant angle α can be obtained. The slant angle α is defined as the angle between the grating vector K_3 of moiré pattern and the y-axis which can be written as [14]

$$\alpha = \tan^{-1}\left(\frac{p_2 - mp_1\cos\theta}{mp_1\sin\theta}\right) = \tan^{-1}\left(\frac{p_2 - \left|1 - \frac{d_2}{f}\right|p_1\cos\theta}{\left|1 - \frac{d_2}{f}\right|p_1\sin\theta}\right) = \tan^{-1}\left(\frac{1 - M\cos\theta}{M\sin\theta}\right), \tag{9}$$

where $m = |1 - d_2/f|$ is the imaging magnification for grating G, θ is the angle between the practical and digital gratings, and M is the period ratio of the two period patterns (captured intensity and digital grating) which equals mp_1/p_2. Therefore, the observation plane is in the grid image given by the test sample under study. It results from the setup of Figure 1 and the magnification formula $m = |1 - d_2/f|$.
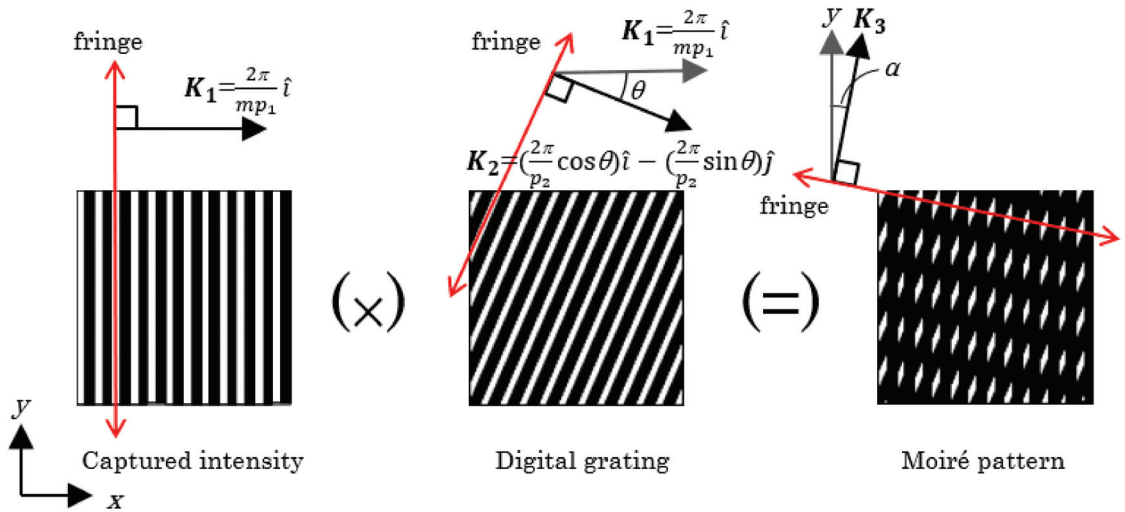
Figure 2. Schematic illustration for the generation of moiré pattern and related orientations.

Accordingly, the focal length of the test samples can be expressed as

$$f = \frac{p_1(\tan\alpha\sin\theta + \cos\theta)d_2}{p_1(\tan\alpha\sin\theta + \cos\theta) - p_2},\tag{10}$$

and the radius of curvature of the test samples can be written as

$$R = -2f = -\frac{2p_1(\tan\alpha\sin\theta + \cos\theta)d_2}{p_1(\tan\alpha\sin\theta + \cos\theta) - p_2}, \text{ (for spherical mirrors)}\tag{11}$$

and

$$R_1 = -R_2 = 2(n_l - 1)f = \frac{2(n_l - 1)p_1(\tan\alpha\sin\theta + \cos\theta)d_2}{p_1(\tan\alpha\sin\theta + \cos\theta) - p_2}, \text{ (for spherical lenses)}\tag{12}$$

where R_1 and R_2 are the radius of curvature of the bi-convex or bi-concave lens's first and second surfaces, and n_l is the refractive index of the lens. Thus, the focal length and radius of curvature of the test samples can be determined using the following experimental parameters: the periods of the practical and digital gratings, p_1 and p_2, respectively; the relative angle between these gratings, θ; the slant angle of the moiré pattern, α; the distance, d_2; and the refractive index of the lens, n_l.

3. Experimental Results and Discussion

To demonstrate the feasibility of the proposed method, three convex mirrors (Edmund Optics) labeled TS1, TS2, and TS3, with focal lengths of -7.751, -25.80, -52.08 mm, respectively, and radius of curvatures of -15.50, -51.60, and -104.2 mm, respectively, and two BK7 concave lenses (Edmund Optics) ($n_l = 1.5151$ @ $\lambda = 0.6328$ μm) labeled TS4 and TS5, with focal lengths -50.00 and -200.0 mm, respectively, and radius of curvatures of -51.51 and -206.0 mm, respectively, were measured. The photos of experiment setup are shown in Figure 3a,b. A Ronchi grating of laser direct writing photomask (MLA150, HEIDELBERG INSTRUMENTS) with a period of 0.2822 mm was used. A 0.6328 μm helium–neon laser was used as the test light source and a digital camera (Canon EOS 650D) was used to capture the intensity of the test light field. The vertical pixel array of the camera was aligned to the pattern of light field along y-direction. For convenience, the distances d_1 and d_2 were both set at 251.7 mm. The captured intensities of TS1–5

(on the observation screen) are illustrated in Figure 4a–e, respectively. The gray-level transformed pictures are illustrated in Figure 4f–j, respectively. The corresponding digital gratings with periods of 9.480, 3.072, 1.659, 1.720, and 0.6410 mm which were set similar to that of the gray-level transformed patterns are shown in Figure 4k–o. The angle θ between the practical and digital grating was set as $30°$. Accordingly, the superimposed moiré patterns were obtained as illustrated in Figure 4p–t, respectively. With these moiré patterns, the obtained slant angles, α, of TS1–5 were $15.46°$, $15.35°$, $15.79°$, $15.83°$, and $15.50°$, respectively. After substituting the relevant parameters into Equations (10)–(12), as listed in Table 1, the focal lengths of TS1–5 were -7.757, -25.67, -52.05, -49.85, and -199.6 mm, respectively, and the radius of curvatures were -15.51, -51.34, -104.1, -51.36, and -205.6 mm, respectively. Compared with commercial reference values, the results exhibited a high accuracy of measurement of the focal lengths and radius of curvatures, and the percent errors were less than 0.5%.
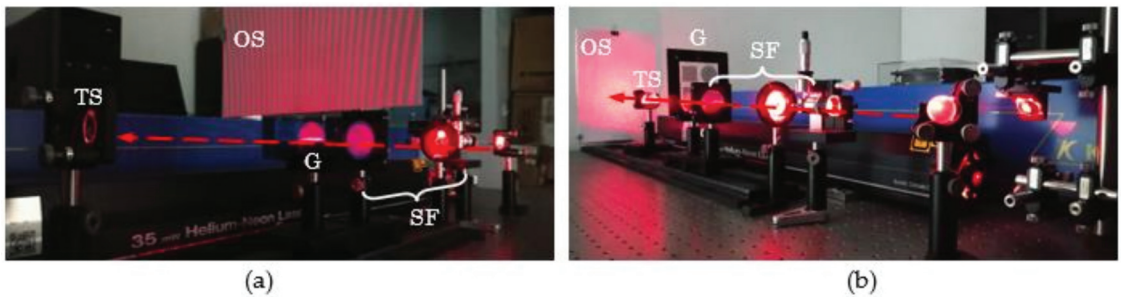
Figure 3. Experiment setup for measuring (**a**) reflection and (**b**) transmission samples. SF, spatial light filter; G, Ronchi grating; TS, test sample; OS, observation screen.
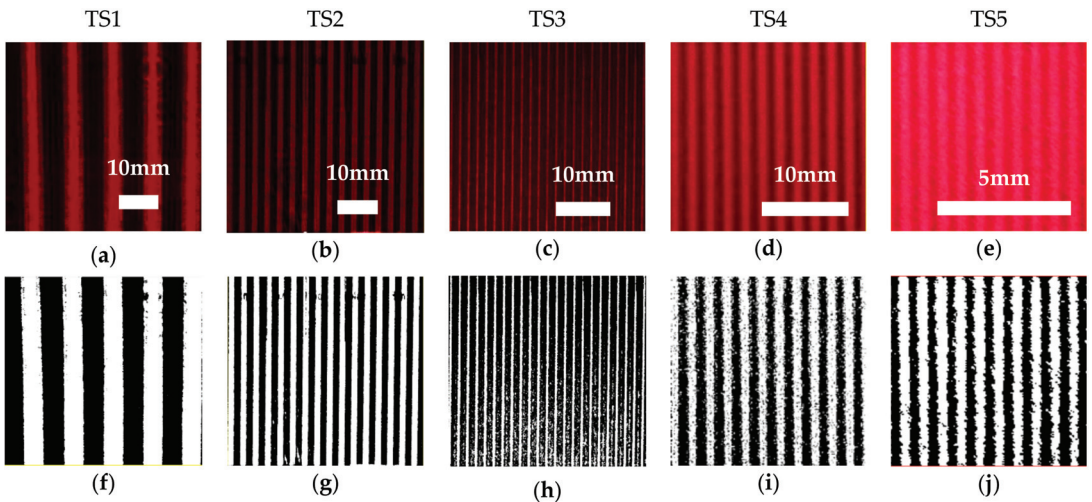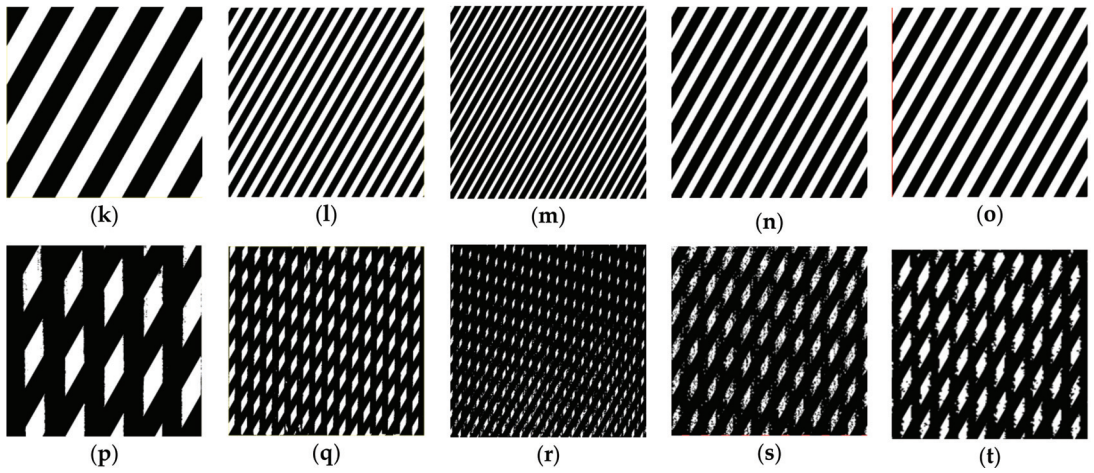

Figure 4. *Cont.*

Figure 4. Captured intensities on the screen for test samples (TSs): (**a**) TS1, (**b**) TS2, (**c**) TS3, (**d**) TS4, and (**e**) TS5. Gray-level transformed images of the captured intensity for the TSs: (**f**) TS1, (**g**) TS2, (**h**) TS3, (**i**) TS4, and (**j**) TS5. Digital gratings with a slant angle of 30° for TSs: (**k**) TS1, (**l**) TS2, (**m**) TS3, (**n**) TS4, and (**o**) TS5. Moiré patterns obtained with digital image post processing of the TSs: (**p**) TS1, (**q**) TS2, (**r**) TS3, (**s**) TS4, and (**t**) TS5.

Table 1. Relevant parameters, experimental results, and percent errors for focal length and radius of curvature measurement.

Test Samples	Angle θ (°)	Slant Angle α (°)	Experimental Value of Focal Length (mm)	Reference Value of Focal Length (mm)	Percent Error (%)
			Experimental Value of Radius of Curvature (mm)	Reference Value of Radius of Curvature (mm)	Percent Error (%)
TS1	30.00	15.46	−7.757	−7.751	0.0774
			−15.51	−15.50	0.0645
TS2	30.00	15.35	−25.67	−25.80	0.5039
			−51.34	−51.60	0.5039
TS3	30.00	15.79	−52.05	−52.08	0.0576
			−104.1	−104.2	0.0960
TS4	30.00	15.83	−49.85	−50.00	0.3000
			−51.36 (R_1)	−51.51 (R_1)	0.2912
TS5	30.00	15.50	−199.6	−200.0	0.2000
			−205.6 (R_1)	−206.0 (R_1)	0.1942

3.1. Determination of the Slant Angle for the Digital Gratings

The relationships between the slant angle α of the moiré pattern and the angle θ between the practical and digital gratings were simulated according to Equation (9). These relationships are associated with the value of M (the adapted period ratio for two period patterns), as shown in Figure 5. When $M = 1$, the relationship between α and θ is linear. In practice, the period of the digital grating typically is slightly different from that of the captured pattern. Bending curves are generated, which gradually deviate from the linear ($M = 1$) according to the deviation of the value of M from 1. When $M < 1$, the curves lie above the linear line. By contrast, when $M > 1$, the curves lie below the linear line. The values of M for TS1–TS5 were 0.9964, 0.9881, 0.9922, 0.9900, and 0.9943, respectively (Figure 5). The value of the slant angle α varies significantly with small variations in the

angle θ when $\theta < 2.5°$. By contrast, α has a gentle slope when $\theta > 10°$. In addition, a large value of α, approaching $90°$ (with a small angle θ), should be avoided to avert an extreme value of the tangent function of α in Equations (10)–(12). Therefore, the ideal angle θ was set as $30°$, as illustrated in Figure 5 and Table 1.
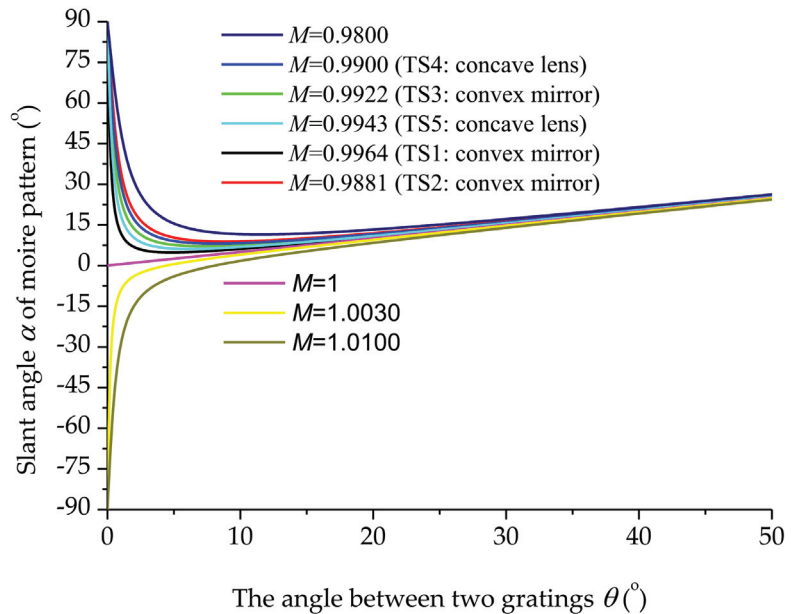

Figure 5. The relationships between the slant angle α of moiré pattern and the angle θ between practical and digital gratings.

3.2. Analysis of Measurement Uncertainty

With Equation (10), the measurement uncertainty of the focal length can be expressed as

$$\Delta f = \sqrt{\left(\frac{\partial f}{\partial p_1}\Delta p_1\right)^2 + \left(\frac{\partial f}{\partial p_2}\Delta p_2\right)^2 + \left(\frac{\partial f}{\partial d_2}\Delta d_2\right)^2 + \left(\frac{\partial f}{\partial \alpha}\Delta \alpha\right)^2 + \left(\frac{\partial f}{\partial \theta}\Delta \theta\right)^2}, \quad (13)$$

with

$$\frac{\partial f}{\partial p_1} = \frac{-p_2 d_2(\tan\alpha\sin\theta + \cos\theta)}{[p_1(\tan\alpha\sin\theta + \cos\theta) - p_2]^2}, \quad (14)$$

$$\frac{\partial f}{\partial p_2} = \frac{p_1 d_2(\tan\alpha\sin\theta + \cos\theta)}{[p_1(\tan\alpha\sin\theta + \cos\theta) - p_2]^2}, \quad (15)$$

$$\frac{\partial f}{\partial d_2} = \frac{p_1(\tan\alpha\sin\theta + \cos\theta)}{p_1(\tan\alpha\sin\theta + \cos\theta) - p_2}, \quad (16)$$

$$\frac{\partial f}{\partial \alpha} = \frac{-p_1 p_2 d_2 \sec^2\alpha\sin\theta}{[p_1(\tan\alpha\sin\theta + \cos\theta) - p_2]^2}, \quad (17)$$

$$\frac{\partial f}{\partial \theta} = \frac{-p_1 p_2 d_2(\tan\alpha\cos\theta - \sin\theta)}{[p_1(\tan\alpha\sin\theta + \cos\theta) - p_2]^2}, \quad (18)$$

where Δp_1, Δp_2, Δd_2, $\Delta \alpha$, and $\Delta \theta$ are errors of the periods of the practical and digital gratings, the distance d_2, the slant angle of the moiré pattern, and the relative angle between these gratings, respectively. The value of Δp_1 equals to 0.005 mm which corresponds to the

fabrication line width of photomask (MLA150, HEIDELBERG INSTRUMENTS). With the assistance of a laser rangefinder (GCL 25, Bosch), the distance from the grating to the vertex of test samples was measured which was used to determine the value of d_2 and therefore Δd_2 equals to 0.3 mm. For spherical mirrors, d_2 equals the measured value. For spherical lenses, d_2 equals the distance from the grating to the lens principal point. Therefore, the distance from the vertex to the principal point which can be estimated as one-third the lens center thickness must be added into the measured value. Because the period p_2, the angles α and θ were measured on digital images, the measurement values and deviations are related to the number of pixels, and the physical scale corresponding to one pixel. Shown in Figure 6 is a digital image of captured pattern with 15 megapixel (5184 pixel $\times$ 2912 pixel) in which an area with 1200 pixel $\times$ 1200 pixel and a scale bar of 50 mm with 1761 pixels are marked. Therefore, the value of Δp_2 equals to 0.028 mm. Figure 7a,b illustrate how to estimate an angle Θ and an angle deviation $\Delta\Theta$ on a digital image with $K \times J$ pixels. The angle Θ can be expressed as

$$\Theta \ = \ \tan^{-1}\left[\frac{K(\text{pixels})}{J(\text{pixels})}\right], \qquad (19)$$

and the angle deviation $\Delta\Theta$ can be written as

$$\Delta\Theta \ = \ \tan^{-1}\left[\frac{1(\text{pixel})}{\sqrt{K^2 + J^2}(\text{pixels})}\right]. \qquad (20)$$
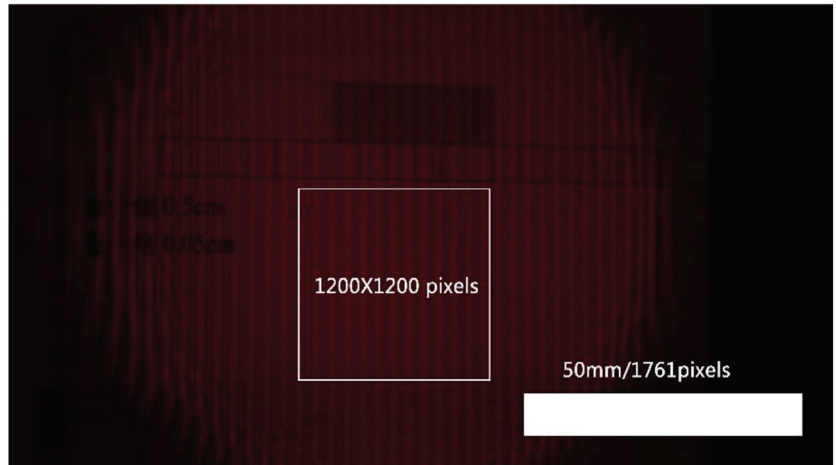
Figure 6. A digital image (5184 pixel $\times$ 2912 pixel) of captured pattern marked with scale bar and number of pixels.
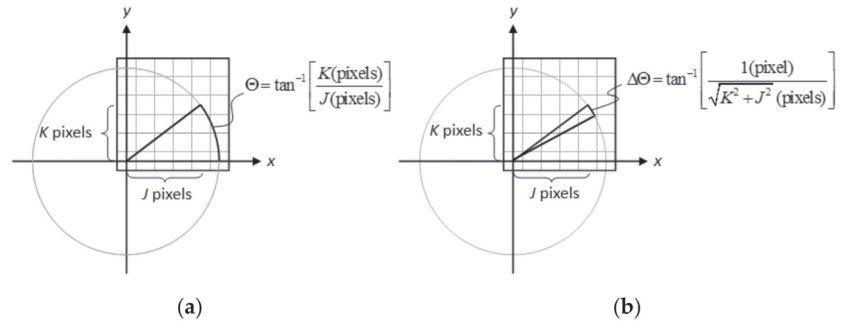
Figure 7. Schematic of the evaluation of (**a**) angle and (**b**) angle deviation on a digital image.

Therefore, with Equation (20), considering the digital image with 1200 × 1200 pixels ($K = J = 1200$) in Figure 6, the angle deviations of $\Delta\alpha$ and $\Delta\theta$ equal to 0.03°. According to Equation (13), the measurement uncertainty Δf of the focal length for TS1–5 can be evaluated with values of 0.2, 0.8, 2.0, 1.9, 18.3 mm, respectively. The values of relevant terms, parameters, and measurement uncertainty Δf are summarized in Table 2. In order to clarify the large measurement uncertainty of TS5, from Equations (14)–(18), we can find that when p_1 and p_2 have close values, the term of $[p_1(\tan\alpha\sin\theta + \cos\theta) - p_2]^2$ in the denominator will magnify introduced errors of Δp_1, Δp_2, $\Delta\alpha$, and $\Delta\theta$ (due to $\tan\alpha\sin\theta + \cos\theta \cong 1$, when $\alpha \cong 15°$ and $\theta = 30°$). By contrast, in the cases of TS1 and TS2, p_2 has a value much larger than p_1 (>>1), therefore the measurement uncertainty can reach sub-millimeter.

Table 2. Values for relevant terms and parameters for the measurement uncertainty of focal length.

Test Samples	$\left|\frac{\partial f}{\partial p_1}\right|$	$p_1\Delta p_1$ (mm)	$\left|\frac{\partial f}{\partial p_2}\right|$	$p_2\Delta p_2$ (mm)	$\left|\frac{\partial f}{\partial d_2}\right|$	$d_2\Delta d_2$ (mm)	$\left|\frac{\partial f}{\partial \alpha}\right|$	$\alpha\Delta\alpha$ (°)	$\left|\frac{\partial f}{\partial \theta}\right|$	$\Delta\theta$ (°)	Δf (mm)
TS1	0.1417	0.282 0.005	0.0236	9.480 0.028	0.0092	251.7 0.3	0.1414	15.46 0.03	0.0684	0.03	0.2
TS2	0.4987	0.282 0.005	0.2565	3.072 0.028	0.0305	251.7 0.3	0.4978	15.35 0.03	0.2428	0.03	0.8
TS3	1.1130	0.282 0.005	1.0602	1.659 0.028	0.0620	251.7 0.3	1.1111	15.79 0.03	0.5249	0.03	2.0
TS4	1.0585	0.282 0.005	0.9725	1.720 0.028	0.0594	251.7 0.3	1.0567	15.83 0.03	0.4978	0.03	1.9
TS5	6.3423	0.282 0.005	15.6363	0.641 0.028	0.2379	251.7 0.3	6.3309	15.50 0.03	3.0550	0.03	18.3

Furthermore, with Equation (9) and condition of $M \approx 1$, Equations (14)–(18) can be rewritten as

$$\frac{\partial f}{\partial p_1} = \frac{-(p_2/M)d_2}{[(p_1/M) - p_2]^2} \approx \frac{-p_2 d_2}{(p_1 - p_2)^2} = \frac{f}{p_1}\cdot S_1, \tag{21}$$

$$\frac{\partial f}{\partial p_2} = \frac{(p_1/M)d_2}{[(p_1/M) - p_2]^2} \approx \frac{p_1 d_2}{(p_1 - p_2)^2} = \frac{f}{p_1}\cdot S_2, \tag{22}$$

$$\frac{\partial f}{\partial d_2} = \frac{p_1/M}{(p_1/M) - p_2} \approx \frac{p_1}{p_1 - p_2} = S_3, \tag{23}$$

$$\frac{\partial f}{\partial \alpha} = \frac{-p_1 p_2 d_2 \sec^2 \alpha \sin\theta}{[(p_1/M) - p_2]^2} \approx \frac{-p_1 p_2 d_2 \sec^2 \alpha \sin\theta}{(p_1 - p_2)^2} = f(\sec^2 \alpha \cdot \sin\theta)\cdot S_1, \tag{24}$$

$$\frac{\partial f}{\partial \theta} = \frac{-p_1 p_2 d_2 (\tan\alpha\cos\theta - \sin\theta)}{[(p_1/M) - p_2]^2} \approx \frac{-p_1 p_2 d_2 (\tan\alpha\cos\theta - \sin\theta)}{(p_1 - p_2)^2} = -f(\tan\alpha\cos\theta - \sin\theta)\cdot S_2, \tag{25}$$

with

$$S_1 = \frac{-d_r|1-d_r|}{[1-|1-d_r|]^2},\tag{26}$$

$$S_2 = \frac{d_r}{[1-|1-d_r|]^2},\tag{27}$$

and

$$S_3 = \frac{1}{1-|1-d_r|},\tag{28}$$

where d_r is defined as relative distance which equals d_2/f. In Equations (21)–(25) (with $\sec^2 \alpha \sin \theta < 1$ and $(\tan \alpha \cos \theta - \sin \theta) < 1$) it is obvious that smaller absolute values of S_1, S_2, and S_3 ensure relatively small introduced errors which are directly related to the relative distance in Equations (26)–(28). Therefore, the relationships between S_1, S_2, and S_3 to the relative distance d_r are plotted in Figure 8a–c. The simulation results reveal that a smaller measurement uncertainty can be achieved with increasing the distance of d_2 for cases of $f > 0$ and $f < 0$. In the case of $f > 0$, a smaller measurement uncertainty can also be obtained when d_2 is near the focal length; meanwhile, the distance of $d_2 = 2f$ must be avoided. In addition, from Equations (21) and (22), properly increasing the period p_1 of the grating can also reduce the measurement uncertainty. Because a small measurement uncertainty ultimately relies on a high-precision control of experimental conditions. Considering errors of $\Delta p_1 = 0.001$ mm, $\Delta p_2 = 0.01$ mm, $\Delta d_2 = 0.01$ mm, $\Delta \alpha = \Delta \theta = 0.01°$ under accurate controls, theoretical evaluations for the measurement uncertainty of focal length under different focal lengths, relative distances, and periods of grating are summarized in Table A1, in Appendix A. Accordingly, this method could be applied to regular commercial spherical lenses and mirrors (-200 mm$< f < +200$ mm) with $\Delta f < 1.6$ mm within a measurement distance of 2 m. Considering the limited length of optical benches, there must be a trade-off between measurement resolution and measurement distance. In addition, distortion of the grid image may occur on the observation screen during measurement which is a function of the off-axis image distance. Therefore, it is necessary to capture the image of the paraxial area to avoid introducing additional errors on the moiré fringes.
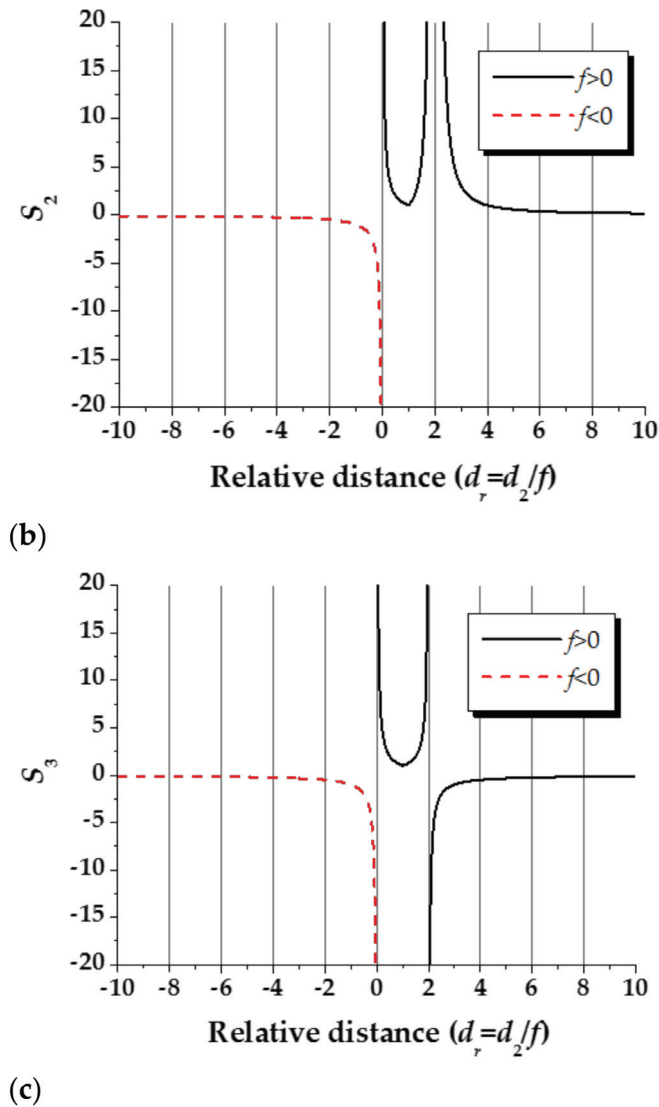

(a)

Figure 8. *Cont.*

(b)

(c)
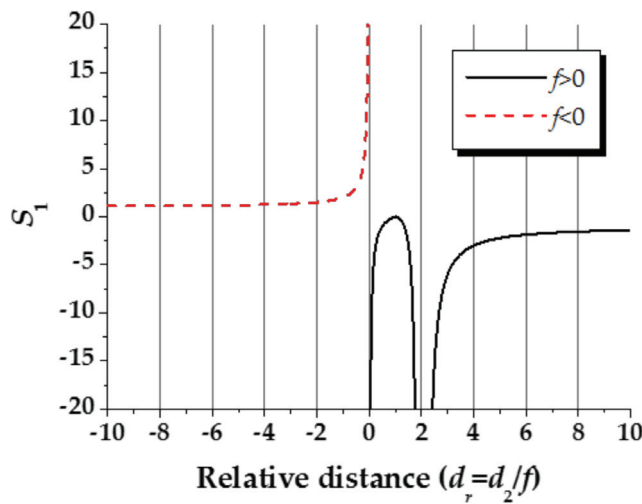
Figure 8. Relationships of (**a**) S_1 versus relative distance d_r, (**b**) S_2 versus relative distance d_r, and (**c**) S_3 versus relative distance d_r.

3.3. Simulation of Light Field Distributions

The intensity behind the grating (with a period $p_1 = 0.2822$ mm) and its intensity profile were simulated according to Equation (2), as shown in Figure 9. The intensities on the observation screen, and their intensity profiles, the corresponding digital grating with $\theta = 30°$, and their moiré pattern for TS1–5 were simulated ($p_1 = 0.2822$ mm, $d_1 = d_2 = 251.7$ mm, and $\theta = 30°$) according to Equation (8), as shown in Figure 10. The simulation results corresponded suitably with the experimental results shown in Figure 4, thus confirming the correctness of the derived equations.
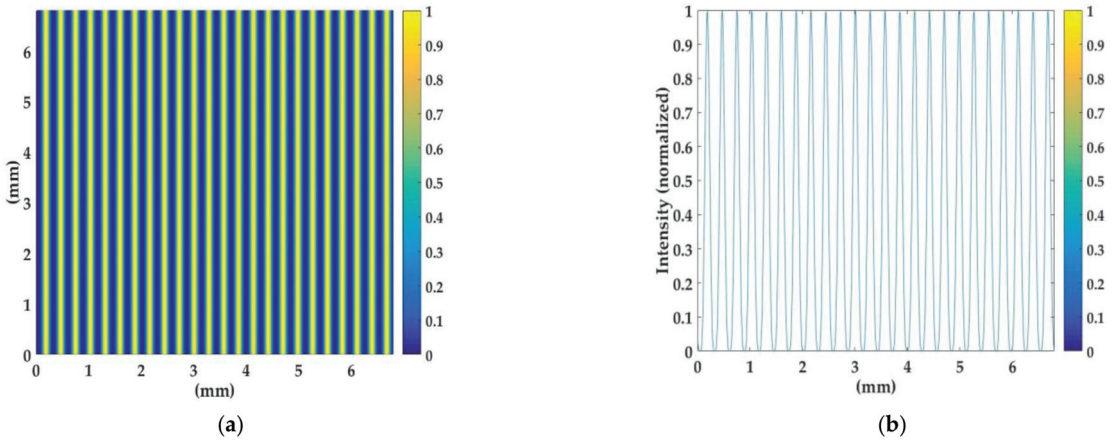
Figure 9. Simulated (**a**) intensities behind the grating (with a period of p_1 = 0.2822 mm) and (**b**) the intensity profile.
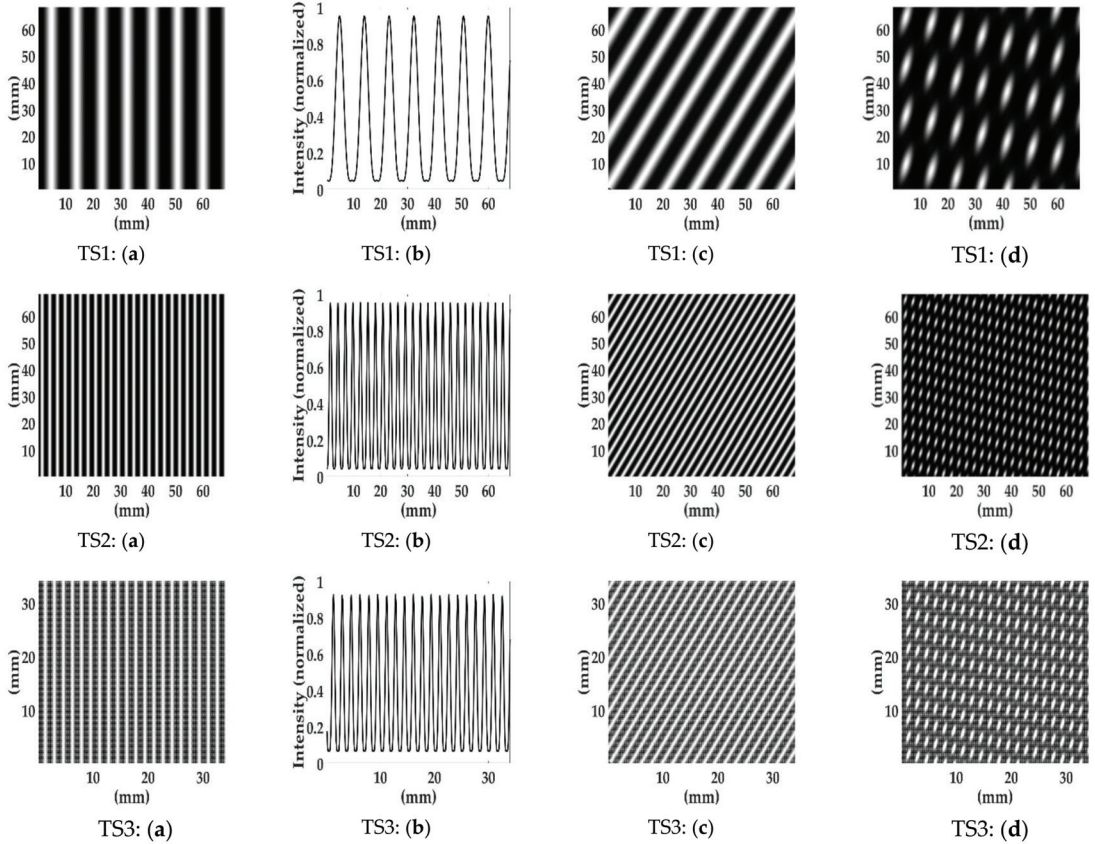
Figure 10. *Cont.*
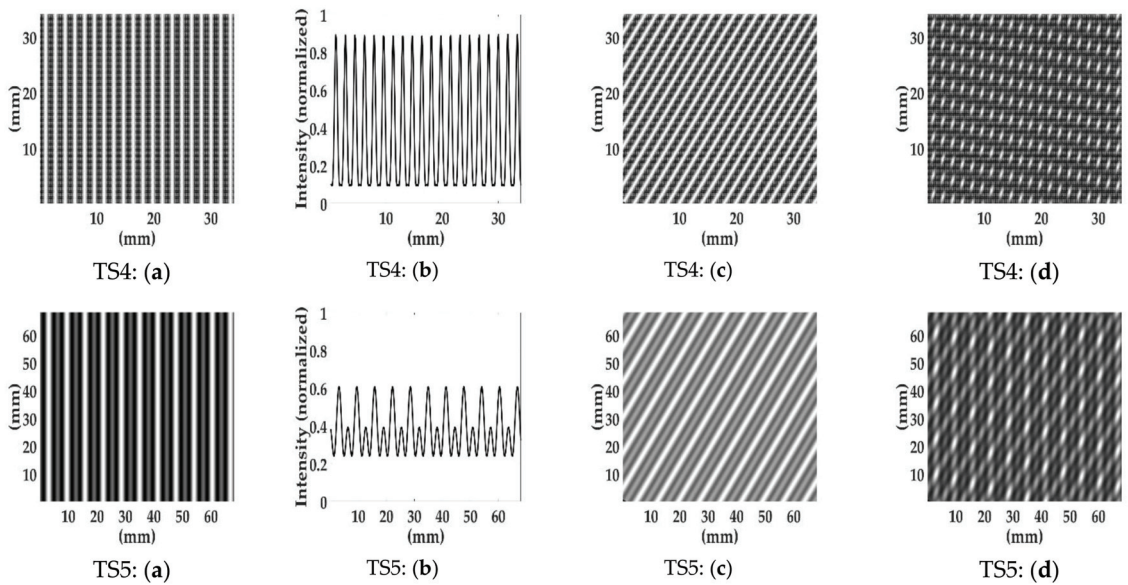
Figure 10. Simulated (**a**) intensities on the observation screen and (**b**) intensity profiles, (**c**) corresponding digital gratings, and (**d**) the moiré patterns for samples: TS1–TS5.

Compared to Equation (2), Equation (8) contains a cosine modulation term, which varies the intensity distribution on the observation screen. Therefore, the principal maximum of the intensity profile decreased and a subsidiary maximum occurred (Figure 10). The energy splitting reduced the intensity contrast. The period of the principal maximum of the intensity profile on the observation screen was $p_1 (1 - d_2/f)$. When the Gaussian law was followed, (i.e., $1/f = 1/d_1 + 1/d_2$), Equation (8) degenerated to Equation (2) with an imaging magnification of $m = | 1 - d_2/f |$. Because of advancements in the technology used in personal computers, the field intensity distribution of light propagation can be visualized. Considering a special case of $d_1 = z_T + 2f$ and $d_2 = 2f$, where $z_T = 2p_1^2/\lambda$ is the Talbot distance, Equation (8) degenerates to Equation (2) with an imaging magnification of $m = 1$, and the simulation of the intensity carpet (d_2 versus x_2) is shown in Figure 11a (with $\lambda = 0.6328$ μm, $p_1 = 0.2822$ mm, $f = 100$ mm). As shown in Figure 11b, at a distance $d_2 = 2f = 200$ mm, the intensity profile is exactly equal to that in Figure 9b, which is the self-image of grating G at $z_T = 251.7$ mm with $m = 1$. In the case of TS5, a sub-moiré pattern was observed (Figure 10 TS5: (d)) because of the subsidiary maximum of the intensity profile. The sub-moiré pattern was parallel to the principal moiré pattern, which did not affect the determination of the slant angle α of the moiré pattern. Because of the introduction of digital-grating, measurements taken using this method require only one practical grating and a single photograph with digital image post-processing. The proposed method could be applied to regular commercial spherical mirrors and lenses (bi-convex or bi-concave).
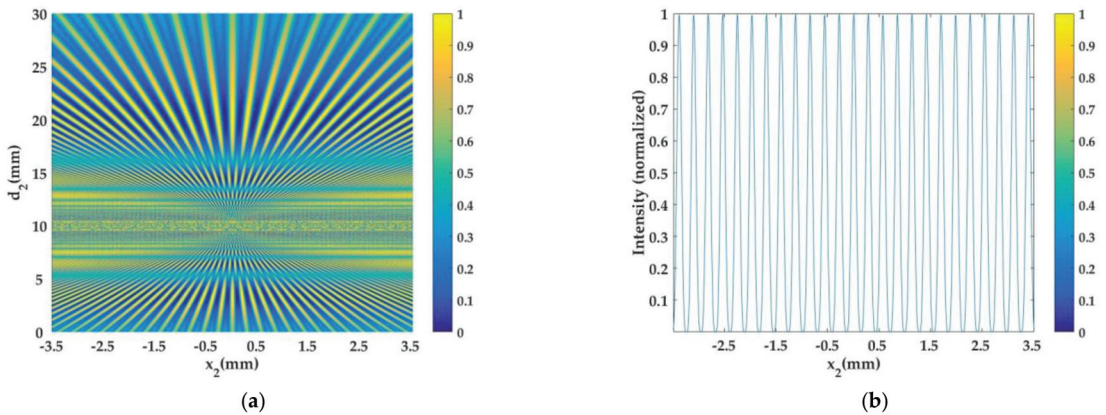
Figure 11. Simulated (**a**) intensity carpet (with $\lambda = 0.6328$ μm, $p_1 = 0.2822$ mm, $f = 100$ mm) and (**b**) the intensity profiles at $d_2 = 200$ mm.

4. Conclusions

By applying digital image post-processing, digital-grating moiré effect was successfully used to measure the focal length and curvature with percent errors lower than 0.5%. The measurement uncertainty and conditions were analyzed and discussed. The field intensity distribution was derived and visualized using simulations, leading to simplified measurements. The proposed method has the advantages of a simple set up, easy operation, high stability, high accuracy, and low cost, and it can be applied to various spherical simple lenses and mirrors.

Appendix A

Table A1. Theoretical evaluation values (orthogonal arrays) for the measurement uncertainty of focal length (unit: mm) under different focal lengths, relative distances, and periods of grating (with $\Delta p_1 = 0.001$ mm, $\Delta p_2 = 0.01$ mm, $\Delta d_2 = 0.01$ mm, $\Delta \alpha = \Delta \theta = 0.01°$).

	$d_r = d_2/f$											
	2.5		5		10		20		30		40	
f	p_1 0.282	p_1 1.00	p_1 0.282	p_1 1.00	p_1 0.282	p_1 1.00	p_1 0.282	p_1 1.00	p_1 0.282	p_1 1.00	p_1 0.282	p_1 1.00
10	3.7	1.3	0.2	0.1	0.1	0.1	0.1	0.1	0.1	0.1	0.1	0.1
−10	0.2	0.1	0.1	0.1	0.1	0.1	0.1	0.1	0.1	0.1	0.1	0.1
25	9.2	3.2	0.6	0.3	0.3	0.2	0.2	0.2	0.2	0.2	0.2	0.1
−25	0.4	0.2	0.3	0.2	0.2	0.2	0.2	0.1	0.2	0.1	0.2	0.1
50	18.4	6.5	1.2	0.7	0.5	0.4	0.4	0.3	0.4	0.3	0.4	0.3
−50	0.8	0.4	0.5	0.3	0.4	0.3	0.3	0.3	0.3	0.3	0.3	0.3
100	36.7	12.9	2.4	1.3	1.1	0.8	0.8	0.6	0.7	0.6	0.7	0.6
−100	1.7	0.9	1.0	0.7	0.8	0.6	0.7	0.6	0.7	0.6	0.7	0.6
150	55.1	19.4	3.6	2.0	1.6	1.2	1.2	1.0	1.1	0.9	1.1	0.9
−150	2.5	1.3	1.6	1.0	1.2	0.9	1.0	0.9	1.0	0.8	1.0	0.8
200	73.5	25.8	4.9	2.7	2.1	1.6	1.6	1.3	1.5	1.2	1.4	1.2
−200	3.4	1.7	2.1	1.4	1.6	1.2	1.4	1.1	1.3	1.1	1.3	1.1

References

1. Kingslake, R. *Applied Optics and Optical Engineering*; Academic Press: New York, NY, USA; Volume I, pp. 208–226.
2. Luo, J.; Bai, J.; Zhang, J.; Hou, C.; Wang, K.; Hou, X. Long focal-length measurement using divergent beam and two gratings of different periods. *Opt. Express* **2014**, *22*, 27921–27931. [CrossRef] [PubMed]
3. Jin, X.; Zhang, J.; Bai, J.; Hou, C.; Hou, X. Calibration method for high-accuracy measurement of long focal length with Talbot interferometry. *Appl. Opt.* **2012**, *51*, 2407–2413. [CrossRef] [PubMed]
4. Chen, J.-H.; Chen, K.-H.; Han, C.-Y.; Wu, C.-W.; Wu, N.-Y. Evaluation of the curvature of an object by Talbot interferometry. *Opt. Rev.* **2009**, *16*, 489–491. [CrossRef]
5. KSriram, K.V.; Kothiyal, M.P.; Sirohi, R.S. Talbot interferometry in noncollimated illumination for curvature and focal length measurements. *Appl. Opt.* **1992**, *31*, 75–79. [CrossRef] [PubMed]
6. Bernardo, L.M.; Soares, O.D.D. Evaluation of the focal distance of a lens by Talbot interferometry. *Appl. Opt.* **1988**, *27*, 296–301. [CrossRef]
7. Arriaga-Hernández, J.A.; Jaramillo-Núñez, A. Ronchi and Moiré patterns for testing spherical and aspherical surfaces using deflectometry. *Appl. Opt.* **2018**, *57*, 9963–9971. [CrossRef]
8. Hong, T.; Li, D.; Wang, R.; Zhang, X.; Liu, X. Method for measuring the radius of mean curvature of a spherical surface based on phase measuring deflectometry. *Appl. Opt.* **2021**, *60*, 1705–1709. [CrossRef] [PubMed]
9. Singh, P.; Faridi, M.S.; Shakher, C.; Sirohi, R.S. Measurement of focal length with phase-shifting Talbot interferometry. *Appl. Opt.* **2005**, *44*, 1572–1576. [CrossRef] [PubMed]
10. De Nicola, S.; Ferraro, P.; Finizio, A.; Pierattini, G. Reflective grating interferometer for measuring the focal length of a lens by digital moiré effect. *Opt. Commun.* **1996**, *132*, 432–436. [CrossRef]
11. De Angelis, M.; De Nicola, S.; Ferraro, P.; Finizio, A.; Pierattini, G. Analysis of moiré fringes for measuring the focal length of lenses. *Opt. Lasers Eng.* **1998**, *30*, 279–286. [CrossRef]
12. Lee, S. Talbot Interferometry for Measuring the Focal Length of a Lens without Moiré Fringes. *J. Opt. Soc. Korea* **2015**, *19*, 165–168. [CrossRef]
13. Goodman, J.W. *Introduction to Fourier Optics*, 3rd ed.; W. H. Freeman: Englewood, CO, USA, 2004.
14. Gåsvik, K.J. *Optical Metrology*; Wiley: Hoboken, NJ, USA, 1987.

An Improved Large-Field Microscopic Speckle Interferometry System for Dynamic Displacement Measurement of MEMS

Chenjia Gao, Zhan Gao *, Yuhao Niu, Xu Wang, Jieming Zhao and Lin Deng

Key Laboratory of Luminescence and Optical Information of Ministry of Education, Beijing Jiaotong University, Beijing 100044, China; 16118443@bjtu.edu.cn (C.G.); 19118036@bjtu.edu.cn (Y.N.); 17118455@bjtu.edu.cn (X.W.); 19118048@bjtu.edu.cn (J.Z.); 20118039@bjtu.edu.cn (L.D.)

* Correspondence: zhangao@bjtu.edu.cn; Tel.: +86-10-5168-8333

Abstract: The traditional microscopic speckle interferometer has limited applications in engineering due to its small field of view. In this paper, we propose a large-field microscopic speckle interferometer which embeds two doublet lens groups in the improved Mach–Zehnder optical path structure to expand its field of view. At the same time, the new system can reduce the coherent noise of reflected light in the optical path. We use this new system to measure the dynamic displacement process of the entire surface of the microchips. The experimental results show that our improved measurement system can achieve large-field, real-time and high-precision dynamic measurement of micro-electromechanical systems (MEMS).

Keywords: large-field; speckle interferometer; MEMS; displacement measurement

1. Introduction

Microscopic interferometry is a combination of an electronic speckle pattern interferometry (ESPI) system and a microscopic optical path. It has the advantages of non-contact, full-field and high precision, and is widely used in dynamic and static measurement of micro devices [1–5]. ESPI has been developed for many years and is very popular in the field of non-contact measurement. By analyzing the interferograms, we can obtain the phase information of the measured object, and then the static morphology or dynamic deformation can be measured. Researchers have designed a variety of optical measurement configurations and phase processing algorithms for different measurement targets. In 1971, Butters, J.N. and Lecndcrtz, J.A. used a camera instead of a holographic dry plate to record the interference phenomenon of speckles. This series of speckle images can be electronically processed to compare the speckle images before and after deformation [6]. Jones, R. comprehensively analyzed the conditions for obtaining the best performance of the ESPI, such as camera characteristic, laser power, interferometer type and operation mode, which provide a general theoretical basis for the system design and optimization of various interferometers [7]. In reference [8], a detailed analysis of the vibration fringes obtained by phase stepping on a time-averaged electronic speckle pattern interferometer was presented. Moore, A.J. presented two phase-stepping algorithms that can calculate phase from ESPI fringes: the subtraction method and the addition method. Corresponding interference experiments were carried out, combining a piezoelectric transducer (PZT) and pulse laser, and the function of the algorithms was demonstrated through the collected interferograms [9]. One-shot phase-shifting optical and speckle interferometry with modulation of polarization was described in reference [10]. The system has the ability to record multiple phase-shifting optical or speckle patterns at the same time, so it can afford to measure rapid changes generated from rapid varying phenomena. However, this method reduced the spatial resolution while increasing the time resolution. Reference [11] reported a simple, compact ESPI incorporating a holographic optical system for the study of out-of-plane vibration. The subtraction method was used to generate the fringe pattern. The

179

background speckle noise was eliminated by introducing a phase shift between consecutive images, and finally the amplitude and phase image were obtained through path difference modulation. D. Malacara summarized and described common phase-detection algorithms in interferometry, such as the least square method, quadrature phase method and discrete low-pass filtering, etc. [12]. These theories are very helpful for us to obtain the phase under a variety of different measurement conditions.

With the rapid development and wider application of MEMS, there are more and more studies on the measurement of micro devices. The measurement of micro devices can be achieved by introducing the microscopic optical path into the interferometry system. Reference [13] described an optoelectronic holography microscope (OEHM) for measuring static and dynamic modes of MEMS accelerometers with submicron accuracy. After obtaining the intensity patterns obtained by the phase-stepping algorithm, the phase value was obtained by the phase-shifting algorithm. Preliminary results indicate that the MEMS accelerometer considered in this study deforms by 1.48 μm. Kumar, U.P. presented a two-wavelength micro-interferometric setup for 3-D surface profile characterization of smooth and rough micro-specimens. The method removed ambiguity associated with the single-wavelength data and also extended the phase measurement range compared to the conventional single-wavelength interferometry. A seven-phase step algorithm was used for quantitative fringe analysis. The experimental results on rough silicon membrane and smooth sample were presented [14]. Reference [15] proposed a multiple-wavelength microscopic holographic configuration. This system used sequentially recorded phase-shifted frames at three different wavelengths to evaluate the relatively large deformation fields at the effective wavelengths. The phase distribution before and after loading the object was obtained by using the eight-phase step algorithm. The design of the system along with the experimental results on small-scale rough specimens under static load was presented.

In addition to the above several configurations, according to the optical path structure and the position of the microscope, the commonly used microscopic interferometry systems can be divided into three types: Michelson type [16–19], Mirau type [20–24] and Linnik type [25–33]. For example, Wiersma, J.T. used the Michelson microscopic system and synchronous phase sensor to realize high precision and repeatable measurement of common vibration [19]; Schmit, J. proposed an improved Mirau interferometer, which can generate orthogonally polarized output beams, and can obtain better fringe contrast by introducing achromatic phase shift [21]; Somekh, M.G. realized a plasmon microscope with sub-micron resolution by using the Linnik interferometer with speckle illumination [26]; Li, X.D. of Tsinghua University measured the thermal deformation of copper microbridges with different sizes (the maximum size is 2175 μm × 1009 μm) in real time using the Linnik microscopic interferometry system, and the accuracy reached submicron level [33].

Compared with ESPI, the microscopic interferometry system can achieve high-resolution measurement of micro devices. However, at the same time, the microscopic system is limited by the field of view of microscope, and the measurement range is very small. Considering that the size of MEMS is in the micron level to the millimeter level, especially after packaging, the size of many MEMS is in the millimeter level. For micro devices in this size range, the microscopic interferometry system is no longer sufficient to achieve full-field measurement. In this paper, a large-field microscopic speckle interferometry system based on an improved Mach–Zehnder structure is proposed. Our measurement system has two main advantages: 1. under the conditions of using the same microscope objective, compared with the traditional Linnik structure, the new system expands the field of view from a circular area with a diameter of 2.4 mm to a rectangular area of 6 mm × 8 mm; 2. it can reduce the reflected light beam in the optical path, thereby reducing the reflected coherent noise.

The phase extraction algorithm used in our work is the wavelet transform (WT) method, which is described in detail in our previous article [34]. Compared with the phase shifting method that appears many times in the above references, the WT does not need to

introduce multiple steps by PZT, which saves a lot of time. Additionally, WT can directly convert the phase change signal from the spatial domain to the frequency domain to realize real-time measurement of the displacement or deformation of the measured object. We used the new system and WT to perform real-time and large-field measurement on a large area of MEMS. Detailed principles and experiments will be introduced below.

2. Principle

2.1. Traditional Linnik Microscopic Interferometry System

The Linnik microscopic interferometry system is a very common interferometry structure used to measure micro devices. We choose the Linnik microscopic interferometry system as a comparison for later analysis of the effectiveness of expanding the field of view of the new system. This system mainly includes the laser, Linnik microscopic interference structure and CCD. The Linnik microscopic interference structure is composed of a beam splitter and two identical microscope objectives. The laser beam is divided into two arms by the beam splitter. One beam enters the measurement arm and focuses on the measured object through the microscope objective, and the other beam enters the reference arm and focuses on the reference object. The speckle interferograms formed by the two beams is captured by the CCD. We can obtain the displacement or deformation information by processing and analyzing these interferograms. The diagram of the Linnik microscopic interferometry system is shown in Figure 1.
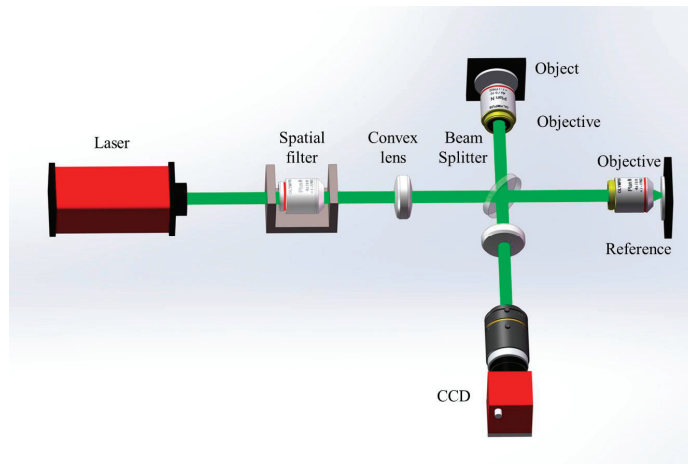

Figure 1. The diagram of Linnik microscopic interferometry system.

The intensity distribution of speckle interferograms can be expressed as:

$$I(x, y, t_0) = I_1 + I_2 + 2\sqrt{I_1 I_2} \cos[\varphi_0 - \varphi_r] \tag{1}$$

where I_1 and I_2 are the light intensities of the object beam and the reference beam, respectively, and $\varphi_0 - \varphi_r$ represents the initial phase difference between them. In the measurement process, when the measured object undergoes continuous out-of-plane displacement, the optical path difference between the object arm and the reference arm changes correspondingly, and the light intensity distribution of the speckle interferogram becomes:

$$I'(x, y, t) = I_1 + I_2 + 2\sqrt{I_1 I_2} \cos[\varphi_0 - \varphi_r + \Delta\varphi] \tag{2}$$

where $\Delta\varphi$ indicates the phase change caused by the displacement of the measured object.

The speckle fringe pattern can be obtained by subtraction mode, and the output intensity can be expressed as:

$$I(x, y, t) = |I'(x, y, t) - I(x, y, t_0)|$$
$$= 4\sqrt{I_1 I_2} \sin[(\varphi_0 - \varphi_r) + \Delta\varphi(t)/2] \cdot \sin[\Delta\varphi(t)/2] \quad (3)$$

where $\sin[(\varphi_0 - \varphi_r) + \Delta\varphi(t)/2]$ is a high frequency term, which is far beyond the acquisition frequency of CCD; $\sin[\Delta\varphi(t)/2]$ indicates the fringes related to the change in the measured object.

In our previous research, we introduced the WT to solve the wrapped phase. The continuous WT is defined as:

$$W_I(a, b) = \langle I(t), \psi_{a,b}(t) \rangle = |a|^{-\frac{1}{2}} \int_{-\infty}^{+\infty} I(t)\psi * \left(\frac{t-b}{a}\right) dt \quad (4)$$

where a is the scale parameter, b is the shift parameter, $I(t)$ is the signal to be analyzed, $\psi(t)$ is the mother wavelet, and $\psi * \left(\frac{t-b}{a}\right)$ is the conjugate function. The amplitude and the phase are given by:

$$A(a, b) = \sqrt{\{Im[W_I(a, b)]\}^2 + \{Re[W_I(a, b)]\}^2} \quad (5)$$

$$\varphi(a, b) = \arctan\{Im[W_I(a, b)]/Re[W_I(a, b)]\} \quad (6)$$

where $Re[W_I(a, b)]$ is the real part of the wavelet coefficient, and $Im[W_I(a, b)]$ is the imaginary part. Then, the final phase can be obtained by the phase unwrapping algorithm, and for:

$$\Delta z(t) = (\Delta\varphi \times \lambda)/4\pi \quad (7)$$

we can find that $\Delta z(t)$, that is, the real-time displacement information of the measured object.

2.2. Large-Field Microscopic Speckle Interferometry System

In this paper, we introduce a new type of large-field microscopic speckle interferometry system. The optical path diagram of the system is shown in Figure 2. In the process of measurement, the laser beam is expanded by the spatial filter and converted into parallel light by the first doublet lens L_1. Then, it is split into the measurement beam and reference beam by beam splitter (BS) BS_1. The measurement beam illuminates the measured object through BS_2, and then reflects back to BS_2, and converges into the field of view of microscope objective through doublet lens L_2 and BS_4. In the experiment, considering that the light is scattered on the rough surface of the measured object, the reflected light intensity gradually weakens as the distance increases, so the distance between BS_2 and L_2 needs to be as small as possible to ensure sufficient light intensity converges into L_2. Therefore, the lens is placed in front of the BS_3. Similarly, the reference beam illuminates the reference object through the BS_3, and finally converges into the field of view of the microscope objective through doublet lens L_3 and BS_4. Two beams converge and interfere in front of the microscope objective, and the time-series interferograms amplified by the microscope objective are collected by CCD.

Our system effectively solves the two problems of small field of view and large reflected light coherent noise mentioned above.
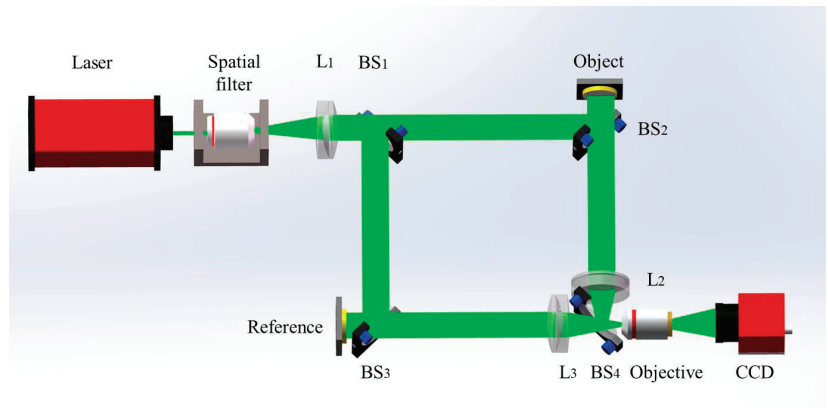
Figure 2. The schematic diagram of large-field microscopic speckle interferometry system. L_1, L_2, and L_3 represent lenses, BS_1, BS_2, BS_3 and BS_4 represent beam splitters.

The first step is to reduce the coherent noise of reflected light. The system is improved on the basis of the Mach–Zehnder structure and greatly reduces the influence of reflected light compared to the Linnik system (Michelson structure), for the Mach–Zehnder structure does not have the light returning to the light source, and the light beam only passes through the microscope objective once, which reduces the back-and-forth reflection phenomenon inside the microscope objective and further reduces the reflection coherent noise. Generally, the reduction in the multiple reflected light in the optical path can improve the image quality. However, it is difficult to carry out a comparative experiment to study how much the coherent noise of reflected light is reduced quantitatively.

Then, we need to expand the field of view while ensuring high imaging quality. The system introduces two doublet lens groups: L_1 and L_2 are one group, and L_1 and L_3 are the second group. Take the L_1 and L_2 group as an example. The two doublet lenses are the same. The light beam is converted into parallel light by the lens L_1 to illuminate the surface of the measured object, and the reflected light is transmitted to the lens L_2 in the manner of parallel light to be converged, then all the information enters the microscope objective. Similarly, the light beam modulated by another doublet lens group illuminates the surface of the reference object. Through the collimation and convergence process of the doublet lens group, more information will enter the microscope objective, and then the expansion of the field of view is realized.

In order to verify that the field of view is effectively expanded while ensuring the high imaging quality, we conducted three sets of comparative experiments. Three imaging modes are used to image the resolution board, respectively:

a. First, the CCD is directly used for imaging. By adjusting the CCD lens, it can image the pattern numbered 60 on the resolution board, as shown in Figure 3. The field of view is a circle with a diameter of 13 mm. It can be seen that a lot of detailed information is lost in the collected image and the stripes cannot be distinguished. It is obvious that only using ordinary CCD can not distinguish the clear imaging of a small object, as shown in Figure 3d;

b. Then, a microscope objective is added to simulate the field of view of Linnik structure. The pattern numbered 60 of the resolution board is imaged by CCD. As shown in Figure 4, the imaging region corresponds to the yellow contour region of Figure 3 We can find that by adding a microscope objective, 60 obvious stripes and clear details can be observed. At this time, the field of view is modulated by the imaging field of the microscope objective, which is approximately a circle with a diameter of 2.4 mm;

c. Finally, the doublet lens group is introduced, and the field of view is shown in Figure 5. At this time, the field of view is modulated by the microscope objective,

doublet lens group and the spatial resolution of the CCD together. It is a rectangular with an area of 6 mm × 8 mm, and its imaging area corresponds to the blue contour region in Figure 3. When we enlarge the selected area in the upper left corner, 60 stripes can also be clearly observed. Therefore, by introducing doublet lens groups, we not only expand the field of view, but also ensure the detailed information of the object.
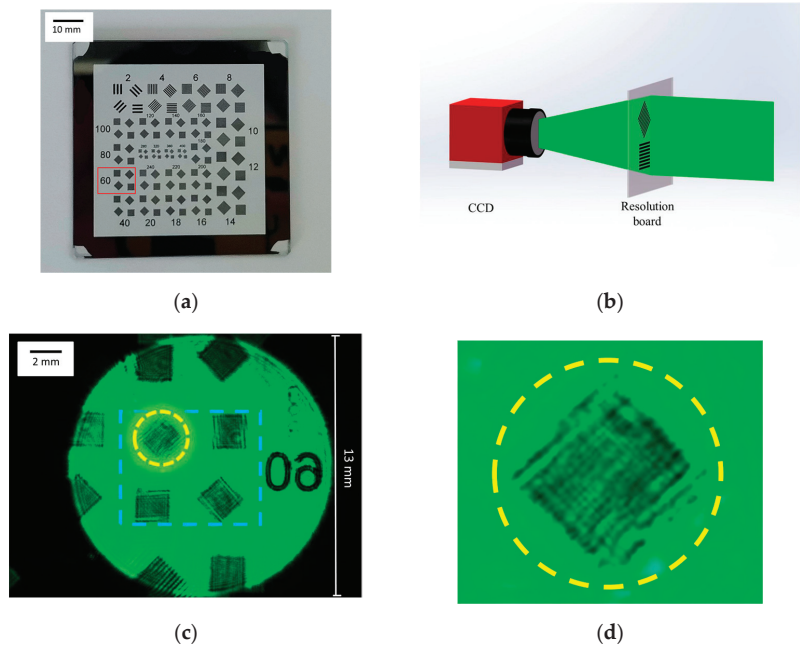

Figure 3. (**a**) Resolution board and the pattern corresponding to number 60; (**b**) schematic diagram of imaging by CCD; (**c**) the captured image; (**d**) the enlarged image of the yellow contour region.
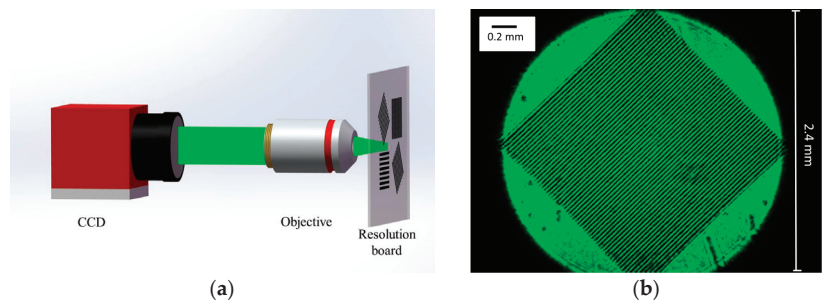
Figure 4. (**a**) Schematic diagram of imaging by CCD and objective; (**b**) the captured image corresponds to the yellow contour region in Figure 3c.

By imaging the resolution board, it is proved that the field of view is effectively enlarged by adding the doublet lens group while ensuring high imaging quality, without distortion or field curvature.
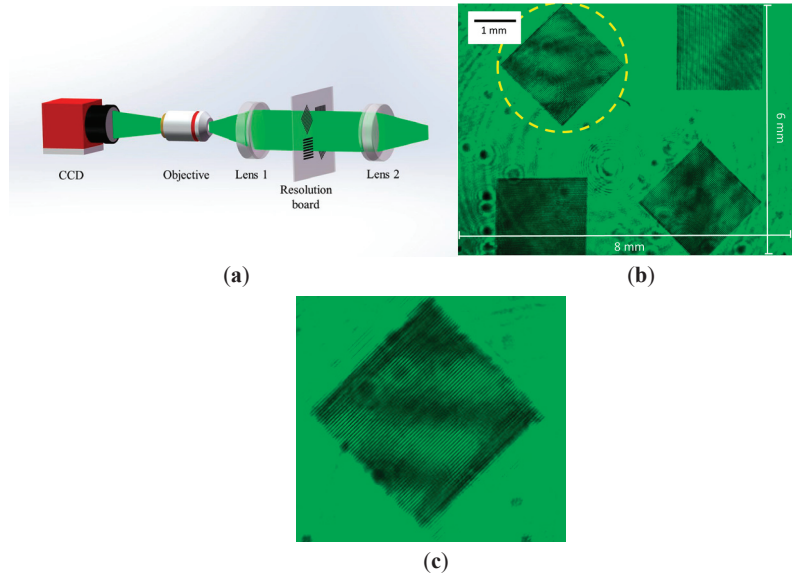
Figure 5. (**a**) Schematic diagram of imaging by CCD, objective and the doublet lens group; (**b**) the captured image corresponds to the blue contour region in Figure 3c; (**c**) the enlarged image of the yellow contour region.

3. Experiment

We built the measurement system according to the light path diagram, as shown in Figure 6. The light source is a single longitudinal mode laser with a wavelength of 532 nm and an output power of 100 mW. The spatial resolution of CCD is 640 × 480. The pixel size of the CCD is 4.8 μm × 4.8 μm. The exposure time in the experiment is 200 microseconds and the acquisition frame rate is 70 frames/s. The numerical aperture of the microscope objective is 0.1 and the magnification is 4×. The focal length of the doublet lens is 50 mm.
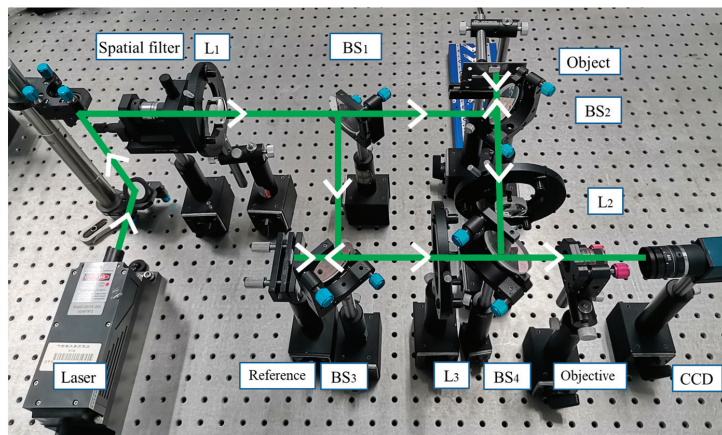
Figure 6. The measurement system diagram with the introduction of doublet lens group.

The traditional Mach–Zehnder uses two mirrors, and the utilization rate of light is really high. Considering that the measured object is not transparent, we use two beam

splitters to replace the two mirrors in our optical path, resulting in only half of the light entering the transmission optical path. However, this phenomenon has little effect, for the current laser power is very high. As in our experiment, the CCD exposure time is only 200 microseconds, and a clear and bright interferogram can be observed.

The measured object and reference object in the experiment are microchips with the size of 5 mm × 6 mm × 1 mm (W × L × H), as shown in Figure 7. We need to measure the displacement of the whole microchip. Because the microchip is similar to a rigid body, it is difficult to generate deformation by heating or loading force. The method we adopt here is to place the measured object on the hinge, the hinge axis is fixed, and the blade is pushed by the Physik Instrumente (PI) displacement platform to simulate the displacement of the measured object. The accuracy of the PI displacement platform is 10 nm. The specific process is shown in Figure 8.
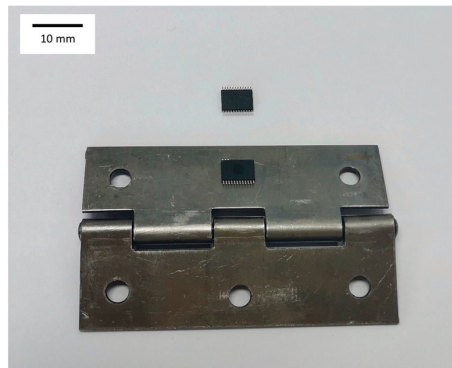
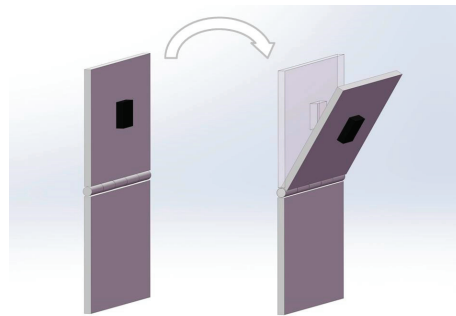**Figure 7.** Two identical microchips.

Figure 8. The process of introducing the displacement by hinge.

The entire displacement process is 4 s, and 280 speckle interferograms can be collected. One of the speckle interferogram collected by CCD during the displacement process is shown in Figure 9, and the interference fringe patterns obtained by the subtraction mode are shown in Figure 10.
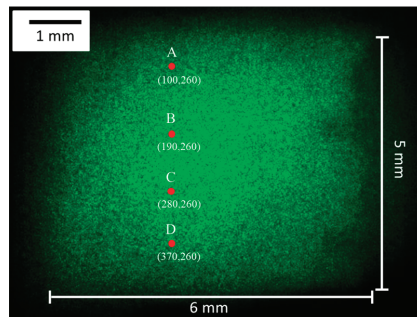
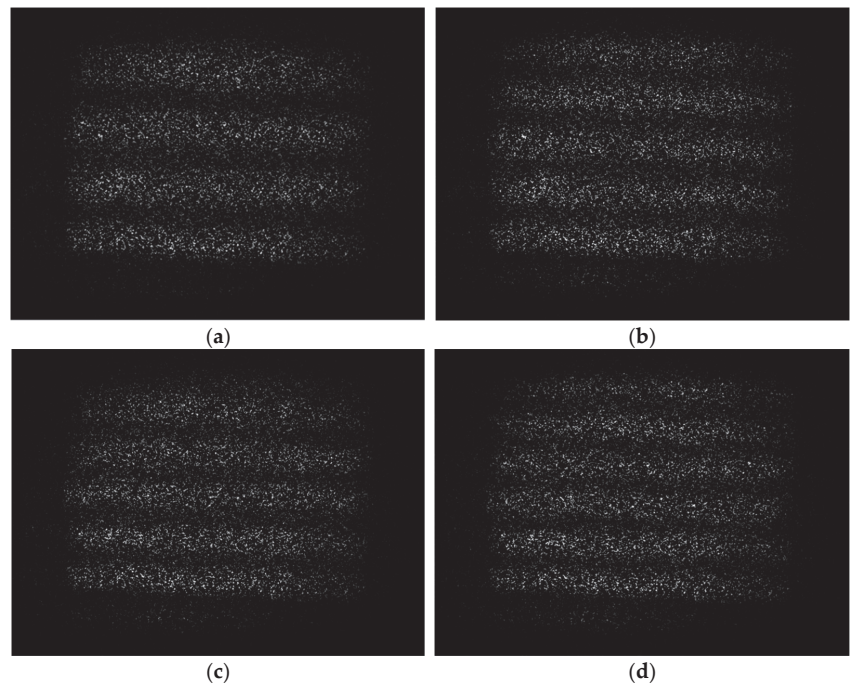**Figure 9.** The speckle interferogram collected by CCD.

Figure 10. The interference fringe pattern obtained by the subtraction mode. (**a**–**d**) represent the 70th, 140th, 210th, and 280th speckle interferogram subtracting the first one, respectively.

Using the WT phase extraction algorithm mentioned above, the time series phase value of each pixel can be calculated. Then, the continuous phase value is obtained by unwrapping, and the corresponding displacement value is finally obtained.

Taking pixels A (100, 260), B (190, 260), C (280, 260), D (370, 260) as examples, we show the phase and displacement maps of these four pixels over time, as shown in Figure 11. The acquisition frame rate of CCD is 70 frames/s. We can obtain the displacements of these four points at 1, 2, 3, and 4 s from the displacement diagrams. The corresponding dynamic displacement map of the microchip is shown in Figure 12.
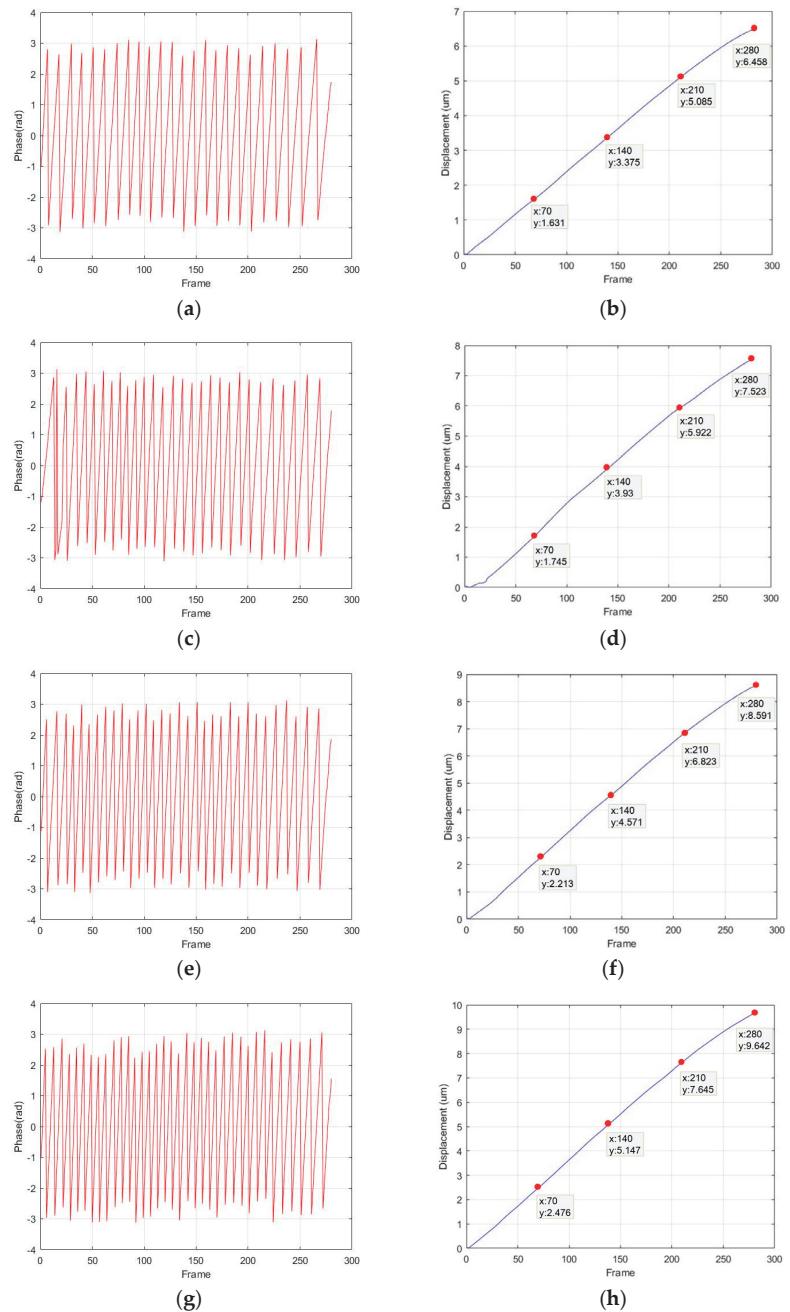
Figure 11. Truncated phase diagrams and displacement diagrams of the 4 pixels. (**a**,**b**) correspond to pixel A; (**c**,**d**) correspond to pixel B; (**e**,**f**) correspond to pixel C; and (**g**,**h**) correspond to pixel D.
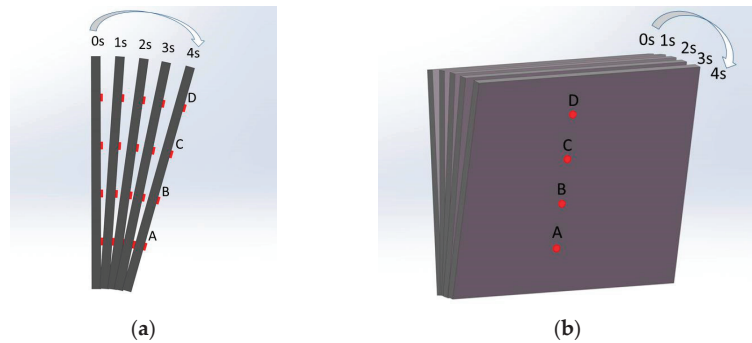
Figure 12. The dynamic displacement map of the microchip over time: (**a**) left view; (**b**) front view.

It should be noted here that when imaging with a doublet lens group, the object and the image are in opposite directions. Therefore, the smaller the x coordinate of the pixel, the closer to the fixed axis of the hinge it is, and the displacement value of the four pixels gradually becomes smaller. The final displacement range calculated from the experimental results is 5.75–10.47 μm, which, respectively, corresponds to the displacement value of the low end and the top end of the microchip.

In order to verify the accuracy of the results, we first use the displacement value introduced by the PI displacement platform to judge whether the displacement range of the measured object is reasonable. The width of the hinge is 16 mm, the width of the measured object is 5 mm, and the distance between the measured object and the low end and top end of the hinge is 6 and 5 mm, respectively; the displacement value introduced by the PI displacement platform at the top of the hinge is 15 μm, which can be used to judge that our measurement range is generally reasonable.

Then, the linear relationship of four points is used in further judgment. Because the four points are selected with an equal pixel interval, and the measured object is approximate to the rigid body and will not deform easily, so the four points should have a linear correlation. The final displacement values of the four points are connected and the correlation coefficient R^2 is calculated to be 0.9994, as shown in Figure 13, which indicates that the linearity is very good. That is, our experimental results have high accuracy.
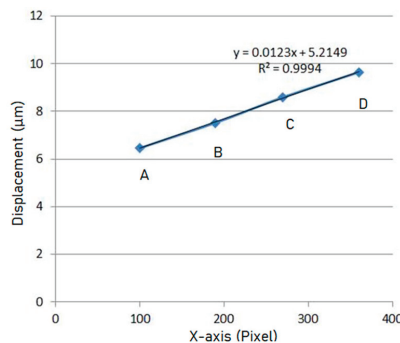

Figure 13. The linear relationship of the displacement of 4 pixels.

In order to verify the full-field performance of the system and the measurement accuracy of different positions, 16 arbitrary pixels were selected to display their displacement values, as shown in Figure 14. Among them, 12 points are in the same row with points A, B, C, D, respectively. According to the displacement direction, the displacement values of these pixels in the same row should be the same. The measuring result is shown in

Figure 14, and the maximum relative error of the 12 points is 0.46%. After traversing all the pixels that record the interference information, the full-field displacement map of the object can be obtained. After calculating the displacement values of all pixels and removing individual dead pixels through smoothing operations, the overall displacement map can be obtained, as shown in Figure 15. In our research, we use MATLAB to calculate the displacement information of each pixel and finally realize the full-field measurement. The entire processing process takes less than 15 s.
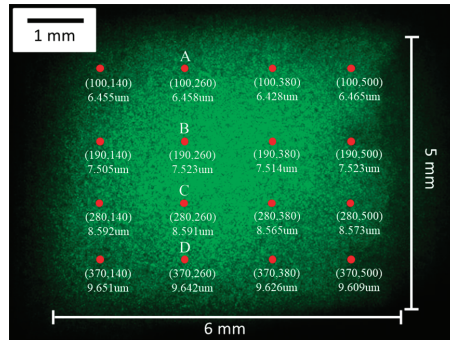

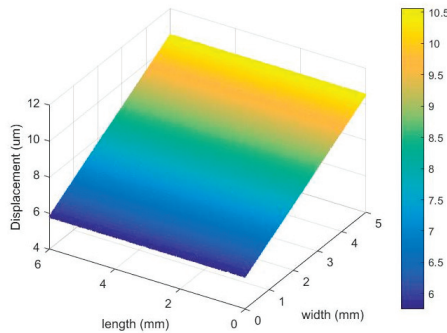**Figure 14.** The final displacement map of the selected 16 pixels.

Figure 15. The overall displacement diagram of the measured object.

4. Discussion

When introducing displacement through the hinge, it is necessary to consider whether the introduced inclination will affect the measurement result. In our experiment, the inclination is very small and has little effect on the measurement of the out-of-plane displacement. The maximum displacement of the top end of the microchip is 9.6 μm, and the distance from the top end to the fixed axis is 11 mm. Thus, the inclination angle is about 0.00087°. Through further calculation, the change in the vertical beam propagation direction does not exceed one pixel, so it will not affect the measurement results. In order to understand the displacement process easily, the angles drawn in Figures 8 and 12 are exaggerated and much larger than the actual angle.

If we want to measure the displacement in the case of a large inclination angle, we can no longer calculate the out-of-plane displacement only by Equation (7), but should consider the influence of the inclination angle and the in-plane displacement [35–37]. Yang, L.X. has summarized various out-of-plane displacement and in-plane displacement measurement methods and applicable conditions in detail [35].

5. Conclusions

In this paper, a new type of large-field microscopic speckle interferometry system based on Mach-Zehnder structure is proposed. By introducing doublet lens groups, the new system expands the field of view from a circular area with a diameter of 2.4 mm to a rectangular area of 6 mm × 8 mm. Additionally, our system effectively reduces the reflected light beam in the optical path, thereby reducing the reflected coherent noise. The experimental results show that our improved measurement system can achieve large-field and high-precision dynamic measurement of MEMS.

There are still some details that need to be further improved. The first limitation of our system is the need to obtain proper field of view with different sizes of measured object. To achieve this purpose, we can combine different microscope objectives and doublet lenses, which require a series of experiments to summarize. At the same time, the measurement accuracy is not very high. We can improve the measurement accuracy by optimizing the algorithm (such as phase subdivision) and adding the anti-reflection film on the surface of optical components to further reduce the coherent noise.

Author Contributions: Study design, data analysis, and writing—original draft preparation: C.G.; project administration, writing—review and editing: Z.G.; software: Y.N.; visualization: X.W.; supervision: J.Z.; investigation: L.D. All authors have read and agreed to the published version of the manuscript.

Informed Consent Statement: Not applicable.

Conflicts of Interest: The authors declare no conflict of interest.

References

1. Abdulhalim, I. Theory for double beam interference microscopes with coherence effects and verification using the Linnik microscope. *J. Mod. Opt.* **2001**, *48*, 279–302. [CrossRef]
2. Lin, S.T.; Hsu, W.F.; Wang, M.S. Phase-shifting interference microscope with extendable field of measurement. *J. Opt.* **2018**, *20*, 1–7. [CrossRef]
3. Niehues, J.; Lehmann, P.; Xie, W. Low coherent Linnik interferometer optimized for use in nano-measuring machines. *Meas. Sci. Technol.* **2012**, *23*, 1–9. [CrossRef]
4. Riquelme, R.; Lira, L.; Perez-Lopez, C.; Rayas, J.A.; Rodriguez-Vera, R. Interferometric measurement of a diffusion coefficient: Comparison of two methods and uncertainty analysis. *J. Phys. D-Appl. Phys.* **2007**, *40*, 2769–2776. [CrossRef]
5. Berguiga, L.; Zhang, S.J.; Argoul, F.; Elezgaray, J. High-resolution surface-plasmon imaging in air and in water: V(z) curve and operating conditions. *Opt. Lett.* **2007**, *32*, 509–511. [CrossRef]
6. Butters, J.N.; Leendertz, J.A. Speckle pattern and holographic techniques in engineering metrology. *Opt. Laser Technol.* **1971**, *3*, 26–30. [CrossRef]
7. Jones, R.; Wykes, C. General Parameters for the Design and Optimization of Electronic Speckle Pattern Interferometers. *Opt. Acta* **1981**, *28*, 949–972.
8. Joenathan, C. Vibration fringes by phase stepping on an electronic speckle pattern interferometer—An analysis. *Appl. Opt.* **1991**, *30*, 4658–4665. [CrossRef]
9. Moore, A.J.; Tyrer, J.R.; Santoyo, F.M. Phase extraction from electronic speckle pattern interferometry addition fringes. *Appl. Opt.* **1994**, *33*, 7312–7320. [CrossRef] [PubMed]
10. Rodriguez-Zurita, G.; Garcia-Arellano, A.; Toto-Arellano, N.I.; Flores-Munoz, V.H.; Pastrana-Sanchez, R.; Robledo-Sanchez, C.; Martinez-Bravo, O.; Vasquez-Pasmino, N.; Costa-Vera, C. One-shot phase stepping with a pulsed laser and modulation of polarization: Application to speckle interferometry. *Opt. Express* **2015**, *23*, 23414–23427. [CrossRef]
11. Bavigadda, V.; Jallapuram, R.; Mihaylova, E.; Toal, V. Electronic speckle-pattern interferometer using holographic optical elements for vibration measurements. *Opt. Lett.* **2010**, *35*, 3273–3275. [CrossRef]
12. Malacara, D.; Servin, M.; Malacara, Z. Periodic Signal Phase Detection and Algorithm Analysis. In *Interferogram Analysis for Optical Testing*, 2nd ed.; Taylor and Francis Group: Boca Raton, FL, USA, 2005; pp. 1–99.
13. Furlong, C.; Pryputniewcz, R.J. Optoelectronic characterization of shape and deformation of MEMS accelerometers used in transportation applications. *Opt. Eng.* **2003**, *42*, 1223–1231. [CrossRef]
14. Kumar, U.P.; Bhaduri, B.; Kothiyal, M.P.; Mohan, N.K. Two-wavelength micro-interferometry for 3-D surface profiling. *Opt. Lasers Eng.* **2009**, *47*, 223–229. [CrossRef]

15. Kumar, U.P.; Mohan, N.K.; Kothiyal, M.P.; Asundi, A.K. Deformation and shape measurement using multiple wavelength microscopic TV holography. *Opt. Eng.* **2009**, *48*, 0236011–0236019. [CrossRef]
16. De Groot, P.J.; Biegen, J.F. Interference microscope objectives for wide-field areal surface topography measurements. *Opt. Eng.* **2016**, *55*, 0741101–0741106. [CrossRef]
17. Denboef, A.J. Scanning force microscopy using a simple low-noise interferometer. *Appl. Phys. Lett.* **1989**, *55*, 439–441. [CrossRef]
18. Dubois, A.; Vabre, L.; Boccara, A.C. Sinusoidally phase-modulated interference microscope for high-speed high-resolution topographic imagery. *Opt. Lett.* **2001**, *26*, 1873–1875. [CrossRef]
19. Wiersma, J.T.; Wyant, J.C. Vibration insensitive extended range interference microscopy. *Appl. Opt.* **2013**, *52*, 5957–5961. [CrossRef] [PubMed]
20. Lu, S.H.; Chang, C.-J.; Kao, C.F. Full-field optical coherence tomography using immersion Mirau interference microscope. *Appl. Opt.* **2013**, *52*, 4400–4403. [CrossRef] [PubMed]
21. Schmit, J.; Hariharan, P. Improved polarization Mirau interference microscope. *Opt. Eng.* **2007**, *46*, 0770071–0770073.
22. Lyulko, O.V.; Randers-Pehrson, G.; Brenner, D.J. Simultaneous immersion Mirau interferometry. *Rev. Sci. Instrum.* **2013**, *84*, 0537011–0537016. [CrossRef] [PubMed]
23. Wang, D.D.; Liang, R.G. Simultaneous polarization Mirau interferometer based on pixelated polarization camera. *Opt. Lett.* **2016**, *41*, 41–44. [CrossRef]
24. Ganjkhani, Y.; Chaysooghi, M.A.; Akhlaghi, E.A.; Moradi, A.R. Super-resolved Mirau digital holography by structured illumination. *Opt. Commun.* **2017**, *404*, 110–117. [CrossRef]
25. Dubois, A. Effects of phase change on reflection in phase-measuring interference microscopy. *Appl. Opt.* **2004**, *43*, 1503–1507. [CrossRef]
26. Somekh, M.G.; Charsooghi, M.A.; Akhlaghi, E.A.; Moradi, A.R. Wide-field high-resolution surface-plasmon interference microscopy. *Opt. Lett.* **2009**, *34*, 3110–3112. [CrossRef] [PubMed]
27. Choi, Y.; Hosseini, P.; Choi, W.; Dasari, R.R.; Peter, T.C.; Yaqoob, Z. Dynamic speckle illumination wide-field reflection phase microscopy. *Opt. Lett.* **2014**, *39*, 6062–6065. [CrossRef] [PubMed]
28. Pitter, M.C.; See, C.W.; Somekh, M.G. Full-field heterodyne interference microscope with spatially incoherent illumination. *Opt. Lett.* **2004**, *29*, 1200–1202. [CrossRef]
29. Dubois, A.; Vabre, L.; Boccara, A.C.; Beaurepaire, E. High-resolution full-field optical coherence tomography with a Linnik microscope. *Appl. Opt.* **2002**, *41*, 805–812. [CrossRef]
30. Abdulhalim, I.; Dadon, R. Multiple interference and spatial frequencies' effect on the application of frequency-domain optical coherence tomography to thin films' metrology. *Meas. Sci. Technol.* **2009**, *20*, 1–11. [CrossRef]
31. Chen, Y.L.; Jian, Z.C.; Hsieh, H.C.; Wu, W.T.; Su, D.C. Nano-roughness measurements with a modified Linnik microscope and the uses of full-field heterodyne interferometry. *Opt. Eng.* **2008**, *47*, 1256011–1256015. [CrossRef]
32. Safrani, A.; Abdulhalim, L. Real-time phase shift interference microscopy. *Opt. Lett.* **2014**, *39*, 5220–5223. [CrossRef] [PubMed]
33. Zhang, Z.; Li, X.; Shen, W. Thermal deformation analysis of copper microbridges with speckle interferometry and finite element. *Key Eng. Mater.* **2007**, *353*, 2871–2874. [CrossRef]
34. Gao, C.J.; Gao, Z.; Wang, X.; Liu, Z.H. Real-time measurement of microcantilever displacement based on Linnik microscopic speckle interferometer. *Opt. Eng.* **2018**, *57*, 1241011–1241016. [CrossRef]
35. Yang, L.X.; Xie, X.; Zhu, L.Q.; Wu, S.J.; Wang, Y.H. Review of Electronic Speckle Pattern Interferometry (ESPI) for Three Dimensional Displacement Measurement. *Chin. J. Mech. Eng.* **2014**, *27*, 1–13. [CrossRef]
36. Gomez-Mendez, G.A.; Rodriguez-Zurita, G.; Martinez-Garcia, A. Phase stepping through polarizing modulation in electronic speckle pattern interferometry. *Appl. Opt.* **2020**, *59*, 6005–6011. [CrossRef] [PubMed]
37. Bhaduri, B.; Mohan, N.K.; Kothlyal, M.P. A dual-function ESPI system for the measurement of out-of-plane displacement and slope. *Opt. Lasers Eng.* **2006**, *44*, 637–644. [CrossRef]

Communication

Optical Fiber Fabry–Perot Interferometer Based Spirometer: Design and Performance Evaluation

Ana Catarina Nepomuceno [1,2]**, Tiago Paixão** [2]**, Nélia Alberto** [1]**, Paulo Sérgio de Brito André** [3]**, Paulo Antunes** [1,2] **and M. Fátima Domingues** [1,]*****

1   Instituto de Telecomunicações and University of Aveiro, Campus Universitário de Santiago, 3810-193 Aveiro, Portugal; catarinanepomuceno@ua.pt (A.C.N.); nelia@ua.pt (N.A.); pantunes@ua.pt (P.A.)
2   Department of Physics & I3N, University of Aveiro, Campus Universitário de Santiago, 3810-193 Aveiro, Portugal; tiagopaixao@ua.pt
3   Department of Electrical and Computer Engineering and Instituto de Telecomunicações, Instituto Superior Técnico, University of Lisbon, 1049-001 Lisbon, Portugal; Paulo.andre@lx.it.pt
*   Correspondence: fatima.domingues@ua.pt

Abstract: Spirometry enables the diagnosis and monitoring of multiple respiratory diseases, such as asthma and chronic obstructive pulmonary disease (COPD). In this paper, we present an optical fiber-based device to evaluate the pulmonary capacity of individuals through spirometry. The proposed system consists of an optical fiber containing an intrinsic Fabry–Perot interferometer (FPI) micro-cavity attached to a 3D printed structure that converts the air flow into strain variations to the optical fiber, modulating the FPI spectral response. Besides providing the value of the flow, its direction is also determined, which enables a differentiation between inhale and exhale cycles of breathing. A simulation study was conducted to predict the system behavior with the air flow. The preliminary tests, performed with the FPI-based spirometer led to average values of forced expiratory volume in 1 s (FEV1) and forced vital capacity (FVC) parameters of 4.40 L and 6.46 L, respectively, with an FEV1/FVC index (used as an airway function index) of 68.5%. An average value of 5.35 L/s was found for the peak expiratory flow (PEF). A comparison between the spirometry tests using the presented FPI system and a commercial electronic device showed that the proposed system is suitable to act as a reliable spirometer.

Keywords: Fabry–Perot interferometer; optical fiber sensor; flow sensor; pulmonary function assessment; spirometry

1. Introduction

Worldwide, the number of people being affected by respiratory diseases continues to establish new records, representing one of the leading causes of death and impairments [1]. This problem is associated with the deterioration of air quality, due to exposure to pollution, secondhand tobacco smoke, and chemical fumes. Chronic obstructive pulmonary disease (COPD) is one of the most commonly diagnosed lung diseases, severely affecting about 65 million people and killing 3 million individuals each year, being the third leading cause of death worldwide [1,2]. Besides COPD, asthma affects more than 334 million people and is diagnosed in 14% of children, creating a predisposition to permanent pulmonary impairments and COPD. Despite asthma and COPD being the most common, there are several other lung-related diseases that impact and restrain the quality of life of countless people [1,3].

To break the upward trend of aggravations caused by respiratory diseases and improve the quality of life of patients, a timely diagnosis and control of the disorder evolution over time are required. To achieve such a goal, suitable and cost-effective tools are essential to provide accurate measurements of the pulmonary capacity. Among the clinical methods to

193

evaluate lung function, the most common is spirometry, which measures the volume and flow of the inhaled and exhaled air during forced breathing cycles [1,4].

The forced expiratory maneuver, characteristic of spirometry, consists of a deep inhalation before a hard and fast exhaling, according to the standardization established by the American Thoracic Society (ATS) and the European Respiratory Society (ERS) [4]. The outcome parameters of spirometric tests are based on the flow–volume and volume–time curves. From these curves, several pulmonary function values can be determined, for instance: the peak expiratory flow (PEF), which is the maximal air flow rate achieved; the forced vital capacity (FVC), which represents the amount of air volume exhaled; the forced expiratory volume in 1 s (FEV1), which corresponds to the maximal air volume in the first second of the maneuver; and the ratio of FEV1/FVC, which is used as an airway function index [4,5].

According to the underlying working principles, the spirometers can be categorized as bellows, pistons, water bells, turbinometers, anemometers, ultrasonic and pneumotachometers, with the latter being the most common one [4,5]. Recently, some authors envisioned the incorporation of wireless data transmission devices with compact affordable spirometers, such as a Lilly pneumotachometer [6] and a platinum anemometer [7], providing a remote access to results through web and smartphone apps. Nevertheless, like other electronic-based devices, these systems present inherent limitations regarding environmental factors and electromagnetic interferences, which could damage the equipment and cause misleading results.

Optical fiber-based sensors appear as an alternative capable of overcome such limitations by offering immunity to electromagnetic interferences and electrical isolation, along with low signal attenuation, high accuracy, and possibility of remote sensing [8]. So far, there are reports of solutions based on the modulation of the fiber Bragg gratings (FBG) response due to the thermal variations associated with the breathing cycles [9,10], the bending losses, or vibrations induced by the air flow that impact on the optical signal intensity [11,12], cantilever mechanisms that apply strain proportional to the air flow onto FBG-based sensors [13,14], among others. An FBG 3D printed system was recently explored by the research team of this paper, also for the spirometry application [15]. In this case it was proposed as a sensor based on two FBGs, to assess the pulmonary function, while providing the thermal effect compensation associated with breathing (hot air in exhalations and cold air in inhalations).

Regarding the use of Fabry–Perot interferometers (FPI), Zhao et al. proposed a device for air flow measurements, where a FPI was produced by splicing a single mode fiber (SMF) to a hollow-core fiber (HCF) at the end of an optical fiber. By conducting the air flow into this fiber end, the FPI cavity length is compressed, and consequently, its spectral response modulated [16]. Nevertheless, this highly sensitive device is only able to monitor stationary air flows, and no dynamic monitoring results, essential for spirometry tests, are presented. Another reported system comprises a FPI micro-cavity produced by attaching a polymer to the end of a SMF. In this case, the polymer volume is dependent on the temperature and, therefore, after its initial heating, the hot polymer is cooled down by the air flow, which changes the FPI cavity length and modulates its spectrum [17].

Furthermore, a solution based on the modulation of the FPI cavity length through the use of the air flow to cool down a heated system was reported in [18]. Another FPI-based technique for flow sensing comprises a multiple cantilever system where their bending modulates the distance between an optical mirror and the fiber end [19]. However, the reported FPI-based solution is not conceived for human breath dynamic flow sensing, requiring a dynamic acquisition upgrade to act as spirometers.

On similar applications, the authors Xu et al. have presented an FPI-diaphragm-based sensor for pressure and acoustic wave sensing, attaining measurement ranges from 5 to 10,000 psi, with a frequency response up to 2 MHz [20]. The multifaceted prospective of FPI sensors render them suitable for a wide range of applications, from the highly sensitive to strain [21], to large-range liquid level monitoring [22].

This paper presents an in-line FPI-based sensor encased in a 3D printed system, designed to evaluate the respiratory condition of individuals and act as an optical spirometer. Since this system is based on the optical fiber technology, all its inherent advantages are included in the proposed sensing solution. Compared with the device presented in [15], the main advantages of the presented FPI-based system are the use of a single optical fiber (and sensor) due to its low sensitivity to temperature, the improved design to maximize the response to strain, and the cost-effective methodology used for the FPI production in relation to the Bragg network recording system. To the best of our knowledge, this is the first time that an inline FPI optical fiber-based sensor is proposed for spirometer applications. Although other solutions have been previously developed for flow monitoring (air or liquids), as detailed above, they are static sensors, while we present a solution which has a good performance for dynamic measures, as is required in spirometry.

The rest of the manuscript is structured as follows: The FPI production, strain characterization, and the spirometer assembly are presented in Section 2. In Section 3, we present the sensing mechanisms and theoretical analysis. Section 4 is dedicated to the testing protocol and the obtained results, and Section 5 provides the conclusion.

2. FPI-Based Spirometer

FPI-based sensors have gained popularity in terms of sensing technology due to their efficiency and accuracy, as well as their versatility and responsiveness [23]. An FPI includes two reflective surfaces forming a resonant micro-cavity. Within the cavity, the optical signal suffers multiple reflections, and the subsequent interaction between the reflected and the incident signals produces an interference pattern. Its intensity profile, I, is given by the optical signal intensities reflected in each reflective surface (I_1 and I_2) and the optical phase difference between two adjacent signals (Φ), according to:

$$I = I_1 + I_2 + 2 \cos(\Phi) \sqrt{I_1 \cdot I_2}. \tag{1}$$

The optical phase difference (Φ) is related with the refractive index of the micro-cavity (n), its physical length (L_m), and the optical signal wavelength (λ), which for a normal incidence can be defined as:

$$\Phi = \frac{4\pi}{\lambda} n L_m. \tag{2}$$

Therefore, the FPI interference spectrum can be modulated by a variation in the micro-cavity length or refractive index, which enables the use of FPIs as accurate sensors. For instance, in the case of fiber elongation, a strain is applied to the FPI, causing an increase in the physical length of the cavity, and consequently a wavelength shift in the FPI spectral response. This is the property that will be used in this work, to determine the air flow dynamics associated with spirometry tests.

Furthermore, given that in biomedical applications, the body temperature can significantly affect some sensing systems and produce inaccurate results, a sensing device suitable for temperature compensation in changing environments is required. In spirometry, different breathing cycles are associated with different temperatures, for instance, in inhalations there is cold air, while in exhalations hot air is in contact with the sensor. However, FPI sensors, similar to the one produced for the instrumentation of the proposed spirometer, present very low sensitivity to temperature [24], which can be negligible if we consider the temperature variation expected during breathing (~5 °C). Therefore, the temperature influence in the spectral response of the proposed FPI cavity can be ignored.

The production of the in-line FPI micro-cavity follows a cost-effective method that was first described in [24]. This technique comprises the recycling of an optical fiber damaged by the catastrophic fuse effect, as it generates periodically spaced voids in the silica fiber core. By splicing the damaged fiber to a standard single mode fiber (SMF), a larger void emerges from the initial voids in the splicing area. To obtain a single FPI micro-cavity, the resultant fiber (containing the open void) is cleaved and spliced again to a similar

SMF [24]. In Figure 1a, a microscopic image of the resultant FPI micro-cavity along with the respective dimensions is represented, whereas Figure 1b depicts the FPI optical spectrum.
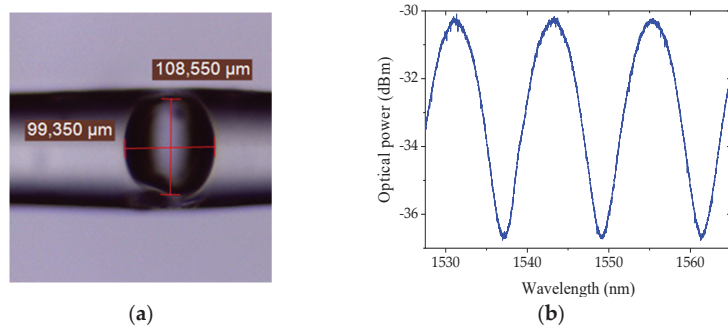

(**a**)

(**b**)

Figure 1. Resultant FPI: (**a**) microscopic image and respective dimensions; and (**b**) optical reflection spectrum.

2.1. FPI Sensor Strain Characterization

Prior to the implementation of the sensor, the FPI was characterized to strain variations, aiming to determine the relation between the strain applied to the optical fiber, ε, and the induced wavelength shift in the FPI spectrum, $\Delta\lambda$, written as:

$$\Delta\lambda = S_l \cdot \varepsilon, \tag{3}$$

where S_l represents the FPI sensitivity to strain variations. This characterization started by attaching each extremity of the fiber containing the FPI sensor to fixed and translation stages, which enables the control of the strain applied to the system. The anchorage points were initially distanced by 24.6 cm, and the applied elongation ranged from 0 to 200 μm, in 20 μm steps. The process was executed for an increasing and decreasing elongation, to evaluate the hysteresis effect on the FPI response. The FPI reflection spectra were monitored using a customized interrogation system based on the I-Mon 512 USB spectrometer (Ibsen Photonics). The experimental data obtained for the described process are represented in Figure 2, along with the respective linear fits. From this test, considering the average value from the increasing and decreasing elongations, a strain sensitivity, S_l, of 3.51 ± 0.07 pm/με, and a hysteresis of 0.02 nm were obtained.
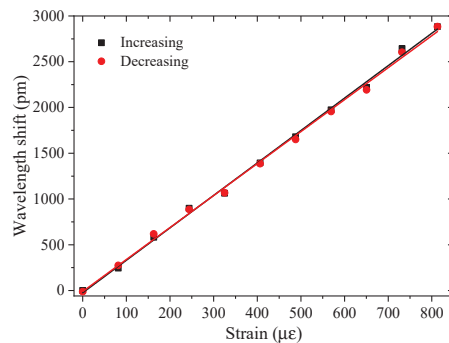

Figure 2. Wavelength shift of the FPI with applied strain. The black and red solid lines represent the linear fits of the increasing and decreasing elongations, respectively.

The FPI sensitivity value is a key factor to find the relation between the air flow and the wavelength shift modulated at the FPI during the spirometry tests. Other parameters

that influence the device feedback are the dimensions of the 3D printed spirometer, which is detailed in the following Sections/sub-Sections.

2.2. Spirometer Sensing Architecture and Implementation

The presented sensing system is build based on a 3D-printed cylinder made of poly-lactic acid material (PLA), with an inner radius of 1.425 cm, which is the size of a standard bacterial filter mouthpiece [15]. The PLA cylinder is printed as two separate halves to simplify its assemblage and enable the analysis of the sensing condition at any moment, if necessary. One of the halves is used as a sliding cover, while the other has a set of rods longitudinally spaced by L (with L = 1.620 cm), with the same height as the cylinder radius (1.425 cm). The set of rods have different dimensions, as one is projected to be flexible with a section area of 0.07×0.40 cm^2 and the other rod has a large base area of 0.70×20 cm^2. The overall structure is illustrated in Figure 3. With this configuration, when the air flow interacts with the sensing system, it will cause a proportional bending of the flexible rod, while the larger rod remains still.
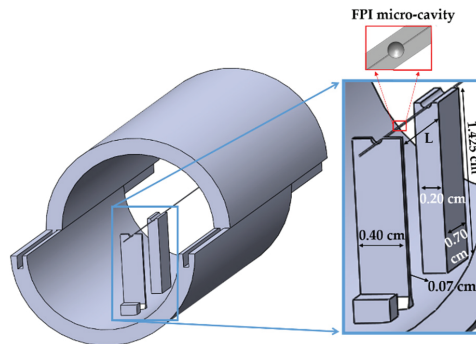

Figure 3. Schematic representation of the overall sensing system detailing the pair of rods configuration and its respective dimensions.

The bending induced in the flexible rod can be translated in a variation of the distance between the two rods (L). If we consider an optical fiber attached to these rods, such distance variation will induce a strain in the optical fiber, which will modulate the optical signal of the intrinsic FPI sensor, placed midway between the rods. Therefore, the bending (and consequently the distance variations) caused by the air flow can be determined through the monitoring of the wavelength shift of the FPI spectrum.

The assembly of the final FPI-based spirometer is of easy implementation and consists of positioning the optical fiber into the set of rods, with the FPI sensor located at the middle. The optical fiber is slightly tensioned and then glued onto the rods, enabling both directions of air flow to cause a spectral variation in the FPI response and, consequently, differentiate the breathing phases (inhalation and exhalation). The resultant sensing unit is depicted in Figure 4a.

The presented device is ready for performing spirometry tests after the attachment of a removable and disposable breathing section, as depicted in Figure 4b, comprising a bacterial filter case along with a mouthpiece, where each individual is asked to breathe into. This breathing section is hooked close to the flexible rod, where a safety tab prevents the contact between the two, securing the sensor's integrity.

In Figure 4c, the overall architecture of the sensing structure for spirometry tests is depicted. The sensing unit, portrayed in Figure 4b, is firmly attached to a vertical adjustable support, with the mouth piece at the volunteer's height. The flexible rod, faces the mouth piece and the volunteer. The optical fiber cable, exits the 3D printed spirometer case on the other extremity, and connects directly to the interrogator systems (I-Mon 512 USB, from Ibsen Photonics) with an acquisition frequency of 1900 Hz. For this spirometry application,

the wavelength shift (due to strain variations) of one selected maximum/minimum of the FPI spectra was continuously monitored during the tests.
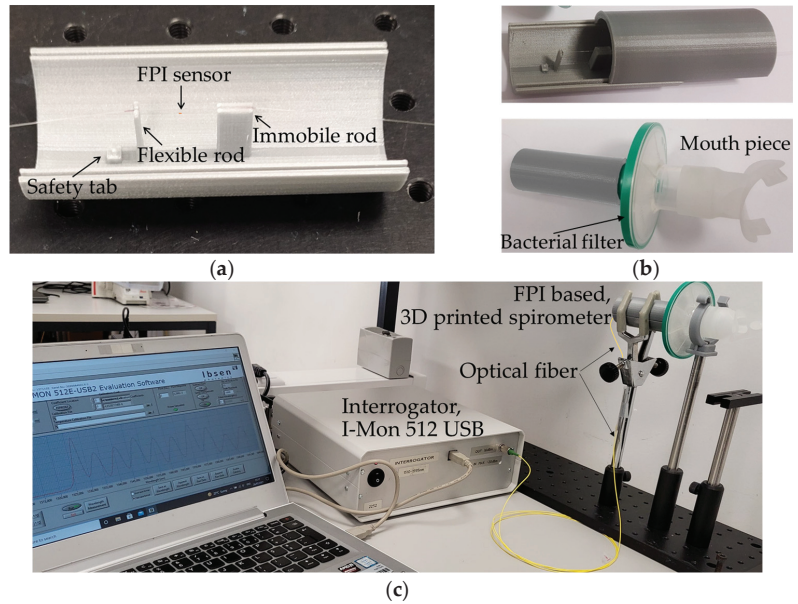

Figure 4. (**a**) Assembled sensing unit; (**b**) final FPI-based spirometer, with the covering lid and breathing section; and (**c**) overall architecture of the sensing structure for spirometry.

When compared with other previously reported airflow monitoring devices, such as the one presented in [16], the device proposed in this manuscript, due to the interrogator software reconfiguration, allows continuous monitoring of the air flow, at the interrogator acquisition rate (1900 Hz). The authors in [16], reported on a device, which, for each value of air flow, the correspondent FPI spectrum is acquired, and afterwards, upon data processing, the FPI spectral shift is analyzed for all the different air flow values tested. Here, the software customized for spirometry applications selects a smaller bandwidth of the FPI spectrum (here, the bandwidth of 1543–1554 nm was selected), and acquires, in a continuous mode at the interrogator acquisition rate, the wavelength shifts of the spectral dip in that bandwidth. For this application, the dip was chosen for its accentuation when compared with the spectral maximum. The wavelength shift is then converted to flow values, according to the theoretical assumptions detailed and demonstrated in the next section.

3. FPI-Based Spirometer Working Dynamics

In order to obtain the air flow dynamic parameters associated to spirometry, which enable the evaluation of the respiratory capacity, both flow and volume of air need to be determined. The volume of air is calculated through time integration of the flow, whereas the air flow ($Flow_{air}$) is achieved by applying the continuity equation to the system, resulting in [25]:

$$Flow_{air} = C_s \, v, \tag{4}$$

where v is the velocity of the fluid (air in this case), and C_s is the cross section area of the 3D printed cylinder, with r = 1.425 cm. Given that any object standing in the flowing stream of air will have a force being applied to it (the drag force), the flexible rod will experience a force F, defined by:

$$F = \frac{1}{2} \varrho \, v^2 \, A_r \, D_c, \tag{5}$$

with the air density $\varrho = 1.0 \ \text{kg/m}^3$, v representing the air velocity, A_r representing the area of the rod facing the flow, and D_c representing the drag coefficient of the rod ($D_c = 1.18$ for a planar body with rectangular shape [23]).

When considering mechanical perturbations in the elastic region of structural components, the Hooke's law gives the relation between the perturbation force, F, and the induced deflection (or relative displacement), δ, as:

$$\delta = F/K, \tag{6}$$

with K representing the stiffness (or elastic constant) of the material. However, when dealing with systems with more than one element, it is also possible to determine the stiffness of the system, i.e., the equivalent stiffness. In the cases where the elements deflection is the same, the equivalent stiffness is given by the sum of each individual stiffness. Considering the rod as a cantilever beam loaded at the end, and the optical fiber as a uniform cylindrical bar subjected to longitudinal loading, the system deflection δ results in [26–28]:

$$\delta = F \left(\frac{Y_{PLA} \, d \, s^3}{4 \, T^3} + \frac{Y_f \, S_f}{h_f} \right)^{-1}, \tag{7}$$

with the first term concerning the rod properties such as the length T, which has the cylinder radius size of 1.425 cm, Young modulus of the rod material Y_{PLA} (3.33 GPa for the used 3D printed PLA), width (d = 0.40 cm), and thickness (s = 0.07 cm). The second term concerns the optical fiber, where h_f represents the length subjected to perturbations (h_f = 1.620 cm), Y_f represents the fiber Young modulus (Y_f = 69.2 GPa [29]), and S_f is the cross section (considering the typical diameter of an uncoated fiber, 125 μm).

At the same time, the strain applied to the optical fiber that induces the modulation on the FPI response is given by the ratio of the distance variation between the two rods, Δl, to the initial rods separation, L (L = 1.620 cm), as:

$$\varepsilon = \Delta l / L. \tag{8}$$

Since the distance variation between the two rods Δl, corresponds to the deflection δ, from the association of (3) and (8), the relation between the rod displacement and the wavelength shift, $\Delta \lambda$, is provided:

$$\delta = \Delta l \ \rightarrow \ \delta = \frac{L}{S_l} \Delta \lambda. \tag{9}$$

By further replacing (4) and (5) into (7), the air flow as a function of the FPI-induced wavelength shift can be obtained:

$$Flow_{air}^2 = \frac{2 \, L \, Cs^2}{\rho \, Ar \, Dc \, S_l} \left(\frac{Y_{PLA} \, d \, s^3}{4 \, T^3} + \frac{Y_f \, S_f}{h_f} \right) \Delta \lambda, \tag{10}$$

where the product is a constant associated with the material properties and dimensions of the cylinder, rod, and fiber. Substituting this term by a denominated flow constant, W, enables to simplify (10) as:

$$Flow_{air}^2 = W \, \Delta \lambda. \tag{11}$$

As the flexible rod is near to the origin of the air flow (the breathing section), exhalation cycles will decrease its distance to the fixed rod, inducing a compressive strain to be applied to the optical fiber. Compressive strains decrease the initial length of the FPI cavity and hence induce a spectral shift, to lower wavelengths, on the FPI spectral response. On the other hand, inhalation cycles will increase the distance between the two rods, causing a

tensile strain and changing the FPI spectrum to higher wavelengths, since it induces an increase in the FPI cavity length.

Simulation of 3D Spirometer Deflection

The Solidworks Simulation and Solidworks Flow Simulation tools of the Solidworks 2019® (SW) program were used on the projected 3D model to corroborate the underlying theory through the simulation of the dynamics and structural impact associated with a forced expiratory maneuver. The forced exhalation was simulated by recreating an air flow within the cylinder and then assessing the rod response to it. The result was a bending of the flexible rod in the same direction as the flow, and since the larger rod remains immobile, the distance between the rods decreases, as expected. Following a similar process to simulate a forced inhalation resulted in the rod bending in the opposite direction, along with the air flow, and consequently, in the increasing of the rods separation. It should be noted that, due to the rod's small thickness, and the optical fiber restraint effect, the displacement between the two rods is higher near the center of the rod. In Figure 5, the lateral section view of the air flow effect on the system is depicted, resultant from the two simulations, considering an air flow of 6 L/s [4]. Along with the illustration, the estimated displacement values of the overall system regarding its initial position are also provided.
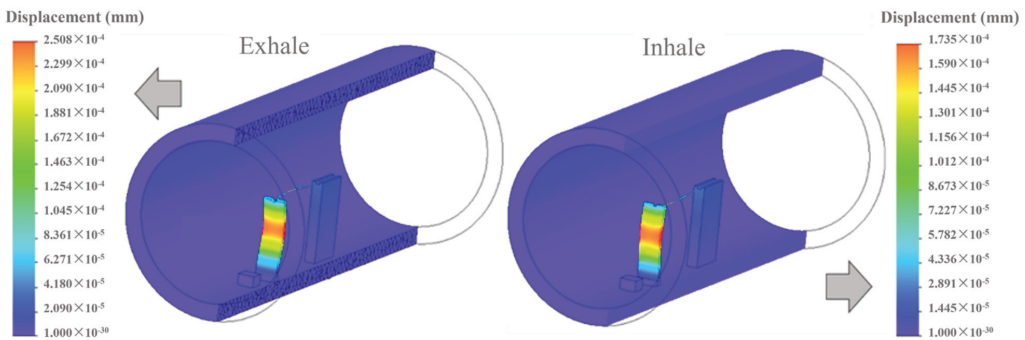

Figure 5. Expected effect of an air flow of 6 L/s on the proposed spirometer, for the exhale and inhale moments.

As one can observe from Figure 5, during the simulated inhalation, the rod bending capacity is lower than the one for the same flow in the exhalation moment. Such movement constraint is related with the attachment of the rod to the optical fiber, since in the inhalation cycles the movement of the rod is restrained by the fiber elongation. Therefore, it is necessary to consider a different flow constant for the inhalation (W_I) and exhalation (W_E) cycles, with W_E being the same as in Equations (10) and (11) and W_I being defined as:

$$W_I = \frac{2\,L\,Cs^2}{\rho\,Ar\,Dc} \left(\frac{Y_{PLA}\,d\,s^3}{4\,T^3} + \frac{Y_f\,S_f}{h_f} \right) p, \tag{12}$$

with p being a restraining factor that reflects the optical fiber resistance to the pulling movement of the rod during the inhalation process.

Considering the different flow constants W_I and W_E for inhalation and exhalation cycles, respectively, Equation (11) is now rewritten as:

$$\text{Flow}_{air} = \begin{cases} \sqrt{W_I} \cdot (-\sqrt{|\Delta\lambda|},\, |\,\Delta\lambda > 0) \\ \sqrt{W_E} \cdot (\sqrt{|\Delta\lambda|},\, |\,\Delta\lambda < 0) \end{cases} \tag{13}$$

By extending this analysis to the typical air flow range expected in spirometry (0 up to 7 L/s) for inhalation and exhalation cycles [4], a relation between the simulated

rod displacement and the air flow can be determined. The obtained displacement can be converted into the spectral wavelength shift of the FPI by linking it with (3) and (8) and considering the strain sensitivity experimentally achieved, $S_l = 3.51 \pm 0.07$ pm/$\mu\varepsilon$. In Figure 6, the relation established according to values retrieved through the SW simulation is displayed, where exhalation cycles are represented as positive flow values while inhalations are portrayed as negative flows.
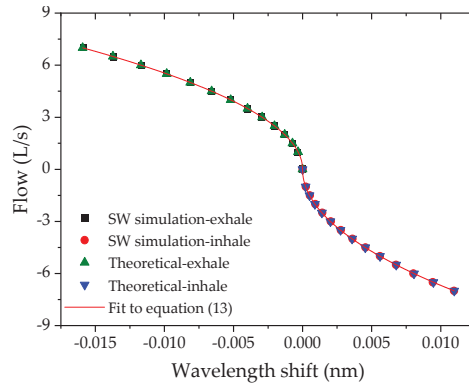

Figure 6. Relation between wavelength shift and flow achieved through SW simulation and theoretical analysis.

The same figure also illustrates the theoretical wavelength shifts for the same values of flow, obtained according to (13), to provide a comparison with the underlying theory described in the previous sub-section. For the restraining factor p in (12), a value of 0.7 was considered, found through data processing. From the fit performed to the data represented in Figure 6, the values of the constants W_I and W_E, were found to be 66.76 L/s·(nm)$^{1/2}$ and 55.43 L/s·(nm)$^{1/2}$, respectively.

It should be noted that the behavior found for the air flow in the FPI spirometer follows the trend previously reported using other optical fiber technology [15], in which the strain applied in the optical fiber has a linear response with the modulated optical signal.

4. Spirometry Tests and Results

To evaluate the performance of the assembled spirometer, the overall sensing and breathing unit was placed in a holding support, where a volunteer was asked to execute a series of spirometry tests. During each trial, the interrogation device (I-Mon 512 USB, from Ibsen Photonics) with an acquisition frequency of 1900 Hz and a wavelength fit resolution of 0.5 pm was used for continuous monitoring of the FPI spectral response.

For the performance evaluation test, a healthy volunteer (female, 23 years) placed the mouthpiece and a nasal clip, to ensure that all the air flow was conducted entirely through the mouth. The test is started with normal breathing, followed by a deep inhale and a forced exhale, which normally should last approximately 6 s [4]. Figure 7 presents the experimental data obtained in two different tests performed by the same person, concerning the forced breathing moment.

Due to the previously mentioned fiber restrains, the acquired signal during the inhalation considerably reflects the constrained movement of the rod. In the represented data, the influence of the optical fiber and the PLA inertia in the rod movement can be observed. The return to the rod's original position also produces a deflection in the opposite direction, reflected by the negative wavelength shift during the inhale moments (which contradicts the predicted behavior). In order to clear the obtained signal, towards a trustworthy feed-

back as expected in a spirometry test, a fit to the obtained curve is performed, represented in blue, in Figure 7.
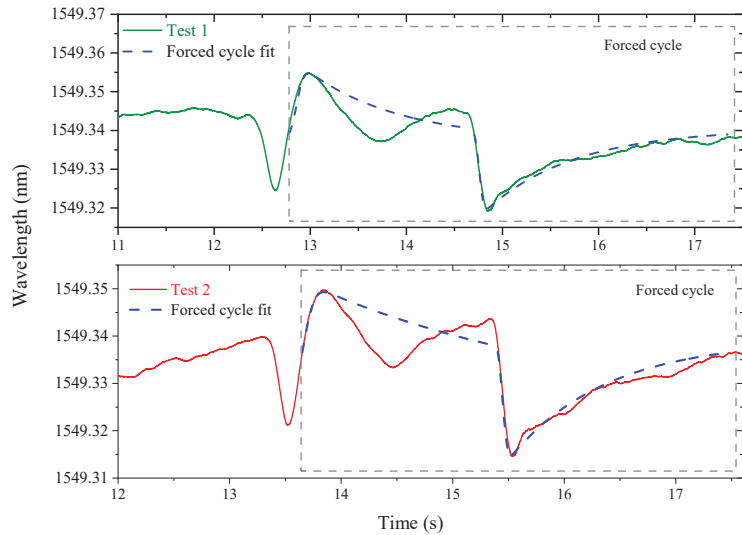

Figure 7. Results obtained using the FPI-based spirometer, concerning the area of the forced breathing cycle.

By applying Equation (13) to the obtained data (from the fit curve), the flow–time curves associated with the spirometry tests can be found. Figure 8 displays the forced breathing section of the flow–time curves from each trial. In spirometry analytical representation, the exhalation process is associated with positive values of flow, whereas the inhalation process is portrayed as negative flow values.
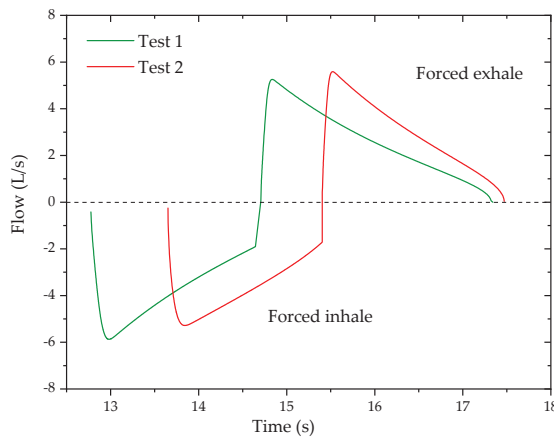
Figure 8. Forced breathing section of the flow–time curves obtained using the proposed sensing system.

In order to obtain the typical outcome of a spirometer, which are the flow–volume and volume–time curves, the exhale cycles of the forced breathing were separately integrated to determine the air volume associated with the process. The resultant flow–volume

and volume–time curves are depicted in Figure 9a,b, respectively, along with the respiratory function parameters assessed during spirometry, such as FVC, PEF, FEV1, and the FEV1/FVC ratio.
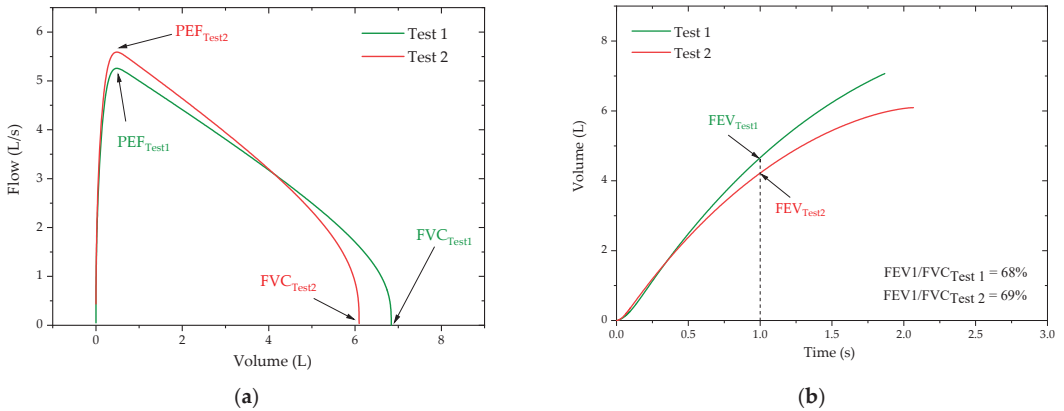

Figure 9. Spirometry curves for two different tests obtained with the proposed system: (**a**) flow–volume curve; (**b**) volume–time curve.

To provide a comparison of results, the same procedure used for the FPI-based spirometer was repeated using a commercial portable spirometer (Electronic Handheld, Digital Spirometer, Quiromed®). The flow–volume and volume–time curves obtained in the tests with the commercial spirometer are displayed in Figure 10a,b, respectively. Along with the empirical curves, represented as red and green lines, a shading area is also depicted, which represents the expected curve based on the ERS reference values [4], provided by the electronic spirometer, and considers the age, gender, height, weight, and smoking habits of the subject.
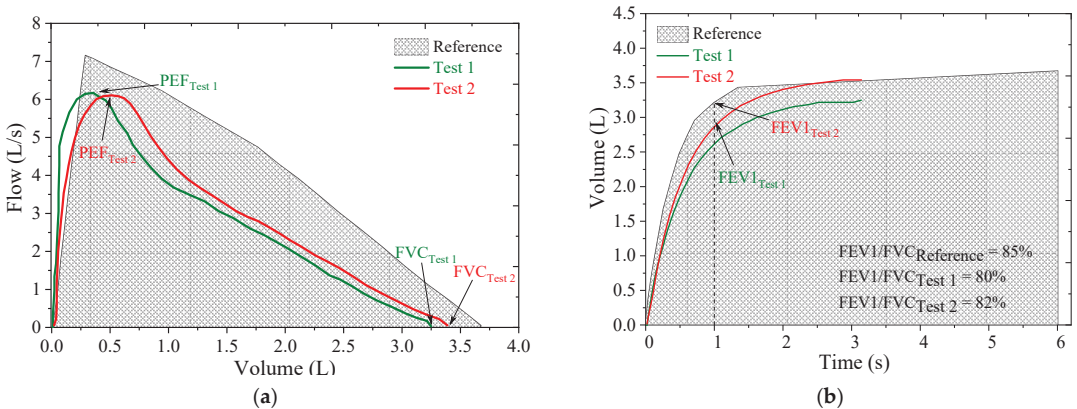

Figure 10. Commercial spirometer and reference spirometric curves: (**a**) flow–volume curve and (**b**) volume–time curve.

By comparing the flow–volume and volume–time curves obtained from the different sensing systems—the commercial spirometer and the proposed one—it is apparent that the shape of the curves is in agreement and according to the expected behavior, as represented by the reference curve. The direct observation of the curves also enables the comparison between the respiratory function parameters, PEF, FVC, FEV1, and FEV1/FVC ratio, typically evaluated in a spirometry test.

The average FEV1 and FVC parameters for the two forced exhalations acquired from the proposed FPI system are 4.40 L and 6.46 L, respectively. Regarding the PEF, an average value of 5.35 L/s was found for the same two tests and a ratio of 68.5% was obtained for the average FEV1/FVC index. Correspondingly, the average FEV1 and FVC parameters determined for the two tests performed with the electronic spirometer are 2.83 L and 3.52 L, respectively. As for the PEF and FEV1/FVC ratio, using the commercial device, average values of 6.19 L/s and 81% were found.

Even though larger values were obtained with the FPI based spirometer than with the commercial one, especially for the FEV and FVC parameters, the FEV1/FVC ratios only differ by ~10%. The existing deviation may be due to a decreasing effort from the subject associated with fatigue, as the tests with the FPI-based device were performed before the ones with the commercial device, but sequentially. The results seem to be proportional and, therefore, a calibration constant (obtained by performing more tests with different volunteers) can answer this discrepancy. Presently, and due to the restrictions imposed by the SARS-CoV-2 pandemic, the recruitment of more volunteers for the sensor constant optimization was not possible.

One of the main advantages of the FPI-based spirometer is the reduced sensitivity to temperature variations [24], which for a small range, such as the one expected between inhalation and exhalation moments (about 5 °C), can be disregarded. Contrarily, the FBG-based sensors require a temperature compensation method to solve their strong dependency with thermal variations [15]. Furthermore, the increase in the strain sensitivity obtained for FPI-based sensors (3.51 ± 0.07 pm/$\mu\varepsilon$ for the FPI implemented) enables a better resolution and more accurate measurements when compared with the ones achieved with the FBG-based spirometer (around 1 pm/$\mu\varepsilon$) [15], which would be of greater importance when considering the monitoring of patients with lower respiratory capacity.

It is also important to consider that precise medical equipment, such as the laboratory spirometers, require a high financial investment only within the reach of established medical institutions. On the other hand, the proposed FPI-based spirometer can be implemented as a cost-effective solution, considering the method used for the FPI micro-cavity production. Furthermore, alternative interrogation techniques, as described in [30,31], may help reduce the cost even more.

5. Conclusions

In this work, an intrinsic optical fiber FPI-based sensor integrated in a 3D-printed case was developed and evaluated as a spirometry device to assess the respiratory health of individuals. To evaluate the air flow dynamics and the induced mechanical impact in the 3D-printed structure, a simulation study with Solidworks software was performed, validating the described theoretical approach.

To evaluate the suitability of the proposed system to perform spirometry, tests were executed using the proposed spirometer and, for comparison, a commercial unit. The shape of the flow–volume and volume–time curves obtained with the FPI-based system are as expected and show a good agreement with the ones obtained through the commercial spirometer. The pulmonary parameters obtained for the different tests can also be considered within the expected range, as the values of 4.40 L and 6.46 L, for the FEV1 and FVC parameters, respectively, with an FEV1/FVC index of 68.5%. Additionally, an average value of 5.35 L/s was found for the PEF.

cable co-funded by the FEDER-PT2020 partnership agreement under the project UID/EEA/50008/2019.

References

1. Forum of International Respiratory Societies. *The Global Impact of Respiratory Disease*, 2nd ed.; European Respiratory Society: Sheffield, UK, 2017.
2. Santos, U.; Garcia, M.; Braga, A.; Pereira, L.; Lin, C.; André, P.; André, C.; Singer, J.; Saldiva, P. Association between traffic air pollution and reduced forced vital capacity: A study using personal monitors for outdoor workers. *PLoS ONE* **2016**, *11*, e0163225. [CrossRef]
3. McGeachie, M.J.; Yates, K.P.; Zhou, X.; Guo, F.; Sternberg, A.L.; Van Natta, M.L.; Wise, R.A.; Szefler, S.J.; Sharma, S.; Kho, A.D. Patterns of growth and decline in lung function in persistent childhood asthma. *N. Engl. J. Med.* **2016**, *374*, 1842–1852. [CrossRef]
4. Quanjer, P.; Stanojevic, S.; Cole, T.; Baur, X.; Hall, G.; Culver, B.; Enright, P.; Hankinson, J.; Ip, M.; Zheng, J.; et al. Multi-ethnic reference values for spirometry for the 3–95-yr age range: The global lung function 2012 equations. *Eur. Respir. J.* **2012**, *40*, 1324–1343. [CrossRef]
5. Carpenter, D.; Jurdi, R.; Roberts, C.; Hernandez, M.; Horne, R.; Chan, A. A review of portable electronic spirometers: Implications for asthma self-management. *Curr. Allergy Asthmr. R.* **2018**, *18*, 53. [CrossRef]
6. Zhou, P.; Yang, L.; Huang, Y. A smart phone based handheld wireless spirometer with functions and precision comparable to laboratory spirometers. *Sensors* **2019**, *19*, 2487. [CrossRef] [PubMed]
7. Laghrouche, M.; Saddaoui, R.; Mellal, I.; Nachef, M.; Ameur, S. Low-cost embedded spirometer based on commercial micro machined platinum thin film. *Procedia Eng.* **2016**, *168*, 1681–1684. [CrossRef]
8. Domingues, M.; Alberto, N.; Leitão, C.; Tavares, C.; Rocon, E.; Radwan, A.; Sucasas, V.; Rodriguez, J.; André, P.; Antunes, P. Insole optical fiber sensor architecture for remote gait analysis—An e-Health solution. *IEEE Internet Things J.* **2019**, *6*, 207–214. [CrossRef]
9. Liang, Y.; Mazzolini, A.P.; Stoddart, P.R. Fibre Bragg grating sensor for respiratory monitoring. In Proceedings of the ACOFT/AOS 2006—Australian Conference on Optical Fibre Technology/Australian Optical Society, Melbourne, VIC, Australia, 10–13 July 2006; pp. 75–77.
10. Manujło, A.; Osuch, T. Temperature fiber Bragg grating based sensor for respiration monitoring. In Proceedings of the Photonics Applications in Astronomy, Communications, Industry, and High Energy Physics Experiments 2017, Wilga, Poland, 7 August 2017.
11. Manjusha, S.; Preethi, S.; Swapna, M.; Sankararaman, S. Fiber sensor based pulmonary function test. *Int. J. Curr. Res. Rev.* **2017**, *9*, 41–43.
12. Höglinger, M.; Wiesmayr, B.; Baumgartner, W.; Stadler, A. A rapid and low-cost lung function testing method based on an optical flow sensor. In *IFMBE Proceedings, Proceedings of the VIII Latin American Conference on Biomedical Engineering, Cancún, Mexico, 2–5 October 2019*; Springer: Cham, Switzerland, 2020; pp. 469–477.
13. Zhao, Y.; Chen, K.; Yang, J. Novel target type flowmeter based on a differential fiber Bragg grating sensor. *Measurement* **2005**, *38*, 230–235. [CrossRef]
14. Ambastha, S.; Umesh, S.; Maheshwari, U.; Asokan, S. Pulmonary function test using fiber Bragg grating spirometer. *J. Light. Technol.* **2016**, *9*, 5682–5688. [CrossRef]
15. Nepomuceno, A.C.; Alberto, N.; André, P.; Antunes, P.; Domingues, M.F. 3D printed spirometer for pulmonary health assessment based on fiber Bragg gratings. *IEEE Sens. J.* **2021**, *21*, 4590–4598. [CrossRef]
16. Zhao, Y.; Wang, P.; Lv, R.; Liu, X. Highly sensitive airflow sensor based on Fabry–Perot interferometer and Vernier effect. *J. Light. Technol.* **2016**, *34*, 5351–5356. [CrossRef]
17. Lee, C.; Liu, K.; Luo, S.; Wu, M.; Ma, C. A hot-polymer fiber Fabry–Perot interferometer anemometer for sensing airflow. *Sensors* **2018**, *17*, 2015. [CrossRef] [PubMed]
18. Zhou, B.; Jiang, H.; Lu, C.; He, S. Hot cavity optical fiber Fabry–Perot interferometer as a flow sensor with temperature self-calibrated. *J. Light. Technol.* **2016**, *34*, 5044–5048. [CrossRef]
19. Mireles, J. Micromachined sensor design for optical-fiber flow measurement. *Sens. Rev.* **2005**, *25*, 33–39. [CrossRef]
20. Xu, J.; Wang, X.; Cooper, K.L.; Wang, A. Miniature all-silica fiber optic pressure and acoustic sensors. *Opt. Lett.* **2005**, *30*, 3269–3271. [CrossRef]

21. Murphy, K.A.; Gunther, M.F.; Vengsarkar, A.M.; Claus, R.O. Quadrature phase-shifted, extrinsic Fabry–Perot optical fiber sensors. *Opt. Lett.* **1991**, *16*, 273–275. [CrossRef]
22. Wang, W.; Li, F. Large-range liquid level sensor based on an optical fibre extrinsic Fabry–Perot interferometer. *Opt. Lasers Eng.* **2014**, *52*, 201–205. [CrossRef]
23. Islam, M.; Ali, M.; Lai, M.-H.; Lim, K.-S.; Ahmad, H. Chronology of Fabry–Perot interferometer fiber-optic sensors and their applications: A review. *Sensors* **2014**, *14*, 7451–7488. [CrossRef]
24. Antunes, P.; Domingues, M.F.; Alberto, N.; André, P. Optical fiber microcavity strain sensors produced by the catastrophic fuse effect. *IEEE Photonics Technol. Lett.* **2014**, *26*, 78–81. [CrossRef]
25. Munson, B.; Yong, D.; Okiishi, T.; Huebsch, W. *Fundamentals of Fluid Mechanics*, 6th ed.; Wiley & Sons: Hoboken, NJ, USA, 2006.
26. Fahy, F.; Thompson, D. (Eds.) *Fundamentals of Sound and Vibration*, 2nd ed.; CRC Press: London, UK, 2015.
27. Shaari, M.; Archansdran, S.; Rosly, M. Characterization of double layer IPMC bending actuation. *ARPN J. Eng. Appl. Sci.* **2016**, *11*, 6536–6540.
28. Beer, F.; Dewolf, J.E., Jr.; Mazurek, D. *Mechanics of Materials*, 6th ed.; McGraw-Hill: New York, NY, USA, 2012.
29. Antunes, P.; Domingues, F.; Granada, M.; André, P. Mechanical properties of optical fibers. In *Selected Topics on Optical Fiber Technology*; Yasin, M., Harun, S.W., Arof, H., Eds.; IntechOpen: Rijeka, Croatia, 2012; Chapter 19. [CrossRef]
30. Domingues, M.F.; Tavares, C.; Alberto, N.; Radwan, A.; André, P.; Antunes, P. High rate dynamic monitoring with Fabry–Perot interferometric sensors: An alternative interrogation technique targeting biomedical applications. *Sensors* **2019**, *19*, 4744. [CrossRef] [PubMed]
31. Díaz, C.A.R.; Marques, C.A.F.; Domingues, M.F.F.; Ribeiro, M.R.N.; Frizera-Neto, A.; Pontes, M.J.; André, P.S.; Antunes, P.F.C. A cost-effective edge-filter based FBG interrogator using catastrophic fuse effect micro-cavity interferometers. *Measurement* **2018**, *124*, 486–493. [CrossRef]